THE UNIVERSITY *of* ADELAIDE

Development of Technologies for Active Wavefront Control of Advanced Gravitational Wave Detectors

by

Huy Tuong Cao

A thesis submitted to the Department of Physics in partial fulfillment of the requirements for the degree of Doctor of Philosophy

December 9, 2019

Supervisors

Prof. Peter Veitch

Prof. David Ottaway

Abstract

The era of gravitational-wave astronomy started with the detection of a binary black hole coalescence on the 14th of September 2015 by the Advanced Laser Interferometer Gravitational-wave Observatory (aLIGO). By the end of 2017, a total number of 11 gravitational wave events have been detected by LIGO and Virgo detectors. One of these events, GW17081, produced by the coalescence of a binary neutron star signaled the dawn of multi-messenger gravitational astronomy, revealing invaluable information about the physics occurring in such cataclysmic event. The work presented in this thesis is part of the ongoing global effort to improve the sensitivity of current detectors and thus improve both the detection rates and the information that can be gleaned from each detection.

The sensitivity of terrestrial interferometric detectors are broadly limited by coating thermal noise and quantum noise. Increasing the circulating laser power and injecting vacuum-squeezed light are employed to reduce the quantum noise. However, the ability to implement these measures and their efficacy is fundamentally limited by absorption-induced wavefront distortion within the interferometer. At the time of writing this thesis, aLIGO detectors are struggling to increase the input power above approximately 30 W and the current observed level of squeezing at aLIGO Livingston and Hanford Observatories are 3dB and 2.2 dB respectively, partly due to wavefront mismatch. New technologies are urgently required to diagnose these issues.

In this thesis, I will will describe the development of a new technologies for the solution of this problem: an advanced "phase camera" that can examine individual RF sideband fields used to control and sense the interferometer and new adaptive optics for active wavefront control and mode-matching within the interferometer.

The new phase camera measures the complex amplitude of a coherent field that is frequency-offset from a reference field, and records the transverse profile with high spatial and temporal resolution. Furthermore, it does so without the use of scanning mirrors and thus is suitable for use during both detector commissioning and low-noise operation.

This thesis also describes the development of new thermally-actuated mirrors for adaptive wavefront control and mode matching in aLIGO. The two designs presented are the thermal-bimorph mirror and the compression-fit mirror. Both of

which show a large and linear actuation range, and low higher-order aberrations. They are currently scheduled for deployment to assist with mode matching between the squeezed light source and the signal recycling cavity of aLIGO and can be extended to other optical interfaces during the detectors A+ upgrade.

Declaration

I certify that this work contains no material which has been accepted for the award of any other degree or diploma in my name, in any university or other tertiary institution and, to the best of my knowledge and belief, contains no material previously published or written by another person, except where due reference has been made in the text. In addition, I certify that no part of this work will, in the future, be used in a submission in my name, for any other degree or diploma in any university or other tertiary institution without the prior approval of the University of Adelaide and where applicable, any partner institution responsible for the joint-award of this degree.

I acknowledge that copyright of published works contained within this thesis resides with the copyright holder(s) of those works.

I also give permission for the digital version of my thesis to be made available on the web, via the University's digital research repository, the Library Search and also through web search engines, unless permission has been granted by the University to restrict access for a period of time.

I acknowledge the support I have received for my research through the provision of an Australian Government Research Training Program Scholarship.

Huy Tuong Cao

September 2019

Acknowledgement

The completion of this thesis would not have been possible without the the support, assistance, and encourage of many people, both in lab, at university and in real life. I would try my best to thank them all here, and my sincere apologies if I have missed anyone.

First and foremost, I would like to thank my supervisors: Peter Veitch and David Ottaway, who have been providing constant support throughout the last three and a half year, encouraging me and trusting me to explore different ideas, creating new opportunities that I am privileged to be a part of.

To Peter: you have always been there since day one and provided me with guidance since my third year as an undergraduate. Talking to you has always been inspiring me to learn more not just about gravitational waves but all areas of physics. I can't thank you enough for the opportunity you have created for me in those years.

To Dave: thank you for providing me with invaluable technical insights of optics, interferometry and electronics. I aspire to one day have half the knowledge that you do.

I also owed a large part of my PhD to Bob and Ramona. Thank you for your amazing work, without your support, I don't think I could have got any results.

Amongst everyone that I have the opportunities to work with, I have to thank Dan, Seb, Deeksha and Craig and Tom. You guys made everyday at work full of fun and excitement. I cannot imagine how I would have possibly made it through my PhD with you. Thank you Dan for always be there in the lab with me up

until 3 am in the morning and out in the middle of nowhere hiking on the rare occasions. I cannot wait to work and learn more from you. Thank you Seb for your logical insights, amazing CAD skills and not minding staying up late for checking my SAMS presentation. Thank you Craig for being a '"father-figure" that always gives great advice and but a smile on my face. Thank you Tom for being my Jaycar buddy and make me constantly learn new electronics knowledge. And to Deeksha, you know you hold a special place in my heart because without you, I don't think I could have made it through.

I have been also extremely fortunate to be a part of OzGrav Adelaide. I would like extend my gratitude to Georgia, Mitchell, Alexei, Ethan, Zac, Miftar for making university, and especially G15 such an enjoyable workplace.

I could not have done this PhD without the support from many of my wonderful friends. Thank you Bowie, Swathi, Tash ,Oli, Andy, Sai, Rohan, Rosie, Lachlan, Katrina, Mitchell,Rosemary and Hayley, university would have been very different without you guys; and I promise I will bake more often in the near future.

Finally, I would like to thank my family for their support over the years. Especially to Mum and Dad, thank you for all the sacrifice that you've made, for the trust that you have in me. I am sorry if can't contact as often as I would like to but I would like you to know my heart is always there with you.

Contents

List of Figures

List of Tables

Acronyms

HWS Hartmann Wavefront Sensor

ITMX Input Test Mass X

ITMY Input Test Mass Y

ETMX End Test Mass X

ETMY End Test Mass Y

SLED Superluminiscent Lighting Emitting Diode

AWC Active Wavefront Control

CFM Compression fit Mirror

QPD Quadrant Photodetector

LSC Length Sensing and Control

ASC Alignment Sensing and Control

BS Beam-splitter

DARM Differential arm length

CARM Common arm length

MICH Michelson cavity length

PRCL Power recycling cavity length

SRCL Signal recycling cavity length

IMC Input mode cleaner

OMC Output mode cleaner

REFL Reflection port

POP Power recycling pick-off

LPF Low-pass filter

EOM Electro-optic modulator

PC Pockels Cell

HWP Half-wave plate

QWP Quarter-wave-plate

PBS Polarising beam-splitter

DM Deformable mirror

MEMS Microelectromechanical System

UHV ultra high vacuum

AO Adaptiv Optics

PDH Pound-Drever-Hall (locking)

EOM Electro-optic Modulator

SQZ Squeezer

FC Filter Cavity

HAM Horizontal Access Module

ISI Internal Seismic Isolation

HTTS HAM Tip-Tilt Suspension

HDS HAM Double Suspension

BHD/BHR Balanced Homodyne Detection/ Balanced Homodyne Readout

OPO Optical Parametric Oscillator (for use of squeezed light)

VOPO In-vacuum OPO

OFI Output Faraday Isolator

Chapter 1

Introduction

September 14th 2015 marked the emergence of gravitational wave astronomy with a detection of gravitational waves from a collision of two black holes by the Laser Interferometer Gravitational Wave Observatorty (LIGO) [2]. The detection heralded a new window for mankind to peer into the universe and to study the physical processes of cataclysmic events that cannot be replicated here on Earth. Since then, within the span of two years, that event was followed by nine other detections of binary black hole mergers (GW151012 [3], GW151226 [4], GW170104 [6], GW170608 [5], GW170729, GW170809, GW170814 [7], GW170818 and GW170823) and one binary neutron star merger, GW170818 [8]. This detection of the binary neutron star merger has ushered in the new era of multi-messenger astronomy. Subsequent identification of transient counterpart across the electromagnetic spectrum further supported the interpretation of this event as a binary neutron star merger. These observations also confirmed that these mergers of neutron stars are significant source of r-processed elements that are heavier that iron, including gold and platinum [83]. At the time of writing this thesis, more than 24 mergers have been detected during the third observation run of LIGO and Virgo. The ever-increasing sensitivity of interferometric gravitational wave detector promises exciting new physics for decades to come.

Section 1.1 of this chapter summarises the physics of gravitational waves, which includes their formulation in Einstein's theory of general relativity and their generation by astrophysical sources. Section 1.2 focuses on the principle of gravitational wave detection using laser interferometry, its technical noise sources and control challenges.

1.1 Gravitational waves

This section provides a brief introduction to gravitational waves. Comprehensive details on treatment of gravitational waves in general relativity framework and cosmology can be found in various textbooks, including Weinberg [210], Misner et al. [147], Maggiore [134] and Schutz [178].

1.1.1 Gravitational wave as a solution to Einstein Field Equations

In 1915, Albert Einstein published his revolutionary theory of general relativity that describes gravity in terms of geometry of spacetime, which remains as the most complete description to date [85].

The main results of general relativity are summarised by a set of 10 coupled second-order differential equations, which is referred to as the Einstein Field Equations, and can be written in a simplified form as:

$$G_{\mu\nu} = \frac{8\pi G}{c^4} T_{\mu\nu} \tag{1.1}$$

where $G_{\mu\nu}$ is the Einstein tensor which is a function of metric tensor $g_{\mu\nu}$ and its derivatives, G is the Newtonian gravitational constant, c is the speed of light, and $T_{\mu\nu}$ is the stress-energy tensor. This set of equations fully describe the interaction between space-time and mass-energy and allow calculation of the metric tensor $g_{\mu\nu}$ given some distribution of mass and energy.

To derive gravitation waves, we consider a small perturbation $h_{\nu\mu}$, $|h_{\nu\mu}| \ll 1$

applied to an otherwise flat space-time, or the Minkowsky space-time $\eta_{\mu\nu}$:

$$g_{\mu\nu} = h_{\nu\mu} + \eta_{\mu\nu} \tag{1.2}$$

Under the Lozentz gauge, the vacuum solution where $T_{\mu\nu} = 0$ to equations the linearised Einstein's equation 1.1 takes the following form [61]:

$$\left(-\frac{1}{c^2}\frac{\partial^2}{\partial t^2} + \frac{\partial^2}{\partial x_i^2}\right) h_{\mu\nu} \tag{1.3}$$

which takes the form of a three-dimensional wave equation, describing propagation of the gravitational wave $h_{\mu\nu}$. For a coordinate system in which the gravitational wave is travelling along the z-direction, the plane wave solution to this equation is given by:

$$h_{\mu\nu} = A_{\mu\nu} e^{i\omega_g(t-z/c)} \tag{1.4}$$

$$A_{\mu\nu} = \begin{pmatrix} 0 & 0 & 0 & 0 \\ 0 & h_+ & h_\times & 0 \\ 0 & h_\times & -h_+ & 0 \\ 0 & 0 & 0 & 0 \end{pmatrix} \tag{1.5}$$

where ω_g is the angular frequency of the gravitational wave, h_+ and $h_\times$ are coefficients denoting two independent polarisations: plus- and cross- modes respectively.

The space-time interval between two separated events in described via the metric tensor $g_{\mu\nu}$ as:

$$ds^2 = g_{\mu\nu} dx^\mu dx^\nu \tag{1.6}$$

Now, consider the case where two free particles at two separated locations: one at the coordinate origin and the other at $x^i = (L, 0, 0)$, both initially at rest. The proper

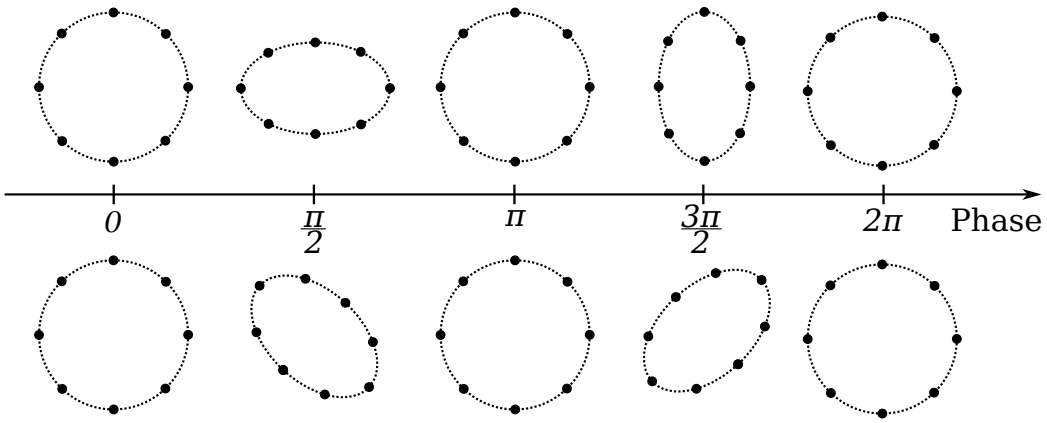

Figure 1-1: A ring of free-floating test particles are being stretched and squashed by a gravitational wave of *plus*- and *cross*- polarisations travelling in a direction that is normal to the page.

length δl between two particles as a gravitational wave passes through is [178]:

$$\begin{aligned}\delta l &= \int \sqrt{|ds^2|} = \int |g_{\mu\nu} dx^\mu dx^\nu|^{1/2} \\ &= \int_0^L |g_{11}|^{1/2} dx \approx \left[1 + \frac{1}{2} h_{11}(x=0)\right] L \\ &= \left[1 + \frac{1}{2} h_+ \sin(2\phi) + \frac{1}{2} h_\times \cos(2\phi)\right] L\end{aligned} \tag{1.7}$$

which is the sum of initial separation and a term that is proportional to the gravitational wave. The angle ϕ is the angle between the observer x, y-axes and the gravitational wave polarisation axes. This expression implies that the perturbation would be more easily detected by a larger detector (greater L), and thus the gravitational wave can be referred to as a strain wave.

If there are now a set of particles distributed on a xy-plane through which a z-propagating gravitational wave is passing, Eq. 1.4 and 1.5 show that there are two independent polarisations of the gravitational wave that will affect the proper distance between these particles. Assuming that the initial distance between these

particles is $L^1 = (L^x, L^y, 0)$, then the displacement $\mathbf{\Delta L}$ is:;

$$\begin{aligned}\begin{bmatrix}\Delta L^x \\ \Delta L^y\end{bmatrix} &= \frac{1}{2}\begin{bmatrix}h_+ & h_\times \\ h_\times & -h_+\end{bmatrix}\begin{bmatrix}L^x \\ L^y\end{bmatrix} e^{i\omega_g(t-z/c)} \\ &= -\frac{1}{2}h_+\begin{bmatrix}L^x \\ L^y\end{bmatrix} e^{i\omega_g(t-z/c)} + \frac{1}{2}h_\times\begin{bmatrix}L^y \\ L^x\end{bmatrix} e^{i\omega_g(t-z/c)}\end{aligned} \tag{1.8}$$

The response of a ring of free-floating test particle to gravitational waves plus- and cross-polarisations is illustrated in Fig. 1-1. Particles separated in a direction transverse to direction of wave propagation have maximum change in separation at four angles. Hence the response of the ring of test particle is quadrupole. By reciprocity, a quadrupolar motion of masses is thus required to generate gravitational waves [178].

1.1.2 Astrophysical gravitational wave sources

In the previous section, gravitational waves are shown to be a solution to Einstein Field Equation. The questions that remain are what types of sources can generate gravitational waves and what strengths can we expect.

The order of magnitude of h can be estimated using the following approximation [180]:

$$h \sim \frac{r_{\text{sch}}}{r}\left(\frac{v}{c}\right)^2 \tag{1.9}$$

where r is the distance between the system that generates gravitational wave and the observer; r_{sch} is the Schwarzchild radius that is associated with the characteristic mass M in quadrupole fluctuation, $r_{\text{sch}} = 2GM/c^3$; and v is the characteristic velocity of the mass. We can also parameterise the efficiency of gravitational wave emission ϵ by writing [135]:

$$\Delta E = \epsilon M c^2, \quad \epsilon \sim \left(\frac{r_{\text{sch}}}{R}\right)^{7/2} \tag{1.10}$$

where ΔE is the energy of emitted gravitational wave, and R is the characteristic

spatial size of the system. For an astronomical system, which is usually bounded by its self-gravity, the kinetic energy and gravitational potential are comparable, such that:

$$Mv^2 \sim \frac{GM^2}{R} \tag{1.11}$$

Combining Eq. 1.9, 1.10 and 1.11, we obtain:

$$h \sim \frac{r_{\text{sch}}}{2r}\epsilon^{2/7} \sim 1.5 \times 10^{-21} \left(\frac{\epsilon}{0.1}\right)^{2/7} \frac{(M/M_\odot)}{(r/17\,\text{Mpc})} \tag{1.12}$$

where the characteristic mass has been scaled by solar mass $M_\odot$, and distance r is scaled by the distance from Earth to the Virgo cluster. Therefore, one can see that gravitational wave strain is minuscule, even if an optimistic efficiency of 10% is used. In the GW150914 event, even though a total $3M_\odot c^2$ of energy was released as gravitational waves, the strain h of this event at Earthwas only $\sim 10^{-21}$ [3]. Thus, detectable sources of gravitational waves are astrophysical in nature, and typically involve extreme dynamics. Here, we briefly review known sources that have been detected and could/ might potentially be detected by terrestrial gravitational wave detectors. Further details of this topic can be found in references [79, 135, 176].

Compact binary coalescences (CBC)

CBC's are the coalescences of two compact objects. These compact objects can be either neutron stars or black holes, and even possibly dense exotic forms of matter. These sources generate a distinctive chirp waveform signal as a function of time and frequency. The chirp waveform can be broken down to three stages: *inspiral*, *merger* and *ringdown*.

During the inspiral phase of a CBC, the two compact bodies are widely separated. They orbit slowly and emit weak gravitational waves. During this process, the separation distance of the two bodies gradually becomes smaller and the orbital frequency increases.

In the merger phase, the orbital radius has become smaller than the innermost stable circular orbit, where a stable circular orbit is no longer allowed. The two

compact bodies then collide and coalesce. The strongest gravitational waves are generated during this phase.

Finally, after merging, the highly asymmetric compact object oscillates, thus emitting gravitational waves which damp the oscillation as it returns to equilibrium. The gravitational wave signal during this phase thus resembles a damped oscillating signal.

These characteristic phases of gravitational waves can be observed in the strain signal of the first detection of a binary black hole inspiral GW150914, as shown in Fig. 1-2.

Detection of such CBC systems allows us to learn more about physical processes at extreme dynamical conditions, including formation mechanism of binary blackholes, and equations of state of neutron stars. Coalescence of binary neutron stars, where electromagnetic counterparts are potentially identified, can also serve as a standard siren to measure cosmological constant such as the Hubble constant [91, 78].

Bursts

Bursts of gravitational waves are expected to originate from astrophysical sources such as spherically asymmetric core-collapse supernovae. The waveform of bursts signals are generally not well-understood. At its design range of sensitivity, aLIGO should be able to detect these sources out to 20 Mpc, where there should be a few events per year [80]. Detection of gravitational wave from these sources will help to understand core collapse dynamics beyond electromagnetic observations, since electromagnetic signals arise from charged particles, whereas gravitational waves originate from mass distribution [168].

Spinning compact stars

Spinning compact stars such as pulsars (spinning neutron stars) are expected to be sources of continuous gravitational waves at an approximately constant =and well-defined frequency. Generation of gravitational waves by these systems are thought

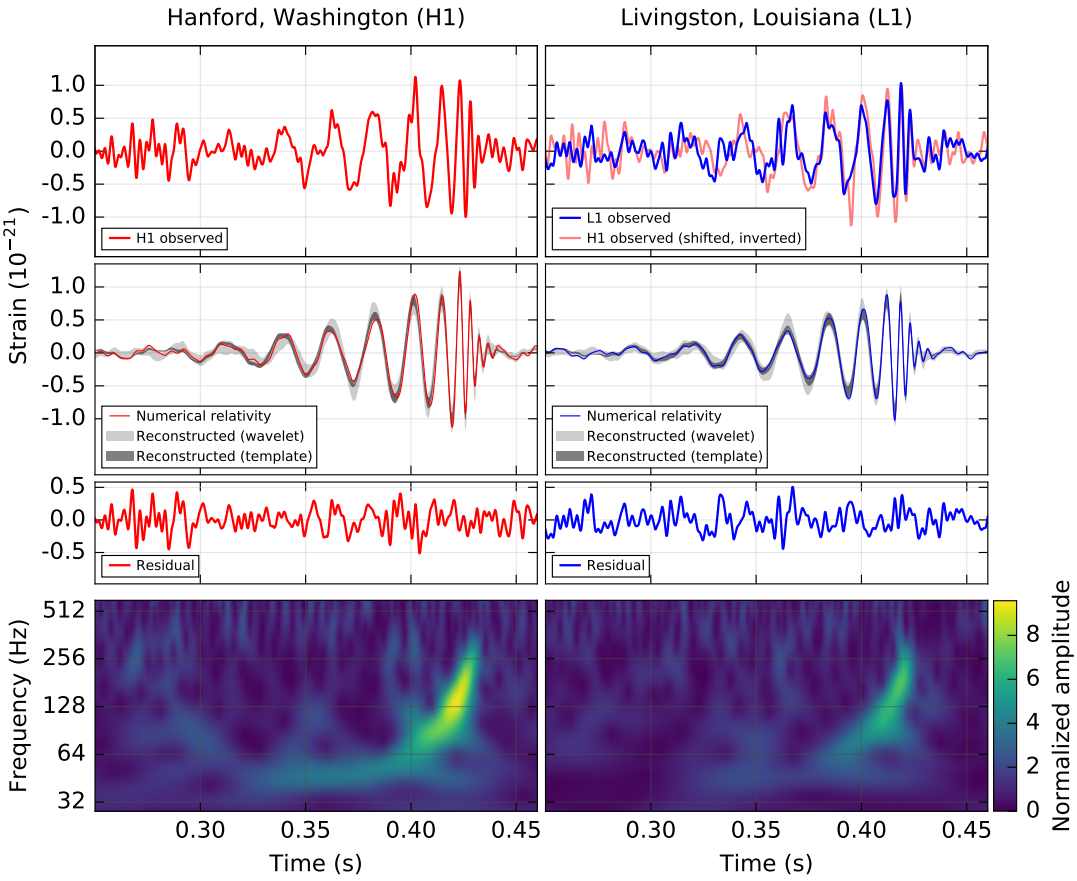

Figure 1-2: The gravitational wave event GW150914 observed by the LIGO Hanford (left column panel) and Livingston (right column panel) detectors [2]. Times are shown relative to September 14, 2015 at 09:50:45 UTC. *Top row:* gravitational wave strain observed by each detector. *Second row*: Numerical relative simulation of the waveform for the GW150914 system of binary black hole coalescence (solid line). *Third row*: Residuals after subtraction of numerical relativity waveform from 30-350 Hz band-passed strain signal. *Bottom row:* A spectrogram of the strain data, showing the characteristic chirp signal of the compact binary coalescence as the signal frequency increases over time.

to result from small "mountains" on the surface of these stars, or due to slight wobble in their rotations. Gravitational waves from these sources are generally much weaker and therefore are more challenging to detect. Long integration time, typically of the order of a few months or years, are needed to build up sufficient signal power [21].

Stochastic gravitational wave background

A stochastic gravitational wave background is expected result from the superposition of a large number of unresolved gravitational wave sources of astrophysical and cosmological origin. Detection of this source should allow access to information about evolution of the universe during its earliest epochs. Recent CBC detections have refined the predictions of stochastic background due to these sources, and suggest that it can be detected in a near future [10].

1.2 Detection of gravitation wave with laser interferometry

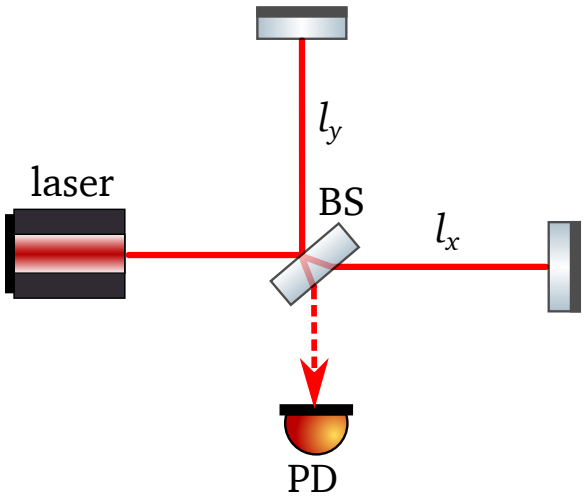

Figure 1-3: Optical configuration of a standard Michelson interferometer: A laser is split into two by a 50/50 beam splitter (BS), which propagate down each arm to reflect off mirrors. The beams return to beam splitter and recombine. A photodetector (PD) is placed at the antisymmetric port (AS).

Following from Section 1.1, it is clear that gravitational wave should be detected by measuring the apparent positions of one or more free-floating test particles in a plane normal to the direction of propagation of a gravitational wave. A classic Michelson interferometer, such as that shown in Fig. 1-3, would appear suitable for detecting a passing gravitational wave.

Consider a gravitational wave propagating towards the interferometer directly from above with a polarisation that aligns with the interferometer. From Eq. 1.7, the time taken for the photons to reach end mirrors in each arm are:

$$\begin{aligned}\tau_x &= 2\frac{l_x}{c} + \frac{1}{2}\int_0^{l_x/c} dx\; h(t) + h(t + l_x/c) \\ \tau_y &= 2\frac{l_y}{c} + \frac{1}{2}\int_0^{l_y/c} dy\; h(t) + h(t + l_y/c)\end{aligned} \tag{1.13}$$

If the time of flight of the photon is much shorter than the period of gravitational wave then $h(t) \approx h(t + l_i/c)\; i = x, y$, then the difference in time of flight of photons in the two arms is:

$$\Delta\tau = \tau_x - \tau_y = \frac{2l}{c}h \tag{1.14}$$

where $l_x = l_y = l$. This expression can be rewritten in terms of differential phase shift [176]:

$$\Delta\Phi = \Phi(\tau_x) - \Phi(\tau_y) = \frac{4\pi}{\lambda}hl \tag{1.15}$$

where λ is wavelength of laser light.

1.2.1 Basic sensitivity limitations

Eq. 1.15 implies the detection of gravitational waves relies on the ability to measure small differential phase shift $\Delta\Phi$ using a Michelson interferometer.

The laser beam E_0 incident on the beam splitter in Fig. 1-3 is divided into two parts that propagate down the x and y arms. The phase of the electromagnetic wave changes by ϕ_x andϕ_y as they travel to the mirror where they are reflected and recombine at the beam splitter.

A photodetector at the antisymmetric port detects the integrated optical power P_{AS}, which is related to the two fields emerging from the beam splitter E_x and E_y by:

$$P_{AS} = \int_\Sigma |E_x + E_y|^2 dA = P_{in}\sin^2(\Delta\Phi) = P_{in}\sin^2(k_x l_x - k_y l_y) \tag{1.16}$$

where $k_x = k_y = k = 2\pi/\lambda$

The question of the minimum detectable gravitational wave amplitude is therefore equivalent to the minimum change in optical power that can be detected. This therefore suggests that there is fundamental limit to measurement precision: photon shot noise. Eq. 1.16 implies that the optimal operating point is when $P_{AS} = P_{\text{in}}/2$, where dP_{AS}/dl is maximum, but this is a "naive" choice of operating point as will be discussed further later. Under this assumption and using Poisson statistics of photon counting, an expression for sensitivity due to photon shot noise can be written as [176]:

$$h_{\text{shot}}(f) = \frac{1}{L}\sqrt{\frac{\hbar c\lambda}{2\pi P_{\text{in}}}} \tag{1.17}$$

where $\hbar$ is Planck constant. To set a sense of scale, we can rewrite Eq. 1.17 as:

$$h_{\text{shot}} = 1.8 \times 10^{-20} Hz^{-1/2} \left(\frac{4km}{l}\right) \sqrt{\frac{\lambda}{1.064\mu m}} \sqrt{\frac{1\,\text{W}}{P_{\text{in}}}} \tag{1.18}$$

Thus there is little margin to spare if we want to detect gravitational waves confidently. Furthermore, other sources of noise have not been included here.

An important consequence of Eq. 1.18 is that the sensitivity of our interferometer improves with increasing input power. In the next sections, we will briefly review the optical configuration of aLIGO, whose variations from the "naive" simple Michelson interferometer enable greater sensitivity.

1.2.2 Advanced LIGO optical configuration

A simplified schematic of the optical configuration of Advanced LIGO (aLIGO) is shown in Fig. 1-4. aLIGO is a dual-recycled Michelson interferometer that differs from a standard Michelson interferometer (shown in Fig. 1-4 inset) by inclusion of Fabry-Pérot cavities in its 4-km-long arms, as well as the partially reflective mirrors: "power recycling mirror" (PRM) and "signal recycling mirror" (SRM) on the symmetric and anti-symmetric ports, to form power- and coupled-resonant cavities.

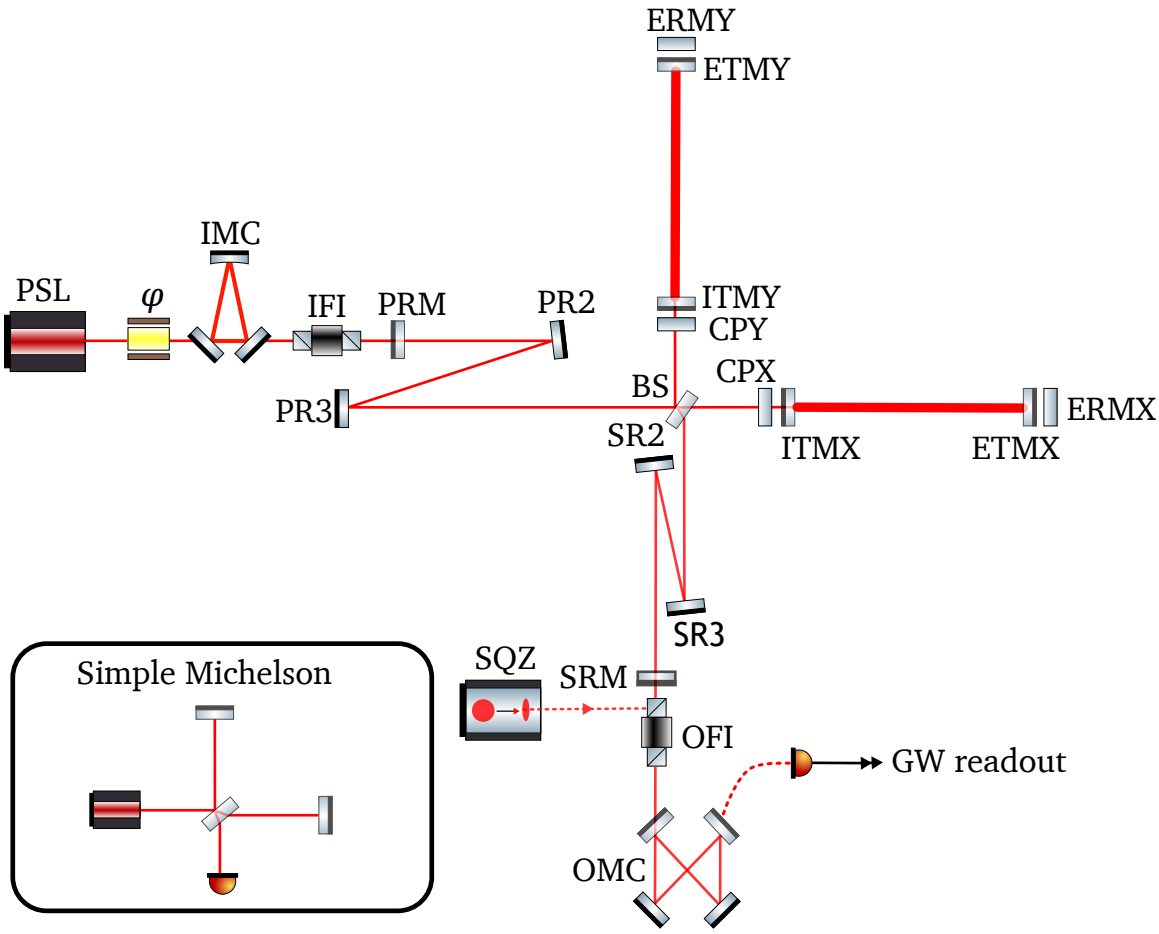

Figure 1-4: Simplified schematic of Advanced LIGO optical configuration, adopted from [1]. The inset shows schematic of a simple Michelson interferometer for comparison. PSL: pre-stabilised laser; φ: phase modulator; IMC: input mode cleaner; PRM,PR2,PR3: power-recycling mirrors; SRM, SRM2, SRM3: signal-recycling mirrors; BS: beam splitter; CPX, CPY: compensation plate X and Y; ITMX, ITMY: input test mass X and Y; ETMX, ETMY: end test mass X and Y; ERMX, ERMY: end reaction mass X and Y; IFI, OFI: input/output mode cleaner; OMC: output mode cleaner; SQZ: squeezed light source.

aLIGO also operates on dark fringe where the nominal optical power at the anti-symmetric (AS) port is close to zero instead of the 3dB point where $P_{AS} = P_{in}/2$ as mentioned in the previous section. Consider a small differential phase shift $\Delta\phi$ caused by a passing gravitational wave, the optical power detected at the AS port is:

$$P_{\text{AS | Bright}} \simeq \frac{P_{in}}{2}(1 - 2\Delta\phi) \tag{1.19}$$

There is thus a large DC term that in dependent on the input power and gen-

erally, it is more challenging to detect small change in a large signal. Furthermore, the reliance on the output power as a measurement of phase means that we are not able to distinguish between a change in laser power and a change in $\Delta\phi$ corresponding to gravitational wave. We thus are susceptible laser noise. LIGO thus operates on the dark fringe at which the power, as well as common mode noise such as laser noise are reflected to symmetric port instead.

The problem with operation at an absolute dark fringe is that the response to phase shift is very small as $dP_{AS}/dl = 0$. The initial and enhanced LIGO remedied this condition by using radio frequency heterodyne detection in which the input laser is phase modulated [176]. In aLIGO, this is replaced by DC readout, in which there is a microscopic offset in the differential length introduced to allow a very small amount of input laser field to leak through to the AS port, which beats against the gravitational wave sideband to generate the gravitational wave signal seen by the AS photodetector [92].

Fabry-Pérot cavity arms

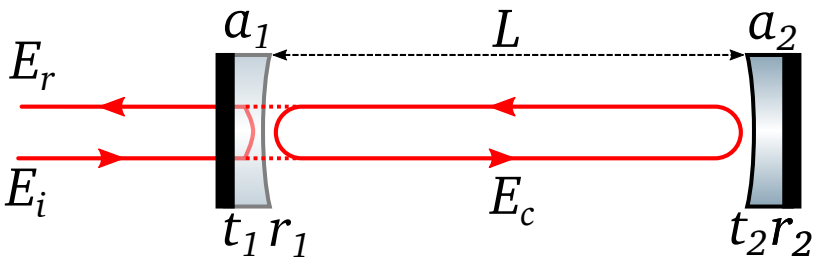

Figure 1-5: Diagram of a simple Fabry-Pérot cavity

Since the strength of gravitational wave signal is proportional to the optical path length difference between the arms. This can be increased by introducing a Fabry-Pérot cavity into each arm of the interferometer, assuming that the storage time for the photons is less than half the period of the oscillating gravitational wave.

A schematic of a simple Fabry-Pérot cavity is shown in Fig. 1-5. It consists of two mirrors that have amplitude reflection, transmission and loss coefficients r_i, t_i

and a_i. The mirrors are separated by a distance L.

A field E_i incident on the input mirror is partially reflected and partially transmitted. The field circulating within the Fabry-Pérot for an over-coupled cavity $R_1 < T_2 + A_2 + A_1$ (where $R_i = r_i^2$, $T_i = t_i^2$ and $A_i = a_i^2$) is given by:

$$E_c = \frac{t_1}{1 - r_1\sqrt{1-\mathcal{S}}e^{i2kL}} E_i \tag{1.20}$$

where $\mathcal{S} = A_1 + A_2 + T_2$. If $kL = n\pi$ then the incident field is resonant in the cavity, yielding a power buildup factor $\mathbb{G}$:

$$\mathbb{G} = \frac{P_c}{P_i} = \frac{1 - r_1^2}{(1 - r_1\sqrt{1-\mathcal{S}})^2} \tag{1.21}$$

which is equivalent to the mean number of bounces a photon experiences before escaping the cavity. The storage time of photons in the arm cavity therefore increases at resonance:

$$\tau_s = \left(\frac{L}{c}\right) \frac{\sqrt{r_1}}{1 - r_1\sqrt{1-\mathcal{S}}} = \frac{L}{c}\frac{\mathbb{F}}{\pi} \tag{1.22}$$

where $\mathbb{F}$ is the finesse of the cavity:

$$\mathbb{F} = \frac{\pi\sqrt{r_1}}{1 - r_1\sqrt{1-\mathcal{S}}} \tag{1.23}$$

The reflected field E_r fort a small deviation δx from resonance is given by [15]:

$$\begin{aligned} E_r &= \left(-r_1 + \frac{t_1^2}{1 - r_1 e^{-2ik\delta x}}\right) \\ &\approx 1 - i\frac{t_1^2}{(1-r_1)^2} 2\delta x = 1 - i\mathbb{G}2\delta x \end{aligned} \tag{1.24}$$

The phase angle of the reflected field relative to the incident field is therefore:

$$\Phi = \mathbb{G}k2\delta x \tag{1.25}$$

which is a factor of $\mathbb{G}$ larger than that for a simple Michelson.

The Fabry-Pérot cavity thus amplifies the response to differential length changes

due to the gravitational wave strain. The shot-noise limited sensitivity (Eq. 1.18) is thus improved to:

$$h_{\text{shot}} = \frac{2}{\mathbb{G}L}\sqrt{\frac{\hbar c\lambda}{2\pi P_{\text{in}}}} \tag{1.26}$$

For aLIGO, $\mathbb{G} \sim 268$ and the circulating power within each arm will be ~ 750 kW at design sensitivity. The consequence of this high circulating power will be discussed in the next chapter.

Power-recycled Fabry-Pérot interferometer

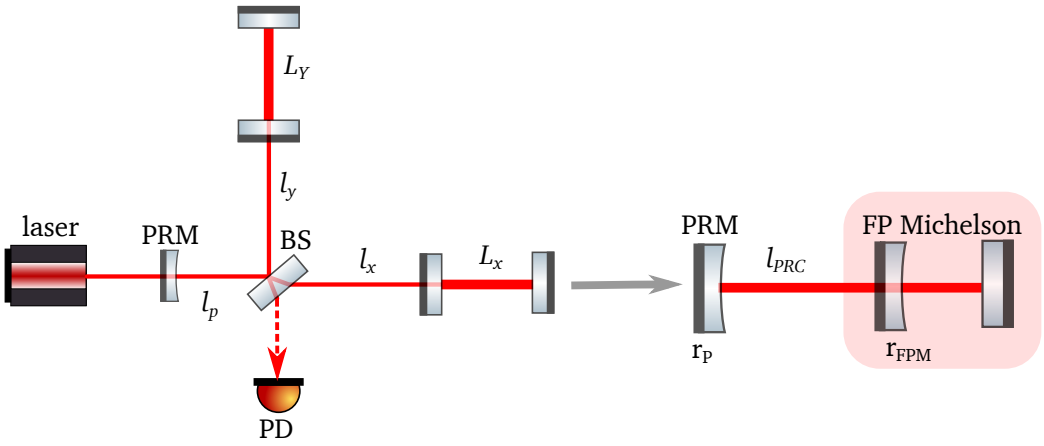

Figure 1-6: A schematic of a power-recycled Fabry-Pérot Michelson interferometer. A partially-reflection coefficient mirror (PRM) with reflectivity r_P is placed at the input of the Michelson, at a distance of l_p from the beam splitter. The Fabry-Perot Michelson can be collapsed to a "mirror" with a frequency-dependent reflection coefficient r_{FPM} at an average distance of $l_{\text{PRC}} = l_p + \frac{l_x+l_y}{2}$ from the PRM [176].

To further improve the sensitivity, advanced gravitational wave detectors employ *dual-recycling* scheme, which includes power-recycling and signal recycling. Here we will briefly discuss the power-recyling and its role in improving the interferometer.

A schematic of a power-recycled Fabry-Pérot Michelson is shown in Fig. 1-6. The dark-fringe operation at the antisymmetric port means that most of the power will propagate back towards the laser. A mirror with amplitude reflection coefficient r_P placed at the input side of the Michelson interferometer reflects power back towards the interferometer, therefore increasing the Michelson optical gain

and reducing the effect of photon shot noise [93, 94].

The mirror, referred to as the power recycling mirror (PRM) forms a coupled-resonant power recycling cavity (PRC), as shown on the right hand side in Fig. 1-6. We can use the standard equations for circulating and reflected fields of a cavity [15] and replace the reflection coefficient of a standard highly-reflecting end mirror with the effective reflection coefficient r_{FPM} of the Fabry-Pérot Michelson to determine the power circulating in the PRC:

$$P_{\mathrm{PRC}} = \frac{1 - r_P^2}{\left[1 - r_P r_{\mathrm{FPM}}\right]^2} P_{\mathrm{in}} \simeq \frac{1 - r_P^2}{\left[1 - r_P\left(1 - \frac{\mathbb{F}}{\pi}\mathcal{S}_{\mathrm{ARM}}\right)\right]^2} P_{\mathrm{in}} \tag{1.27}$$

where $\mathcal{S}_{\mathrm{ARM}}$ is the loss in the arms, either due to mode mismatch, absorption or scattering. Therefore, minimising the loss within the arm is important to achieve a high optical gain in the PRC.

Dual-recycled Fabry-Peŕot interferometer

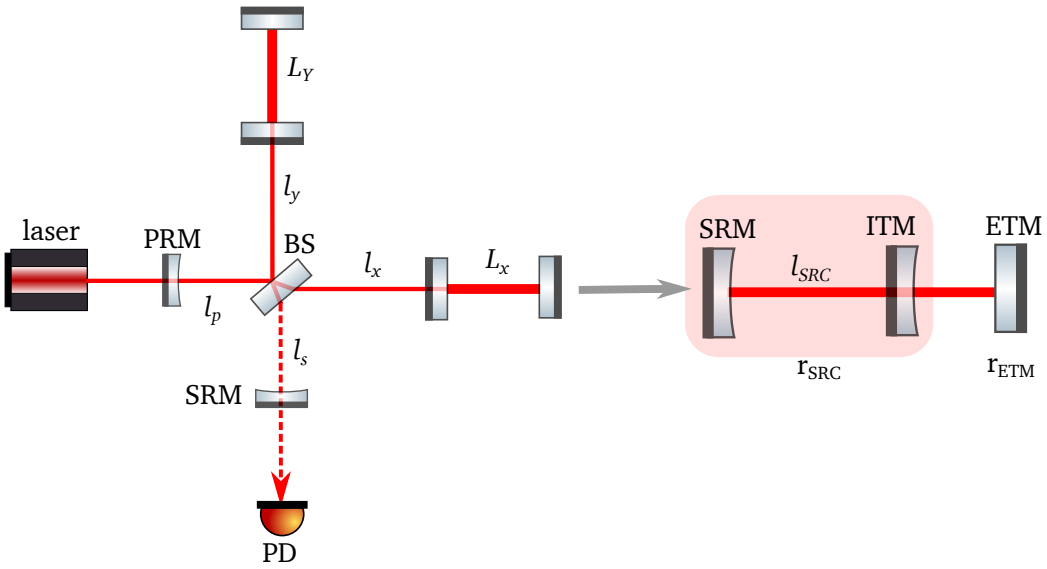

Figure 1-7: A schematic of a dual-recycled Fabry-Pérot Michelson interferometer. An additional partially reflective mirror (SRM) is added to antisymmetric output of the detector to form the signal-recycling cavity. The SRM and ITM can be collapsed into a single system with a reflectivity of r_{SRC} and an average length of $l_{\mathrm{SRC}} = l_s + \frac{l_x + l_y}{2}$, which forms a coupled cavity with the ETM

Addition of a signal recycling mirror (SRM) at the anti-symmetric output of the

detector, as shown in Fig. 1-7 was one of the major differences between the Initial LIGO and Advanced LIGO. This mirror reflects the gravitational wave signal back into the interferometer so itcan be coherently enhanced [26]. The SRM, together with the ITMs, form the signal recycling cavity (SRC) whose microscopic length can be tuned to shape the interferometer's response to gravitational waves. There are two modes of operations; often referred to as the signal recycling and the resonant sideband extraction .

1. **Signal recycling :** In the signal recycling scheme, the SRM couples with the differential Fabry-Pérot arms to form a high finesse cavity. The signal is reflected by the SRM back into the interferometer where it adds coherently with more signal coupled out of the carrier by the action of the gravitational wave [144]. The frequency response of the interferometer in this scheme is narrow.

2. **Resonant Sideband Extraction :** In the resonant sideband extraction scheme, which is the current scheme used by aLIGO, the SRM is tuned such that it effectively reduces the arm cavity finesse for the gravitational wave signal, but increases the finesse for the carrier, therefore increasing the carrier storage time. This allows a broader detector bandwidth without sacrificing significant detector sensitivity. Details about the resonant sideband extraction scheme can be found in [148, 149].

1.3 Readout and control

The previous section has shown us that multiple mirrors are added to the standard Michelson interferometer to improve its sensitivity to gravitational waves. Each mirror is suspended and presents new degrees of freedom that require precise control so that the interferometer can operate in a low noise condition. Here, a brief overview of readout and control is presented, mainly to emphasise the importance of phase modulated sidebands, which are the motivation for the technology

developed in the scope of this thesis. For a more detailed discussion of readout and control, see [183, 113].

As seen in Fig. 1-7 , we denote the length of the two arm cavities L_x and L_y. The lengths between the beam splitter and the arm cavities are l_x and l_y. The lengths between PRM and the SRM to the beam splitter are l_p and l_s respectively. Since the interferometer operates with the AS port near the dark fringe, it is simpler to treat common mode and differential mode separately. Therefore, the five degrees of freedom that require control are:

$$\begin{aligned} L_- &= L_x - L_y \quad \equiv (\text{DARM}) \\ L_+ &= L_x + L_y \quad \equiv (\text{CARM}) \\ l_- &= l_x - l_y \quad \equiv (\text{MICH}) \\ l'_p &= l_p + \frac{l_x + l_y}{2} \quad \equiv (\text{PRCL}) \\ l'_s &= l_s + \frac{l_x + l_y}{2} \quad \equiv (\text{SRCL}) \end{aligned} \tag{1.28}$$

where DARM is s the differential arm length, CARM is the common average arm length. MICH is the Michelson differential length, PRCL and SRCL are the power recycling cavity and signal recycling lengths.

There are three different inteferometric readout techniques used in aLIGO: DC readout, which is a type of homodyne readout, is used for sensing DARM [92]. The Pound-Drever-Hall (PDH) technique [173] senses CARM, PRCL and SRCL and the Schnupp technique senses MICH [112]. Both the PDH and the Schnupp sensing scheme requires RF modulation sidebands.

1.3.1 DC readout

A static offset between the L_x and L_y of order tens of picometers is intentionally introduced in DC readout. This static offset allows some carrier leakage to propagate to the AS port. When L_- is dynamically disturbed by a small amount due to a gravitational waves or seismic motion for example, a pair of audio frequency

sidebands around the carrier are generated. The audio sidebands interfere with the carrier field at the AS port, which serves as the local oscillator. This results in intensity modulation measured by a photodetector.

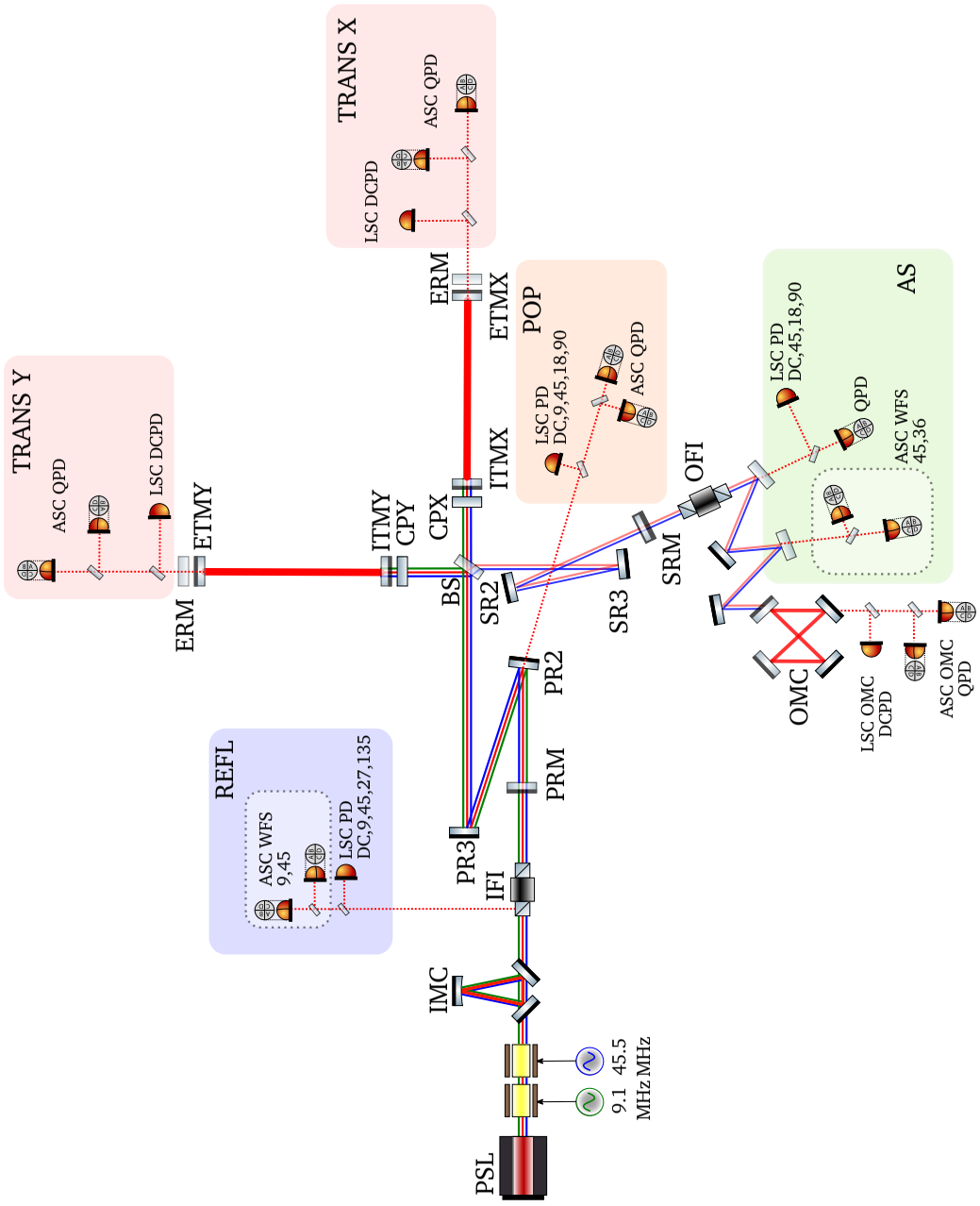

Figure 1-8: Advanced LIGO full interferometer optical layout with the addition of photodectectors (PD) at different signal ports (REFL: reflected off SRM, POP: pick-off in PRC, AS: antisymmetric, TRANS: transmission through ETMs). The two pairs RF sidebands 9.1 MHz and 45.5 MHz are coloured green and blue respectively and shown here to resonate in different part of the the interferometers. RF signals are demonulated at these ports to give error signals for length sensing and control (LSC) and alignment sensing and control (ASC). The numbers shown next to the PDs and the wavefront sensors (WFS) indicate the radio frequencies at which the signals are demodulated.

1.3.2 RF readout

In aLIGO, two frequencies are currently used for RF readout sensing: 9.1 MHz and 45.5 MHz. Using the Jacobi-Anger expansion, the phase modulated field is expressed as linear combination of 5 frequencies: the carrier field, at the PSL frequency, and the 2 pairs of RF sidebands at $\pm$9.1 MHz and $\pm$45.5 MHz relative to the carrier frequency. Therefore, the input field E_{in} of the interferometer can be written in the form of:

$$\begin{aligned} E_{\text{in}} &= J_0(\Gamma_1)J_0(\Gamma_2)E_0 e^{i\omega_0 t}\left\{1 + i\sum_{n=\pm 1}\left[\frac{J_1(\Gamma_1)}{J_0(\Gamma_1)}e^{in\omega_{m1}t} + \frac{J_1(\Gamma_2)}{J_0(\Gamma_2)}e^{in\omega_{m2}t}\right]\right\} \\ &= E_c + E_{sb+,\omega_{m1}} + E_{sb-,\omega_{m1}} + E_{sb+,\omega_{m2}} + E_{sb-,\omega_{m2}} \end{aligned} \tag{1.29}$$

where E_0 is the input field amplitude from the PSL, ω_0 is the angular frequency of this input carrier field. Γ_1 and Γ_2 are the modulation depths of the RF sidebands, J_0 and J_1 are Bessel functions of the first kind.

The carrier field is resonant in the arm cavity. RF sidebands resonate in different parts of the interferometer to enable all of the degrees of freedom to be sensed [191], as shown in Fig. 1-8. Only the carrier field is resonant in the arm cavities. The macroscopic lengths of the PRC and SRC are selected such that appropriate resonance condition is achieved. PRCL is set such that all carrier and sideband fields are simultaneously resonant and SRCL is set such that the 9.1 MHz does not resonate. The Schnupp asymmetry offset is chosen to couple most of the 45.5 MHz sidebands into the SRC.

The reflected, transmitted, or internal pickoff fields within the interferometer can be described as a linear combinations of the frequency components in the input field, whose phases and amplitudes are modified by the transfer functions of the various parts of the detector that it interacts with. These fields are measured at various sensing ports, including the asymmetric (AS), the reflection at PRM (REFL) and pick-off and the power-recycling cavity (POP). The photocurrent generated by

the fields at the photodetectors at these ports are demodulated in both the in-phase and quadrature-phase, from which errors signal for different degrees of freedom are extracted to feedback and control the optics. Details of which signals are expected at these readout points can be found in references [20, 18, 19].

The alignment sensing and control system (ASC) shares many common features with the length sensing and control system, including using the RF phase-modulated sidebands to generate angular control error signals. These signals are derived from the ASC wavefront-sensors (WFS).

The various sensors that generate error signals for these complex sensing schemes are shown in Fig. 1-8.

1.4 Noise sources

The previous sections have described techniques employed to improve the responsivity of a Michelson interferometer to gravitational waves.The sensitivity of the detector is determined by a variety of noise sources. This section will give an overview of the major noise sources, their coupling to the interferometer readout and methods to reduce them. The noise budget for the strain sensitivity of aLIGO at the design sensitivity is shown in Fig. 1-9.

1.4.1 Quantum noise

Quantum noise originates from the quantum nature of light and the photodetection process in gravitational wave dectectors. The two sources of quantum noise are: *shot noise* and *radiation-pressure noise*. The quantum mechanical description of an interferometer constructed by Caves [64, 62, 63] showed that these two noise sources enter via laser light incident on the symmetric port and via vacuum fluctuations from the antisymmetric port. Photon shot noise is the dominant quantum noise source above about 80Hz and is the main sensing noise source above 200 Hz, whereas the radiation pressure sets the quantum noise limit below 80Hz.

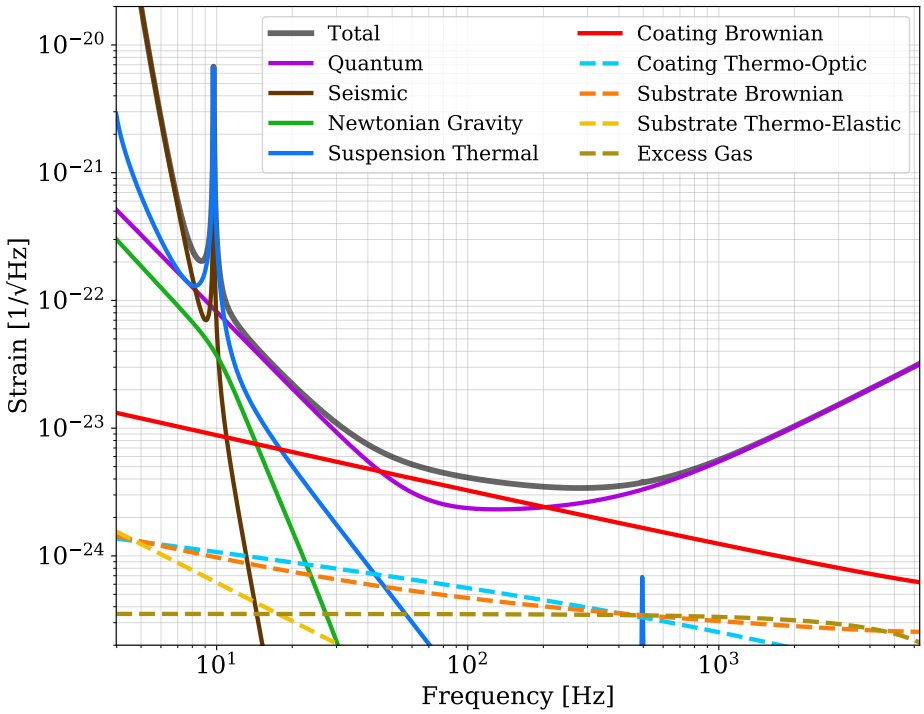

Figure 1-9: Noise budget of Advance LIGO, created using the Python Gravitational Wave Interferometer Noise Calculator (PyGWINC). The BNS range for this total strain noise is 176 Mpc.

Shot noise:

Shot noise arises from uncertainty due to quantum mechanical fluctuation in the number of photons at the output of the interferometer. These fluctuations are sensed in the gravitational wave readout but have no impact on the displacement of the test masses. Shot noise is therefore a type of sensing noise. Its effects on the sensitivity of strain measurement has been previously discussed in section 1.2.1. Generally, shot nose is constant with frequency. However in aLIGO detectors, the Fabry-Perot cavities and the SRC are used to shape the interferometer response to shot noise, therefore optimise for the frequency range of interest [54, 53, 55].

As seen in Eq. 1.26, the signal-to-noise ratio due to shot noise scales with $1/\sqrt{P_{\text{circ}}}$ where P_{circ} is the circulating power in the arm cavities. Therefore, the shot noise level of the inteferometer can be reduced by increasing the circulating power. An-

other method to reduce the quantum shot noise is the injection of phase-squeezed state of light, which will be discussed briefly in section 1.5.1.

Radiation pressure

The quantum radiation pressure noise arises from uncertainties in the mirror positions due to quantum fluctuations of the internal fields inducing radiation-pressure fluctuations that drive the mirror. The Heisenberg uncertainty principle for position and momentum of a particle states that: A measurement of the particle's position imparts an unknown amount of momentum via radiation pressure, which prevents prediction of the outcome of subsequent position measurements since position and momentum do not commute. A mirror of mass M which has laser intensity I_0 impinging on it to interrogate its position observe fluctuations in position, whose power spectrum density is given by [68]:

$$S_{\mathrm{RP}} \propto \frac{I_0}{(Mf^2)^2} \tag{1.30}$$

where f is the frequency at which the measurement is made. The radiation pressure noise is therefore a source of displacement noises, which cause direct movement of the interferometer's suspended mirrors.

Eq. 1.30 implies that either reducing the circulating power or increasing the mass of the optics will reduce quantum radiation pressure noise. However, recall that quantum shot noise improves with increasing circulating power. The overall sensitivity of the interferometer therefore lies in the balance between radiation pressure and shot noise. This sensitivity limit is called the Standard Quantum Limit. Future upgrades of aLIGO will introduce frequency-dependent squeezing, in which injection of phase-squeezed of light is performed at high frequency to reduce shot noise and amplitude-squeezed state of light at low frequency to reduce radiation pressure noise [162]. This technique should allow aLIGO to reach sensitivity better than the Standard Quantum Limit.

1.4.2 Seismic noise

Seismic noise is the greatest contributior at low frequency, as seen in Fig. 1-9. It is caused by the coupling of ground motion into the local position of the interferometer mirrors. There are various sources that contribute to seismic noise, which can be natural (movement of tectonic plates, ocean waves, etc.) or man-made disturbances (automotive traffic, operation of industrial machinery). Natural sources of seismic noise is highest in the frequency region up to 0.3 Hz, whereas anthropogenic sources dominate between 3 and 10 Hz.

The test masses of aLIGO are suspended from quadruple pendulum systems [27], which are in turn attached to actively controlled seismic isolation platforms [140]. The quadruple pendulum stages suppress the amplitude of seismic motion experience by its test mass at the frequencies above its resonance frequency by $1/f^8$. This leads to the quick roll-off in seismic noise in Fig. 1-9. These techniques enable the suppression of the ground motion whose nominal amplitude is $10^{-9}/\sqrt{\text{Hz}}$ at 10 Hz down to $10^{-19}/\sqrt{\text{Hz}}$.

1.4.3 Thermal noise

Thermal noise arises from the motion of the mirror's surface caused by the fact that they are held at a finite temperature. The individual particles that make up the test mass and the mirror suspension are in radiative thermal equilibrium with the vacuum. The thermal (or Brownian) motion of theses particles induces undesired variations in the optical length of the interferometer. Thermal noise and quantum noise are dominant noise at frequencies between 35 and 100 Hz [14]. The thermal noise is generally decomposed into suspension thermal noise and test mass thermal noise.

The suspension thermal noise, which is shown in blue in Fig. 1-9 is caused by the mechanical loss of the fused-silica fibers used in test mass suspension, which can be calculated from the fluctuation-dissipation theorem [77]. Fused silica was selected due to its low mechanical loss property [58]. The *peak* features seen in

Fig. 1-9 of suspension thermal noise are caused by the violin and pendulum modes of the suspensions.

Both coating and bulk substrate contribute to the thermal noise of the test masses. Fig. 1-9 shows that the coating Brownian noise is the dominant noise that will limit aLIGO sensitivity in the 50-80 Hz. Both substrate and coating Brownian thermal noises are also associated with mechanical loss of the materials. The fused-silica substrate of the test masses has a significantly lower mechanical losses compared to that of the multilayer Ta_2O_5/SiO_2 coating. The non-homogeneous distributed loss in these coating also causes treating coating thermal noise more challenging. Low mechanical loss optical coatings are an active area of research where different are being tried out , including annealing coatings, varying dopants concentrations and layer thicknesses [170, 188].

Other test masses thermal noises include coating thermo-optic noise and substrate thermo-elastic noise. These are caused by heat deposited by the laser power incident on the test masses.

1.4.4 Newtonian noise

Newtonian noise originates from terrestrial gravity fluctuations that contributes to noise below 30 Hz [175, 98]. These fluctuations predominantly come from two sources: density perturbation in the atmosphere and seismic fields. Seismic surface field produced by surface Rayleigh waves are predicted to be the main contribution to Newtonian noise [82]. As these seismic waves pass through the medium around the test mass, they cause density fluctuations in medium and therefore result in fluctuation in gravitational attraction between the test mass and the surroundings. Under normal circumstances, Newtonian noise is expected to lie below seismic noise and other interferometer technical noise. However, it can increase above at times of high environmental noise and seismic activities [82]. Newtonian noise cannot be easily reduced but possibly measured and fed-forward or subtracted off-line[82, 108].

1.4.5 Residual gas noise

Residual gas in the vacuum system causes statistical fluctuations in refractive index, therefore results in phase noise in the optical path. Residual gas is also a problem between the test masses and the reaction masses, which contributes some damping to the test mass suspension and potentially increase thermal noise [1]. This second effect is however not included in Fig. 1-9.

1.4.6 Other technical noises

There are also various other technical noise sources that affect the strain sensitivity of aLIGO that are not shown here in Fig. 1-9. These include:

- **Charging noise**: Displacement noise caused by static electric charges on the glass mirrors with the metal of vacuum enclosures and mirror supports [106].
- **Laser intensity and frequency noise**: Laser intensity noise couples through various mechanisms, which include the DARM offset for DC readout, different circulating powers in each arm, and differential thermal lensing due to test mass absorption of optical power. Laser frequency noise is coupled to the AS port due to intentional asymmetry introduced to the Michelson interferometer to produce the necessary interference conditions for RF sidebands [20, 18, 19].
- **Auxiliary degree-of-freedom noise:** Cross-coupling between length and alignment control signals and gravitational readout
- **Beam jitter**: Pointing fluctuations of laser beam, coupled through as intensity noise
- **Electronic noise**: Noises generated from analog and digital electronics that are used to measure the signal itself
- **Scattering**: Backscattering from baffles, vacuum enclosures modulates the main beam in phase and amplitude.

Martynov et al. [138] provides a detailed summary of these noise sources.

1.5 A+ Upgrade

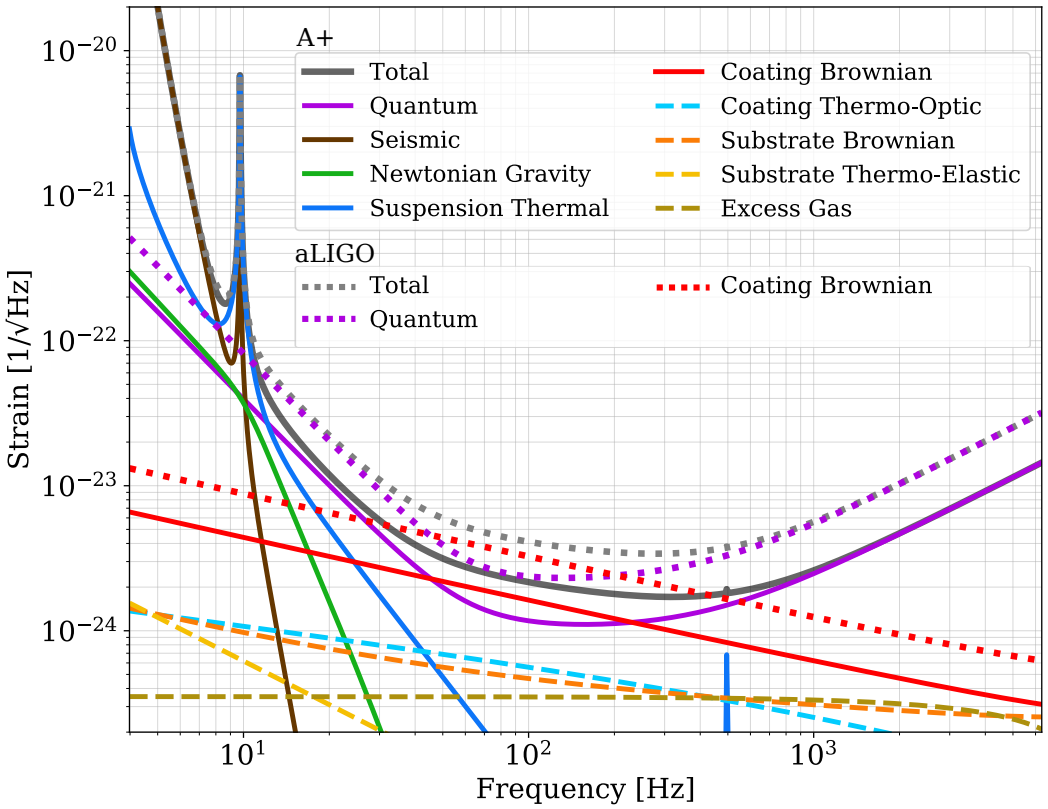

Figure 1-10: Noise budget of A+ upgrade created with PyGWINC. Dotted lines present total, coating Brownian and quantum noise limits of aLIGO for comparison. The BNS inspiral range for this given total noise budget of A+ is 330 Mpc.

A+ is modest-cost upgrade to aLIGO. The astrophysics goal of this upgrade is to increase the BNS inspiral range by a factor of 1.9 times compared to the aLIGO design, therefore reaching 330 Mpc. It is currently scheduled to complete by 2024 for the fifth Observing run (O5) [9].

The A+ upgrade proposal includes [65]:

- Frequency-dependent squeezing using a 300 m filter cavity.
- Balanced homodyne readout.
- Improved optical coatings.

- Larger diameter beam splitter.
- New fused-silica suspension fibers from upgraded pulling and welding system.

Implementation of frequency-dependenct squeezing and coating thermal noise are crucial to the prospect of doubling aLIGO detection range in A+ [145]. Balanced homodyne detection readout allows elimination of DARM offset, therefore reducing unwanted noise couplings into the GW readout channel. It also allows fine tuning the reference phase to optimise squeezed light performance [187, 95, 189].

1.5.1 Injection of squeezed state

As discussed in Section 1.4.1, we show that one of the fundamental noise sources of the interferometric gravitational wave detectors is quantum noise, which is composed of shot noise and radiation pressure noise. However, their effects can be modified by manipulating the vacuum state with correlated photons and injecting these states of light to the antisymmetric port of the interferometer. This is referred to as injection of squeezed state of light. In this section, a brief review of squeezed state injection is given, which will subsequently allude to why active wavefront control is crucial for future upgrades of gravitational wave to fully leverage squeezed light.

Quantisation of electromagnetic fields

By solving the Maxwell equations for the free electromagnetic field, it has been shown that the electric field tten as a sum of a series of orthonormal mode function set $\mathbf{u}_k$:

$$\mathbf{E}(\mathbf{r},t) = i\sum_k \left(\frac{\hbar\omega_k}{2\epsilon_0}\right)\left[a_k\mathbf{u}_k(\mathbf{r})e^{-i\omega_k t} - a_k^\dagger\mathbf{u}_k^*(\mathbf{r})e^{-i\omega_k t}\right] \tag{1.31}$$

where $\hbar$ is the Planck constant, ω_k is the angular frequency of the k^{th} mode, ϵ_0 is the vacuum permitivity, and a_k is the dimensionless amplitude of the k^{th} mode.

Since photons are bosons, a_k and $a_k^\dagger$ are chosen to follow the boson operator commutation relations:

$$[a_k, a_{k'}] = [a_k^\dagger, a_{k'}^\dagger] = 0, \quad [a_k, a_{k'}^\dagger] = \delta_{kk'} \tag{1.32}$$

The Hamiltonian, which represents the total energy of electromagnetic filed, can be written in term of a_k an $a_k^\dagger$:

$$\begin{aligned} H &= \frac{1}{2}\int \epsilon_0 \mathbf{E}^2 + \mu_0 \mathbf{H}^2 \quad d\mathbf{r} \\ &= \sum_k \hbar\omega_k \left(a_k^\dagger a_k + \frac{1}{2}\right) \end{aligned} \tag{1.33}$$

which is analogous to the Hamiltonian of a quanum harmnic oscillator. The eigenstate of the quantised Hamiltonian in which there are exactly N photons are referred to as the Fock states, or number states that form a complete orthonormal basis.

$$\hat{H}_k = \hbar w_k \left(N_k + \frac{1}{2}\right) \tag{1.34}$$

where $N_k = a_k^\dagger a_k$ is the number operator. The a_k and $a_k^\dagger$ operators act as annihilation and creation operator that are similar to the raising and lowering ladder in the case of a quantum harmonic oscillator. Notice that in this equation, when there is no photon (a vacuum) state, there is still energy.

The a_k and $a_k^\dagger$ operators are however not Hermitian and are therefore not observables. However, one can derive quadrature operators X_1 and $X2$ that a observables by rewriting a quantised electric field of a single spatial optical mode in term of sine and cosine quadratures:

$$\begin{aligned} E(t) &= \sqrt{\frac{\hbar\omega_k}{2\epsilon_0}} \left(a(t)e^{-i\omega} + a^\dagger(t)e^{i\omega t}\right) \\ &= \sqrt{\frac{\hbar\omega_k}{2\epsilon_0}} \left[X_1(t)\cos(\omega t) + X_2(t)\sin(\omega t)\right] \end{aligned} \tag{1.35}$$

where the quadrature operators are given by:

$$X_1(t) = a(t) + a^\dagger(t) \tag{1.36}$$

$$X_2(t) = -i(a(t) - a^\dagger(t)) \tag{1.37}$$

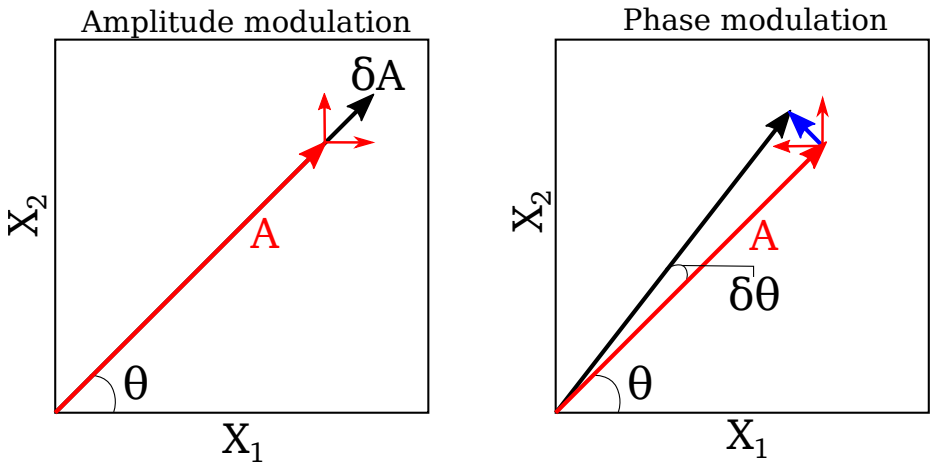

Figure 1-11: Amplitude and phase noises in the electric field presented in the picture of quadratures. In this plane, the polar coordinate represents the phase of the field, whereas the radial coordinate represents the amplitude of the field. Each of the individual frequency components is shown in red while the total field is shown in black. The carrier filed with amplitude A has a constant phase θ while upper and lower sidebands rotate around it at some angular frequency Ω in opposite directions.

These two quadratures can be written in terms of static and fluctuating parts: $X_{1,2} = \bar{X}_{1,2} + \delta X_{1,2}$. The static part describes the carrier field while the fluctuation δX describes modulations that describe noise sidebands symmetric around the carrier [84]. Fig. 1-11 shows amplitude and phase modulations represented in the plane of two quadrature operators.

An arbitrary quadrature operator can be defined as a linear combination of X_1 and X_2 [52]:

$$X(\theta) = X_1(t)\cos\theta + X_2(t)\sin\theta \tag{1.38}$$

By choosing θ to be the phase of the carrier, $\delta X(\theta)$ then describes amplitude noise while $\delta X(\theta + \pi/2)$ is phase noise.

Using the commutation relation of a and $a^\dagger$ in Eq. 1.32, the commutation rela-

tion for the single mode quadrature operator is:

$$[X_1, X_2] = 2i \tag{1.39}$$

Hence the uncertainties in X_1 and X_2 are related by:

$$\Delta X_1 \Delta X_2 >\geq 1 \tag{1.40}$$

This uncertainty gives rise to a fundamental quantum limit in the precision of measuring amplitude and phase of an electromagnetic field simulataneously. In the case of interferometers, their excitations imprint changes in the phase of the laser light. The classical quantum limit of the interferometers are therefore set by the uncertainty principle associated with phase and amplitude of light.

States of light

Vacuum and coherent state

The ground state $|0\rangle$ of a harmonic oscillator corresponds to the vacuum state of the field. As seen from Eq. 1.34, there is still energy while there is no photon in the ground state. The variance in quadratures $X(\theta)$, which is defined as $\Delta X^2 = \langle X^2 \rangle - \langle X \rangle^2$, can be shown to be unity [209]:

$$\langle 0| \Delta X_1^2 |0\rangle = \langle 0| \Delta X_2^2 |0\rangle = 1 \tag{1.41}$$

The vacuum state therefore has equal variance in each quadrature and no coherent amplitude. Representation of the vacuum state in the stick-and-ball picture is shown in Fig. 1-12(c).

A field from a stabilised laser can be described by the coherent states $|\alpha\rangle$. These states are eigenstates of the single mode annihilation operator:

$$a |\alpha\rangle = \alpha |\alpha\rangle \tag{1.42}$$

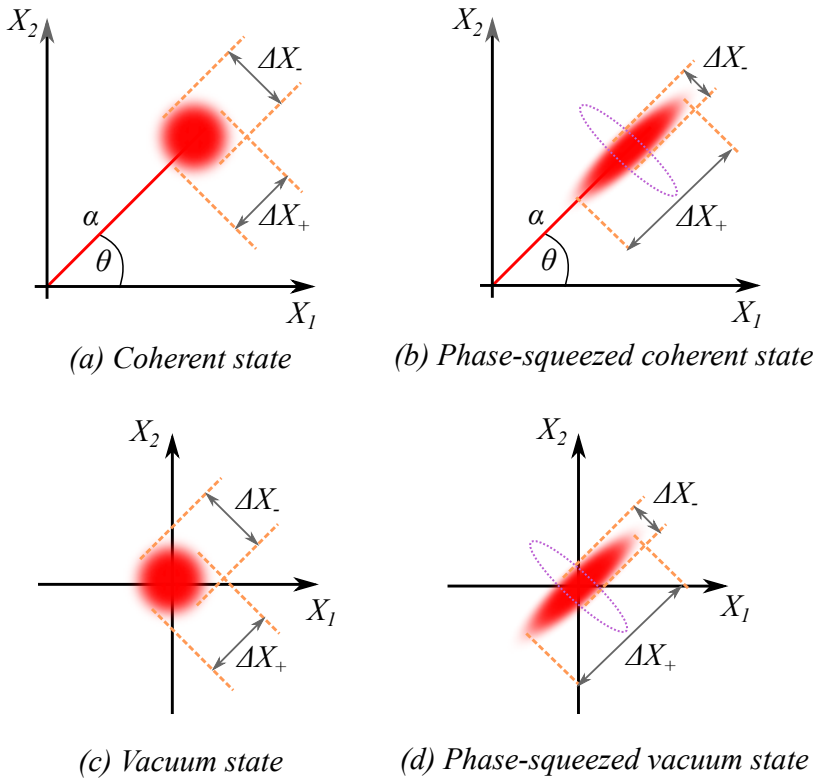

Figure 1-12: Stick-and-ball pictures of four different minimum states: (a) a coherent state, (b) a phase-squeezed coherent state, the purple ellipse shows how the "ball" of uncertainty would look like for an amplitude-squeezed coherent state, (c) a vacuum state and (d) a squeezed vacuum states. α is the magnitude of the state, whereas θ is the phase of the state measured with respect to the quadrature bases X_1 and X_2. ΔX_+ and ΔX_- are the uncertainties in amplitude and phase quadratures respectively.

The vacuum state is therefore a special case of the coherent state in which the eigenvalue α is zero. For a coherent state, $|\alpha|^2$=N, so photon number measurements on a coherent state would result in a Poisson distribution [105]. The coherent state is also a minimum uncertainty state of light, but with coherent amplitude and equal variance in both phase and amplitude quadratures $\langle\alpha|\,\Delta X_1^2\,|\alpha\rangle = \langle\alpha|\,\Delta X_2^2\,|\alpha\rangle = 1$. Its stick-and-ball representation is given in Fig. 1-12(a)

Squeezed state

The uncertainty principle imposes a minimum on the product of the quadrature variances but does not place any minimum on the variance of individual quadra-

tures. It is therefore possible redistribute this uncertainty to produce a *squeezed* state

The squeezed state is a minimum uncertainty state with unequal variances in two quadratures. One quadrature has less noise than a coherent state whereas the other has greater noise. For a squeezed state $|\alpha, \epsilon\rangle$ with ϵ level of squeezing , the variance of the quadratures are:

$$\langle \alpha, \epsilon | \, \Delta X_1^2 \, | \alpha, \epsilon \rangle = e^{-2r}, \langle \alpha, \epsilon | \, \Delta X_2^2 \, | \alpha, \epsilon \rangle = e^{2r} \tag{1.43}$$

where r is the squeezing factor and related to ϵ by $\epsilon = re^{i\theta}$. θ is the squeezing angle. Eq. 1.43 is obtained when θ is correctly tuned to align with the phase of the carrier field to maximum phase squeezing or $\pi/2$ in excess of the carrier phase to optimise-amplitude squeezing. Therefore, while squeezed states still abide to the uncertainty principle, its quadratures will have different level of noise. These characteristics are represents in stick-and-ball pictures in Fig. 1-12(b) and (c)

Injection of squeezed state in GW detectors

As mentioned previously, Caves [62] showed that quantum noise couples to the interferometers as vacuum fluctuations via the dark port, whose uncertainties are equal in both quadratures.

In the case of interferometry, because the measurement is based on optical phase difference accumulated between the interferometer arms, the sensitivity can be enhanced by the injection of phase-squeezed state of light through the dark port. However, the increased phase-quadrature squeezing is necessarily accompanied by the increase in noise of the amplitude quadrature. Recall the quantum back-action dictates that each photon reflection event at the interferometer is accompanied by an an impulse that drives the motion of the mirror, leading to radiation pressure noise. The increase in intensity fluctuation due to phase-squeezing therefore worsens radiation pressure noise, which strongly affects the detector sensitivity at low frequency.

To achieve broadband squeezing improvement in which shot noise is reduced at high frequencies and radiation pressure noise is reduced at low frequency, the squeezing angle θ must be tuned such that it is frequency dependent. The production of frequency-dependent squeezing is achieved by reflecting a standard frequency-independent squeezed state off a low loss cavity, known as a filter cavity [119, 121, 99, 117]. Spectral components of the squeezed state lies within the linewidth of the cavity will experience a change in their phase upon reflection and those outside do no. Detuning the filter cavity allows differential phase imparted upon upper and lower squeezed state sidebands, resulting in frequency-dependent quadrature rotation [163].

1.5.2 Balanced homodyne detection readout

Current aLIGO detectors utilise DC readout in which a DARM static offset is intentionally introduced to generate a weak static carrier field leaking through to AS port. This current technique offers several advantages over the RF readout of Initial LIGO:

- Lower quantum noise [56]
- Clear path for injection of squeezed light [141]
- The local oscillator (carrier field) is automatically mode-matched and co-aligned with the signal field [95]

However, the DC readout also presents some drawbacks, which include:

- Coupling of the SRC length noise due to backscattering of AS light into the interferometer [95].
- Non-zero carrier field in the AS port results in a static DC offset on the alignment wavefront sensors that requires careful subtraction to recover alignment signals. [95] ‘

- Static DARM offset allows the direct coupling of laser intensity noise to at the AS port [138].
- There is no easy method to vary the phase of the local oscillator for demodulation and thus enable choosing readout quadrature to take full advantage of frequency-dependent squeezed state injection [107]

These are the main motivations for switching to balanced homodyne detection (BHD) readout in the A+ upgrade.

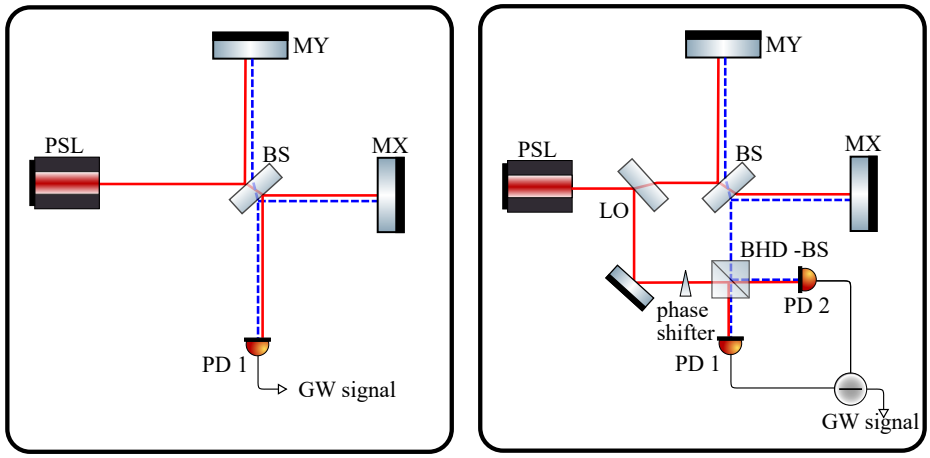

(a) DC readout (b) Balanced homodyne detection readout

Figure 1-13: Simplified optical layouts of DC readout (a) and BHD readout (b) schemes. In both schematics, the laser field is presented in red, and GW sideband field is presented as a blue-dashed line. In DC readout, a static offset in arm length is introduced so that a weak carrier filed is leaked to the AS port and beat against the GW signal field. In the BHD scheme, a local oscillator delivered from a pick-off before the interferometer is allowed to interfere with the GW signal field at the BHD beam splitter (BHD-BS). Both readout ports of the BHD-BS are detected with photodiodes PD1 and PD2

Fig. 1-13 shows the simplified optical layouts of DC and BHD readout schemes. In the BHD readout scheme, the interferometer is held on dark fringe. A local oscillator field interferes with the AS port field at the BHD-BS. Both outputs of this readout are sensed by photodiodes PD1 and PD2. All of the noises which enter with the LO field appear in the linear combination of PD signals PD1+PD2, where as the GW signal appears in their difference [95]. GW signal readout is thus in principle insensitive to noise on the local oscillator beam.

1.6 Conclusion

This first chapter has summarised the formulation of gravitational waves, their generation by astrophyical sources which hold important information about cataclysmic processes in the universe. It has also emphasised why GW detection is challenging and how advanced LIGO detectors achieved such feat using laser interferometry. There are however challenges that lie ahead for terrestrial GW detectors on their quest to increase detection rates. One of the most important limiting factors is the quantum noise. Key solutions to address include increasing circulating power in the Fabry-Pérot arms and the injection of squeezed light.

Chapter 2 will show how wavefront distortion and laser field mode mismatch can hinder the success of these technologies and why there is an urgent need to control optical wavefront in the immediate future. These will lead us to the development of new sensors and actuators to address the issue of mode mismatch described in the subsequent chapters.

Chapter 3 presents the demonstration of camera, a new 2D sensor that allows measurement of the spatial profiles of RF sideband fields used in length and alignment controls, and which are susceptible to mode mismatch due to thermal processes in the interferometer.

Chapter 3 provides an overview of the suspended active matching stages (SAMS), that will allow controlling of the optical wavefront. Chapter 5 and 6 describes two new adaptive optics as candidates for use in SAMS. The final chapter 7 summarises these developments and outlines the future plan for their implementation at LIGO observatories.

Chapter 2

Active Wavefront Control

In the previous chapter, we have seen that quantum noise will ultimately limit the sensitivity of gravitational wave detectors. Increasing the circulating power within each Fabry-Pérot arm will increase the sensitivity of the detector by reducing shot noise. Injection of squeezing will further improve the sensitivity of the detectors. In practice, however, the circulating power is limited by optical absorption in the test mass substrate and coating. The resulting thermal expansion and the temperature dependence of refractive index results in distortion of optical wavefronts and lead to *mode mismatch* that in turn will limit the power build up in the arm cavities as well as affect the controllability of the instrument.

In the first section of this chapter, a brief review of mode-matching is given in terms of Gaussian optics. This background knowledge allows us to understand how mode-mismatch affect the operation of GW detectors. These adverse effects are discussed in Section 2.2. Section 2.3 outlines the operation of the thermal compensation system. Together with Section 2.2, they highlight the current shortage of facility to address mode mismatch in GW detectors. This leads us to the establish of the active wavefront control (AWC) working group whose goals and strategies are presented in Section 2.4. At the end of this chapter, it will become apparent how the projects covered within this thesis will directly impact AWC and provide

important tools for optimisation of the instrument sensitivity.

2.1 Hermite-Gauss modes and mode-matching

Mode mistmatch, in the context of GW interferometers control, is best understood in the Gaussian beam formalism. Details of Gaussian beam optics can be found in Appendix D.

Hermite-Gauss (HG) modes are a complete orthogonal set of solutions of the paraxial scalar electromagnetic wave equation for waves propagating in isotropic free space [15]. They can be expressed as:

$$\begin{aligned} HG_{mn}(x,y,z) = E_{mn}\frac{w_0}{w(z)}H_m\left(\frac{\sqrt{2}x}{w(z)}\right)H_n\left(\frac{\sqrt{2}y}{w(z)}\right)\exp\left(-\frac{x^2+y^2}{w^2}\right) \\ \times\exp\left\{-i\left[kz+\frac{k(x^2+y^2)}{2R(z)}-(m+n+1)\zeta(z)\right]\right\} \end{aligned} \tag{2.1}$$

where the $1/e^2$ radius of the mode $w(z)$:

$$w^2(z) = w_0^2\left[1+\left(\frac{z}{z_R}\right)^2\right] \tag{2.2}$$

the radius of curvature of the wavefront, $R(z)$:

$$R(z) = z\left[1+\left(\frac{z}{z_R}\right)^2\right] \tag{2.3}$$

the Rayleight range, z_R:

$$z_R = \frac{\pi w_0^2}{\lambda} \tag{2.4}$$

and the Gouy phase:

$$\zeta(z) = \tan^{-1}\left(\frac{z_0}{z}\right) \tag{2.5}$$

and H_m nd H_n are the Hermite polynomials. The simplest or fundamental HG

mode is HG_{00}, often labeled as TEM_{00} mode:

$$HG_{00} = AE_{00}\frac{w_0}{w(z)}e^{-\frac{r^2}{w^2(z)}}e^{-ik\frac{r^2}{2R(z)}}e^{i(\zeta(z)-kz)} \tag{2.6}$$

HG modes are convenient for discussing mode-matching as stable lasers ideally produce TEM_{00} beams and the eigenmodes of stable optical cavities are essentially HG modes. In a well-aligned Fabry-Pérot cavity, for example, the radius of curvature of the wavefront of the eigenmode matches the curvature of the mirrors, which prescribes w_0 for those eigenmodes.

If a TEM_{00} mode is incident on the cavity but its shape does not fit the TEM_{00} cavity eigenmode due to either misalignment of the optical axes or shape mismatch, then only some of its power will couple in the cavity TEM_{00} and the remaining power may scatter into its higher-order modes. The coupling into the

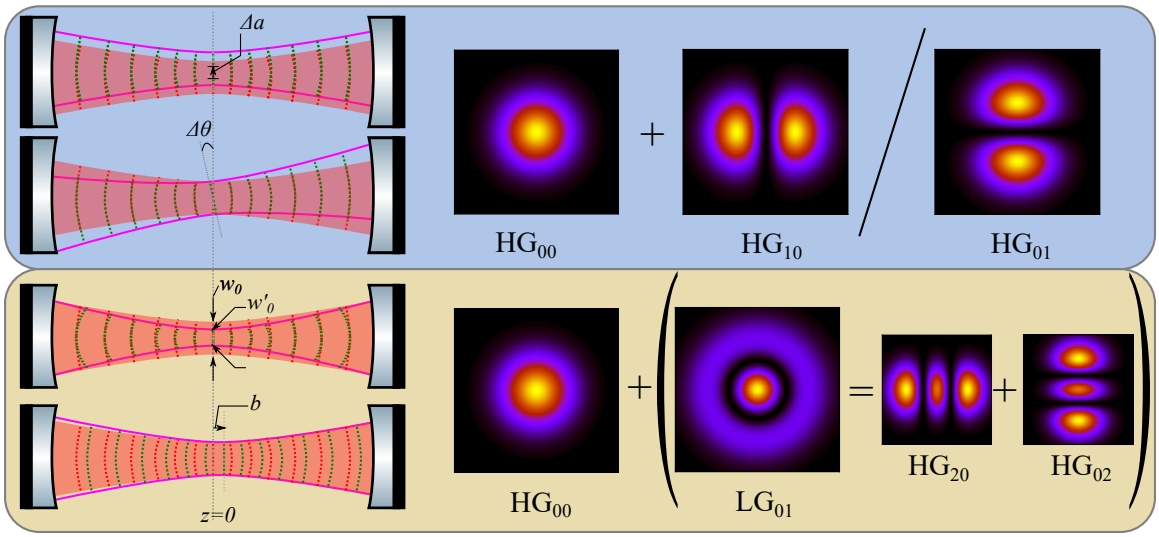

Figure 2-1: The top panel shows the two types of misalignment relative to a cavity mode and the higher order Hermite-Guassian (HG) modes coupled through due do misalignment. The lower panels shows the coupling caused by mode mismatch. Here, LG stands fo Laguerre-Gaussian modes, which also forms a complete orthonormal set that are solutions to paraxial wave equation. The LG_{01} mode is a superposition of HG_{02} and HG_{10}

eigenmodes can be calculated using normalised overlap integrals [30, 22, 150, 102], which assume that the frequency of the wave matches the eigenfrequency associated with that eigenmode. Examples of higher-order modes excited by small mis-

alignments and mismatch are shown in Fig. 2-1 and Table 2.1 .

	Perturbations	Quantity	Coupling coefficient	Mode
Misalignment	Lateral shift	$\Delta a_{x,y}$	$\Delta a_{x,y}/w_0$	HG_{10}/HG_{01}
	Tilt	$\Delta\theta_{x,y}$	$ik\Delta\theta_{x,y}w$	HG_{10}/HG_{01}
Mismatch	Waist size	w_0'	$w_0'/w_0 - 1$	$HG_{20} + HG_{02}$
	Axial waist position	Δz	$i\Delta z/2kw_0^2$	$HG_{20} + HG_{02}$

Table 2.1: Coupling coefficients of the fundamental Gaussian mode to higher order modes due to small misalignments and mismatches to an optical cavity. $\Delta a_{x,y}$ represents the amount of transverse displacement of the input field relative to the cavity mode, $\Delta\theta_{x,y}$ is the yaw/pitch angle of th input beam relative to the cavity optical axis, w_0' is th input beam waist, and b is the axial shift of the beam waist position along the optical axis. These parameters are illustrated in Fig. 2-1

As seen in Table 2.1, the first order coupling of misalignment results in scattering into the first order modes HG_{10} or HG_{01} dependent on whether the misalignment is in the x- or y- direction, whereas mismatch results in coupling into HG_{20} and HG_{02}. The intensity profiles of these transverse modes are shown in Fig. 2-1. Coupling coefficients of misalignment caused by beam tilt and mismatch caused by the axial shift in beam waist location are complex, which indicate there is a 90 degree phase difference between the fundamental Gaussian mode and the coupled higher order modes. On the other hand, the high-order modes that result from lateral shift and change in waist size are in-phase with the Gaussian mode. This phase difference becomes apparent in Fig. 2-1. For example, in the case of change in waist size, there is no apparent difference in phase of the input mode and cavity mode in the near field around its waist position. However, diffraction means that the beam with a smaller waist size will diverge more quickly and will accrue a phase change in its wavefront more quickly. Therefore, there is a phase difference in the far field. On the other hand, axial shift of the waist position results in a phase difference in the near field. However,as the two fields propagate a long distance, their phase will be similar in the far field.

In conclusion, mismatch and misalignment cause scattering of a fundamental Gaussian mode into higher order modes. If these mismatch and misalignment are large, first order coupling description will not be sufficient since more power from

the fundamental mode will scatter to much higher order transverse modes.

2.2 Effects of mode mismatch

2.2.1 Mode mismatch and high power operation

The mode scattering discussed in the previous section reduces the amount of total power circulating within the interferometer. This directly impacts the maximum achievable sensitivity of the detector. Additionally, an eigenmode mismatch between the two arm cavities will degrade the interference at the AS port, causing excess carrier light to leak out and thus increase shot noise.

In the Fabry-Pérot arms, the main cause of mode mismatch is wavefront distortion due to optical absorption in the substrates and coatings of mirrors. The nominal absorption of the high reflectivity coating of is 0.5 ppm [50]. In more details, the absorption leads to heating which gives rise to wavefront distortion via the following mechanisms:

- **Thermoelastic effect:** The non-uniform heating of the mirror causes the surface of the mirrors to expand and change its curvature.

- **Thermooptic effect:** The temperature gradient resulting from the heating combined with the temperature dependence of the refractive index of fused-silica results in significant wavefront distortion as the beam propagates through the mirror substrate.

- **Elasto-optic effect:** The thermal gradient also causes thermals stress within the fused silica substrate, which generates mechanical strain that varies local refractive index. However, the low thermal expansion coefficient of fuse-silica means that this effect is much smaller then that caused by the two aforementioned effect

These effects are illustrated in Fig. 2-2. Distortion caused by these effects have

been studied analytically in details by Hello and Vinet [103, 104] and can be modelled numerically.

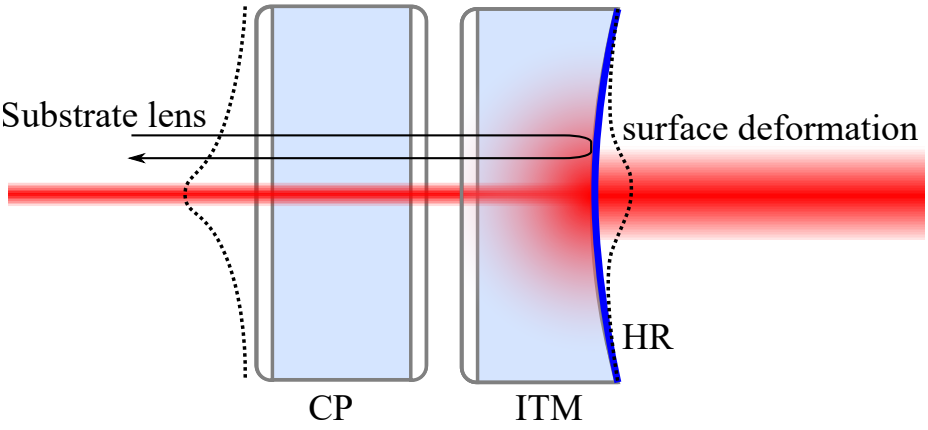

Figure 2-2: Finite absorption in coating during high power operation causes distortion of optical path due to thermoelastic deformation of the mirror surface and thermal lensing in the test mass substrate.

As discussed in Section 1.3.2, the sideband and carrier fields propagate within different parts of the in the interferometer and thus will see different wavefront distortion. Yamamoto [211] has shown that while the carrier field, which resonates in both PRC and the arm cavities is to first-order-insensitive to thermal lensing in the input test mass (ITM), the sidebands, which are anti-resonant inside the arm experience a first-order mode scattering that is proportional to the amount of lensing:

$$\begin{aligned} E_{\text{resonant}} &= -\frac{1}{1+i\alpha} HG_{00} + \mathcal{O}(\alpha^2) \\ E_{\text{anti-resonant}} &= \frac{1}{1+i\alpha} HG_{00} - \frac{i\alpha}{\sqrt{2}(1+i\alpha)^3}(HG_{20} + HG_{02}) + \mathcal{O}(\alpha)^2 \end{aligned} \tag{2.7}$$

where α is defined as:

$$\alpha = \frac{kw^2}{4}\left(\frac{1}{R_{in}} + \frac{n-1}{R_{ITM}} - \frac{1}{f_{TL}} + \frac{1}{R_{ITM}}\right) \tag{2.8}$$

where R_{in} is the radius of curvature of the incoming field, R_{ITM} is the radius of curvature of the ITM, f_{TL} is the focal length of the thermal lens, w is the input

waist size, which is assumed to match that of the cavity eigenmode. This difference in wavefront distortion seen by different fields has important consequences, including reducing the PRC gain. It also degrades error signals used to control the interferometer. Additionally, as was observed in O1, differential lensing in the two arms causes errors in the control of the SRM mirror, which degrades the efficiency of the resonance sideband extraction [213]. Accurate diagnosis and correction of wavefront distortion due to absorption of test masses is therefore crucial for low-noise operation of the detectors at high circulating power.

2.2.2 Mode mismatch and squeezing

The level of achievable squeezing is highly susceptible to loss. Loss occurs when any light is coupled out of the main mode of a beam, either by absorption, scattering or imperfect transmission or reflection [161]. Scattering into higher order modes is therefore also a source of loss.

The effect of loss on the effective level of squeezing is plotted in Fig. 2-3.

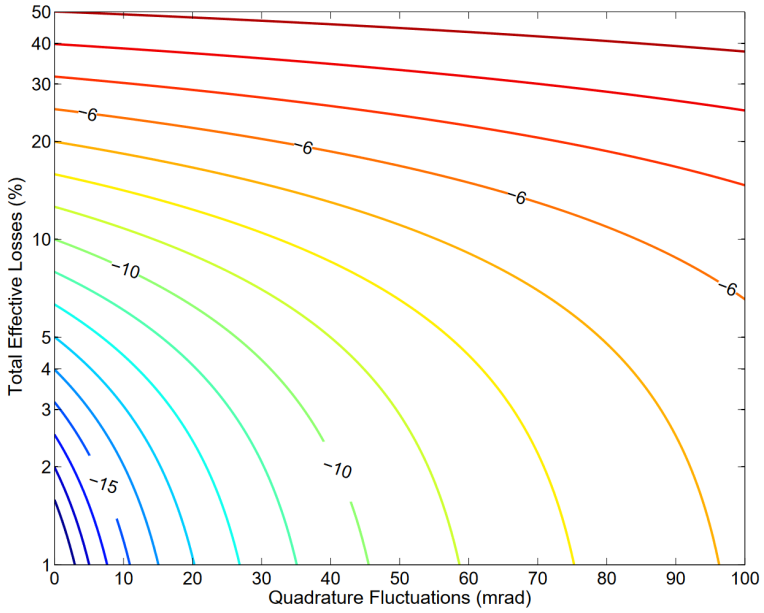

Figure 2-3: Maximum level of "effective" squeezing measurable in the presence of optical losses and squeezed quadrature fluctuations [161]. The squeezing level relative to shot noise is expressed in decibels.

Current aLIGO aims to achieve 3dB squeezing and 6dB after the A+ upgrade. However, at the time of writing this thesis, the best squeezing level measured at LIGO Hanford (LHO) and Livingston (LLO) observatories are 2.2 and 3.1 dB respectively [118]. The inferred loss due to mode matching between the in-vacuum optical parametric oscillator (VOPO), from which the squeezed light is emerges, to the output mode cleaner (OMC) is 30% [124]. An increase to 6dB squeezing will require a more stringent loss budget, in which mode-mismatch loss between the VOPO and the filter cavity (FC) for frequency-dependent squeezing is limited to 4%. The mode mismatch between the FC and the OMC must also be reduced to 4% [143]. A squeezing goal of 10 dB would require extreme wavefront control that is beyond current fabrication tolerance.

2.2.3 Mode matching and balanced homodyne detection

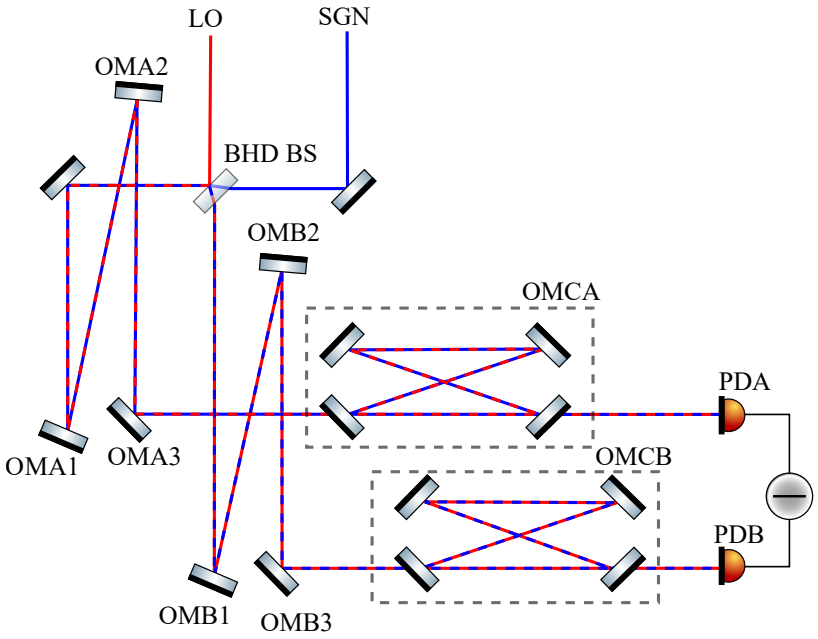

Figure 2-4: Schematic of a tentative optical layout for balanced homodyne detection readout in A+ upgrade. Here we see the 2 local oscillator (LO) and signal (SGN) fields interfere at the BHD beams splitter (BHD BS). OMAi's and OMBi's are steering mirror that guide the 2 outputs of BHDBS to the two OMCs (OMCA and OMCB) before being sensed by the two PDs (PDA and PBD)

A tentative optical layout for balanced-homodyne detection (BHD) readout in

A+ upgrade is shown in Fig. 2-4. The important feature that differs from the schematic presented in Fig. 1-13 is the inclusion of the two OMCs after the BHDBS. The OMC is important for rejecting higher order modes leaking out of the AS port due to wavefront mismatch as they introduce excess noise, and for removing the RF sidebands used for interferometer control. In aLIGO, there is only one OMC in the signal path. However, the stringent length-noise requirement imposed on the LO and SGN paths prior to their interference at the BHDBS ($< 2 \times 10^{-18}$ m/$\sqrt{\text{Hz}}$ at 100 Hz [214]) rules out this option due to coating Brownian noise of the OMC optics and its piezo noise [23]. Thus, there must be two OMCS located after the BHDBS [215]. The use of a dual OMC signal extraction relies on common-mode noise rejection. Thus, it is important that there is good mode-matching control.

2.3 Thermal compensation system

The correction of dynamic wavefront distortion in aLIGO has thus far relied entirely on the thermal compensation system (TCS), which focuses on the compensation of wavefront distortion due to thermal effects in the arm cavities. The current TCS strategy is as follows [208, 205]:

1. Estimate distortion caused by the interferometer self-heating and calibrate with the Hartmann wavefront sensors, which will be discussed in the subsequent section.

2. Pre-load the ring heater to correct for the self-heating thermoelastic deformation

3. Use CO_2 lase compensate the negative lens in the test mass substrate and maintain a nominal f =50 km substrate lens to assist with lock acquisition.

A more detailed description of the TCS system can be found in [126, 50]. A brief description of the TCS is given the following subsections.

2.3.1 Actuators

Two types of actuators are used in the TCS, as shown in Fig. Fig:RH: ring heaters (RH) placed around the barrel of the test masses, and CO_2-laser-beam heating of compensaton plates (CP)

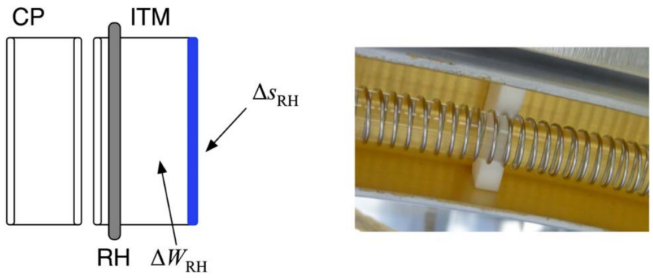

Figure 2-5: (a) aLIGO ring heater torus around a test mass. (b) A ring heater consists of a semi-circular glass rod wrapped in nichrome wire. *Image source:*Brooks et al. [50]

The ring heater consists of a toroidal glass cylinder around which a nichrome wire heater is wrapped. Passing a current though the wire increases its temperature and radiatively heats the barrel of the test mass. By heating the barrel, the ring heaters induce a negative thermo-optic lens and a thermoelastic radius of curvature change.

A toroidal CO_2 laser beam produced outside the detector is used to heat the compensation plateand produce a wavefront that balance out the thermo-optic effect due to the axial heating of the test mass substrate by the main science beam.

2.3.2 Hartmann wavefront sensor (HWS)

Measurement of the steady-state wavefront distortion due to heating of the test masses by the main interferometer beam is crucial for the TCS, as an appropriate compensation scheme must be derived. This can be very challenging to detect when the coating absorption is typically less than one part in a million. The Hartmann Wavefront Sensor (HWS) developed by Brooks et al. [48] at the University

of Adelaide are able to achieve such sensitivity.

At LIGO observatory, these Hartmann sensors are used to sense the wavefront distortions of core optics during power-up and lock loss.

In this thesis, HWS are also used to characterise the new adaptive optics (see Chapter 5, 6). Details on the operation of the HWS can be found in [48], [47], [49]. Thus, in this section, a brief review of the HWS principle of operation, its performance and application at aLIGO will be given.

HWS operation

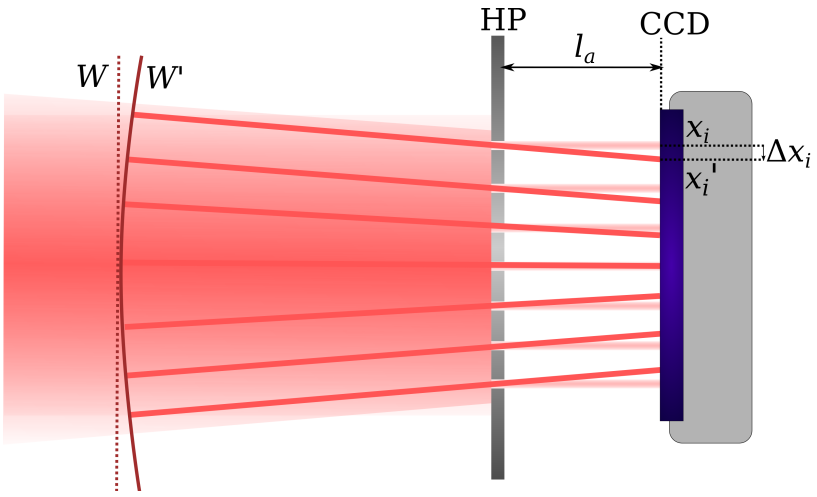

Figure 2-6: Wavefronts W and W' are incident on the HP , producing Hartmann rays that travel distance l_a to the CCD sensor. The spot position x_i' is found from centroiding the spot's intensity profile. The positions of reference spots x_i, resulted from a reference wavefront W are indicated with lighter rays. Transverse displacements Δx_i allows computation of wavefront gradients, from which the wavefront change ΔW can be obtained from numerical integration.

A differential HWS measures changes in the local gradient of wavefront, ΔW_{HWS} relative to some reference state [48, 101]. The gradient change is integrated numerically to obtain the wavefront distortion.

Measurement of the wavefront gradients is achieved in by sampling the wavefront using an array of apertures in an otherwise opaque plate, which is often referred to as a Hartmann plate (HP). This HP is positioned in front of charged-coupled device (CCD) sensor at a distance referred to as the lever-arm length l_a, as

shown in 2-6. When a wavefront is incident on the HP, beams of light created by each aperture propagate perpendicularly to the local wavefront, creating an array of spots at the CCD. Changes in the incident wavefront results in transverse displacements of the spots that are proportional to the change in local slopes of the wavefront and the lever arm distance between the HP and the CCD sensor.

$$\left.\frac{\delta \Delta W}{\delta x}\right|_i = \frac{\Delta x_i}{l_a} \tag{2.9}$$

From the measured gradients, a wavefront can be reconstructed using numerical integration method or least-squares fitting to a 6$^{\text{th}}$ order polynomial wavefront [206]:

$$W(x, y) = \sum_{j=1}^{27} a_j \Psi_j(x_i, y_i) \tag{2.10}$$

where $\Psi(x, y)$ are a set of linearly-independent polynomial functions of the form $\Psi_j = x^n y^m$ where $0 \leq n, m \leq 6$ and a_j are the corresponding polynomial coefficients, which can be calculated using the least-squares fit. x_i and y_i denotes the x, y coordinates at the object plane.

The spherical power S, which describes the radius of curvature of a wavefront, is computed directly from these polynomial coefficients using:

$$S = a_3 + a_5 - 0.5C \tag{2.11}$$

$$C = 2\sqrt{(a_3 + a_5)^2 + a_4^2} \tag{2.12}$$

where the coefficients $a_3,\ a_4,\ a_5$ correspond to $\Psi_i = x_i^2,\ x_i y_i,$ and y_i^2 respectively.

The sensitivity of the HWS can be determined by uniformly illuminating the HP with a light from a single-mode-fibre-coupled super-luminiscent-LED (SLED) and analysing the reproducibility of the spot pattern. This reproducibility is quantified by the RMS wavefront difference between adjacent holes of the HP $\sigma_{\Delta W}$ [47]:

$$\sigma_{\Delta W} = \frac{h_p}{l_a} \sigma_{\Delta y} \tag{2.13}$$

where h_p is the pitch between adjacent holes on the HP and $\sigma_{\Delta y}$ is the average RMS error in the individual centroid.

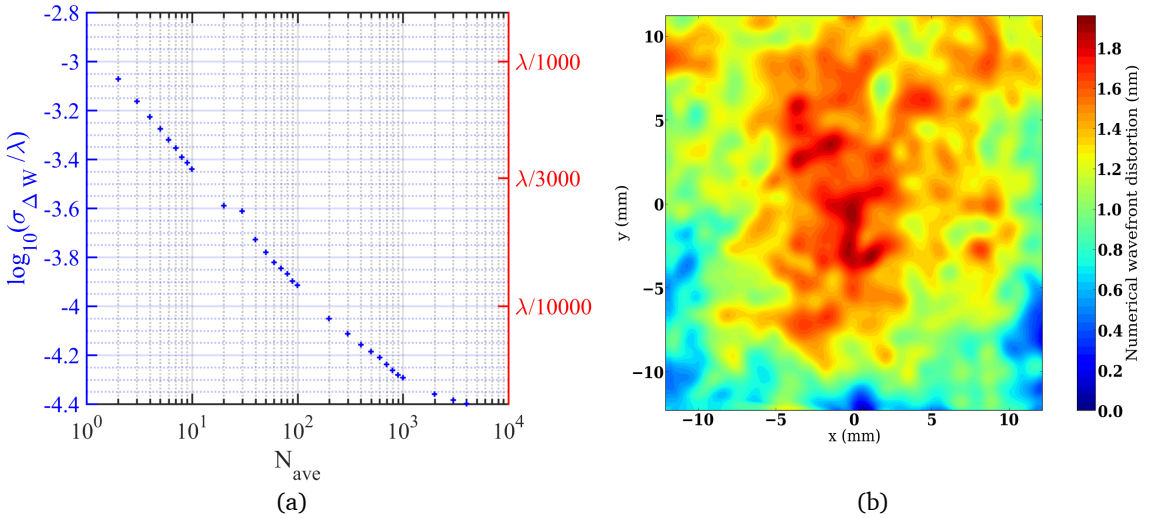

Figure 2-7: (a) Improvement in HWS sensitivity due to averaging over N_{ave} Hartmann images. (b) Wavefront map of HWS noise floor constructed from an average of 10 Hartmann frames

A typical map of the wavefront sensitivity, determined using two spot patterns separated in time by 15 seconds, is plotted in Fig. 2-7(b). This map yields a sensitivity of $\approx$ 0.5 nm_{RMS}, which is consistent with that expected from photon shot-noise. The sensitivity can be further improved by using averaged spot patterns, as shown in Fig. 2-7. This graph plots the the wavefront RMS error $\sigma_{\Delta W}$ as a function of number of spot pattern averaged N_{ave} , showing that the HWS has a single-frame sensitivity of $\lambda/1500$ at $\lambda = 680nm$ (or 0.5 nm_{RMS}), and can be improved to $\sigma_{\Delta W} < 16000$ at N_{ave} =1000.

The optical layout of the HWSs used for the ITMs in aLIGO is shown in Fig. 2-8 [50]. There are four HWS's at each observatory to measure curvature changes in the ITMs and ETMs. Two SLED beams are injected into the vacuum system, through an imaging telescope with a magnification of nominally 17.5, formed by two lens L1 and L2. This telescope collimates and expands the beams such that they are approximately 200 mm in diameter at the HR surface of the ITMs. The retro-reflected beams are recorded and analysed by separate HWS. Using refer-

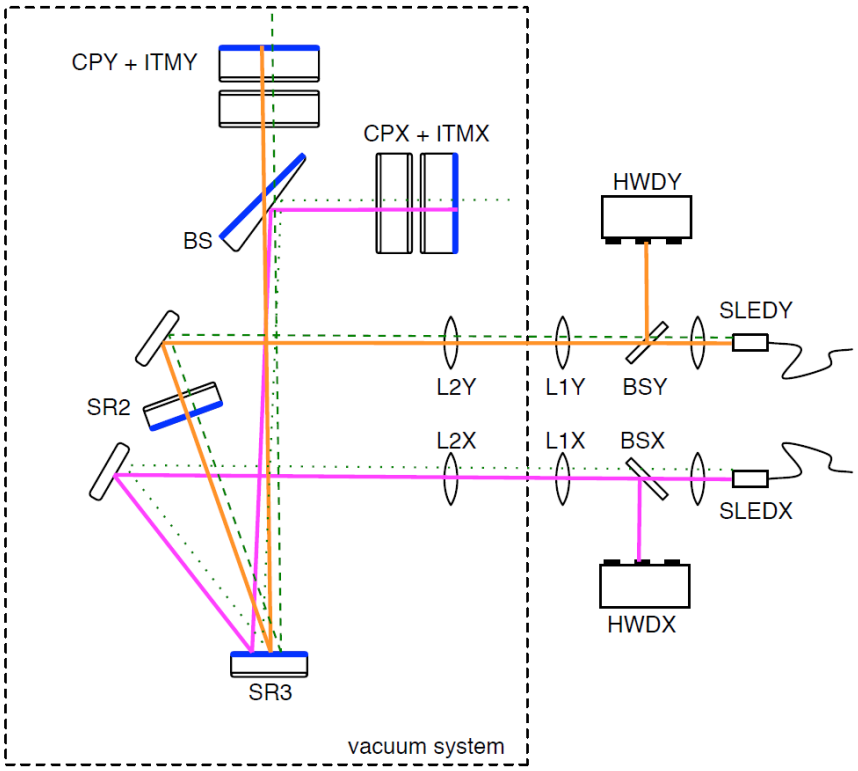

Figure 2-8: Optical layout of ITMX and ITMY Hartmann wavefront sensors. The wavelengths of the two probe beams (X-arm: magenta, Y-arm: orange) generated from fibre-coupled superluminiscent diodes two SLEDX and SLEDY are 800 nm and 833 nm respectively and have a 4-nm linewidth [50]. The beam are sent into the vacuum system and retro-reflected off ITMX and ITMY back towards the HWS.

ence wavefronts recorded with the ITMs in cold states, the HWS generate gradient vector fields and perform numerical integration to yield the wavefront change due to thermal lensing of the test masses.

Observation of point absorbers with HWS

The development on the TCS system was based on uniform Gaussian beam heating which only cause low spatial frequency distortion and therefore would introduce coupling into second order Hermite-Gaussian modes. Unfortunately, this is not the case in practice. During the second observation run (O2), the Hartmann Wavefront sensors were able to identify a point absorber on ITMX of LHO, which resulted in excess of intensity noise coupled directly into DARM, even at low in-

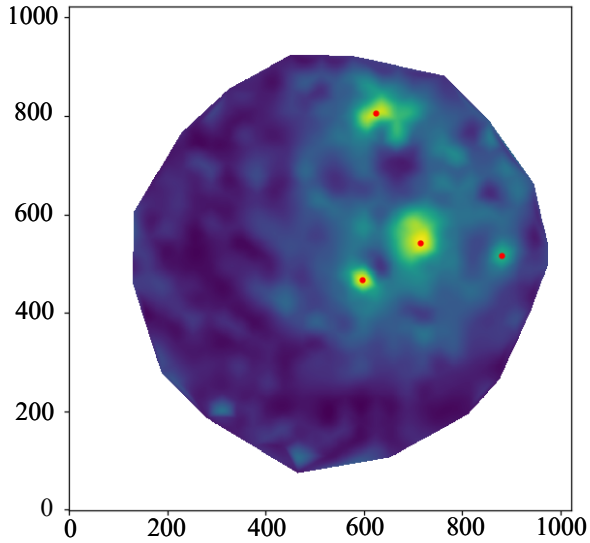

Figure 2-9: Numerical wavefront map measured by the HWS shows point aborbers on ITMY at LHO during O3

put power (30W) [42]. During O3, additional point absorbers were also detected on ITMY and ETMX of LHO, which showed similar charateristics. The wavefront map of ITMY at LHO is shown in Fig. 2-9 and clearly shows these point absorbers. There is also evidences of point absorbers on ETMX and ETMY of point absorbers in LLO [46]. The nature and causes of these point absorbers are currently unclear and is an active area of research.

The wavefront distortion due to these point absorbers scatter the carrier light in the arm cavity into higher order modes and distort the power recycling cavity, preventing the buildup of the RF sidebands in the PRC, which make alignment control and sensing particularly challenging [81]. They are also suspected to cause coupling of modes of the 9 MHz sidebands into the SRC and then the OMC, introducing excess intensity noise on the OMC DC photodetector at the OMC transmission [24]. However, there has not been any direct measurements of the effects of this wavefront distortion on these on sidebands. The ability to observe the spatial structure of the RF sidebands at various sensing ports is therefore attracting great interest as this would allow us to understand the behaviours of the interferometer and potential identify a short-term remedy to mitigate the issues.

2.4 Active Wavefront Control

The realisation of the multiple effects of wavefront distortion and mode mismatch on the sensitivity of GW detectors has prompted the formation of the Active Wavefront Control (AWC) working group. The AWC aims to optimise the mode matching at various optical interfaces, which are divided into 3 regions:

1. **Input optics:**
   (a) Pre-stabilised laser (PSL) to input mode cleaner (IMC)
   (b) IMC to power-recycling cavity (PRC)
2. **Dual recycled Michelson interferometer (DRMI):**
   (a) PRC to the arm cavities
   (b) Signal recylcing cavity (SRC) to arm cavities
3. **Ouput optics**:
   (a) SRC to OMC
   (b) Squeezed beam (SQZ) to filter cavity (FC)
   (c) FC to SRC

For the input AWC, the goal is to ensure a total throughput of 75% from the PSL and to reduce the amount of higher order mode incident on the PRM to <5%, thus resulting in $> 95\%$ mode matching into the arm cavity mode from PRC [40]. Input AWC should improve technical noise sources coupled to REFL sensors and therefore control of CARM and SRCL degrees of freedom.

DRMI AWC will be designed to meet two main goals: maximising coupling of carrier light from the PRC to the arm cavities and maintain extraction efficiency of the GW sidebands through SRC.

Most of the current efforts in AWC (pre O3, O4 and A+ upgrade) is to improve the mode-matching for the output optics. This is mainly driven by the need to improve transmission efficiency of the GW sidebands to the photodetector and

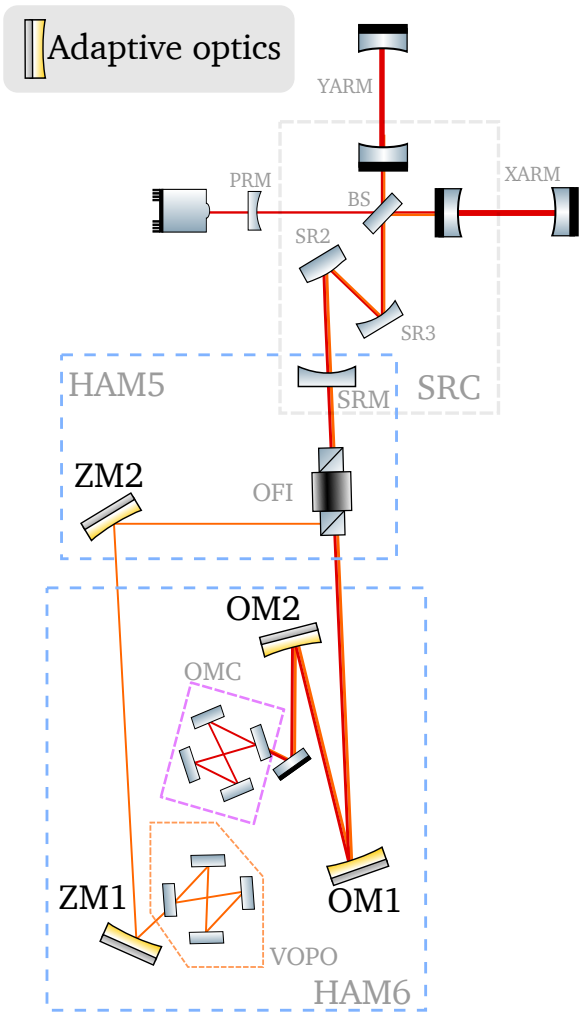

Figure 2-10: Proposed optical layout for the HAM5 and HAM6 chambers in O4 to incorporate adaptive optical elements. In particular, two units of adaptive optics are proposed to be placed at ZM1 and ZM2 for improving mode matching between the in-vacuum OPO (VOPO) of SQZ and the SRC. Another pair of adaptive optics are also proposed for OM1 and OM2 to improve mode matching from the SRC to the OMC. [44]

stringent optical loss requirements for by squeezed light injection. Oelker et al. [161] have specified a minimum of 98% mode matching from the interferometer to the OMC.

2.4.1 AWC in O4

The third observation run (O3) will finish in early 2020. During the commissioning for O4, AWC will aim to install adaptive optics in the HAM5 and HAM6 chambers

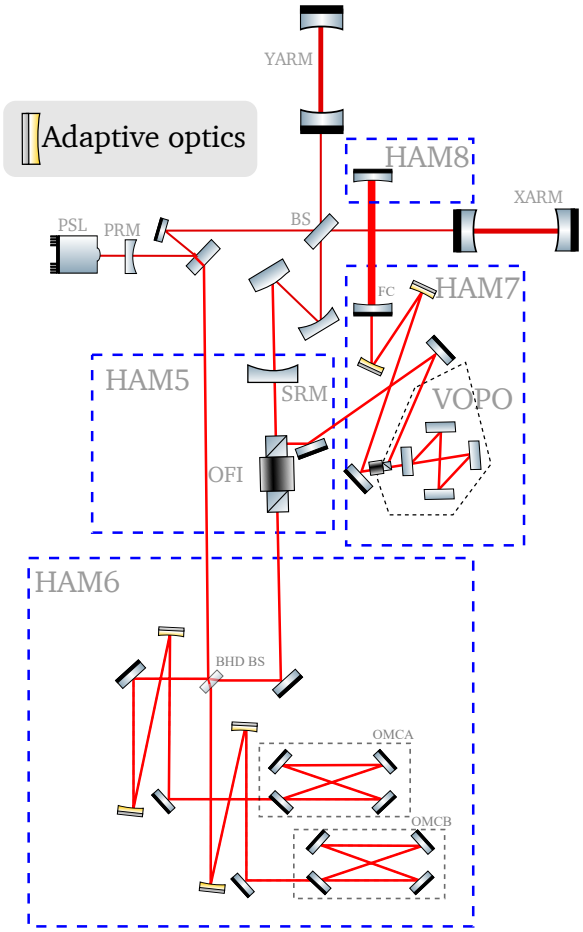

Figure 2-11: Simplified schematic of the optical layout to accommodate AWC adaptive optics in A+. The HAM6 chamber will house the BHD readout. At least four units of adaptive optics are required here to assist with mode-matching in to the two OMCs. The HAM7 chamber will house the squeezer VOPO and at least two adaptive optics required to assist with mode-matching between OPO and FC. A more detailed conceptual layout of A+ is given in [201].

to assist with mode matching between VOPO and the OMC, which will help improve squeezing. Schematic of the propose optical layout is shown in Fig. 2-10.

2.4.2 AWC in A+

Fig. 2-11 shows the simplified optical layout of A+, which include the implementation of BHD readout and frequency-dependent squeezing. Multiple adaptive optical elements will be employed. There are at least four adpative optics used for active mode-matching of the dual OMCs in BHD scheme and two are used

for mode matching of FC. The addition of these adaptive optics aim to achieve a mode-matching goal as follows [143],[43] :

- **OPO to FC:** mode-matched better than 96%, target of >98%
- **FC to the interferometer:** mode-matched better than 96%, target of >98%
- **IFO to OMC:** mode-matched better than minimum 96%

2.5 Conclusion

The series of problems discussed in this chapter has emphasised that mode mismatch and wavefront distortion are becoming one of the most pressing issues that potentially will inhibit the advancement in sensitivity of terrestrial gravitational wave detectors. Unless addressed properly, they will inhibit the success of various techniques employed to reduce noise, including injection of squeezed light, high power laser and balanced homodyne detection. Active wavefront control is therefore crucial for the future of the instruments. In order to successfully combat the issues caused by wavefront distortion, development of new sensors and actuators are required.

While the Hartmann wavefront sensors have been providing us with important information about issues with the core optics, they do not provide information about how these defects manifest and affect various optical fields at different frequencies in the interferometer. On the other hand, existing wavefront sensors based on resonant quadrant-photodetectors cannot provide information about high spatial frequency structure of high order modes. We thus need a new type of sensor that can simultaneously discern different frequencies in a complex optical field and provide their high resolution spatial maps. This type of sensor was developed during my PhD research and will be presented in the next chapter.

Active wavefront control also requires the development of new actuators to manipulate wavefront and reduce mode-mismatch at various optical interfaces.

Chapter 4, 5 and 6 will present some of these new actuators, which have been developed to assist with mode-matching in O4 and A+ upgrade.

Chapter 3

Demonstration of advanced phase camera

This chapter details the development of advanced phase cameras. This work builds on my previous Honours work, which covers the initial construction of the test field generator and exploring potential methods to implement the next generation phase camera theoretically. During my PhD, I performed further analysis of the test filed generator, simulate the optical system with the interferometry simulation software package FINESSE, optimising the control loop of cavity locking to acquire a stable output for phase camera testing. Later on during the PhD project, I constructed the advanced phase camera and testing its operation in different configurations, which will be detailed here in this chapter.

This chapter is laid out as follows: Section 3.1 introduces the concept of phase cameras and provides a brief review of state-of-the-art technologies and their existing limitations. The working principle of the advanced phase camera demonstrated in this thesis is discussed in Section 3.2. In Section 3.3 , the experiment design for testing this camera is presented. In Section 3.4 and 3.5, more detailed and technical aspects of two main components of the experiment- the test field generator and the phase camera are presented, together with results from advanced

phase camera demonstration.

3.1 Introduction to phase camera

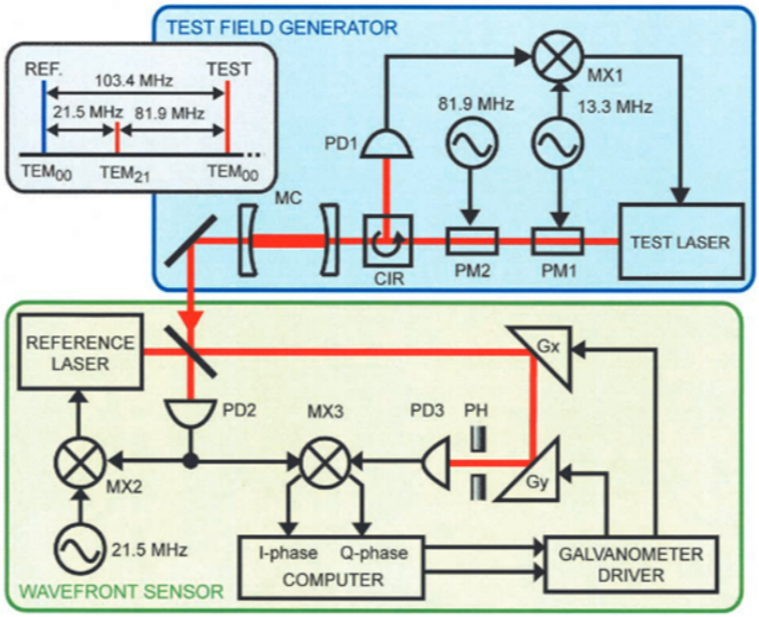

Figure 3-1: Schematics of existing phase camera developed by Goda et al. [96]. The test field generator is shown in blue box. The phase camera itself is in the green box. MC: mode cleaner cavity; REF: reference field; CIR: circulator; PM1, PM2: Phase modulators 1,2; Gx, Gy: Galvanometers scanning x and y axes of the transverse plane. PD1, PD2, PD3: Photodetectors 1,2,3.

A phase camera is a frequency selective optical field sensor, which allows spatial mapping of the amplitude and phase of a beatnote between a carrier field and a RF sideband field at a selected frequency of interest.The first phase camera was developed and demonstrated at MIT by Goda et al. [96]. Schematics of this phase camera is shown in figure 3-1. In this phase camera system, the optical field of interest is scanned across a photodiode by a pair of galvanometers G_x and G_y. A pinhole is placed in front of the phototdetector to increase resolution. Output signal from PD3 is demodulated in two quadratures at the frequency of interest. The spatial dependence of I- and Q-phase voltages are used to obtain phase and

amplitude of the beatnote:

$$|E(x,y)| = \sqrt{V_I(x,y)^2 + V_Q(x,y)^2} \tag{3.1}$$

$$\angle E(x,y) = \arg(V_I(x,y) + iV_Q(x,y) \tag{3.2}$$

where $V_I(x,y)$ and $V_Q(x,y)$ are the spatial dependent demodulated voltages in I- and Q-phases.

Early model of the phase camera achieved 1000 samples at 5 Hz acquisition rate [96]. Recent models developed for the Advanced Virgo detector to optimise performance of thermal compensation system [203], allows 128×128 sampling points at 1 Hz frame rate [16, 204, 17].

The main limitation with existing type of phase camera is the use of scanning galvanometers, which create backscatter into the interferometer. This backscatter injects excess noise [164]. This means that the original phase camera cannot be used when astrophysical science data is being collected.

Scanning from point-to-point also means that there is as strong trade-off between frame rate and spatial resolutions.

In this chapter, we detail the development of a motion-free phase camera with high spatial resolution and high frame rate.

3.2 Working principle of the advanced phase camera

Our advanced phase camera performs heterodyne detection by demodulation in the optical domain, in contrast to previous phase cameras, which perform demodulation in electronic domain [96]. This modulation can be explained quantitatively by following the schematics shown in figure 3-3. In this picture, we will consider only a signal seen by a single pixel to simplify the argument, without the loss of generality:

1. An input field consists of a carrier field $E_c(x,y)\exp[i(\omega_c t+\varphi_c(x,y))]$and an RF sideband field $E_s(x,y)\exp[i(\omega_s t+\varphi_s(x,y))]$. The difference in the frequency

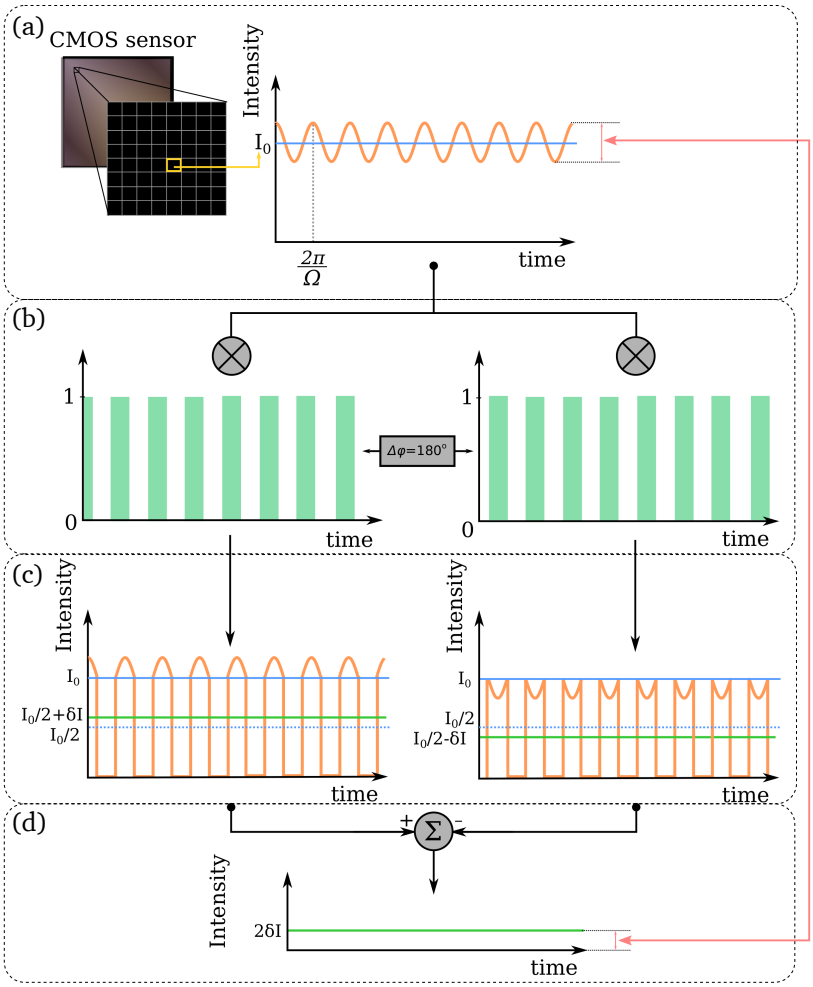

Figure 3-2: Schematics represents qualitatively the principle of working of an advanced phase camera. In this picture, we consider only a single pixel of the camera and and the light incident on such pixel, which is shown in the top panel (a). The optical switching is approximated as logical square wave, as shown in the panel (b). This synchronous switching results in a different intensities seen by the pixel (c) depending on the phase of switching relative to the signal's phase. This allows us to extract out a signal that relates to both magnitude and phase of the beat note (d)

of the two fields is $\Omega_m = \omega_s - \omega_c$. Measuring this composite field with a broadband photo detector would yield a voltage that is proportional to its intensity:

$$V(x,y) \propto E_c(x,y)^2 + E_s(x,y)^2 + 2E_c(x,y)E_s(x,y)\sin(\Omega_m t + \varphi(x,y)) \quad (3.3)$$

where $\varphi(x,y) = \varphi_c(x,y) - \varphi_s(x,y)$. This signal is presented as the oscillating

orange curve in Fig. 3-2(a). Each pixel of a standard off-the-shelf camera resembles a photodiode with a low pass filter (LPF). Any fast oscillating signal will be averaged to a DC signal I_0 (green line in(a)). Information regarding the beat note at Ω_m is thus lost.

2. The underlying working principle of the proposed phase camera is the introduction of optical switching. The optical switch "turns on and off" the light field incident on the camera's pixel at the same frequency Ω_m synchronously with the beat note. This switching on and off is expressed as a logical square wave as in second panel from the top. In this case, we consider scenarios where action switching is "in-phase" ($\phi = \varphi = 0$ in the case shown in Fig. 3-2) and "out-of-phase"($\phi = \varphi + \pi = \pi$) with the beat note.

3. Now we consider each case separately:

   - **In-phase case:** The pixel on the camera will observe all the "crest" instances of the incident optical field. This is the result of multiplying the true signal $V(x, y, t)$ and an in-phase square wave. Camera's low pass filter nature then averages this new oscillating signal V_ϕ, which results in a new DC signal that is slightly greater that half of the original DC signal: $V_\phi = (V_c + V_s)/2 + \delta V$ where $V_{c/s}$ are due to $E_{c/s}(x, y)^2$ terms.
   - **Out-of-phase case:** If the switch is out of phase with the beat signal, the camera will observe all the instances of the "troughs" of the incident optical field. The DC signal resulted would therefore be $V_{\phi+\pi} = (V_c + V_s)/2 - \delta V$

4. By subtracting the "out-of-phase" signal from "in-phase" signal, the common part $(V_x + V_s)/2$ is removed and allowing extraction of the differential term $2\delta V$. The magnitude of $2\delta V$ is related to both magnitude and phase of the beat note. The full magnitude and phase can be fully reconstructed from switching at 4 orthogonal demodulation phases $\phi = \{0, /2, \pi, 3\pi/2\}$.

$$\mathbb{I} \equiv V_0 - V_\pi \tag{3.4}$$

$$\mathbb{Q} \equiv V_{3\pi/2} - V_{\pi/2} \tag{3.5}$$

$$|E_c(x,y)E_s(x,y)| \propto \sqrt{\mathbb{I}^2 + \mathbb{Q}^2} \tag{3.6}$$

$$\phi = \arctan\left(-\frac{\mathbb{Q}}{\mathbb{I}}\right) \tag{3.7}$$

In practice, the synchronous switching is implemented with intensity modulation using Pockels effect. As discussed later in section ,a quarter wave voltage on the Pockels cell is required to switch the incident light on and off. Our Pockels cell consist of a pair of RTP crystal whose dimension is 6×6×10 mm each. Its quarter wave voltage is 1.2 kV. The capacitance of the Pockels cell is approximately 6 pF. The electrical charge Q_{PC} stored by the Pockels cell is therefore $Q_{\mathrm{PC}} = VC_{\mathrm{PC}} = 7.2$e-9 C. A square wave switching at a fundamental frequency of 15.4 MHz requires a switching bandwidth that exceeds its 7$^{\mathrm{th}}$ harmonic, beyond which the change in rise time is small. The approximate rise time τ_r of a 107.8 MHz bandwidth switch is:

$$\tau_r \approx \frac{0.35}{\text{bandwidth}} = 3.2 \text{ ns} \tag{3.8}$$

The required electrical power P to perform such switching is therefore

$$P = \frac{VQ_{\mathrm{PC}}}{\tau_r} \approx 2.7 \text{ kW} \tag{3.9}$$

which is not practical. We therefore use sinusoidal demodulation and a resonance tank circuit to implement synchronous switching with the Pockels cell. The detailed treatment of sinusoidal demodulation in context of the advanced phase camera can be found in Appendix B.

3.3 Experiment design

Fig. 3-3 shows a simplified optical layout of the phase camera experiment. The

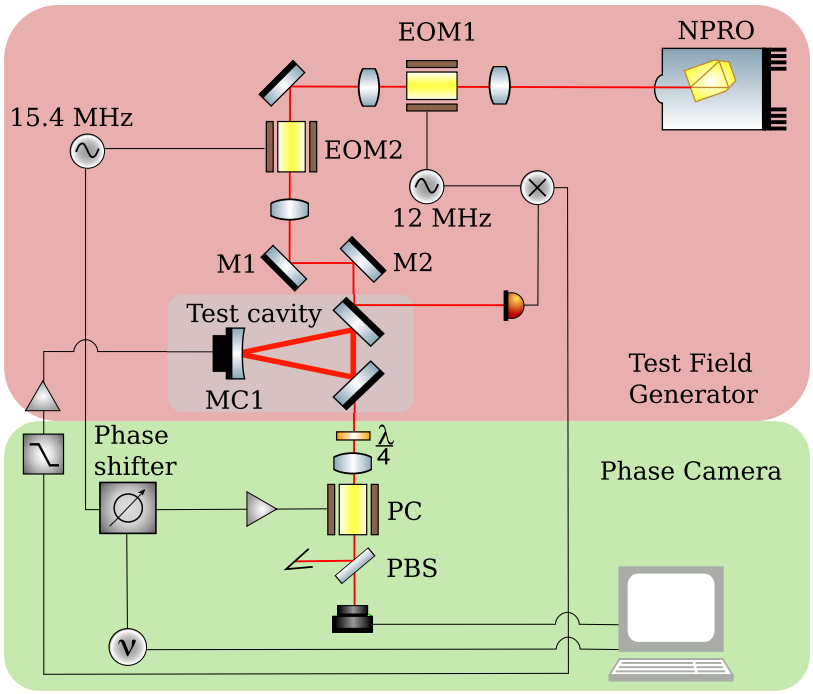

Figure 3-3: Simplified optical layout of experiment for testing the advanced phase camera, which consists of two main components: the test field generator (in red box) which generates a light field that is similar to the field that can be expected in the detector. This light field consists of a carrier field and a radio frequency sideband field whose spatial profile is known. The second component of the experiment is the phase camera itself, which is shown in the green box above.

experiment consists of two parts: a test field generator whose output is an optical field that resembles that expected at one of the sensing ports of aLIGO detector; and the implementation of the proposed advanced phase camera. There are two potential implementations of this phase camera: single camera or dual camera operation. The single camera operation, which is shown here in Fig.3-3, uses one camera at one of the outputs of the PBS and observation of the "in-phase" and "out-of-phase" is carried out by phase shifting the RF signal driving the Pockels cell. In dual camera operation, two cameras are placed at both reflection and transmission outputs of the PBS to observe "in-phase" and "out-of-phase" signals simultaneously. In the subsequent sections, we will discuss in details these two parts of the experiment.

3.4 Test field generator

The test field generator outputs an optical field consists of a carrier signal at laser's frequency ω_c and a much weaker radio frequency sideband field at frequency $\omega_{sb} = \omega_c + \Omega$, whose spatial profile is understood. This optical field is generated by locking an optical cavity to a reference NPRO Nd:YAG laser whose wavelength is 1064 nm. Pound-Drever-Hall (PDH) locking scheme is used for locking the cavity.

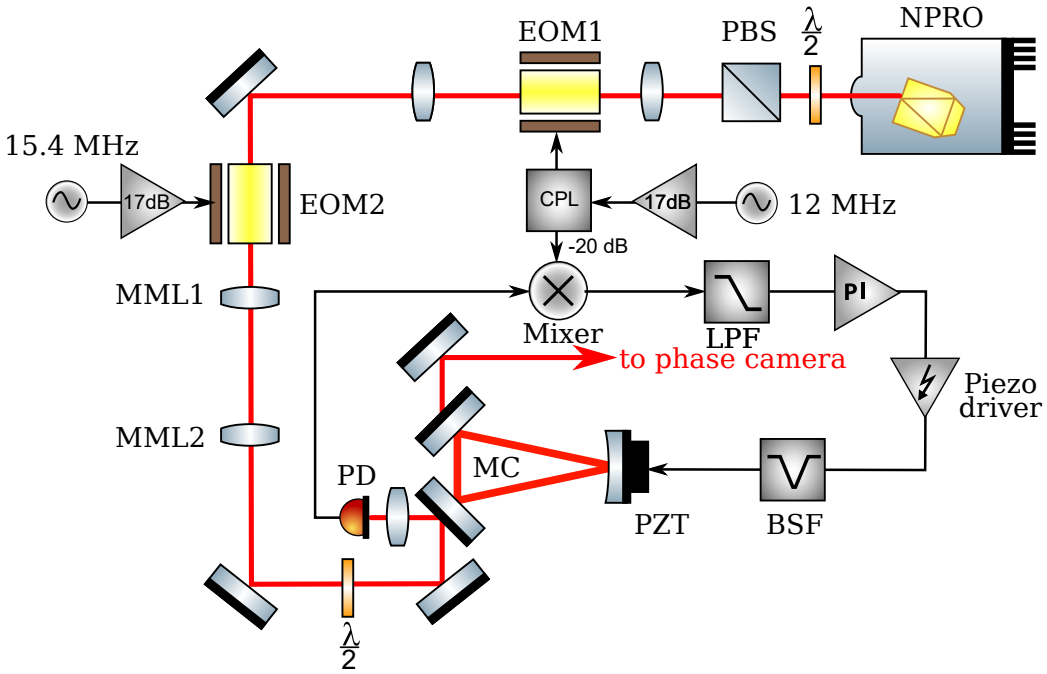

Figure 3-4: Schematics showing experimental layout of test field generator for testing phase camera: A triangular mode cleaner (MC) cavity is locked to a 1064 nm Nd:YAG NPRO laser using PDH with RF phase modulation generation generated by EOM1. Injection of a second pair of RF sidebands to couple to a higher order transverse mode of MC is implemented with the secoond EOM (EOM2). MML: mode-matching lens, CPL: directional coupler, LPF: low-pass filter, BSF: band-stop filter.

The layout of the test field generator is shown in Fig. 3-4. The output of the laser is elliptically polarised and 2.1 mm in diameter with the maximum output power of 300 mW. Throughout this experiment, an output of 10 mW was found to be sufficient. The laser output is passed through a polariser to allow only s-polarisation transmission, which is required for phase modulation at 12 MHz by a

resonant electro-optic phase modulator EOM1 (NewFocus 4003). A VCO is used to generate -3 dBm 12 MHz signal, which is subsequently amplified by 17.15 dB RF amplifier. Part of this LO (-20dB) is split off to demodulate the reflected beam signal off the cavity in PDH scheme via a directional output coupler (CPL). The output port of the CPL drives EOM1, resulting in a modulation index of approximately 0.2 radians.

A pair of sidebands at 15.4 MHz are added to the carrier field by a second EOM2 (broadband phase modulator New Focus 4004). This upper frequency 15.4 MHz sideband coincides with frequency of TEM_{30} and TEM_{12} of the test cavity. Fine adjustment of steering mirrors M1 and M2 controls the coupling of the 15.4 MHz upper sideband to these transverse modes.

3.4.1 Optical cavity for generation of test field

Fig. 3-5 shows the mechanical design of the mode cleaner cavity. The cavity is shaped unto a double-tapered "football" shape with an overall length of 258 mm. The structure provides mechanical stiffness with reduced mass so its mechanical resonances are above 10 kHz. This allows wider and higher bandwidth servos to be achieved.

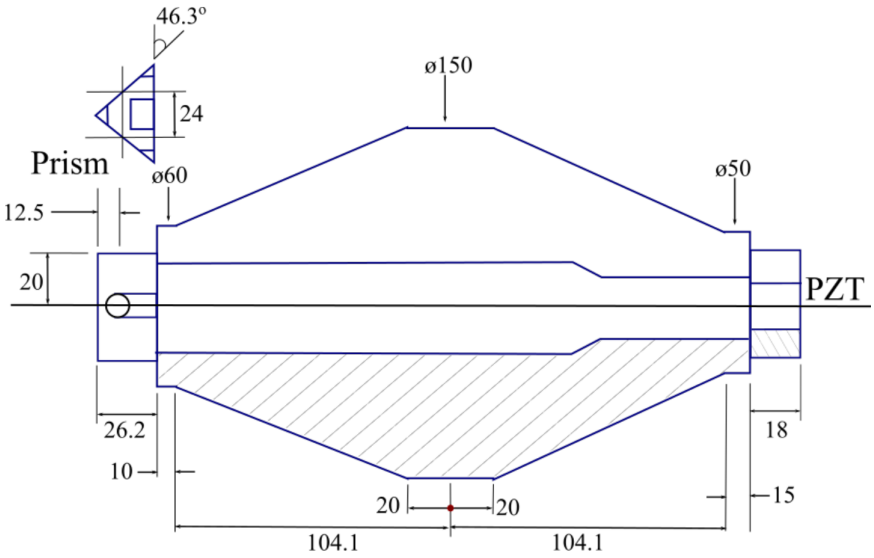

Figure 3-5: Mechanical design of the mode cleaner optical cavity. Units are in mm.

The cavity consists of three fused-silica mirrors with maximum reflectivities $\geq$ 99.95% for s-polarised in wavelength range between 996-1134 nm region. The front surfaces of two of the mirrors are planar and are glued onto a small aluminium prism at one end. The distance between the two flat mirrors is 24 mm. The mirror at the other end is a curved mirror with a 1-meter radius of curvature. This mirror is bonded to a ring stack piezoelectric actuator, which is in turn glued onto the body of the football-shaped spacer.

The optical layout of the mode cleaner and its equivalent representation as a series of lenses is shown in Fig. 3-6. The waist of the cavity mode lies half way between the two flat mirrors, as deduced from symmetry. To characterise the eigenmodes of our cavity, we present the cavity as a series of lenses, which allows application of self-consistency method [212] (see Fig. 3-6(b)).

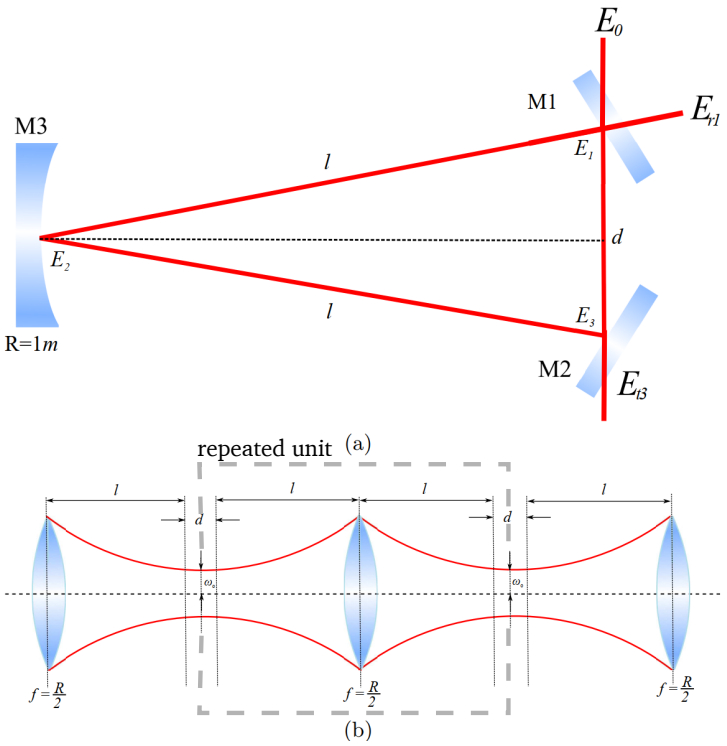

Figure 3-6: *(a)*: Optical layout of the ring cavity. *(b)*: Representation of the cavity as a series of lenses for self-consistency analysis.

Here we choose the reference plane to be at the mid point between the two flat mirrors. ABCD matrix representing one round trip is constructed with reference

to this plane. For a triangular cavity as in our case, the ABCD representing the system must take into account two complicating factors:

- **Astigmatism**: In a ring cavity, the cavity rays reflects off the curved optics at a finite angle. This introduced angle results in an astigmatism. The effective radius of curvature seen by rays that are in the plane of reflection is $R^{\mathrm{h}}_{\mathrm{eff}} = R\cos\theta$ where θ is the angle of incidence. Whereas the effective radius of curvature seen by rays that are orthogonal to the plane of reflection is $R/\cos\theta$. The matrix representing the thin lens in our lens-series picture is therefore:

$$\begin{aligned} \mathcal{F}^{\mathrm{h}} &= \begin{bmatrix} 1 & 0 \\ -\frac{2}{R\cos\theta} & 1 \end{bmatrix} \\ \mathcal{F}^{\mathrm{v}} &= \begin{bmatrix} 1 & 0 \\ -\frac{2}{R/\cos\theta} & 1 \end{bmatrix} \end{aligned} \tag{3.10}$$

- **Parity**: The displacement and angle of a ray are inverted on reflection. This inversion only has a physical consequence when there is a defined plane in a cavity, such as the horizontal plane of our triangular cavity. Reflection about the vertical coordinate does not require such inversion. To accommodate this inversion, we introduce the parity matrix upon reflection [182]:

$$\begin{aligned} \mathcal{M}_{\mathrm{h}} &= \begin{bmatrix} -1 & 0 \\ 0 & -1 \end{bmatrix} \\ \mathcal{M}_{\mathrm{v}} &= \begin{bmatrix} 1 & 0 \\ 0 & 1 \end{bmatrix} \end{aligned} \tag{3.11}$$

The round-trip ABCD matrix $\mathcal{C}$is therefore can be written as:

$$\mathcal{C}_{\mathrm{h/v}} = \mathcal{S}\left(\frac{d}{2}\right)\mathcal{M}_{\mathrm{h/v}}\mathcal{S}\left(l\right)\mathcal{M}_{\mathrm{h/v}}\mathcal{R}_{\mathrm{h/v}}(R)\mathcal{S}\left(l\right)\mathcal{M}_{\mathrm{h/v}}\mathcal{S}\left(\frac{d}{2}\right) \tag{3.12}$$

where $\mathcal{S}$ is ABCD matrix of propagation in free space.

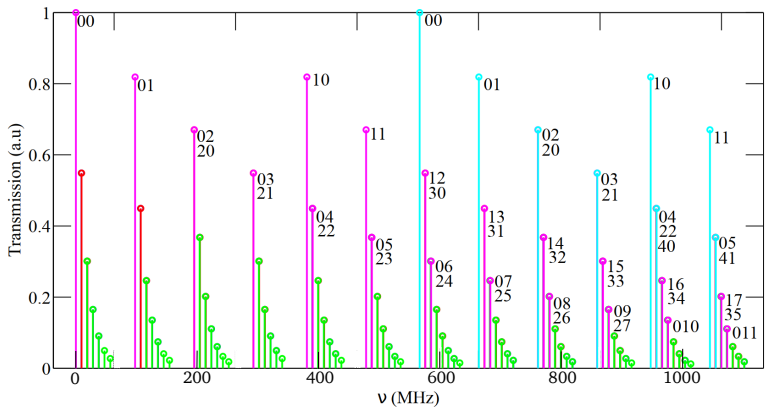

Figure 3-7: Theoretical transmission spectrum of s-polarised light computed Eq. 3.14 for q=1,2,3,4 (green,red, magenta and cyan respectively).For each q, n and m satisfy the following condition: 0≥n,m≤ 20.

From the computed ABCD matrix, accumulated Gouy phase shift after one round trip is computed using:

$$\zeta_{h/v} = 2\cos^{-1}\left[\operatorname{sgn} B_{h/v}\sqrt{\frac{A_{h/v}+D_{h/v}+2}{4}}\right] \tag{3.13}$$

where A, B and D are elements of the ABCD matrix. This accumulated Gouy phase expression only applies to field in resonant cavity. Its derivation can be found in Appendix D. The transverse mode spacing of the triangular mode cleaner is then given by:

$$\nu_{q,mn} = FSR\left[q + \left(m+\frac{1}{2}\right)\zeta_h(L_p) + \left(n+\frac{1}{2}\right)\zeta_v(L_p)\right] \tag{3.14}$$

where $FSR = \frac{c}{L_p}$ is the free spectral range and L_p is the round trip distance. $\zeta_{h/v}(L_p)$ denotes phase accumulation after a round trip. The full expression of 3.14 in term of cavity parameters can be found in Appendix D.

Considering that distances d and l (see figure 3-6) are 24 and 264 mm respectively, the angle of incidence at the curved mirror is $\theta = 2.60°$ and a round trip length L_p of 552 mm. The FSR is therefore 543.5 MHz, and the two Gouy phases are $\zeta_- = 243.35°, \zeta_+ = 63.42°$. Fig. 3-7 shows the theoretical spectrum of the mode cleaner cavity. As expected from parity, modes with a common $m+n$ are split into two groups of odd and even m transverse mode an are separated by approxi-

mately half of FSR. This theoretical calculation of eigenfrequencies are verified by scanning the cavity length using a PZT across one FSR. The map of the modes is shown in figure 3-8

Frequencies of eigenmodes are also dependent on polarisation of incoming beam because of parity. P-polarised light accumulates a π phase difference relative to s-polarised. Hence, p-polarised transverse modes of the same m, n are shifted by a half of an FSR relative to s-polarised ones in frequency space. Furthermore, microscopic phase shift due to coating are also different for s- and p- polarisation.

Since the reflectivities of cavity's mirrors are lower for p-polarised light, the cavity finesse is also expected to be lower. FWHM of p-polarised eigenmodes are therefore broader compared to those of s-polarisation. The fundamental mode of p-polarised light is labeled gray in Fig. 3-8

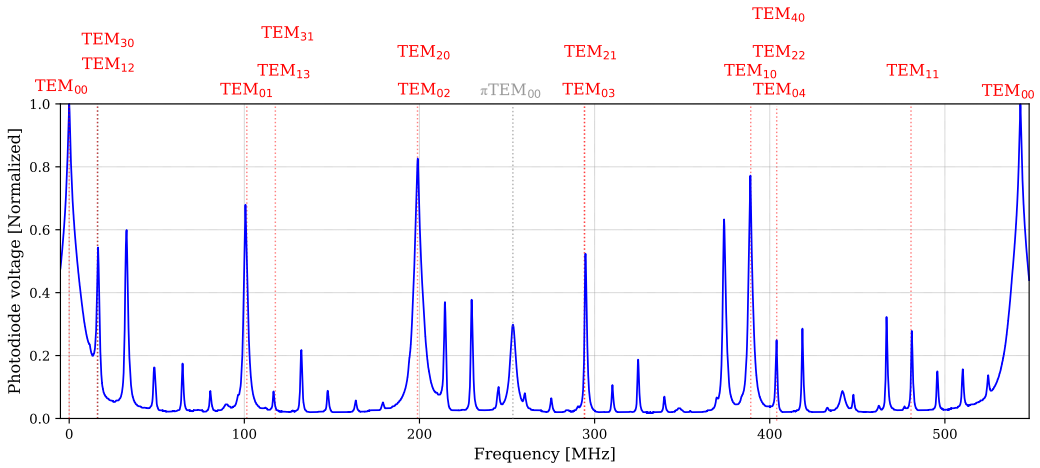

Figure 3-8: Transmission spectrum of mode cleaner cavity obtained from scanning one FSR with PZT actuator. Transverse mode with $m + n \leq 4$ are labeled on the diagram in red. P-polarised TEM_{00} appears as a broad peak at approximately 0.5 FSR (labeled in gray) due to small amount p-polarisation transmitted through the cavity

Additional to transverse mode spacing, computed ABCD matrix of a cavity round trip in self-consistency analysis also allows estimation of cavity beam $1/e^2$

radii w and radii of curvature R a different planes [212]:

$$w = \sqrt{\frac{\lambda}{\pi n}} \frac{\sqrt{\pm B}}{\left[1 - [(D+A)/2]^2\right]^{1/4}} \tag{3.15}$$

$$R = \frac{2B}{D-A} \tag{3.16}$$

where n is the refractive index at the measurement plane.

The non-normal angle of incidence at the curved mirror of the cavity thus results in a slightly astigmatic cavity mode. Table 3.1 shows w and R of cavity's beam at each mirror and cavity's waist. These quantities allows appropriate selection of lenses and distances to mode match the optical beam from the NPRO laser to the cavity. This selection is assisted with JAMMT mode matching tool [197].

Axis	Location	w(μm)	R(m)
Vertical	waist	389.2	∞
	M1	389.1	16.64
	M2	389.6	16.64
	M3	457.2	1.000
Horizontal	waist	389.0	∞
	M1	389.4	16.64
	M2	389.4	16.64
	M3	457.4	1.000

Table 3.1: Calculated beam spot sizes and radii of curvature R at cavity's waist w and each cavity internal mirror.

3.4.2 Locking cavity to laser

Locking of the mode cleaner cavity to the laser is done using the standard Pound-Drever-Hall technique (PDH) [35], whereby the 12 MHz sidebands reflected off the cavity. The resulting beat note between these and the carrier are detected by a photodiode and mixed down to baseband to generate an error signal for controlling the PZT on the cavity. Readout from the photodetector is mixed with a local oscillator signal from coupling the output of directional coupler shown in figure 3-4. Demodulation phase is adjusted by selecting appropriate coaxial cable length

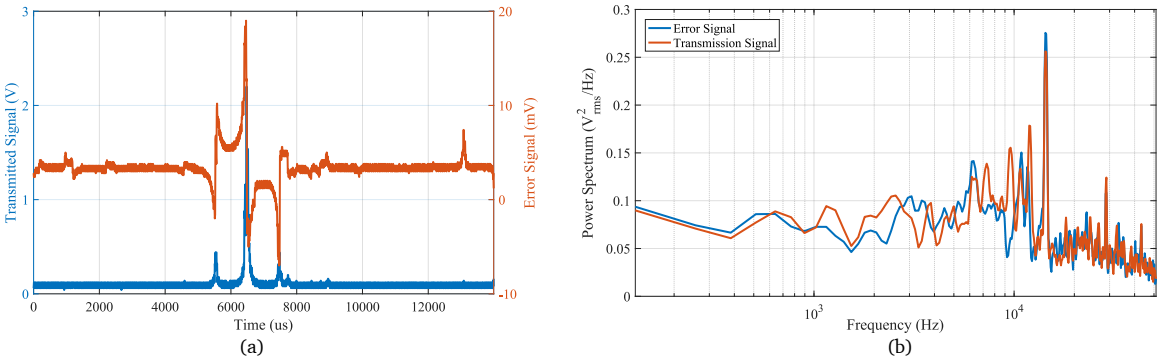

Figure 3-9: (a) Transmission of test cavity (blue) and error signal (red) after demodulation of the photodetector signal at cavity's reflection output with a 12 MHz and low-pass filtered. Both signals are obtained while scanning the cavity length with PZT. This error signal is obtained with a coaxial cable of approximately 4.2 meter to provide appropriate demodulation phase. (b) shows frequency spectrum of optical cavity during initial lock shows excess of noise at approximately 12.7 kHz. This was caused by resonance of stacked piezoelectric actuator used for length control of the cavity

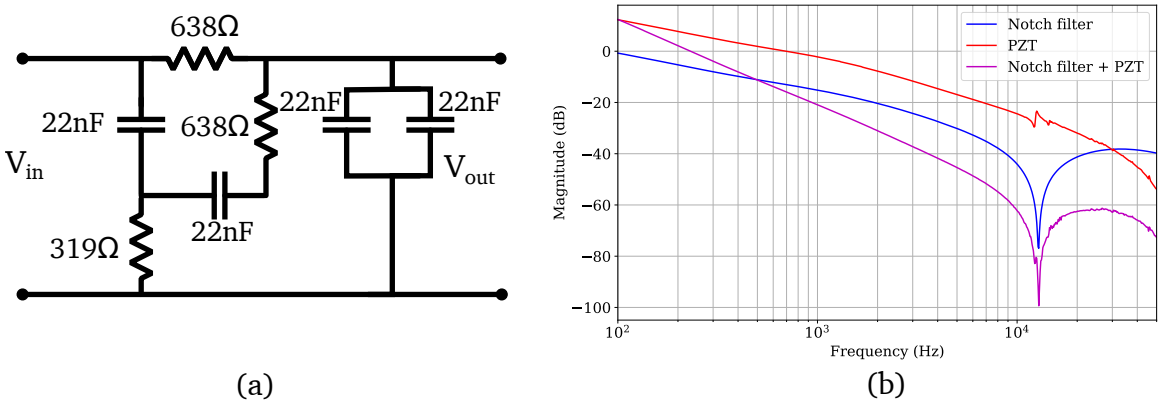

Figure 3-10: (a): Circuit diagram of a passive notch filter after PZT driver to suppress 12.7 kHz resonance. (b): Transfer functions of the notch filter (blue) measured with an audio spectrum analyser. Transfer functions of PZT with and without the notch circuit are show in red and magenta respectively.

(RG58, phase delay $\simeq 21.4°$/meter at 12 MHz). The error signal after selection of appropriate phase delay is shown in Fig. 3-9(a).

The demodulated signal is low-pass filtered with corner frequency at 100 kHz. The filtered signal is input into an analog frequency servo controller built by Slagmolen [185], which implements PI control. Initial locks of the cavity to the laser shows excess of noise at around 12.7 kHz, as seen in Fig.3-9(b).

Testing of frequency response of the PZT shows that there is resonance at 12.7

kHz, which injects excess noise at this frequency to the optical plant. To address this issue, we construct a simple passive notch filter to reject noise at 12.7 kHz, whose diagram is shown in Fig. 3-10(a). Fig. 3-10(b) shows the transfer function of this notch filter (blue). The red trace in the same figure indicates the response of PZT without the notch filter. Introduction of the notch filter after PZT driver suppresses the noise at 12.7 kHz by 60dB, allowing a more stable lock of cavity with duration of up to 6 hours. Fig. 3-11 shows the trasmitted beam intensity profile on a CMOS camera:

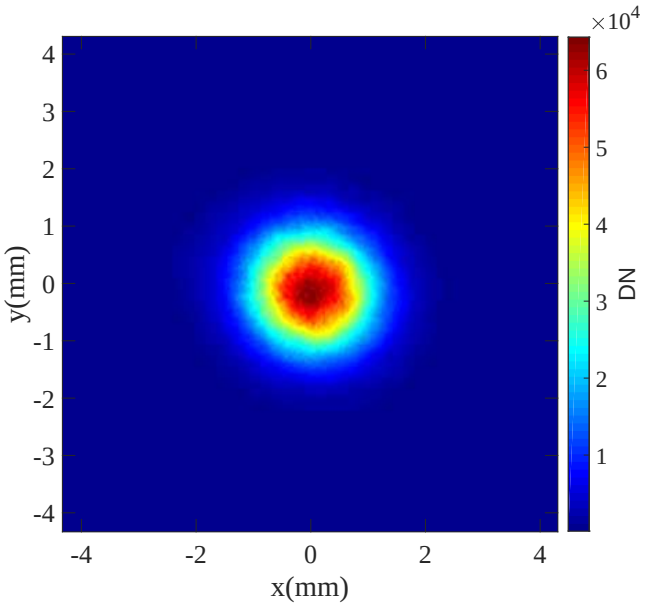

Figure 3-11: Intensity profile of cavity transmission output shows a Gaussian beam corresponding to its fundametal TEM mode

3.5 Advanced phase camera

Fig. 3-12 shows the details of the phase camera set up. The polarisation of the cavity mode is first cleaned with a Wollaston polariser in case that removes any residual p-polarisation that is transmitted through the cavity. S-polarisation is transformed into circular polarisation by the quarter wave plate (QWP). Adjustment of QWP using retro-reflection off a mirror immediately after QWP back through the

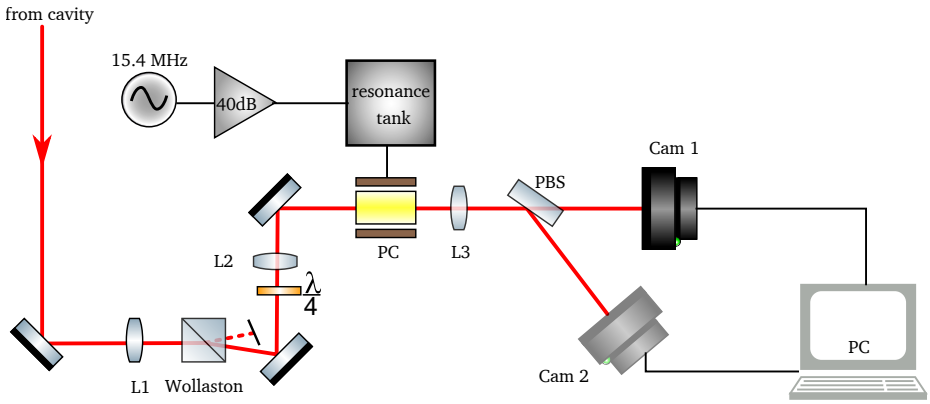

Figure 3-12: Schematics of phase camera layout, which consists of a QWP ($\lambda/4$) , a Pockels cell (PC) and a polarising beam splitter to perform optical demodulation of incoming field which consists of carrier and a sideband field at 15.4 MHz.

Wollaston prism. Rotation of QWP was finely tuned until the p-polarised output of the Wollaston prism was maximised. The resulting circularly polarised beam is then focused down onto a Pockels cell by f=200 mm lens. the Pockels cell used here is a pair of x-cut RTP crystals from RAICOL, each with dimensions of $6 \times 6 \times 10$ mm. The overall length of the crystal pair is 25 mm. The quarter-wave voltage of this Pockels Cell is $\simeq$ 1200 V.

Output of Pockels cell is focused down onto polarising beam splitter which transmits p-polarisation and reflects s-polarisation at 56^o. The PBS used here is an Eskma thin film PBS 420-488HE with an extinction ratio of 1000:1. In the single camera operation, one camera is positioned at the transmitted port. In the dual camera operation, two cameras are used. Each looks at an orthorgonal polarisation.

To drive the Pockels cell, we use the second output from a two-channel-SIGLENT signal generator SDG 2042X. This output is internally phase-locked to the first input of the signal generator, which drives the broadband EOM2 to generate the 15.4 MHz sidebands. The 15.4 MHz LO from the signal generator is amplified by 40 dB using MINI-CIRCUITS high power amplifier LY-22+ before going to resonance tank circuit.

3.5.1 Resonance tank circuit

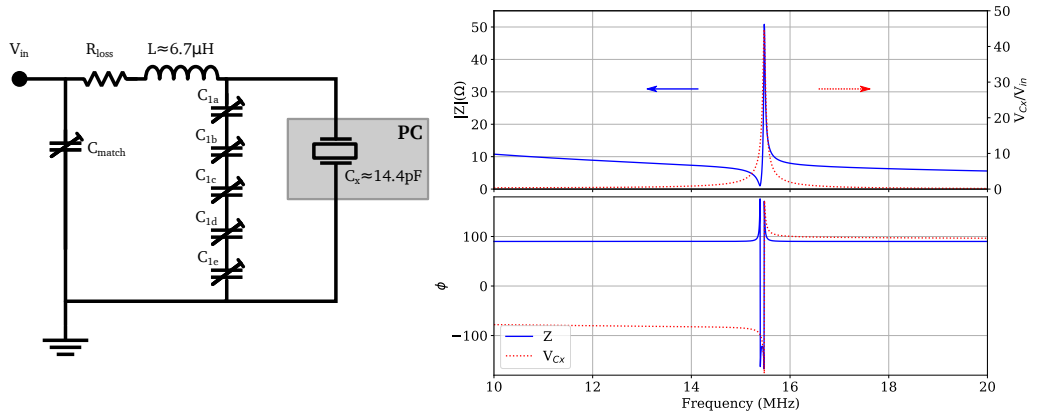

Figure 3-13: *Left:* Schematics of resonant tank LC circuit used to drive the Pockels Cell at 15.4 MHz and the pi-network for impedance matching the circuit to a 50Ω load. *Right:* LTSpice simulation of circuit impedance and voltage gain across PC crystal for an assumed loss resistance of 1 Ω. Capacitance of 5 series variable capacitors in parallel with C_x is set to C_{1i}=6pF. At this assumed loss, the matching capacitance C_{match} is 1.45 nF. The top and bottom plots show magnitude and phase respectively.

A series LC resonance tank circuit is used to provide sufficient voltage across the Pockels cell for amplitude modulation at selected frequency without the need for extremely high RF electrical power, as discussed previously in section 3.2. Diagram of this circuit is shown in Fig. 3-13. The Pockels cell acts as a capacitive component with a capacitance C_X of approximately 14 pF. A variable capacitor C_1 connected in parallel with this circuit allows tuning of resonance frequency. In practice capacitor C1 consists of 5 variable air capacitors (labeled as C_{1a}-C_{1e} on circuit diagram in Fig. 3-13) in series so that the voltage across each capacitor does not exceed its rating, which is up to 300 V. These capacitors and the crystal are connected in series with an air-core inductor made from winding ⌀1.25 mm enamel coated copper wire onto a ⌀33 mm delrin tube.

In a series LC circuit, resonance occurs when the total impedance approaches zero. Resonance frequency occurs at:

$$f = \frac{1}{2\pi\sqrt{LC}} = \frac{1}{2\pi\sqrt{L(C_2 + C_x)}} \tag{3.17}$$

A pi-network circuit, which is based on a capacitive voltage divider, is used for impedance matching the resonance tank to the RF voltage source [25]. This provides 50 Ω impedance on the desired resonance frequency. Simulation of the circuit impedance Z is shown in figure 3-13. At an assumed loss of 1 Ω, the required matching capacitance C_{match} is 1.45 nF. Since the loss in the circuit is challenging to estimate, this value provides and initial "guessed" capacitance, which is subsequently iteratively tuned to acquire impedance matching. Impedance match-

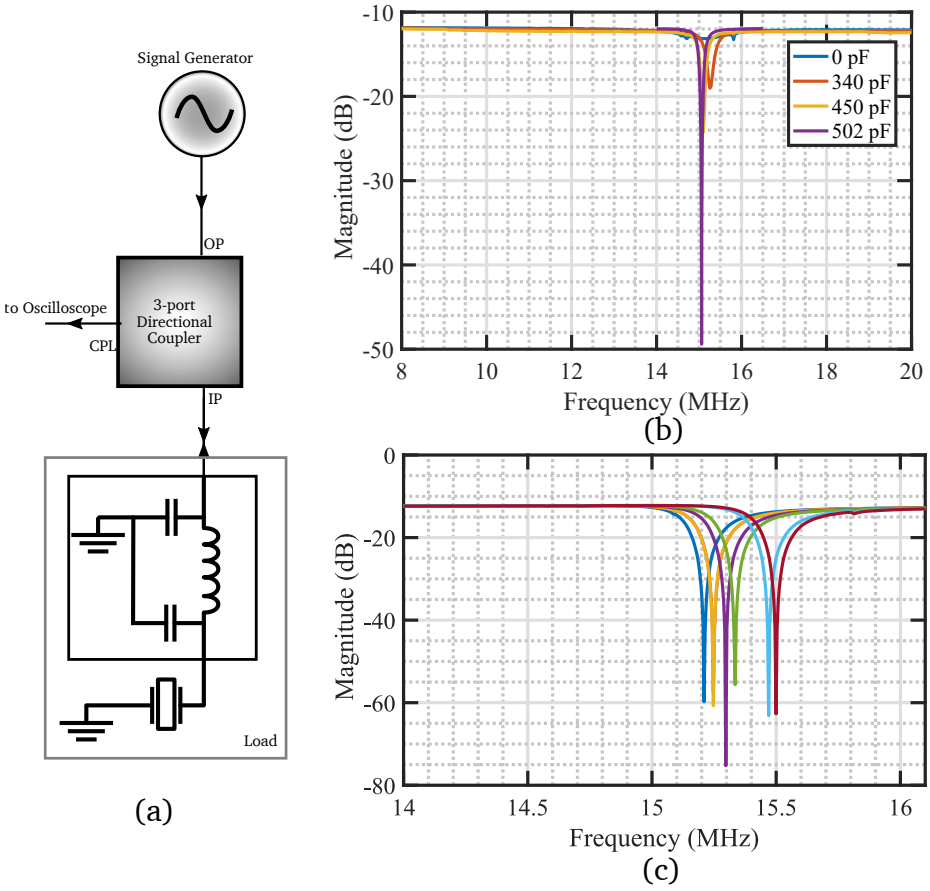

Figure 3-14: (a): Schematics of the impedance matching test of the resonance tank circuit. (b): Measured reflected signal from the circuit with different values of matching capacitor C_{match} shows input impedance of the circuit iteratively approaches 50Ω as we changed the capacitor, resulting in less signal reflected. (c): Measured reflected signal with variable capacitors used for both C_{1i} and C_{match} tuned for circuit's resonance between 15.2 and 15.6 MHz

ing was tested with an RF signal generator and a directional coupler as shown in Fig. 3-14(a). The output of a signal generator is connected to the output port of a

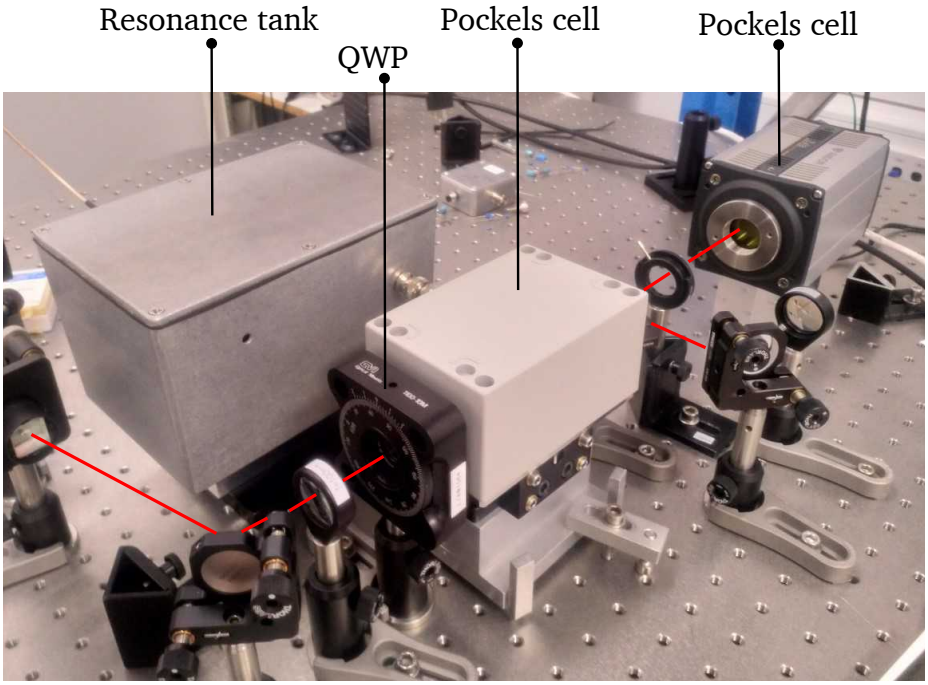

Figure 3-15: Image of an assembled phase camera, in which the resonant tank and Pockels cell are housed in diecast box for RF shielding. The polarising beam splitter is placed directly after the Pockels cell and is not shown in this image. The red trace represents the path of the test optical field through the optical layout of the phase camera.

10dB directional coupler. The reflected signal due to impedance mismatch arriving at the directional coupler's input is coupled and measured on an oscilloscope. C_{match} is iteratively changed until a minimised coupled reflected signal is achieved. Fig. 3-14(b) shows the magnitude of the reflect signal at the coupling port of the directional coupler as a function of frequency. As we changed the value C_{match} to better impedance matching, reflection at 15.4 MHz was reduced and a "dip" feature could be observed. At optimal tuning, this dip had a FWHM of approximately 300 kHz. The upper limit of the Q-factor of the circuit is approximately 50. During phase camera testing, -5 dBm 15.4 MH is output from signal generator and amplified up to 35 dBm before fed into the resonance tank circuit. Intensity modulation of up to 75% of DC signal is observed at a photodetector located after the PBS. Fig. 3-14(c) also shows that the variable capacitors use for C_{1i}'s and C_{match} allows fine tuning of resonance frequency tuning while maintaining reasonable

impedance matching.

Both the Pockels cell and the rest of electrical components, which together formed the resonance tank circuit were housed in two diecast boxes to provide RF shield, as shown in Fig. 3-15. The two boxes are connected directly using a pair of male-female miniature high voltage connectors to mimimise RF signal distortion and parasitic capacitance in coaxial cables.

3.5.2 Alignment through Pockels Cell

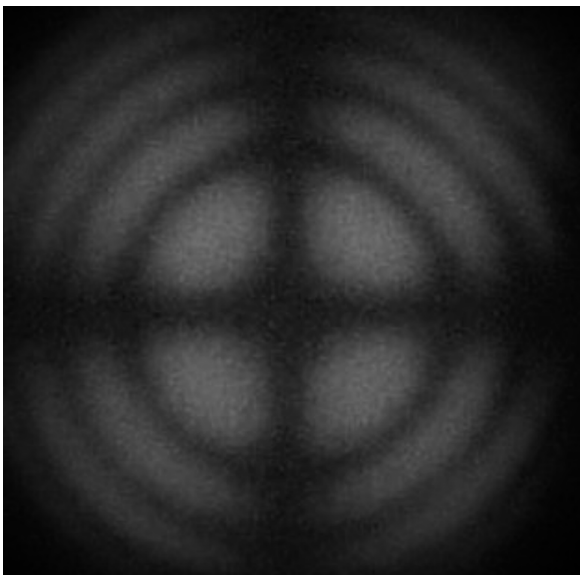

Figure 3-16: Isogyre image of p-porised light after PBS seen on a CCD camera when the PC is well aligned relative to transmitted optical beam, assuming that the incident beam is s-polarised.

Alignment procedure of test beam through PC is outlined in the following step:

1. Mount the PC on a 4-axis kinematic stage (Newport 9081).

2. Use a lens to focus the test field to the mid-point of the PC.

3. Steer the beam through PC using 2 mirrors so that the beam is in the vicinity of each crystal's center.

4. Check whether there are two beams diverging out after PC. If there are, align

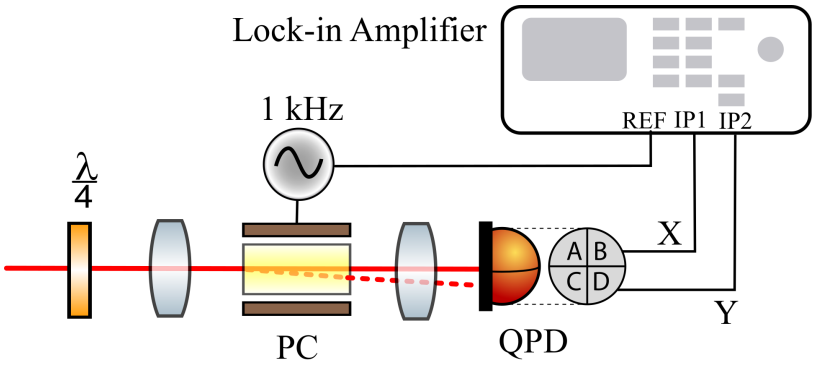

Figure 3-17: Once the PC is close to good alignment, a 1 kHz voltage is applied between PC. Here a 60 V_{pp} was used. The transmitted beam is incident on a quadrant-photodetector (QPD), whose X- and Y- position outputs are fed into a lock-in amplifier with the reference signal from the 1 kHz local oscillator. This method allows fine adjustment of PC alignment.

steering mirror or/and kinematic mount until the two beams cannot be discerned.

5. Remove the QWP so that the beam incident on PC is purely s-polarised and position a camera at the transmission of the PBS to look at p-polarised light.

6. Adjust the kinematic mount until a symmetrical isogyre pattern is observed as seen in Fig. 3-16.The isogyre pattern is a result of interference of the diverging light at angles corresponding to directions at which an additional wavelength of path difference has been added by the birefringence of the crystal [37].

7. Follow Fig. 3-17 to verify and adjust alignment finely. A 60 V_{pp} local oscillator signal whose frequency is 1 kHz is applied across the PC. This causes a small change in polarisation of input beam. Small misalignment of the beam causes modulation in beam propagating angle, which is then picked up by a quadrant-photodetector (QPD).

8. The X and Y positional values from the QPD are input to a lock-in amplifier with 1 kHz from the local oscillator as the reference. Kinematic stage is slightly adjusted such that the R-values of both X- and Y- signals are minimised.

3.5.3 Camera consideration

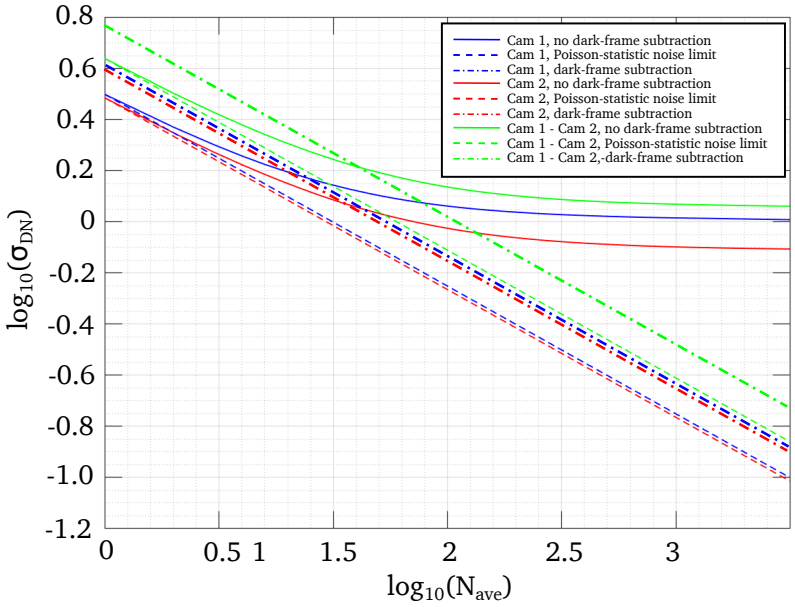

Figure 3-18: Standard deviation of DN across two Zyla sCMOS sensors plotted as function of number of frames averaged over. The Poissonian statistics noise limits are shown as dashed-lines.

A camera with a large dynamic range is essential so that the phase camera can detect weak field fields buried amongst brighter ones, such as the carrier field in our case. The dynamic range of a camera, which is defined as the ratio between the maximum output signal level without saturation and the minimum detectable signal. The maximum output signal is determined by a camera's full-well capacity.The camera usedan in our experiment is Andor Scientific CMOS (sCMOS) Zyla 4.2. The camera's full well depth is specified to be 30,000 electrons by the manufacturer [194]. The camera output is 16-bit disgitsation image (thus 65,536 levels). The number of useful levels were 65,440 since the sensor has an offset level whose mean was measured to be 96 digital numbers. During the camera's nominal operation condition (TEC cooled at 0°C), its dark frame's standard deviation in pixel value is 2.8 digital numbers.This is equivalent to $\simeq 1.2\ e^-_{RMS}$ noise, which is slightly higher than the manufacturer's claim ($0.9\ e^-_{RMS}$) [194]. The noise sources here are mainly dark current noise and readout noise. Both follow Poisson statistics. These

numbers imply that Zyla 4.2 has a dynamic range ratio of 25,000:1 (or 88 dB) instead of 33,000 as specified, which is sufficiently high for our purpose.

Pattern noise

Fig. 3-18 shows the standard deviation in pixel values of dark frames σ_{DN} with increasing number of averaged frames. Had noise in dark frames been simply readout noise and dark current noise, measured $\log_{10}(\sigma_{\mathrm{DN}})$ would have decreased with a slope of -0.5. However, existence of the fixed pattern noise, which is caused by the pixels in the camera having slightly different dark current, limits the reduction of noise with increasing number of frames averaged over. The (solid) curves therefore plateau out atlarge number of frames (figure 3-18). Subtraction of these dark frames with themselves removed the fixed pattern noise [171]. The resultant frame had Poissonian readout noise and dark current noise, whose magnitudes decreases with increasing $\sqrt{N_{\mathrm{ave}}}$ (dash-dotted lines). However, the need to subtract dark frames results in a doubling of noise magnitude. For dual camera operation of a phase camera in which two cameras are used, each image of the optical field recorded by a camera requires subtraction withthe dark frame of that camera. In single camera operation, since a set of images is subtracted from another set taken by the same camera, there is no need to perform dark frame subtraction.

Bright frame noise

The total effective noise of the camera when a "bright" frame acquired is the quadrature sum of dark current noise (σ_{d}), readout noise (σ_{r}) and photon shot noise (σ_{s}):

$$\sigma_{\mathrm{tot}} = \sqrt{\sigma_{\mathrm{d}}^2 + \sigma_{\mathrm{r}}^2 + \sigma_{\mathrm{s}}^2} \tag{3.18}$$

Photon shot noise is a statistical noise associated with the arrival time of photons at a camera's pixel. It also follows Poissonian statistics and is dependent on signal level:

$$\sigma_s = \sqrt{(\mathrm{QE})N_\gamma t} \tag{3.19}$$

where QE is quantum efficiency, N_γ is the number of photons per second and t is exposure time. Assuming that the sensor has high linearity (>99.8% per manufacturer's specification [194]), the photon shot noise can be estimated in term of digital numbers (DNs). To avoid deviation from linearity close to saturation, the mean maximum signal on the camera is maintained at 65270 digital numbers. The fluctuations due to shot noise is therefore approximately 250 digital numbers. The dominant noise source in a bright frame is the photon shot noise. The Poissonian statistics of this type of noise means that improvement of signal-to-noise ratio can be achieved by averaging frames and pixel binning.

Linearity

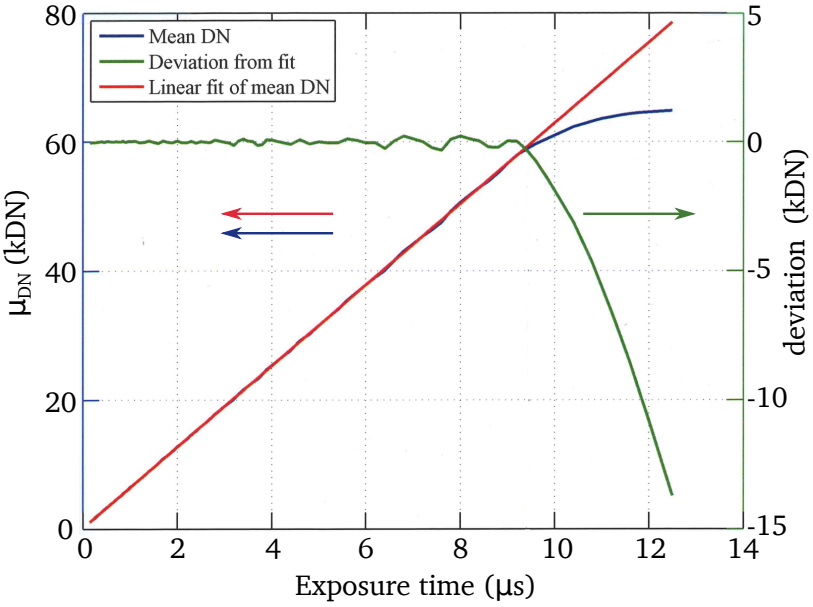

Figure 3-19: Verification of sCMOS Zyla 4.2 linearity with mean DN across the entire sensor as a function of exposure time (left y-axis). Right y-axis shows deviation of measured mean DN from a linear fit.

Linearity of a camera is measured from a plot of mean signal as a function of exposure time [194]. A sCMOS Zyla is uniformly illuminated with a 1064 nm beam. This is achieved by focusing a 1064 nm collimated laser beam with an f=8 mm lens. The camera is placed at 500 mm away from the the lens. A black anodised alumininium beam tube is placed in front of the camera to prevent stray reflection

from camera's C-mount thread. Camera I/O pin 2, which outputs TTL exposure timing signal [195], is monitored on an oscilloscope. The width of each pulse from this pin shows the actual exposure time of the camera. Fig. 3-19 shows the mean digital number across the sensor array as a function of exposure time measured on the scope (blue). As seen in this figure, at approximately 9.5 μ, the mean DN stops increasing linearly but plateaus out. This is caused by pixels reaching their saturation level. A linear fit is applied to exposure time periods shorter than 9.5μs (red). Deviation of measured mean value from this linear fit is given by the green trace in Fig.3-19. Non-linearity of a camera is defined as [166]:

$$\text{Non-linearity}(\%) = 100\% \frac{\text{Max. positive deviation + Max negative deviation}}{\text{Maximum signal}} \tag{3.20}$$

From the data obtained, non-linearity of Zyla sCMOS with 1064 nm uniform illumination is 0.75%. Linearity is therefore 99.25%, which is only slightly lower than manufacturer's specification.

3.5.4 Dual camera operation

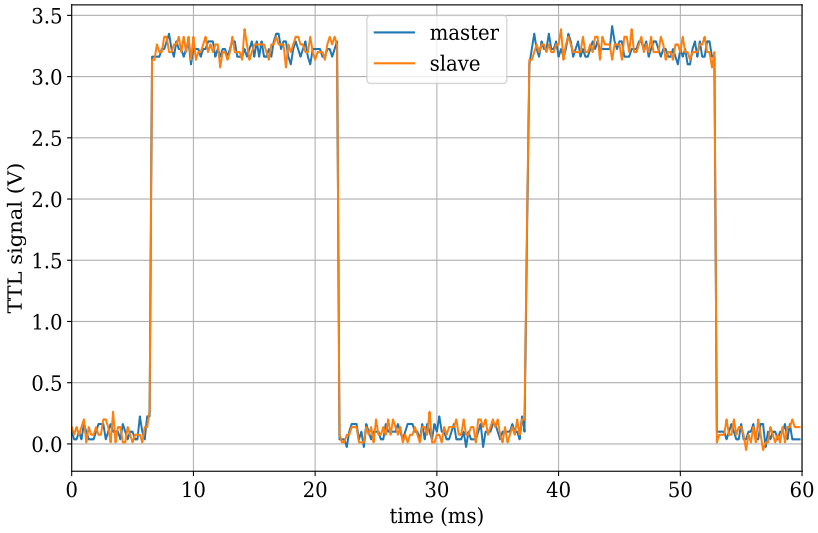

Figure 3-20: Auxiliary outputs of two Zyla sCMOS cameras, which show time at which the first row of each camera's sensor is exposed after synchronisation.

In the dual camera operation, it is important that the two cameras must take

images synchronously and the optical paths seen by two beams split from PBS are as close to identical as possible.

The first condition is easily achieved by synchronising the two Zyla cameras. In this operation, one camera acts as a "master" which sends out trigger signal to the second camera, which is referred to as a "slave" camera. The master camera exposure mode is set to internal trigger. Pin 4 of camera's IO pins, which indicates the exposure of first master camera's first row is used for trigger slave camera (pin 7 of IO pin). The slave camera is set to external exposure triggering mode. Auxiliary outputs of the two cameras (pin 2) are plotted on Fig. 3-20, which shows that exposures of the CMOS cameras coincide with one another have the same exposure time.

Ensuring that the optical path seen by the two beams on the two cameras proved to be significant more challenging. In the following sections, we outline methods to minimise these differences.

Alignment of two cameras

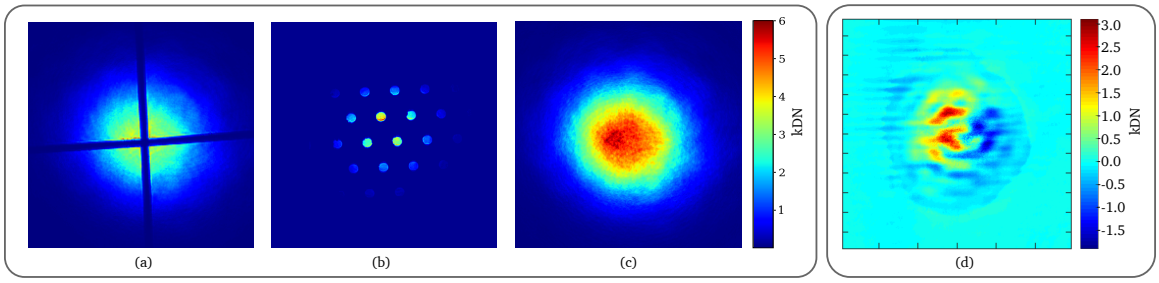

Figure 3-21: (a): a typical image of a crosshair used in first step of alignment once imaging condition is achieved. (b): A mask of hexagonal-packed holes are used to finely tune pitch and yaw of cameras. (c): Gaussian beam on a camera after alignment and removal of the mask. (d): Subtraction of images of an identical with no RF sideband at 15.4 MHz shows an underlying structure due to a small difference in beam alignments

We first attempt to minimise the optical path difference by ensuring that there is an imaging condition set up at the sensors' plane. To set up this imaging condition, a mask is introduced after the PC and before the PBS and each camera is mounted on a 5-axis (X, Y, Z, θ_X, θ_Y) kinematic mount (Newport 9081). Two masks were

tried: a cross hair and a hexagonal pack of holes with 150 $\varnothing\mu m$. Lens L3 in Fig. 3-12 images this mask to both cameras.

The initial alignment uses cross-hair mask (Fig. 3-21(a)). The two cameras are first translated along the optical axes (after PBS) until they are at positions that are close to imaging condition. Once they are in this location the kinematic bases are locked onto the optical table, z-axis translation is tuned finely with the kinematic mount until fringes around the cross-hairs are minimised on both cameras. Other axes are tuned so that the position and alignment of cross-hair images are approximately the same on each sensor.

The cross-hair mask is then replaced with the hexagonal-packed hole array mask once a good imaging condition has been acquired (Fig. 3-21(b)). The hexagonal packed pattern allows finer tuning of pitch and yaw of the two cameras by comparing the size of each hole on the pattern. Images from the two camera are overlaid over one another to compare the position of each hole. If there is a significant difference, one camera was readjusted until the positions of the pattern are closely matched. This readjustment may causes the deviation from imaging condition, at which point, one need to to return to alignment with the cross-hairs. This process continues until no further improvement in the imaging and alignment occurs. The process can take a long period of time and require frequent checking after finishing in case there is a drift any camera's position. The hexagonal array mask is then removed and images of the Gaussian beam are acquired by the two synchronised cameras (Fig. 3-21(c)). To further align the image of the Gaussian beam on the sensors, the centroid of each image is computed. Images taken from the slave camera is translated by the difference in centroid positions. The difference between the two images are then computed and shown in Fig. 3-21(d). The test optical field in this image does not contain any RF field at 15.4 MHz. Image resulted from an ideal subtraction of such field should result in shot noises. However, Fig. 3-21(d) shows that there is underlying structure which consist of a positive and a negative regions, resulting in an averaged difference magnitude of 3000 DN in the region of radius 1 beam size w. This structure indicates that there is a small misalignment

of the optical fields seen by the two cameras, mainly due to rotation of the beam about optical axes Z. This limitation is first due to the lack of control of θ_Z d.o.f on the kinematic base. Further more, the method of finding centroid is susceptible to ambient light, which results in non-zero signal in the region of the sensors that is outside of the test optical field.

Image matching of two cameras

To improve matching images between two cameras for subtraction, we perform computational transformation of one image so that it matches the other. One image is transformed using affine transformation, which preserves collinearity.

Affine transformation include translation, rotation, scale ad shear, in which translation and rotation are the main transformations of interest. Scaling and shearing have been fined tuned using physical alignment by optimising imaging condition.

Formulation of the problem

Considering the simplest case where we have some unknown translational mismatch between the two images taken by the two camera. Let $\mathbf{X}$ be the image taken by p-polarisation camera and $\mathbf{Y}$ the image taken by s-polarisation camera. For example, $\mathbf{Y}$ is a copy of $\mathbf{X}$ that is t pixels translated in x-direction. We now would like to transform $\mathbf{Y}$ such that it matches with our reference image $\mathbf{X}$. Then we let $\mathbf{Y}_t$ be the translated $\mathbf{Y}$ in x by t pixels.

To quantify how good our matching of the two images $\mathbf{X}$ and $\mathbf{Y}$ is,we use a figure of merit quantity referred to as the *mismatch function* $M(\mathbf{X}, \mathbf{Y})$ and require that $M(\mathbf{X}, \mathbf{Y}_t) < M(\mathbf{X}, \mathbf{Y})$ [39].

We therefore want to find the translation t that results in the minimum value $M(\mathbf{X}, \mathbf{Y}_t)$:

$$\hat{t} = \texttt{argmin}_t \left[\mathbf{X}, \mathbf{Y}_t\right] \tag{3.21}$$

In most of these cases, we would like to perform sub-pixel translations. Re-sampling the 2D image array is therefore important. This re-sampling will be even more

crucial for other transformation, such as rotation. Re-sampling is achieved with bilinear interpolation which is a 2D version of a linear interpolation in 1D array. This re-sampling can be implemented with `scipy` function `affine_transform`.

We then choose a metric for image mismatch M and attempt to minimise the mismatch. Our method of matching here uses correlation of pixel value at each pixel as the metric [39]. A well-matched pair of images means that value of pixel $(x_i, y_j)_1$ of camera 1 is equal, or close to that of $(x_i, y_j)_2$ of camera 2 for $0 \leq i, j \leq 2048$. The correlation coefficient used here is the Pearson correlation coefficient:

$$r_{xy} = \frac{\sum_{i=1}^{n}(x_i - \overline{x})(y_i - \overline{y})}{\sqrt{\sum_{i=1}^{n}(x_i - \overline{x})^2}\sqrt{\sum_{i=1}^{n}(y_i - \overline{y})^2}} \tag{3.22}$$

where we have raveled the 2D image arrays $\mathbf{X}$ and $\mathbf{Y}$ into 1D arrays of size 2048^2. x_i and y_i are thus the pixel value of pixel i in the 1-D $\mathbf{X}$ and $\mathbf{Y}$ image arrays. $\bar{x}$ and $\bar{y}$ are the mean pixel values of the two arrays $\mathbf{X}$ and $\mathbf{Y}$. The quantity r_{xy} varies between 0 and 1, where 1 indicates a perfect correlation, hence a perfect match between two images. The mismatch M can then be defined as $-r_{xy}$ and therefore is minimum at $r_{xy} = 1$. The correlation coefficient can be computed directly with `numpy` function `corrcoef`.

The next step is to optimise this metric. Here we use `scipy` Python library function `fmin_powell` to find the minimum of the cost function, which is the mismatch M using Powell's method. Powell's method is an algorithm developed by to find the minimum of a function without the need to calculate its derivatives [169], which can be noisy due to photon shot noise in an image. This function would try different values of translations until the minimum value of M is achieved.

This procedure can then be extended to other transformation, namely y-translation and rotation. Function `affine_transform` can be used again to implement all of these transformations. Minimisation process will involve the following step:

- Adjust the rotational angle until the mismatch in rotation is minimum.
- Adjust x-translation until the mismatch in x-translation is minimum.

- Adjust y-translation until the mismatch in y-translation is minimum.
- Repeat the first three steps iteratively until the minimum for all three parameters are stable.

Simulation

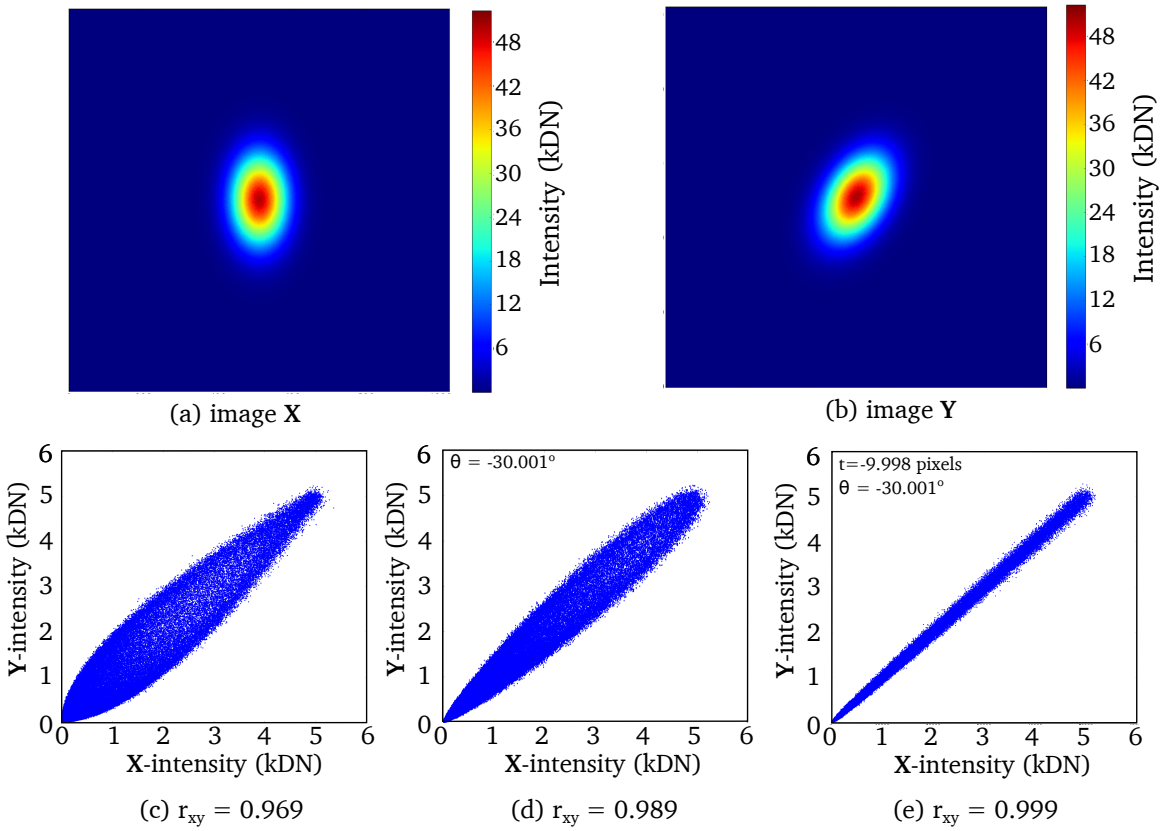

(a) image **X** (b) image **Y**

(c) r_{xy} = 0.969 (d) r_{xy} = 0.989 (e) r_{xy} = 0.999

Figure 3-22: The top panel shows the two images generated for testing the image matching algorithm. Each image consists of a Gaussian beam intensity profile. Image **X** (a) is the reference image. Image **Y** (b) is the image of the transformed beam. The raveled 1D image arrays of (a) and (b) are plotted against each other in (c).(d) shows the same plot if only rotation transformation optimisation was performed on (b) and (e) shows the result when both translation and rotation transformations were performed on image (b).

Fig. 3-22 shows a simulated example in which an elliptical Gaussian beam profile with photon shot noise has been generated as a reference image **X**. This beam profile is translated by 10 pixels and rotated by 30° clockwise. The transformed profile assumes a different shot noise profile. This gives us a second image **Y** for image matching testing. The raveled 1D arrays of images **X** and **Y** are plotted

against each other in Fig. 3-22(c). The correlation coefficient r_{xy} between the raw data is 0.969. Performing rotation matching gives us plot (d) and a correlation coefficient r_{xy} of 0.989. Iterative matching process to optimise both translation and rotation matching gives us an x-shift of -9.998 pixels and rotational shift 30° anticlockwise as the transformations to best match $\mathbf{Y}$ to $\mathbf{X}$, which agree with the initial input. As seen in Fig. 3-22(e), the two raveled arrays have become significantly more correlated with a correlation coefficient r_{xy} of 0.999.

Application to real data

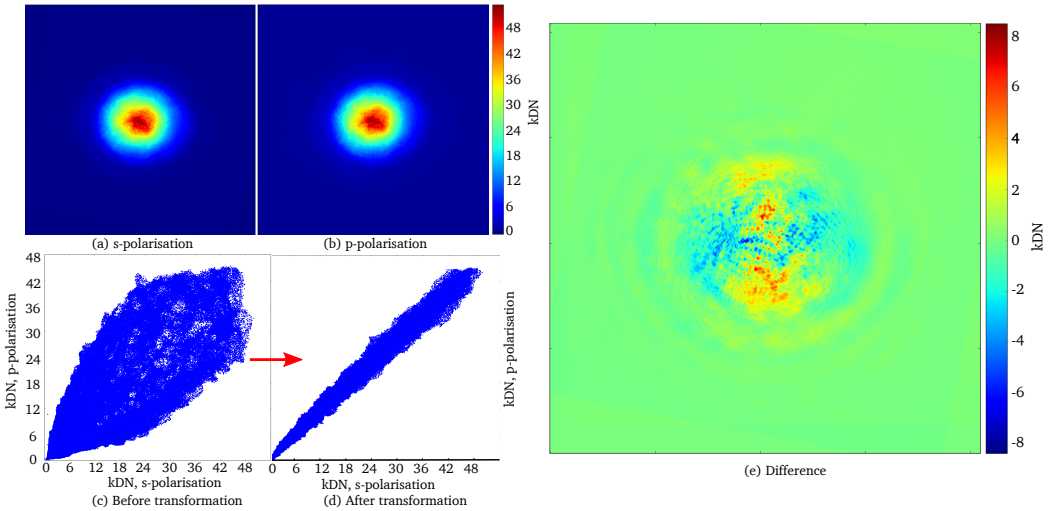

Figure 3-23: (a) Intensity profile of the optical field observed by the camera at reflection of PBS (s-polarisation). (b) Intensity profile of the optical field observed by the camera at transmission of PBS (p-polarisation). (c) Scatter plot of raveled pixel values of the two images (a) and (b) are plotted against one another. (d) The same scatter plot after image recorded by s-polarisation camera has been transformed to match the other. (e) Difference between the two images after image matching.

Application of image matching is shown in Fig. 3-23. Images of intensity profiles seen by two camera and reflection and transmission of PBS are shown in 3-23(a) and (b). Fig. 3-23(c) shows the two image arrays corresponding to (a) and (b) raveled and plotted against each other. The correlation coefficient of the raw arrays as seen by camera is 0.892. After transformation of s-polarisation camera image, the correlation coefficient is improved to 0.996. The scatter plot after matching two images is presented in Fig. 3-23(d), showing reduction in the degree of scattering. Implementation of this image matching process can be found in Appendix E.

Fig. 3-23(e) shows the difference in two matched images. The low spatial-frequency difference in figure 3-21 is improved significantly. There remain high spatial frequency structures caused by imperfection in optical system as they propagate and are distorted after splitting at PBS. The average difference magnitude is reduced to approximately 1000 (from 3000), which is 10% relative to the maximum intensity of the sum of the two frames. Observation of RF sideband fields whose magnitudes are 0.1% to 1% of carrier field can therefore be challenging to realise even with image matching.

3.5.5 Single camera operation

The complication of matching images in the dual camera operation can easily be eliminated with a single camera operation in which there is only one camera observing either s- or p- polarisation after PBS. The optical field seen by the other camera can be acquired by phase shifting the the local oscillator driving the Pockels cell by 180°. All optical distortion due to optical imperfections in the propagation path become common mode and get removed in subtraction.

Results

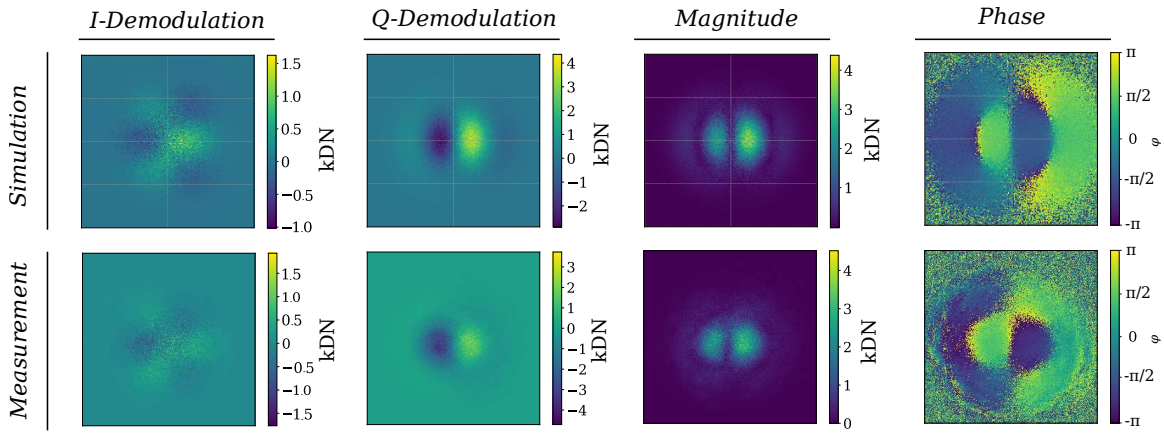

Figure 3-24: Comparison between I, Q demodulation maps and magnitude and phase maps from camera measurements and predictions from a FINESSE simulation. The digitized pixel values are given in units of thousands of digital-numbers (kDN) and plotted using the false-color scale bars.

Typical $\mathbb{I}$ and $\mathbb{Q}$ images and the result of a numerical simulation of the test-field generator using FINESSE[51] are shown in Fig. 3-24. As expected from frequency of test cavity's HOMs, we observe both TEM_{30} and TEM_{12} at 15.4 MHz demodulation. In this case, the TEM_{30} mode is apparent in the Q demodulation while the TEM_{12} mode occurs mostly in the I demodulation. Only the two central maxima of the TEM_{30} mode are observed in this demonstration as the amplitude of the TEM_{00} reference field is much smaller at the location of the outer maxima. Both magnitude and phase maps of this field are also shown in Fig. 3-24 and agree well with simulation.

The FINESSE simulation used plausible misalignments and included shot noise to reproduce outputs of the optical system. For the simulation shown in Fig.3-24, the ratio of the power in higher-order mode to that in the TEM_{00} was 14% for the TEM_{30} and 8% for the TEM_{12} modes, and thus the magnitude is dominated by the TEM_{30} mode but the phase shows some influence of the weaker TEM_{12} mode, which degrades the spatial resolution we are able to demonstrate in the next section. The code used for simulation of phase camera can be found in Appendix F.

Noise floor and sensitivity

The sensitivity and noise floor of phase camera are investigated first by removal of the 15.4 MHz modulation and recording frames with demodulating phase alternating between 0 and π. A typical image of V_0 and V_π frame is shown in Fig. 3-25(a), which shows a Gaussian intensity profile which is characteristic to TEM_{00} mode of the carrier field. The magnitude of a typical e $V_0 - V_\pi$ image is shown in Fig. 3-25(b) in logarithmic scale. The difference between two such images is shot-noise limited. There is no underlying structure as in this subtraction compared to the subtraction of the two cameras in dual camera operation. By taking multiple sets of V_0 and V_π images (200 sets used here) and compute the RMS of $|V_\pi - V_0|$ as function of difference frames averaged, one can obtain a plot similar to that shown in Fig. 3-25(b). The fitted straight line has a slope of -0.5 in logarithmic scale, which implies that

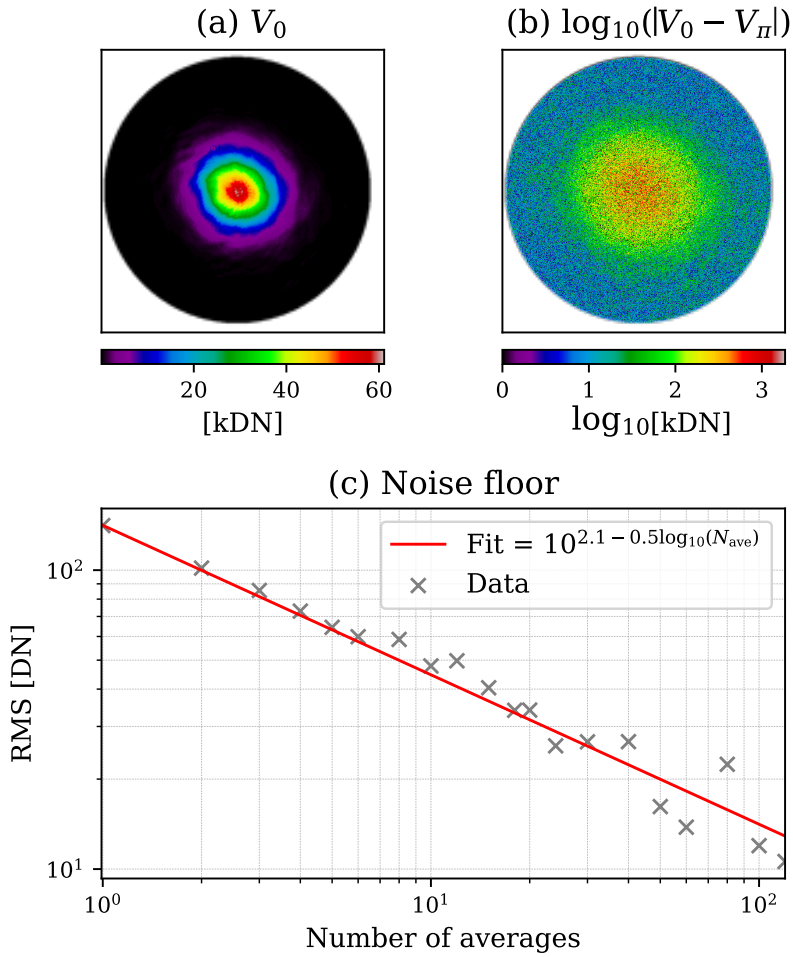

Figure 3-25: (a) Typical images V_0, V_πi, $V_{\pi/2}$ or $V_{3\pi/2}$ optical field seen by phase camera,which shows a strong Gaussian intensity profile of the carrier field.(b) shows the logarithmic of $(|V_0 - V_\pi|)$ for a single pair of images when there is no RF sideband within the field at 15.4 MHz. (c) shows how the RMS of $|V_\pi - V_0|$ decrease with increasing number of frames averaged.

residual noise is proportional to $\frac{1}{\sqrt{N_{\text{ave}}}}$ where N_{ave} is the number of averages. The residual noise therefore follows Poissonian statistics.

Fig. 3-26 further shows that this residual noise is dominated by photon shot noise. The plot shows a cross-section along x-axis of transverse plane of $|V_0 - V_\pi|$ shows magnitude of noise. By dividing the difference image into consecutive circular regions, the standard deviation of fluctuation in intensity is computed over region and shown in red in Fig. 3-26. The maximum intensity of the beam recorded by camera (Fig. 3-25(a)) is approximately 58,000 DNs. Photon shot noise

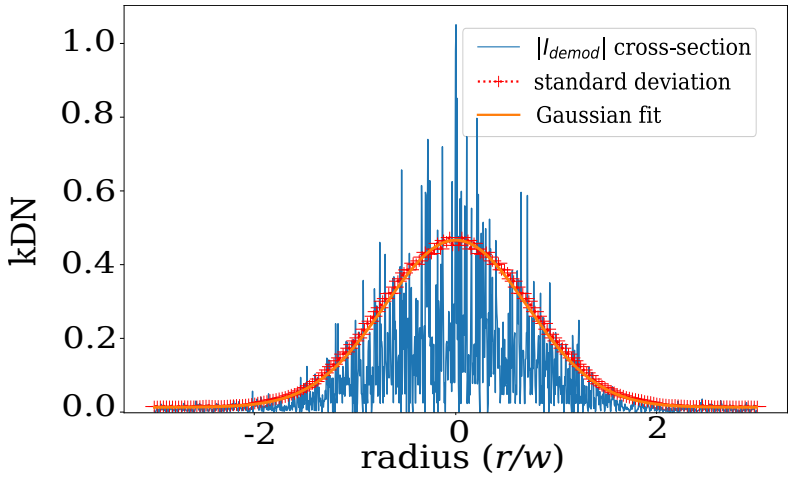

Figure 3-26: Cross-section of $|V_0 - V_\pi|$ image shows noise scaling with beam intensity

at the maximum intensity is therefore $\approx$ 240 DNs for a single frame. The shot noise results from subtraction of V_0 and V_π images is the sum of shot noise from each frame. Therefore, the expected magnitude of shot noise in $V_0 - V_\pi$ image is$\approx$ 480 DNs, which is confirmed in figure 3-26. Furthermore, since the intensity of incident beam is well described by a Gaussian: $I(x, y) = I_{\max} \exp(-2r^2/w^2)$, $\sigma_{V_0 - V_\pi} \propto \exp(-r^2/w^2)$, whose $1/e^2$ radius is as twice as large as w. This is again verified with the Gaussian fit on Fig. 3-26.

This photon shot-noise limitations alludes to the fact that improvement in sensitivity of phase camera can be achieved with averaging more frames and pixel binning:

Improvement in sensitivity due to averaging and binning by reintroducing the 15.4 MHz modulation of EOM2 and recording twenty frames at each of the four demodulation phases. In the case of N_{ave}= 20, 2×2 pixel binning is also employed. The magnitude and phase of the beat signal with $N_{\text{ave}} = 1$ and $N_{\text{ave}} = 20$ are shown in figure 3-27(a), (b), (d) and (e) respectively. The use of averaging and pixel binning improves the signal-to-noise ratio in the maps, as seen in Fig. 3-27(c) and (f).

The minimum signal power detectable can be estimated from the ratio of the digital number (DN) noise on the central peaks in Fig. 3-27(d), approximately

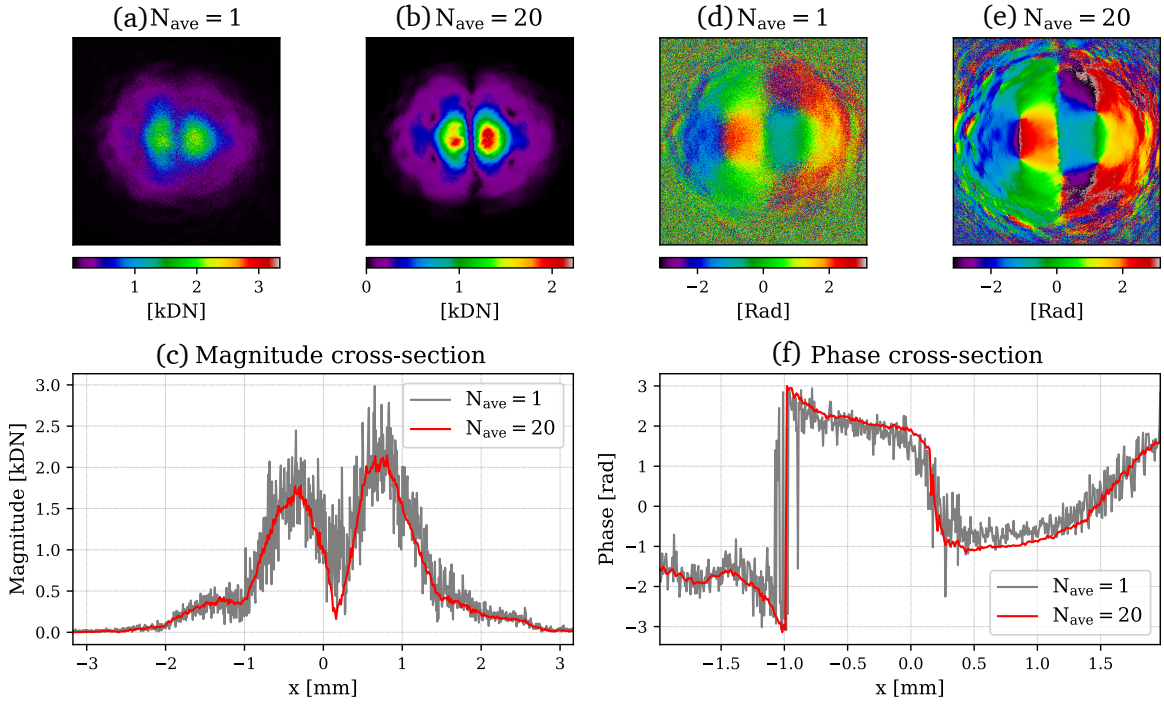

Figure 3-27: (a) and (b) are magnitude maps of heterodyne beat for $N_{\text{ave}} = 1$ and $N_{\text{ave}} = 20$. (d) and (e) are phase maps of heterodyne beat for $N_{\text{ave}} = 1$ and $N_{\text{ave}} = 20$. (c) plots the magnitude variation along the center line of (a) and (b). (f) plots the phase variation along the center line of (d) and (e)

0.1 kDN, to the DN of the reference field in Fig. 3-25(a), approximately 60 kDN: as $2E_sE_r/(E_r)^2 \approx 0.1/60$ and thus $(E_s/E_r)^2 \approx -62$ dB below the power in the reference field, a 12 dB improvement on that reported by Goda et al. [96].

Sensing optical state with phase camera

Fig. 3-28 shows that phase camera can be a powerful tool for investigating optical states of a system. In this demonstration, we recorded the variation of magnitude and phase of the heterodyne beat seen by the phase camera as well as the beat seen by a photodetector at the cavity transmission. As expected, alignment improvement reduces the amplitude of the 15.4 MHz beat observed by the photodetector. The reason for this improvement is apparent from the captured images: improving the the pitch alignment decreases the coupling to the TEM_{12}, and improving the yaw alignment reduces the coupling to the TEM_{30} mode.

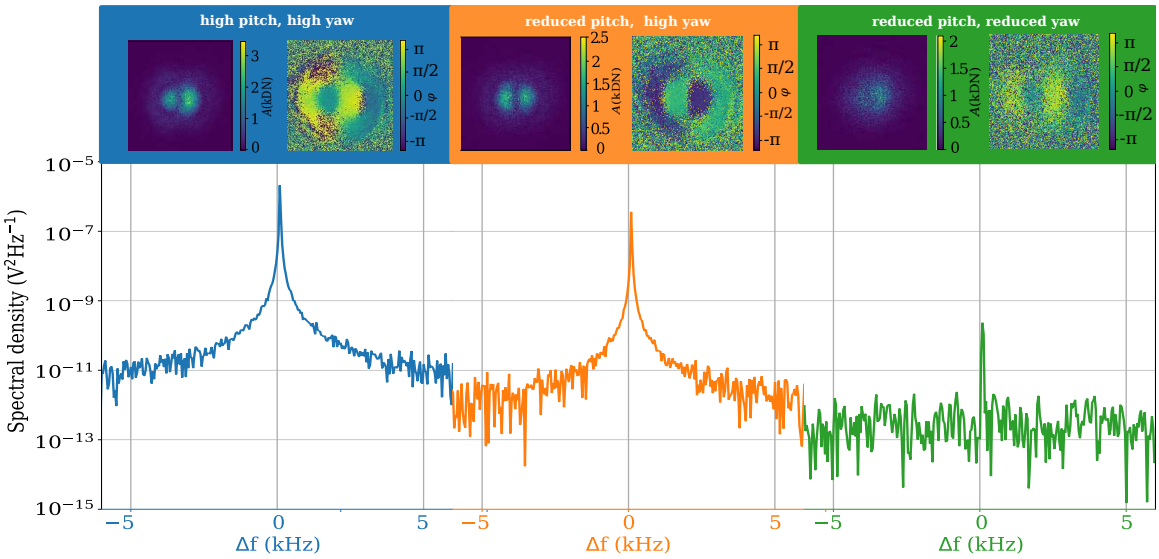

Figure 3-28: Plots of the 15.4 MHz beat signal measured using a photodetector, and the corresponding magnitude and phases maps measured with the phase camera, recorded as the alignment of optical field into the cavity was improved.

3.5.6 Separation of optical fields at a common sideband frequency

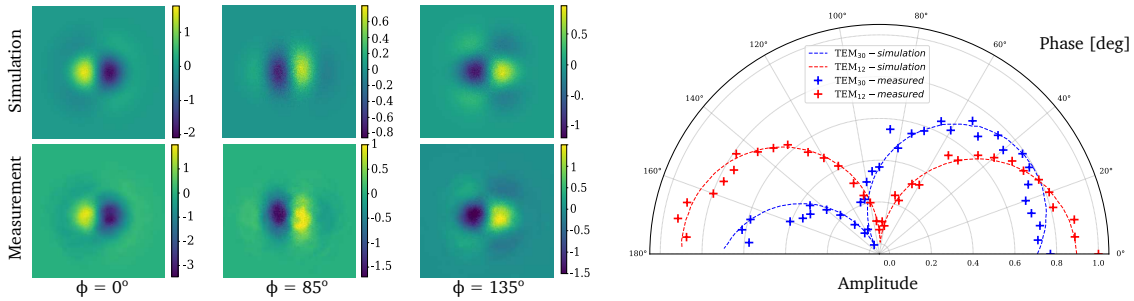

Figure 3-29: The measured and simulated demodulated signal mode content. $\phi = 0^o, 85^o, 135^o$ are shown on the left with the corresponding simulation showing the individual modes. The data and model have been scale normalized.

Fig. 3-29 shows that the modal content can be extracted from a demodulation phase sweep of a phase camera. In this section, we will show that each eigenmode of a common frequency sideband field can be observed separately with a phase camera, provided that these modes are beating against the carrier at different phases. These phases are determined by misalignment and mismatch state of the optical system [30] as well all the Gouy phase difference accumulated by each transverse mode. Consider an RF sideband field consists of two HG modes U^s_{mn}

and U^s_{kl} ($m \neq k, n \neq l$): $E_s = bU_{mn} + cU_{kl}$, in which b and c are complex coefficients determined by the alignment state of the system and U^s_{mn} are HG bases of optical system under consideration (which is the triangular cavity in our experiment) and U^s_{mn} is given by [15]:

$$\begin{aligned} U_{mn} = &\left(\frac{2}{\pi}\right)^{1/2} \left(\frac{1}{2^{m+n} m! n! w(z)^2}\right)^{1/2} H_m\left[\frac{\sqrt{2}x}{w(z)}\right] \\ &\times H_n\left[\frac{\sqrt{2}y}{w(z)}\right] \exp\left[-\frac{x^2+y^2}{w(z)^2}\right] \exp\left[-i\frac{k\,(x^2+y^2)}{2R(z)}\right] \\ &\times \exp\left\{ i\left[\left(m+\frac{1}{2}\right)\eta_x(z) + \left(n+\frac{1}{2}\right)\eta_y(z)\right]\right\} \end{aligned} \tag{3.23}$$

Difference between Gouy phases $\eta_x(z)$ and $\eta_y(z)$ depends on astigmatism of optical system. The strong fundamental mode carrier field is thus described by $U_{00}(x, y, z)$. The test field then can be rewritten as:

$$E = aU^c_{00} e^{i\omega t} + \left(bU^{sb}_{mn} + cU^{sb}_{kl}\right) e^{i(\omega+\Omega_1)t} \tag{3.24}$$

Demodulation map extracted from demodulations at PC with signals $\cos(\Omega_1 + \phi)$ and $\cos(\Omega_1 + \phi + \pi)$ is thus given by:

$$I_{\text{demod}} = \Re\left[ab^* U^c_{00} U^{sb*}_{mn} e^{i\phi}\right] + \Re\left[ac^* U^c_{00} U^{sb*}_{kl} e^{i\phi}\right] \tag{3.25}$$

Substitution of equation 3.23 into the first term of 3.25, and rewriting a, b in polar form results in the following:

$$\begin{aligned} &\frac{2}{\pi}\frac{1}{w(z)^2}\left(\frac{1}{2^{m+n}m!n!}\right)^{1/2} H_m\left[\frac{\sqrt{2}x}{w(z)}\right] H_n\left[\frac{\sqrt{2}y}{w(z)}\right] \times \exp\left[-2\frac{x^2+y^2}{w(z)^2}\right] |ab| \\ &\Re\left\{ \exp\left[i\frac{k^{sb}-k^c}{2R(z)}(x^2+y^2)\right] \times \exp\left[i\left(\left[\varphi_a - \varphi_b\right] - \left[m\eta_x(z) + n\eta_y(z)\right] + \phi\right)\right] \right\} \end{aligned} \tag{3.26}$$

in which k^{sb} and k^c are wavenumber of carrier and sideband frequency. Since Ω_1 is of order 10^6, and physical dimension of light field is small (on the mm scale),

the transverse-dimension dependent exponential term varies slowly spatially and close to 1. Therefore, 3.26 is approximately proportional to:

$$H_m H_n \exp\left(-2\frac{x^2+y^2}{w(z)^2}\right) \times \cos\left(\Delta\varphi_{ab} - [m\eta_x(z) + n\eta_y(z)] + \phi\right) \tag{3.27}$$

A demodulation phase can thus always be found to maximize or minimize the selected mode content. If $\phi = [m\eta_x(z) + n\eta_y(z)] - \Delta\varphi_{ab} + \pi/2$, the first term of 3.25 vanishes, and only the second term is observed. If $\Delta\varphi_{ab} = \Delta\varphi_{ac}$ and $[m\eta_x(z) + n\eta_y(z)] = [k\eta_x(x) + l\eta_y(z)]$, a cylindrical lens Gouy phase telescope can introduce different Gouy phase accumulation between the two phases, and an appropriate demodulation phase can be used to achieve separation of modes.

These results are summarised and presented as a publication in Appendix A.

3.6 Conclusion

We have developed a new type of phase camera that does not use any moving components, which reduces the risk of backscattered light reducing the sensitivity of Advanced gravitational wave detectors and enables operation of phase camera during scientific runs. We have also demonstrated that this new phase camera can produce high spatial resolution maps of the phase and intensity of a coherent light field at a higher acquisition rate and resolution than previous phase cameras.

The results of our proof-of-principle measurements are in excellent agreement with theoretical precdictions from a FINESSE model. We also demonstrate that its sensitivity is limited purely by photon shot noise and can be improved significantly simply with averaging and pixel binning, resulting in a noise floor of -62 dBc from data recorded in 2 seconds. This performance can be easily improved by using faster or more sensitive cameras, such as InGaAs array, which can achieve >100 Hz frame rate.

Our future plan is to apply this new phase camera at LIGO observatory as a diagnostic tool to study various effects on the various RF sideband fields used

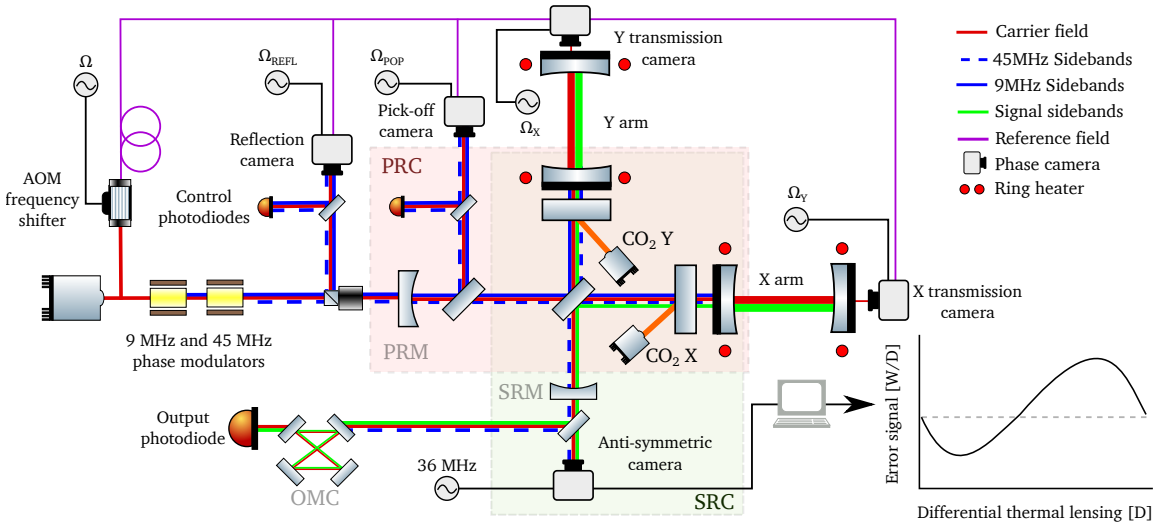

Figure 3-30: Schematic of a detector similar to LIGO and possible locations for phase cameras. Highlighted are the power recycling (PRC), signal recycling (SRC), output mode cleaner (OMC), arm cavities (XARM and YARM). The RF modulation sidebands at 9 and 45 MHz are used for controlling the interferometer.Fve potential locations of phase cameras are shown: at reflection port (REFL), pick-off port (POP), anti-symmetric port (AS), XARM transmission (X-TRANS) and YARM transmission (Y-TRANS). Combining the sampled field with a reference file that is frequency-offset locked to the main laser, and choosing the appropriate demodulation frequency on phase camera's Pockels Cell would allow both amplitude and phase of each field to be mapped.

in length and alignment control of the interferometer. Fig. 3-30 shows various diagnosis schemes that can be implemented with a phase camera. Here, two sets of phase-modulation sidebands at 9 MHz and 45 Hz are generated. The carrier field, 9 MHz and 45 MHz resonate in the PRC. The carrier and 45 MHz fields are simultaneously resonant in the SRC.

In the simplest mode of operation, a phase camera would analyse the heterodyne beat between the sampled carrier and the sideband field. This allows the direct measurement of spatial structure of error signals that are used for controlling the interferometer. An independent frequency-offset reference field can also be used to diagnose the carrier field and sideband fields individually. This is achieved by using an AOM on a pick-off of the pre-stabilised laser (PSL) after the pre-mode-cleaner.

The balance of 9 MHz sideband pair and the mode-matching into the PRC can

be analyzed by placing phase cameras at POP and REFL respectively. Whereas the balance of 45 MHz sideband pair can be analysed with a phase camera at AS port. Differential wavefront distortion can cause the 9 MHz sidebands to "leak" into SRC and result in 36 MHz beat note. Switching with an AS phase camera at 36 MHz would allow diagnosis of this differential wavefront distortion.

Furthermore, phase cameras can also be placed at the transmission of XARM and YARM to diagnose if there is unexpected high-order mode contents in the arm cavities caused by parametric instability [89]. The optical profiles resulting from parametric instability have not been imaged, therefore diagnosis relies on modelling and observed frequencies. Phase cameras can potentially image these fields and thus form part of future active control scheme to detect and suppress these instabilities [216, 132]

Chapter 4

Suspended Active Matching Stages

Chapter 2 of this thesis has emphasised the importance of mode matching for sensitivity of terrestrial gravitational wave detectors. Adaptive optics whose curvature can be finely tuned will therefore pivotal roles in aiding active wavefront control to achieve its goal.

Suspended Adaptive Matching Stages (SAMS) project aim to develop an adaptive optics that is integrable into LIGO suspension stage. A complete SAMS aims to provide the following capabilities:

1. Provide sufficient seismic isolation, which is driven by balanced homodyne readout and filter cavity design requirement.

2. Provide mode matching capability (controllable optics' radius of curvature)

3. Provide tip-tilt steering capability (DC pointing actuation and potentially AC dithering)

In this chapter, we will provide an overview of SAMS with a particular focus on the adaptive optics requirements

4.1 Suspension architecture

A symbolic rendering of a possible suspension architecture is shown in Fig. 4-1 [151]. These SAMS suspension will house the relay optics. The maximum allowable length noise of a suspension stage is constrained by the backscatter noise requirement. Below 20 Hz, the length noise of the single tip-tilt stage does not meet backscatter noise requirement of the filter cavity[143]. Therefor, SAMS will be a double stage suspension to provide sufficient seismic isolation, which allows suppression of length noise to a safe level.

The upper stage is similar to the existing HTTS, which consists of suspension blades to provide vertical isolation and 4 optical sensor electromagnetic motors (OSEM) to provide active damping and DC steering.

The lower stage houses the adaptive optics. Suspension blades at the bottom stage will provide further vertical isolation. Installation of 4 voice coils for dithering alignment is also an open option.

4.2 Adaptive optics design requirement

Curvature actuation range

The target actuation range adaptive optics integrated into SAMS is 200 mD in defocus (or also referred to as spherical power) [142]. Defocus ΔS is defined as the reciprocal of wavefront radius of curvature (ROC).

Higher order aberration

Higher order aberration due to mirror's deformation during actuation results in scattering of optical field into higher order mode. Amount of high order mode scattering (HOMS) can be quantified using overlap integral between an optical field E_2 whose phase is given by the residual wavefront ΔW describing deviation

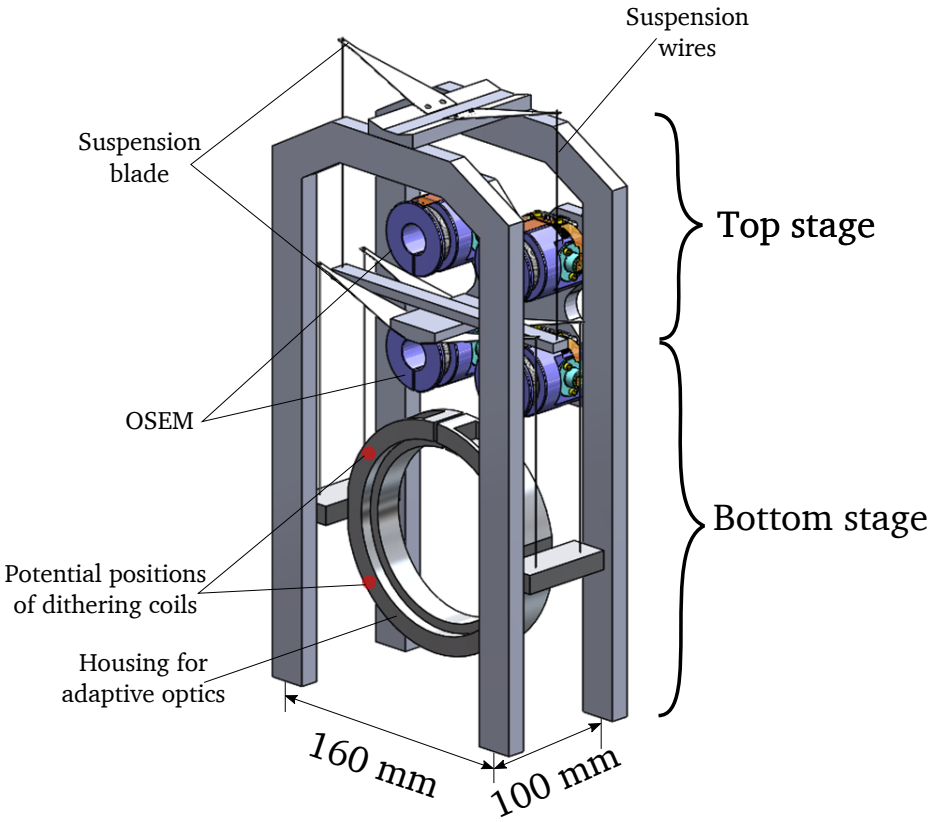

Figure 4-1: Symbolic rendering of SAMS possible arcitecture [151]. The footprint requirement of SAMS is 166×108 mm

from a quadratic surface with the target TEM_{00} mode E_1:

$$
\begin{aligned}
E_1 &= a_1 \exp\left(-\frac{r^2}{w^2}\right) \\
E_2 &= E_1 \exp\left(ik\Delta W(r)\right) \\
\text{HOMS} &= 1 - \frac{\int_0^\infty r E_1 E_2^* dr \int_0^\infty r E_2 E_1^* dr}{\int_0^\infty r E_1 E_1^* dr \int_0^\infty r E_2 E_2^* dr}
\end{aligned}
\tag{4.1}
$$

HOMS of actuator in SAMS is required to be maximum 0.4% [43].

Optical surface quality

Optical specifications are likely to be similar to HTTS mirrors. Surface figure is therefore at least $\lambda/10$ over central 85% and surface roughness is given by 10-5 scratch-dig , also over central 85% [45].

Bandwidth

Longer time constant on the order of 30 minutes is acceptable since this is similar to thermal time constant of the interferometer. However, actuator with higher bandwidth is preferred if achievable since this will speed up commissioning.

Noises

- *Phase noise*: The phase noise requirement is dependent on location of the actuators. It is most stringent at locations before the BHD beam splitter in A+. However, all SAMS units are planned for locations after BHD beam splitter. Phase noise is therefore less concerned [43].

- *Backscatter noise* Assuming a BHD readout scheme with the use of one SQZ Faraday isolator, the amount of spurious backscatter light reaching FC is 5 nW [143].The backscatter-induced length noise imposed on relay optics between VOPO, FC and OFI at 10 Hz is 10^{-13} m/$\sqrt{\text{Hz}}$ [143]. The double stage suspension of SAMS should allow it to meet this requirement. Further details of backscatter noise can be found in section 6 of A+ filter cavity design requirement document [143].

- *Thermal noise* Displacement noise induced by thermal noise of adaptive optics in SAMS need to be less than that of existing tip-tilt stage, which is given by HAM-ISI table motion filtered by a single-stage pendulum suspension and approximately equal to 10^{-12} m/$\sqrt{Hz}$ at 10 Hz [123].

- *Mode-matching noise* Modulation in ROC of SAMS actuators will couple to the transmitted power in OMC especially when there is mode-mismatch. This coupling is most stringent at SAMS units that see LO field in BHD scheme. The limit imposed on mode-matching noise is driven by the design displacement noise floor of A+. This noise requirement is also dependent on science beam size at a given optics. The requirement is less stringent for smaller beam size. At 100 Hz and 1 mm beam radius, SAMS defocus noise need to

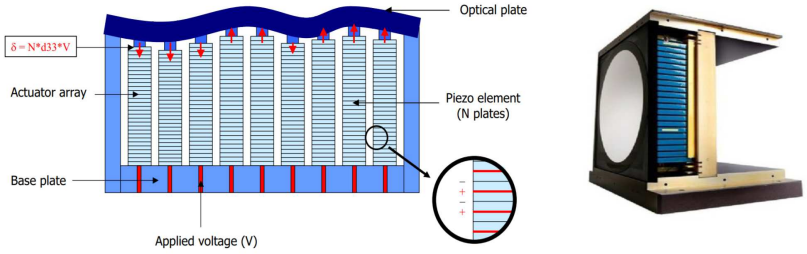

Figure 4-2: *Left:* Schematics showing stacked array DM's concept, which use a large number of stacked actuators to address local mirror deformation. *Right:* Stacked array mirror from CILAS. *Image source: CILAS* [184]

be less than 6 nD [43]. Defocus noise requirement curve for various beam sizes can be found from T1800480 [43].

Testing of SAMS noise is beyond the scope of this thesis and is currently scheduled for late September 2019 when a full suspension prototype with integrated adaptive optics has been assembled.

4.3 Review of adaptive optics

In this section, we review existing adaptive optics (AO) that are potential candidates for SAMS and identify whether there is a need for a new type of AO that is suitable for GW detectors. Here we explore mainly front surface reflective AO to avoid loss that is caused by transmission through materials.

4.3.1 Existing reflective AO

Reflective AO or deformable mirrors (DM) can be classified into the 5 types: stacked-array DM, bimorph DM, voice coil DM, and MEMs [133].

Stacked-array DM

Figure 4-2 shows the concept of stacked array DMs, which consist of an array of stacked actuators bonded onto a rigid base substrate. A flexible reflective optical plate is then bonded to actuator array, and polished and coated to achieve a high

quality surface finish [181]. The stacked actuators are either piezoelectric or electrostrictive type, which are currently available commercially from CILAS (Compagnie Industrielle des LASers) and Xinetics respectively.

In a stacked-array DM, the voltage applied to each actuator is chosen to produce the required change in the mirror surface. A large number of actuators allows reduced higher order aberration of the reflected wavefront. A high dynamic range requires that each actuator have a large stroke. The cross-sectional area of each actuator and thus the actuator pitch must therefore increase to provide a higher shear stiffness [133, 184]. This imposes a lower limit on the diameter of the optic required for low higher-order aberration performance.

The use of a large number of actuators, bulky electronics and large bundle of cables would degrade the seismic isolation. Additionally, while other types of DMs from CILAS and Xinetics are specified to be vacuum compatible, the stacked arrays are not.

Unimorph and bimorph piezoelectric DM

The concept of bimorph and unimorph (or monomorph) pizoelectric DMs is shown in Fig. 4-3. A bimorph mirror consists of two oppositely-poled piezoelectric layers. The layers are coated on both surfaces to form electrodes and then bonded together. At a given applied voltage, one layer compresses while the other elongates. This causes the structure to bend in a manner similar to that of a bimetallic strip.

The active layers are often embedded between two glass sheet, one of which is used as the reflective mirror surface. The other glass sheet is used to provide the DM with an improved insensitivity to variation in temperature. However, the glass layers reduce the stroke of the DM. Therefore, each glass layer has to be sufficiently thin to allow efficient bimorph action [177] .

The same out-of-plane bending can also be achieved using only one active piezoelectric layer bonded to a glass plate. This allows the glass plate to be thicker, thus achieving a better surface figure. Nevertheless, the glass plates in bimorph

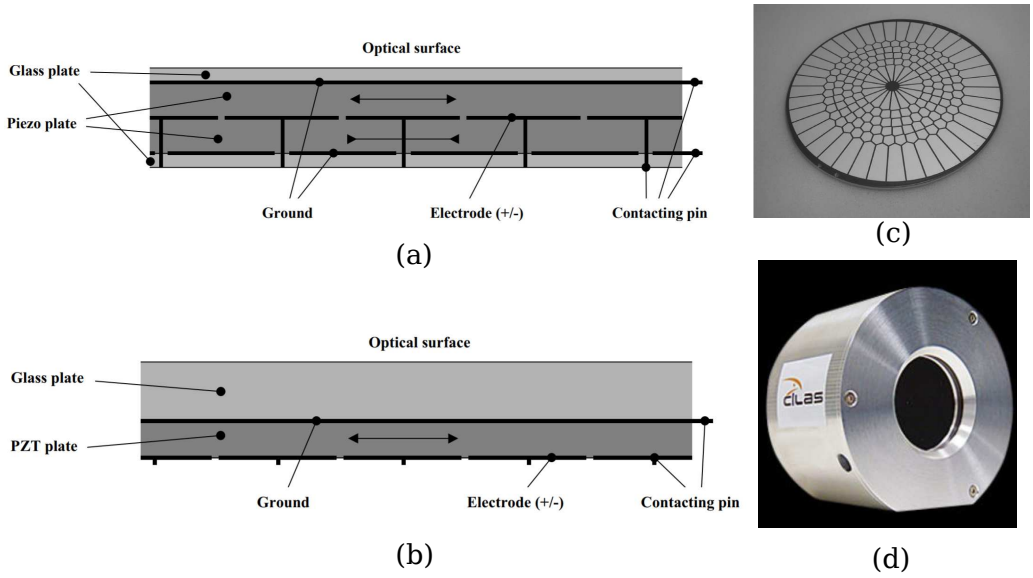

Figure 4-3: *(a)*: Bimorph DM concept [184]: two oppositely polarised piezoelectric wafers are bonded together. An array of electrodes is deposited between the two wafers for controlling local curvature. This bilayer is sandwiched between two glass plates. One glass plate is polished and coated for use as mirror's reflective surface.*(b)*: Unimorph DM concept is similar to the bimorph mirror but only requires one active layer [71]. *(c)*: Electrode patterns of bimorph DM delivered by CILAS to the Subaru Telescope [165]. *(d)*: CILAS Monomorph mirror, which has been developed for ultra high-vacuum applications. (Image source: CILAS)

and unimorph DMs are still remain too thin to achieve LIGO's surface finish requirement.

The use of piezoeletric wafers to provide sufficient stroke also requires high voltage operation, and thus more bulky electrical racks, which is not ideal for our application [172]. Also, these mirrors require adhesive for bonding the layers. While CILAS monomorph mirrors were developed for vacuum environment in space missions. they would require significant testing before use in the LIGO vacuu . The cost of bimorph DMs is also relatively high for A+ budget.

Micro Electro Mechanical Systems (MEMS) DMs

The basic structure of MEMS DM and its principle of operation is illustrated in figure 4-4. They are based on a scalable array of parallel-plate electrostatic actuators, fabricated in silicon via semiconductor batch processing [32] . Each actua-

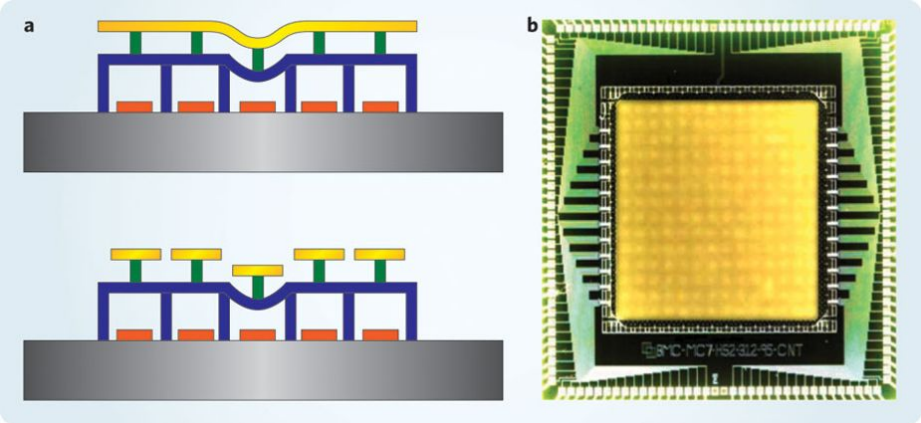

Figure 4-4: *a:* Cross-sections of continuous (upper) and segmented (lower) MEMS deformable mirrors. A metal-coated thin-film mirror is attached by silicon posts to an array of electrostatic actuator membranes. Voltages applied to the array of electrodes on the wafer substrate gives rise to attraction between the membrane and the electrode, thereby changing the shape shaping of mirror. *b:* a MEMS continuous DM with 140 actuators . *Image source: Boston Micromachines* [33]

tor plate (membrane) is supported along its edges above individually addressable electrodes. An electrostatic force causes the actuator plate to bend, which displaces a thin mirror layer on mirror segments and thus deforms deforms the mirror.

MEMS DMs have thin mirror layers, which prevents high optical quality. Furthermore, these DMs are currently not suitable for UHV application as the mirrors motion, transitions from overdamped in air to underdamped in the vacuum. Vibration measurements of these MEMS mirror shows strong vibration resonance at 75 Hz when the pressure dropped to 6 Torr [69].

4.3.2 Existing AOs developed for GW astronomy

Various adaptive optics have been developed for gravitational wave detectors including

- CO_2 laser projection [48, 125]: The absorption of fused silica at CO_2 laser wavelength (10 μm) allows projection of spatially tunable heat distribution onto a fused-silica compensation plate, creating a thermal lens as the result of thermo-refractive effect. The use of CO_2 lasers however adds more complexity to the system and require costly and bulky electronics.

- Ring heater [48, 125]: Ring heater actuators consists of a glass torus, wrapped in nichrome wire through which current is passed. The resulting Ohmic heating is radiatively transferred to the barrel of the test masses to balance the central heating due to absorption of the 1 μm laser beam. The maximum achievable change in wavefront defocus is approximately 5 mD.

- Rear surface radiative heaters: A ceramic ring heater [72] is used to radiatively heat the rear surface of the mirror SR3. Thermo-elastic deformation changes the curvature of the front reflective surface, but with a small response: 2.45μD/W [41].

- An array of individually addressable resistors mounted on a PCB [115, 114, 60]was applied to a rear surface mirror to radiatively induce thermo-refractive effect within the mirror substrate.

- University of Florida segmented barrel heater [130]: A segmented electrical heater consisting of 4 strips mounted on the barrel of optical element made from SF57 glass which has high thermo-refractive and thermo-elastic coefficients. Independent control of each quadrant heater results in a controllable "thermal lens".

4.4 A new class of GW adaptive optics

The discussion above shows that the commercially available technologies are not suitable for SAMS due to either poor optical quality, vacuum incompatibility, or seismic short risk. Most AOs previously adapted for GW detectors require transmissive optics due to their reliance of thermo-refractive effect. The few AOs which use thermo-elastic deformation do not meet SAMS actuation range requirement. It is therefore important to develope a new class of front-surface reflective AOs that are suitable for use in GW detectors.

4.4.1 Thermal-driven deformable mirror

The two thermal-driven deformable mirrors proposed for SAMS are: the thermal bimorph mirror (TBM) and compression fit mirror (CFM), which will be covered in details in chapter 5 and 6 . Both of these DMs rely on difference in thermal expansion coefficient between fused silica (mirror's substrate) and aluminium (actuating structure) to induce stress which deforms mirror spherically.

4.4.2 Piezo-driven deformable mirror

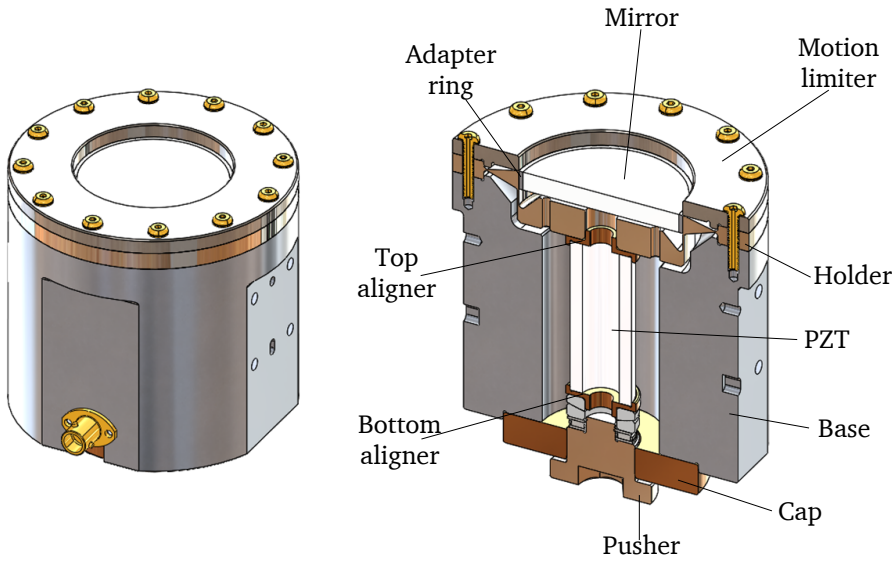

Figure 4-5: Drawing of the assembly of the piezo-driven deformable mirror and its cross-section [155].

A piezo-driven deformable mirror is also proposed for SAMS. Fabrication of the first prototype is underway at Massachusetts Institute of Technology (MIT). Drawing of PDM's assembly and its cross-section are shown in figure 4-5.

The main components of a piezo-driven deformable mirror are a mirror and a PZT stack. The mirror is captured into the bore of the flexure holder, where the adapter mediates the mirror and flexure to accommodate for uncertainty in mirror's diameter. The axisymmetric flexure holder converts axial force of the PZT stack into moment mirror's periphery. Details on design and stress analysis of the piezo-driven mirror can be found in [151, 152, 153, 154, 155, 156].

Chapter 5

Thermal-Bimorph Deformable Mirror

The need for a new front-surface reflective adaptive optics that cater for GW detector requirements lead us to develop new deformable mirrors. In this chapter, I present here a new thermal-bimorph mirror (TBM) for use in SAMS deformable mirror. The operating principle is described in Section 5.1. Stress analysis of the TBM is presented in Section 5.2. Simulation of the TBM deformation and stress concentration with finite element analysis (FEA) program is discussed in Section 5.3. The TBM assembly procedure and characterisation method are described in Section 5.4. Results from characterisation are discussed in Section 5.5

5.1 Principle of working

The underlying principle of the thermal-bimorph mirror is similar to that of bimetallic strips, often found in thermostats. It relies on thermal expansion mismatch between the two materials that are bonded together to induce a change in curvature as the temperature changes from the bonding temperature. In our case, the TBM consists of a fused-silica mirror with thickness t_1 bonded to an aluminium-6061 plate with a thickness t_2 at temperature T_0. These materials were chosen due to the large difference in their thermal expansion coefficients (TEC), α_1 and α_2 respec-

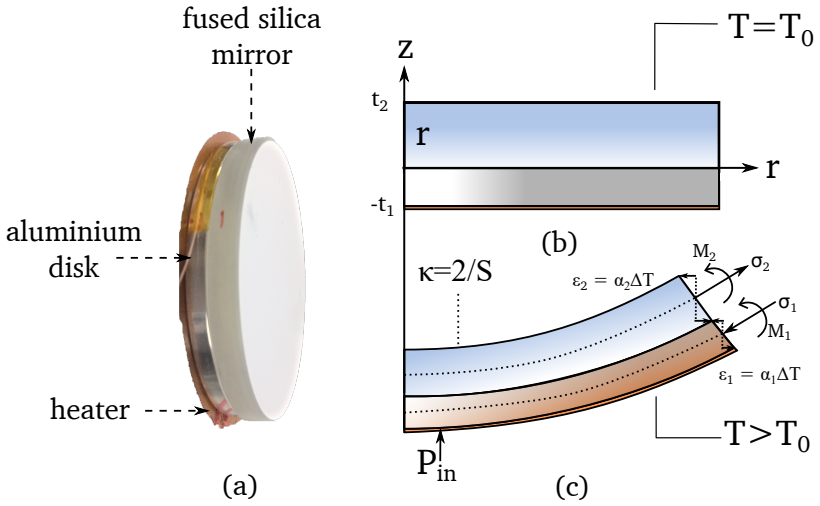

Figure 5-1: (a) Image of an assembled thermal-bimorph mirror. (b) 2D-axisymmetric schematics of a thermal-bimorph mirror, which consists of a fused-silica mirror and an aluminium plate bonded together at room temperature T_0. (c) The mirror deformation due to thermal expansion mismatch when heated.

tively. An image and schematic of the TBM is presented in Fig. 5-1(b) and (c).

At the bonding temperature, which is often room temperature (T=21°C) for our prototypes, the bimorph is in a relaxed state, if we assume that curing of the epoxy bond does not create stress, and thus the curvature of mirror is unchanged. Upon a change in the temperature, the dimensions of the fused-silica and aluminium will change differently due to the different TECs. This mismatch creates a large stress at the bimorph interface. The stress σ_1 acting on the aluminium is compressive. The stress σ_2 acting on the fused-silica is tensile. To release the stress, the bimorph structure bends out of plane. During this bending, the structure will change its stress state and generate bending moments M_1 and M_2. Thus in equilibrium , the mirror surface becomes more concave relative to its relaxed state.

Due to the large radial-length-to-thickness ratio of each layer in the TBM, the extensive work on bi-metallic strips and semiconductor bimorph actuators can be used to guide the design of the mirror [198, 193, 31]. At equilibrium, the stresses

(σ_1, σ_2) and moments (M_1, M_2) acting on the bimorph structure are balanced:

$$\sigma_1 = \sigma_2 = \sigma \tag{5.1}$$

$$\sigma\frac{t}{2} = M_1 + M_2 \tag{5.2}$$

where $t = t_1 + t_2$

From the theory of plates and shells [199], the curvature and moments are related by:

$$\begin{bmatrix} M_x \\ M_y \end{bmatrix} = D \begin{bmatrix} 1 & \nu \\ \nu & 1 \end{bmatrix} \begin{bmatrix} \xi_x \\ \xi_y \end{bmatrix} \tag{5.3}$$

where:

$$\xi_x = \frac{1}{R_x}, \quad \xi_x = \frac{1}{R_y}, \quad D = \frac{E_i t_i^3}{12(1-\nu_i^2)} \tag{5.4}$$

where D is flexural rigidity, ν_i is the Poisson's ratio. R_x and R_y are the radii of curvature along in x and y axes. In our case, $M_x = M_y = M$:

$$\xi_x = \xi_y = \frac{M}{D(1+\nu)} \tag{5.5}$$

We therefore have the following expressions:

$$\begin{aligned} M_1 &= \frac{E_1 t_1^3}{12(1-\nu_1)R} \\ M_2 &= \frac{E_2 t_2^3}{12(1-\nu_2)R} \end{aligned} \tag{5.6}$$

where we have let $R_x = R_y = R$ due to the axi-symmetry nature of the TBM. Substitution of the above expressions into Eq. 5.2 gives:

$$\sigma\frac{t}{2} = \frac{1}{12R}\left(\frac{E_1 t_1^3}{1-\nu_1} + \frac{E_2 t_2^3}{1-\nu_2}\right) \tag{5.7}$$

Now consider the deformation of the composite structure: the strain in the

longitudinal fibres of the fused-silica along the interface is given by:

$$\epsilon_{\text{silica}} = \alpha_2 \Delta T + \frac{\sigma_2(1-\nu_2)}{E_2 t_2} + \frac{t_2}{2R} \tag{5.8}$$

where the first term $\alpha_2 \Delta T$ is due to thermal expansion, the second term is caused by the tensile stress acting along the fused-silica mirror, and the last term is due to bending of the fused-silica.

Similarly, the strain in the longitudinal fibres of the aluminium along the interface is given by:

$$\epsilon_{\text{Al}} = \alpha_1 \Delta T - \frac{\sigma_1(1-\nu_1)}{E_1 t_1} - \frac{t_1}{2R} \tag{5.9}$$

The negative sign in the second term is due to the action of axial compressive stress instead of tensile stress. The negative sign in the third term is due to the location of the boundary relative to the neutral plane.

Assuming that the epoxy layer can support the elongation of the fused-silica and aluminium at their boundary, the strain in the fused-silica and aluminium at the interface must be equal:

$$\alpha_1 \Delta T - \frac{\sigma_1}{E_1 t_1} - \frac{t_1}{2R} = \alpha_2 \Delta T + \frac{\sigma_2}{E_2 t_2} + \frac{t_2}{2R} \tag{5.10}$$

Substitution of Eq. 5.7 gives:

$$\frac{t}{2R} + \frac{1}{6tR}\left(\frac{E_1 t_1^3}{1-\nu_1} + \frac{E_2 t_2^3}{1-\nu_2}\right)\left(\frac{1-\nu_1}{E_1 t_1} + \frac{1-\nu_2}{E_2 t_2}\right) = (\alpha_1 - \alpha_2)\Delta T \tag{5.11}$$

Rearrangement of this equation gives the change in radius of curvature R and spherical power S of the mirror due to a change in temperature ΔT [198]:

$$\frac{S}{2} = \frac{1}{R} = \frac{6\Delta\alpha\Delta T(1+m)^2}{t\left(3(1+m)^2 + (1+mn)\left(m^2 + (1/mn)\right)\right)} \tag{5.12}$$

where $\Delta\alpha = \alpha_1 - \alpha_2$, $m = t_2/t_1$, and $n = E_2'/E_1'$, $E_i' = E_i/(1-\nu_i)$. The properties of materials we used are listed in Table 5.1.

Eq. 5.12 shows that larger deformations can be achieved with smaller total

thicknesses for a given thickness ratio. However, the minimum thickness of fused-silica mirror that can be used is 6 mm as most vendors suggest that superpolishing of 50-mm diameter fused-silica mirror with a thickness below 6 mm is very challenging. Given this minimum mirror thickness, the thickness ratio for the maximum deformation depends solely on the ratio of the modified Young's modulii:

$$m = \left(\sqrt{\frac{1}{n^2} - \frac{1}{n^3}} + \frac{1}{n}\right)^{1/3} + \left(n\sqrt{\frac{1}{n^2} - \frac{1}{n^3}} + \frac{1}{n}\right)^{-1/3} \tag{5.13}$$

For a fused-silica - aluminium bimorph, the maximum distortion is thus achieved when $m = 1.94$. The aluminium plate thickness should therefore ≈3 mm for maximum actuation rate.

5.2 Stress analysis

The maximum stresses occur at the interface between fused-silica and aluminium. In the fused-silica, the total stress is due to both the axial tensile stress and bending stress [198]:

$$\sigma_{\text{max,2}} = \frac{\sigma}{t_2} + \frac{t_2 E_2}{2R(1-\nu_2)} \tag{5.14}$$

Substituting Eq. 5.7 into Eq. 5.14, we have:

$$\sigma_{\text{max,2}} = \frac{S}{2}\left[\frac{1}{6tt_2}\left(\frac{E_1 t_1^3}{1-\nu_1} + \frac{E_2 t_2^3}{1-\nu_2}\right) + \frac{t_2 R_2}{2(1-\nu_2)}\right] \tag{5.15}$$

This stress was calculated using the parameters listed in Table 5.1 and plotted in Fig. 5-2.

The tensile strength of fused-silica varies between 50-55 MPa, depending on surface flaws [109, 110, 70], whereas its compressive strength exceeds 1100 MPa [110, 70]. Tensile failure of the fused-silica would most likely result in structural rupture due to its brittle nature. The region within which this failure is expected is shaded blue in Fig. 5-2.

Property	**fused-silica**	**aluminium**
Thermal expansion coefficient, α (1/K)	0.55×10^{-6}	2.34×10^{-5}
Heat capacity, C_p (J/(kg·K))	740	900
Thermal conductivity, k (W/(m·K))	1.38	238
Density, ρ (kg/m^3)	2203	2700
Young's modulus, E (Pa)	73.6×10^{9}	68.9×10^{9}
Poisson's ratio, ν	0.17	0.33
Relative emissivity, ϵ_r	0.93	0.06

Table 5.1: Properties of fused-silica and aluminium alloy 6061 used for t thermal-bimorph mirror.

A similar expressioncan be found for the aluminium:

$$\sigma_{\text{max},1} = -\frac{S}{2}\left[\frac{1}{6tt_1}\left(\frac{E_1t_1^3}{1-\nu_1}+\frac{E_2t_2^3}{1-\nu_2}\right)+\frac{t_1R_1}{2(1-\nu_1)}\right] \tag{5.16}$$

The negative sign indicates that the maximum stress in the alumnium along the interface is compressive. Aluminum 6061-T6 has a tensile strength of 310 MPa and a yield strength of 276 MPa. Its compressive strength is similar to its tensile strength [66]. Compressive failure of the aluminum is therefore not expected to be the limiting factor.

These expressions for maximum stresses are relevant to the regions of the mirror that are far from the circumferential edge of the interface. The stress distribution near the edge is more complicated. Firstly, shearing stresses arise between the two materials during heating [198]. Since the fused-silica and aluminium have different Young's modulii and thicknesses, peel stress, which is a normal stress along the interface, will also be produced during heating [198]. It is important that the epoxy bond withstand these stresses to support the mirror's deformation. The two quantities that determine the epoxy's ability to withstand these stresses are its lap-shear strength and its tensile strength. The maximum lap-shear stress τ_{max} and peel stress p_{max} applied to the epoxy are given by [192]:

$$\tau_{\text{max}} = \frac{\Delta\alpha\Delta T}{k\kappa} \tag{5.17}$$

$$p_{\text{max}} = \frac{\mu}{\kappa}\Delta\alpha\Delta T \tag{5.18}$$

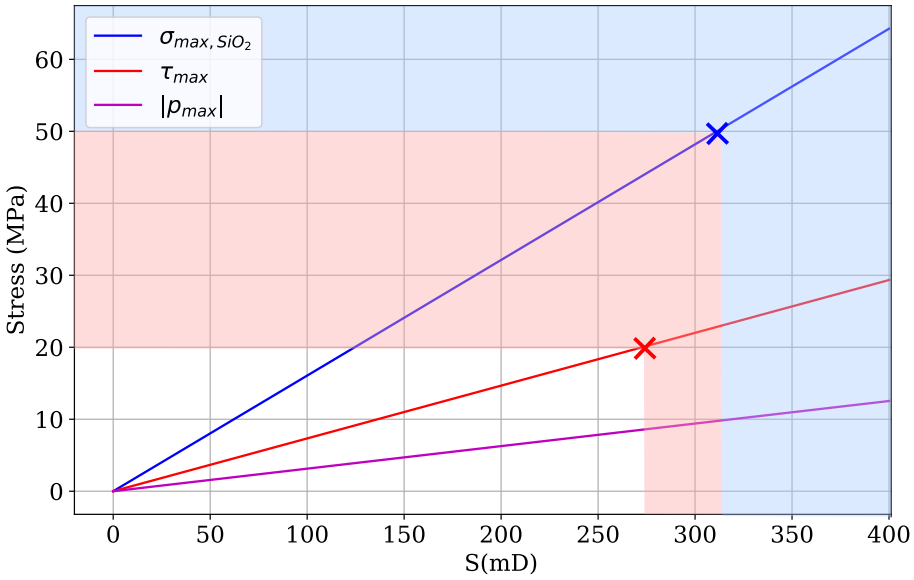

Figure 5-2: Maximum tensile stresses in fused-silica, interfacial shear and peel stresses as functions of spherical power as predicted by Eq. 5.15, 5.17 and 5.18 for a standard thermal-bimorph mirror design with 6-mm-thick fused-silica and 3-mm-thick aluminium. Lap-shear strength of the adhesive is expected to limit mirror's bending to 270 mD. Bending of mirror beyond 325 mD is predicted to cause rupture in fused-silica due to material's tensile strength limit.

where κ, the sum of the interfacial compliances of the two layers, is given by:

$$\kappa = \frac{2(1+\nu_1)t_1}{3E_1} + \frac{2(1+\nu_2)t_2}{3E_2} \tag{5.19}$$

k and μ are given by:

$$k = \lambda_1 + \lambda_2 + \frac{t^2}{4(D_1+D_2)}, \quad \mu = \frac{t_1 D_1 - t_2 D_2}{2(D_1+D_2)} \tag{5.20}$$

where λ_i is in-plane compliances and flexural rigidities of each layer:

$$\lambda_i = \frac{1-\nu_i^2}{E_i t_i} \tag{5.21}$$

Rearrangement of Eq. 5.12 and substitution into Eq. 5.17 and 5.18 yields the maximum interface shear and peel stresses as a function of S, which are also plotted in Fig. 5-2.

The epoxy used in the thermal-bimorph mirror is MasterBond EP30-2, as it is

approved for use in the LIGO vacuum. Its lap-shear strength is 20-25 MPa when bonding two aluminum surfaces [139, 73], and the strength of the glass-metal bond shear strength is expected to be similar to that of the aluminum-aluminum bond. The tensile and compressive strengths are 70-75 MPa and 95-100 MPa, respectively. Thus, failure of the epoxy bond would thus most likely be caused by the interface shear stress exceeding the lap-shear strength, triggering slow delamination of the bond. The region of actuation range within which there is a high likelihood of this failure mechanism is shaded red in Fig. 5-2.

5.3 Finite element analysis

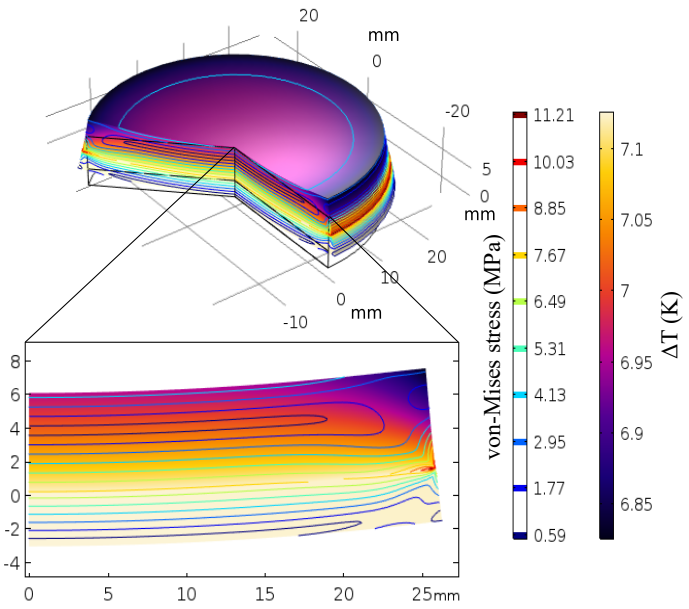

Figure 5-3: COMSOL FEA simulation of a thermal-bimorph mirror consisting of a 6-mm thick fused-silica mirror and 3-mm thick aluminium plate when there is a 200 mW power applied to its rear surface. The filled colormap represents temperature of the structure, whereas the contour lines show von Mises stress.

The analytic expressions in Section 5.2 were developed for bimetallic strips, for which the length-to-thickness ratio is very large and the thermal conductivity and emissivity of the two materials are similar. A finite element analysis (FEA) of the thermal-bimorph mirrors provides a more accurate estimate of the deformation

and stresses.

We simulated the bimorph mirror using an axi-symmetric COMSOL FEA model with z-axis axis as the axis of symmetry. The mirror is simply-supported along its circumference. Thus, the displacement in z-direction at radius r_0 is given by:

$$w(r_0, -t_1) = 0 \quad \text{edge is pinned to support and does not deflect} \tag{5.22}$$

$$\ddot{w}(r_0, -t_1) = 0 \quad \text{edge is free to rotate and does not experience any torque} \tag{5.23}$$

The mirror is uniformly heated on its rear surface with an input power P_{in}, and is cooled via radiation from surfaces with an emissivity of 0.06 (aluminium surface) and 0.93 (fused-silica surfaces) to the surroundings at an ambient temperature of 293 K. Fig. 5-3 shows a 3D rendered model of a thermal-bimorph mirror from the FEA model, including the temperature and von-Mises stress map when the mirror is heated at the rear surface with 200 mW input power.

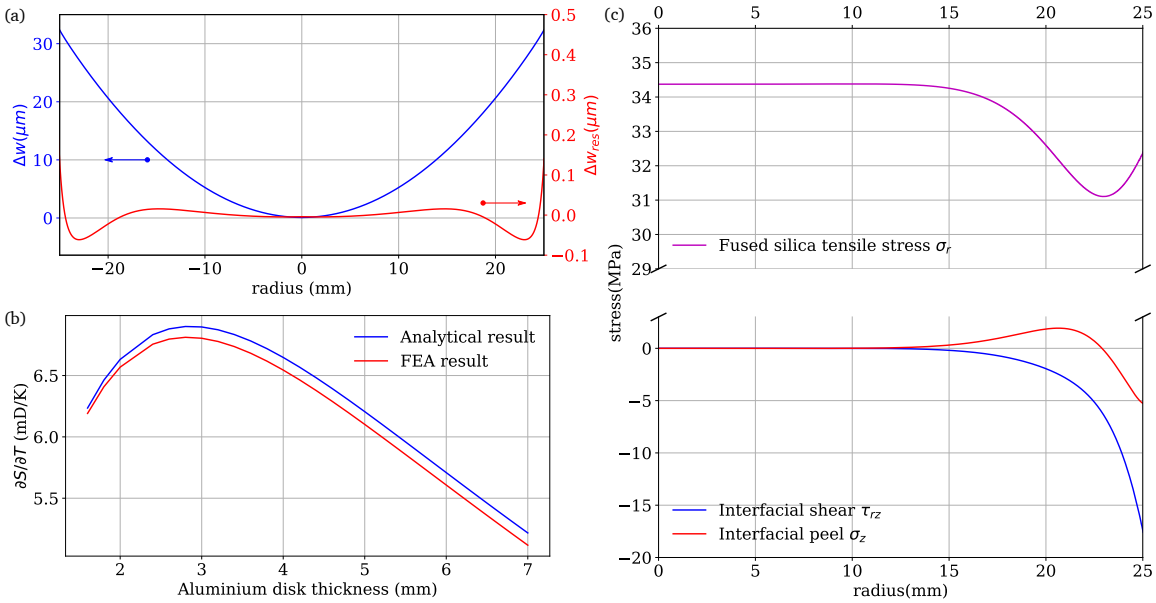

Figure 5-4: (a) Mirror deformation for $P_{\text{in}} = 600$ mW (blue), and deviation from best-fit quadratic (red). (b) comparison of predicted spherical power S as a function of aluminium plate's thickness from analytic expression (Eq. 5.12) and COMSOL FEA model, (c) Tensile stress in the fused-silica, and shear stress and peel stress applied to the epoxy.

The predicted deformation of the mirror relative to the centre of the mirror for

a heating power of 600 mW is plotted in Fig. 5-4(a). The deviation from the best-fit quadratic is also plotted, showing deformation is mostly quadratic expect outside the mirror's central 80%. This highly quadratic distortion means that we can estimate spherical power directly from FEA model using the following expression:

$$S = 4\frac{|v(r = w_{\text{interest}}) - v(r = 0)|}{w_{\text{interest}}^2} \tag{5.24}$$

where w_{interest} is the beam radius of interest. Thus, for data in Fig. 5-4(a), S$\simeq$ 180 mD.

The optimum thickness of the aluminium plate was also investigated using the FEA model. The predicted actuation rate as a function of thickness is plotted in Fig. 5-4(b) and compared with the result from analytic expression Eq. 5.12. The FEA actuation rate is 1.5% lower than that predicted by the analytic result. Nevertheless, the FEA result confirms that the maximum actuation rate is achieved when the aluminum plate thickness is approximately half of that of the fused-silica's (3 mm).

More importantly, the FEA model allows a more careful look at the stress within the TBM. The predicted tensile stress in the fused-silica, and the interfacial lap-shear and peel stresses are plotted as functions of the mirror's radius in Fig. 5-4(c), for S=180 mD. As seen on this plot, the main stress occuring within the centre of a TBM is that arising from axial stress and bending stress of the layer, which is tensile in fused-silica. This stress is $\simeq 75\%$ of the lower limit for its tensile strength. Near the edge of the TBM, there are high shear and peel stress. For ΔS=180 mD , the shear stress is 25% higher than that calculated using Eq. 5.17 and approaches the epoxy's lap-shear strength. The peel stress is comparable to that calculated using Eq. 5.18.

5.4 Experimental procedure

5.4.1 Mirror assembly

The first prototype of the TBM used 1" fused-silica mirror and was bonded using TorrSeal due to the availability of other epoxies at the time. All subsequent TBMs used Masterbond EP30-2 epoxy. This epoxy has been approved for LIGO vacuum while opertaing at ambient temperature. Its vacuum compatibility at an elevated temperature still requires verification. Collaborative work with Aidan Brooks and Antonio Perecca from Caltech also investigated Epo-Tek-353ND as bonding epoxy. However, Epo-Tek-353ND's lap shear strength (13 MPa) and glass transition temperature (90°C) are both lower than that of Masterbond 30-2 [87, 139].

For heating the TBM, a circular 2-inch-diameter flexible Kapton heater was used. These heaters have a resistance of 480 Ω and a thickness of 0.2 mm [86]. They are coated with pressure sensitive adhesive and could be applied directly to the TBM.

The following procedure describes assembly of a TBM:

1. Measure diameter and thickness of a fused-silica for bonding. Mirrors used here are 2"-diameter Thorlabs fused-silica mirrors with 6-mm thickness and a protected aluminium coating. Surface flatness was specified to be $\lambda/4$ at λ=632.8 nm and surface quality of 40-20 scratch-dig.

2. Machine an aluminium plate with the same diameter as that of the mirror and a thickness of 3 mm.

3. In a clean environment, clean rear surface of fused-silica mirror and a surface of aluminium plate.

4. Prepare two parts of Masterbond EP30-2 with ratio 10:1 by weight. Slowly mix the two parts to avoid trapped air bubbles.

5. Apply a thin layer of thoroughly mixed epoxy onto the back of the fused-silica mirror. Position the aluminium plate on top. Carefully move it around while gently pressing to spread the epoxy evenly.

6. Placed a small weight over the two layers and cure for 48 hours at room temperature

7. After curing, apply the flexible Kapton heater to the TBM back.

8. Replace heater lead wires with AWG28 wires to prevent seismic short during suspension. Connect heater wires to vacuum feedthrough.

9. Attach a thermistor to the barrel of the TBM and secure using either Kapton tape or UV-cured epoxy.

10. Clean the reflective surface of the mirror using isopropanol.

5.4.2 TBM characterisation

A schematic of the system used to measure the change in curvature of the TBM is shown in Fig. 5-5. The TBM was suspended in the vacuum chamber using two loops of wire, secured with Kapton tape on each side of the mirror. This method was chosen instead of a standard mirror mount secured with grub screw as the deformation of the TBM is sensitive to external stress, which could induce higher order aberrations and may lead to premature mirror failure. After suspending the TBM, a plate with 4 Nd:FeB magnets was positioned 5 mm from the rear face of the TBM to suppress slow pendulum modes of the suspension via eddy current damping (see Fig. 5-5)

The change in curvature of the TBM was measured using a differential Hartmann wavefront sensor (HWS) [48, 116, 47], which has been demonstrated to have a reproducibility of 0.5 nm_{RMS} and an accuracy of 0.25 nm. The operation of the HWS is described fully in Section 2.3.2. Briefly, the output of the single-mode fiber-coupled 680 nm super-lumniscent diode (SLED) was expanded and projected onto

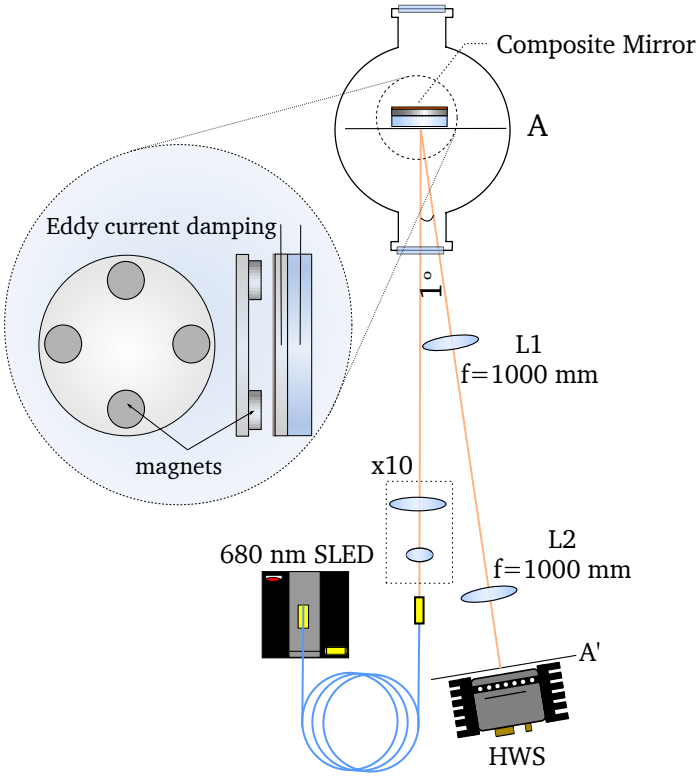

Figure 5-5: A schematic of the system used to test the thermal-bimorph mirror. The mirror is isolated from the surroundings by suspending it as a pendulum within a vacuum, and suppressing the motion using eddy-current damping. The 10X telescope projects a large diameter, 680 nm probe beam onto the mirror with an angle-of-incidence of 0.5°. The lenses L1 and L2 image the mirror surface onto the Hartmann wavefront sensor (HWS).

the mirror surface. The reflected wavefront was imaged onto the HWS, resulting in an array of Hartmann spots on the HWS camera. Heating the TBM causes the reflected wavefront to change and thus the Hartmann spot pattern changes. This change is analysed to determine the change in curvature of TBM.

The 680 nm SLED produced a maximum power of 1 mW with a central wavelength of 676 nm and a spectral linewidth of 10 nm. This implies a short coherence length of 14.5 μm, which helps to minimise the effects of interference as the probe passes through multiple optical elements. In our measurements, the SLED power was set at 0.7 mW and the camera exposure time was 20 ms. The SLED output was collimated using an aspheric lens to yield a beam diameter of 2.4 mm, which was then expanded by 10 times using a Thorlabs GBE10-B beam expander.

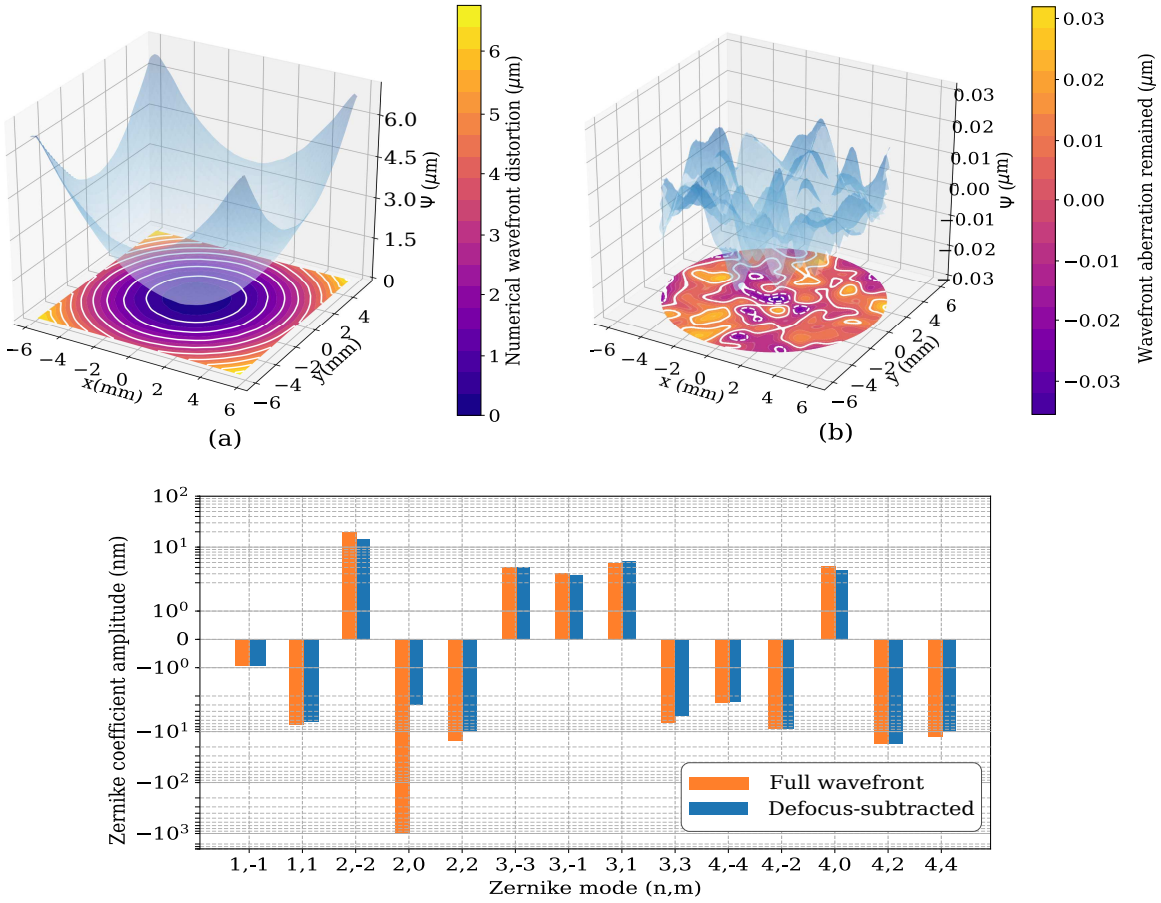

Figure 5-6: (a) Numerical reconstruction of wavefront change at the TBM with ΔT=26 K (b) Residual wavefront after removal of quadratic component of wavefront. (c) Zernike coefficients of the full wavefront and the defocus-subtracted wavefront

The expanded beam was steered onto the TBM with a 0.5^o angle of incidence. The small angle of incidence allows simple separation of the reflected beam without the introduction of extra optics. A larger angle of incidence would result in excessive astigmatism of the reflected wavefront. The reflected beam was imaged onto the HWS using an image-relay telescope with a nominal magnification of 1 formed by 2 lens, each of nominal focal length $f = 1$ m. Thus, the distance from the TBM to the first lens L1 is 1 m, between L1 and L2 is 2 m, and from L2 to HWS is 1 m. Such an imaging system can be described with $ABCD$ matrix in which B and C elements are $\sim$0, and thus both the intensity and wavefront are imaged. The choice of long focal lengths allowed placing of the lenses t be placed at locations

that will not clip incident probe beam. It also reduces the sensitivity to errors in focal lengths and distances between them. The focal lengths of the lenses were measured using a differential Hartmann technique [116](see Apppendix), giving f_1= 1.013±0.002 m and f_2 1.009±0.002 m respectively.

The imaging condition of the telescope was confirmed using a 1951 USAF resolution test chart plate placed at the TBM. The positions of lens are adjusted until a sharp image was formed on the CCD sensor of HWS. The measured magnification of the image-relay telescope was 0.996±0.02.

5.5 Results

5.5.1 Steady state response

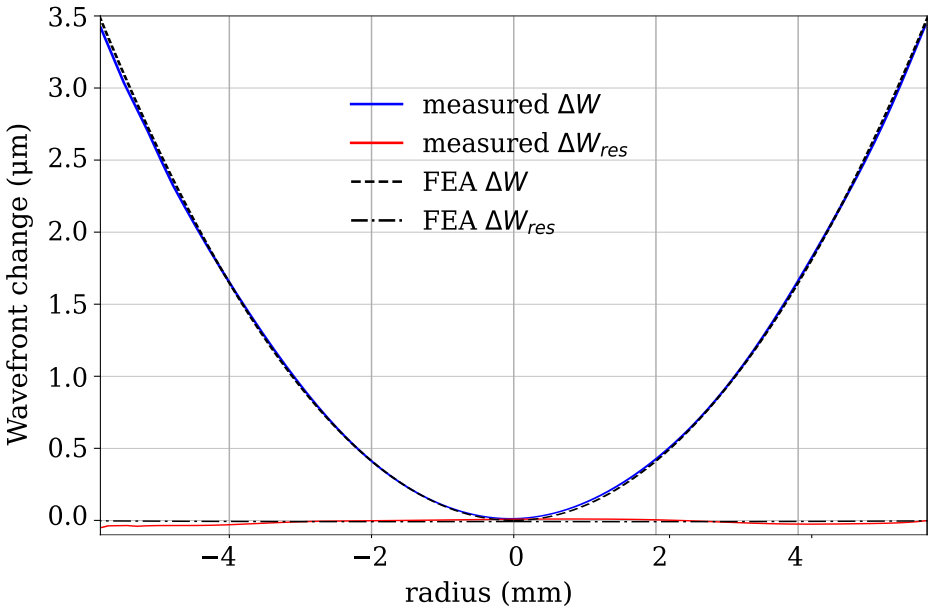

Figure 5-7: Cross-section of measured and FEA-predicted total and residual wavefront changes for $\Delta T = 26$ K.

The wavefront change produced by 0.69 W of electrical heating that resulted in Δ T=26 K, is plotted in Fig. 5-6(a). The change is mostly quadratic with S= 195.8 mD, which was obtained by performing least-squares fitting polynomial wavefront [47, 206] . The change can also be expressed in terms of Zernike func-

tions, as described in Appendix C and shown in Fig.5-6(c). The defocus calculated using this approach is 195.8 mD. also agrees with that obtained from polynomial fitting (S=195.8 mD).

The reproducibility of the wavefront change was checked by continually cycling the mirror over a three week period: yielding a maximum variation of 0.1 mD, or 0.05% .

A comparison of the measured and FEA-predicted cross-section of the wavefront change is shown in Fig. 5-7. From this plot, it can be seen that deformation of TBM is accurately predicted by the FEA model.

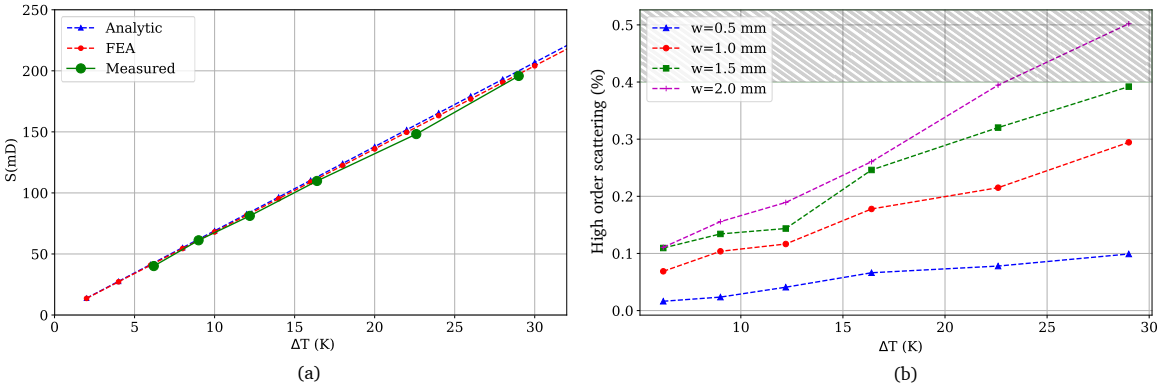

Figure 5-8: (a) Measured spherical power from Hartmann sensor (green) shows good agreement with analytic and FEA predictions, (b) Estimated higher order scattering from residual wavefront as a function of change in temperature for various Gaussian beam radii. The shaded region indicates the maximum scattering allowed.

The linearity of the response of the TBM was confirmed by measuring S vs ΔT. The results are shown in Fig. 5-8(a), indicating that the response of the TBM for $S < 200$ mD is linear with ΔT at an actuation rate $\partial S/\partial T$ =6.77 mD/K, which agrees well with FEA.

Removing the quadratic component of the wavefront change yields the residual error shown in Fig. 5-6(b), which would scatter light from an incident Gaussian beam. The amplitude of the error could be reduced by averaging, suggesting that it is largely random and thus probably associated with the measurement process. Nevertheless, the fractional energy scattered out of a Gaussian beam by the observed error was calculated using overlap integrals (Eq. 4.1) and is plotted for

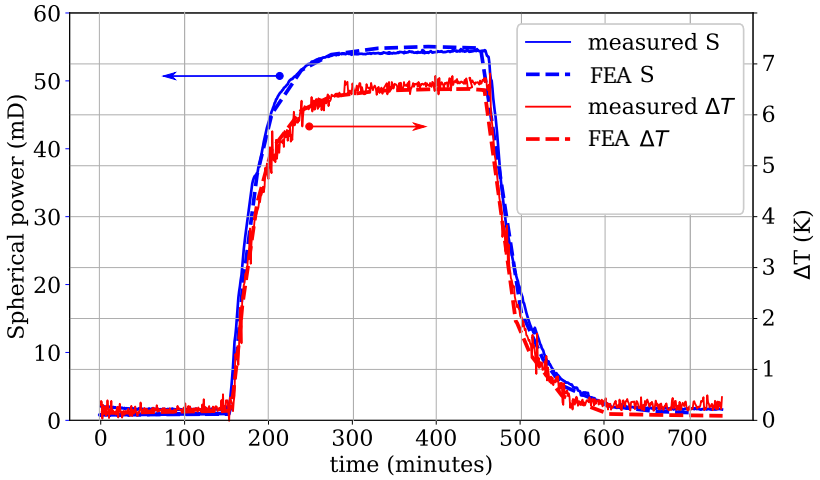

Figure 5-9: Measured and predicted response of the thermal-bimorph temperature and spherical power to a step input of 0.17 W

various beam radii in Fig. 5-8(b). This result indicates that an actuation range up to 200 mD can be used for a beam radius up to 2 mm with scatter less than 0.4% as required [43].

5.5.2 Transient response

The measured and predicted transient response of the TBM spherical power and temperature during heating and cooling are plotted in Fig. 5-9, showing good agreement.

The thermal time constant (τ) of the TBM was calculated using:

$$S = S_0(1 - \exp^{-t/\tau}), \quad \text{for heating} \tag{5.25}$$

and for cooling:

$$S = S_0 \exp^{-t/\tau} \tag{5.26}$$

where S is spherical power after sudden change in input power. S_0 is defined as spherical power at "hot" state during equilibrium.

Curve fitting of the experimental data yields τ for both eating and cooling $\simeq 35$ minutes . This time constant could be could be reduced significantly by coating the aluminium with high-emissivity ceramic coating such as aluminium oxide [11].

5.5.3 Actuation limit

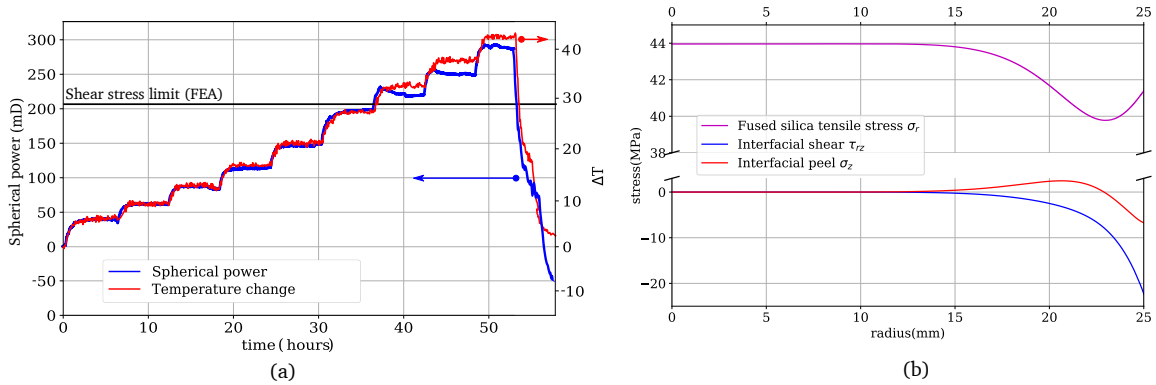

Figure 5-10: (a) Response of the thermal-bimorph mirror to step-change increases in the heating power. Note that the curvature of the mirror did not return to its original value when the heating power was removed. (b) FEA simulation of tensile stress in fused-silica, and TBM interfacial shear and peel stress at P_{in}=800 mW

The TBM actuation limit was investigated by increasing the temperature of the mirror via a series of step changes in heating power over about 2 days. The resulting temperature and spherical power are plotted in Fig. 5-10(a). The horizontal line in this plot shows the FEA prediction of the temperature increase and resulting S for which the interfacial shear stress is equal to 25 MPa, the upper limit of the EP30-2 lap-shear strength.

The predicted stresses within the TBM for an input power of 820 mW, which is slightly larger than that for which the measured started to deviate from linear response, is shown in Fig. 5-10(b). The FEA result shows that a fully deformed TBM at this input power would experience a maximum 25 MPa interfacial shear stress, which is the upper limit of MasterBond EP30-2 lap shear strenth [139].

We believe this failure is due to incremental delamination of the epoxy bond as the fused-silica was not ruptured.

5.6 Conclusion

We have described a thermally-actuated bimorph deformable mirror suitable for active wavefront control in gravitational wave detectors. These mirrors are low-

cost and easy to assemble. Additionally, our approach enables the use of mirror substrates with a thickness sufficient to enable a good surface figure. Using a 2" diameter, 6mm thick, fused-silica mirror, We demonstrated 200 mD of spherical power actuation with a linear actuation rate of ≈6.8 mD/K and very low higher-order aberrations.

Higher actuation of the TBM is limited by interfacial shear stress exceeding the strength of bonding epoxy. While a stronger epoxy may be used, we expect fused-silica's tensile strength to be another limiting factor as the tensile stress at bearing approaches 35 MPa at 200 mD.

To intergrate TBM into SAMS, further characterisation of epoxy layer would be required. While MasterBond EP30-2 outgassing rate at room temperature operation has been verified to meet LIGO UHV requirement [73], this may not be true at an elevated temperature. Furthermore, thermal noise of epoxies are difficult to estimate and highly dependent on thickness [100]. Ensuring that all TBM fabricated with a constant uniform epoxy layer is a challenging task. We therefore sought another solution that eliminates the use of epoxies. This leads us to the design of compression fit mirrors, which will be presented in the next chapter.

Chapter 6

Compression Fit Mirror

A compression fit mirror (CFM) is a new type of deformable mirror developed to meet requirements of SAMS. Investigation into this configuration is motivated by the need to eliminate the complication arising from the epoxy bonding in the thermal-bimorph mirror. This chapter is laid out as follows: section 6.1 briefly describes the principle of operation of the CFM. Stress analysis of the CFM is presented in section 6.2. Simulation of the CFM deformation under a thermal load is presented in section 6.3. Section 6.4 details the assembly procedure. Section 6.5 and 6.6 describes the results from characterising mirror deformation at ambient temperature and when heated. The design of SAMS is considered in the context of SAMS requirements in Section 6.7 and a modification to the standard design is proposed to meet those requirements.

6.1 Principle of working

The working principle of the CFM is similar to that of the TBM: it exploits the difference between thermal expansion coefficients of fused silica mirror and aluminium to thermally control the curvature of mirrors. For the CFM, however, the heating is used to create a convex spherical deformation of the mirror surface at

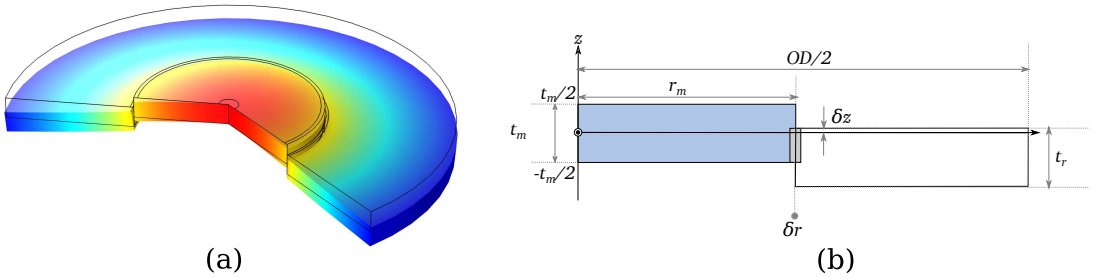

Figure 6-1: Schematic demonstrating concept of CFM. (a): 3D rendering in FEA of deformation of a CFM after cool-down to room temperature (b): Axial-symmetric schematic of a standard CFM with a mirror of thickness t_m, radius r_m, an aluminium ring of thickness t_r and a radial interference of δr. The upper surface of the aluminium annulus is offset δz below the neutral plane of the mirror barrel

ambient temperature by "shrink fitting" an annular aluminium ring around the mirror, as shown in Fig. 6-1 and then changing the curvature by re-heating the aluminium ring as required.

The shrink-fitting is accomplished by heating the aluminium ring until the outer diameter (OD) of the fused-silica mirror fits within the ring, and then removing the heat. This process results in a compressive stress applied to the barrel of the mirror, which can produce a bending moment and a convex deformation of the mirror.

The bending moment applied to the mirror can be calculated using:

$$\mathbf{M} = \begin{bmatrix} M_{rr} \\ M_{tt} \end{bmatrix} = \int_{-t_m/2}^{t_m/2} \begin{bmatrix} \sigma_{rr} \\ \sigma_{tt} \end{bmatrix} z dz \tag{6.1}$$

where σ_{rr} and σ_{tt} are the radial and tangential stresses (or hoop stress) on the mirror barrel and t_m is its thickness. If the mirror and ring are positioned symmetrically around $z = 0$ then the integrand in Eq. (6.1) is odd and there is no bending

moment. Introducing an axial offset δz as shown in Fig.6-1 results in:

$$\begin{bmatrix} \sigma_{rr} \\ \sigma_{tt} \end{bmatrix} = \begin{cases} \begin{bmatrix} 0 \\ 0 \end{bmatrix}, & \delta z < z \leq t_m/2 \\ \begin{bmatrix} \sigma_{rr} \\ \sigma_{tt} \end{bmatrix}, & -t_m/2 \leq z \leq \delta z \end{cases} \tag{6.2}$$

Eq. 6.1 then becomes:

$$\int_{-t_m/2}^{\partial z} \begin{bmatrix} \sigma_{rr} \\ \sigma_{tt} \end{bmatrix} z dz = \frac{1}{2} \begin{bmatrix} \sigma_{rr} \\ \sigma_{tt} \end{bmatrix} \left(\partial z^2 - \frac{t_m^2}{4} \right) \tag{6.3}$$

Since $|\partial z| < t_m/2$ and $\sigma_{rr} < 0$ due to the radial compression, the radial moment M_{rr} is always positive and thus acts in the clockwise direction. This results in a convex deformation of the front surface of the mirror. If the thickness of the actuating ring is similar to that of mirror, then the maximum bending moment can be achieved if the front surface of actuating is at the mid point of the flat optics barrel.

The maximum radial stress is determined by the difference between the outer and inner diameters of the mirror and ring, respectively, at room temperature, which we refer to as the "interference". Assuming an initial mirror OD $\varnothing_{\text{mirror}}$ and ring ID $\varnothing_{\text{ring}}$, we require:

$$\begin{aligned} \varnothing_{\text{mirror}}(1 + \alpha_{SiO_2} \Delta T) &= \varnothing_{\text{ring}}(1 + \alpha_{Al} \Delta T) \\ \therefore \varnothing_{\text{ring}} &= \varnothing_{\text{mirror}} \frac{1 + \alpha_{SiO_2} \Delta T}{1 + \alpha_{Al} \Delta T} \end{aligned} \tag{6.4}$$

where ΔT is the temperature increase required for the assembly, $\alpha_{Al} = 23.6 \times 10^{-6}$ K^{-1} and $\alpha_{SiO_2} = 0.55 \times 10^{-6}$ K^{-1}. Therefore, for $\varnothing_{\text{mirror}}$ = 50.8 mm, we require $\varnothing_{\text{ring}} > 50.706$ mm, assuming $\Delta T = 80°$C, which corresponds to a interference of 94 μm . Large ΔT could be used, which would result in a larger dynamic range, if

the mirror coating is confirm to not suffer from any adverse effect caused by high temperature.

The ID of the ring must also allow for roughness of the contact surfaces, and to allow for uncertainties in the micrometers used to measure the diameters. We used Mitutoyo micrometer (103-139-10H) with ± 5 μm precision to measure the mirror OD and Mitutoyo tri-ball micrometer (368-170) with ± 3 μm to measure aluminium ring ID. With these considerations, we used a target interference of 75μm for a nominal 2-inch mirror. For the 1-inch mirror prototype, the interference was 36μm.

6.2 Stress analysis

6.2.1 Analytical model

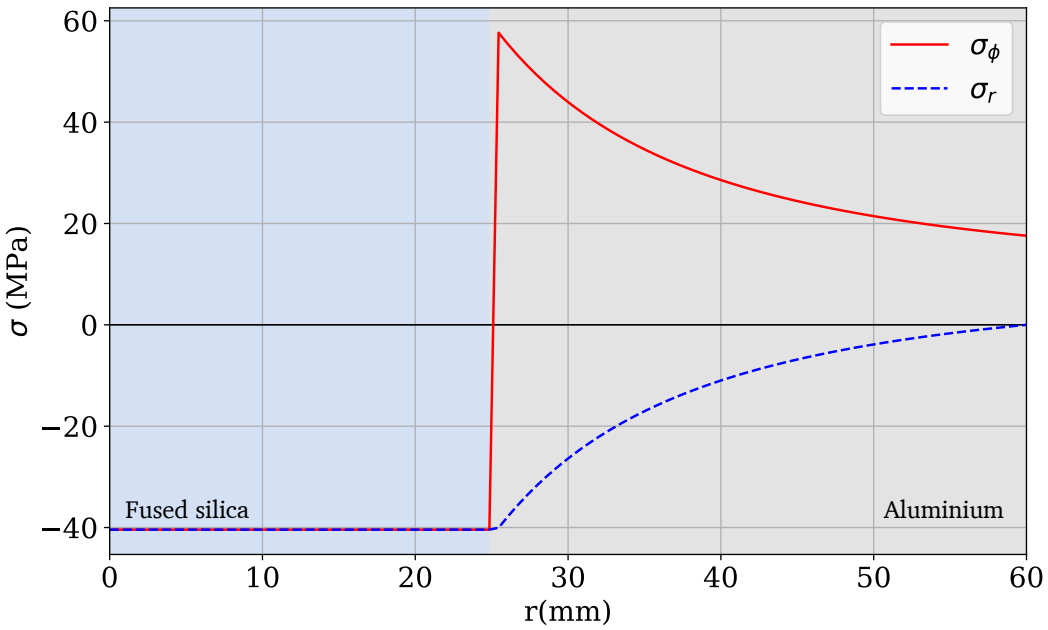

Figure 6-2: Analytic model radial and hoop stresses (σ_r and σ_ϕ respectively) within a fused-silica mirror and an aluminium annular ring for a 50.8 mm-diameter mirror and an annular ring with $2r_{ro}$ =120 mm and δr=37.5μm

The stress state of the mirror in the region along its contact surface is approximated by the stress state of a cylinder under uniform external pressure. Similarly, the stress on the annular ring is approximated by a thick-wall cylinder subjected to

uniform internal pressure. The contact pressure p created by the shrink fit is thus given by [159]:

$$p = \frac{\delta r}{\frac{r_{\text{ri}}}{E_{Al}}\left(\frac{r_{\text{ro}}^2+r_{\text{ri}}^2}{r_{\text{ro}}^2-r_{\text{ri}}^2}+\nu_{Al}\right)+\frac{r_{\text{ri}}}{E_{SiO_2}}\left(1-\nu_{SiO_2}\right)} \tag{6.5}$$

where r_{ro} and r_{ri} are the outer and inner radii of the annular ring, and E_i and ν_i are Young's modulii and Poisson ratios respectively. From Eq. 6.5, the equilibrium radial and hoop stresses (σ_r and σ_ϕ) can be estimated for each component [13]:

For the mirror:

$$\sigma_{\phi,\text{m}} = \sigma_{r,\text{m}} = -p \tag{6.6}$$

For the annular ring:

$$\sigma_{\phi,\text{r}} = p\frac{r_{\text{ri}}^2}{r_{\text{ro}}^2-r_{\text{ri}}^2}\left(1+\frac{r_{\text{ro}}^2}{r^2}\right) \tag{6.7}$$

$$\sigma_{r,\text{r}} = p\frac{r_{\text{ri}}^2}{r_{\text{ro}}^2-r_{\text{ri}}^2}\left(1-\frac{r_{\text{ro}}^2}{r^2}\right) \tag{6.8}$$

The radial and hoop stresses for an interference $\delta r = 37.5$ μm, $2r_{ro} = 50.8$ mm and $2r_{ri} = 120$ mm are plotted as functions of radius in Fig. 6-2. Within the fused-silica substrate, both hoop and radial stresses are compressive and constant at -40 MPa. In the aluminium ring, the hoop stress is tensile with a maximum of 58 MPa at the contact surface. The radial stress is also compressive and maximum at the contact surface, at which it is -40 MPa.

For an interference fit, the yield strengths of the materials need to exceed these stresses to maintain integrity [159]. Aluminium 6061-T6 has a yield strength of 276 MPa [131], which is higher than the maximum radial stress. Fused silica is however a brittle material and cannot be characterised by yield strength since brittle materials tend to fail via rupture rather than permanent deformation. We will therefore use Griffith criterion for brittle fracture as our guide [76]. Since both principle stresses are predicted to be negative, we require that neither of these stresses exceed the compression limit, which is 8 times tensile strength of fused silica. As discussed in chapter 5, the tensile strength of fused-silica is $\sim$50 MPa. Thus, both

σ_ϕ and σ_r must not exceed 400 MPa in compressive stress. This condition is therefore satisfied.

6.2.2 Finite element analysis

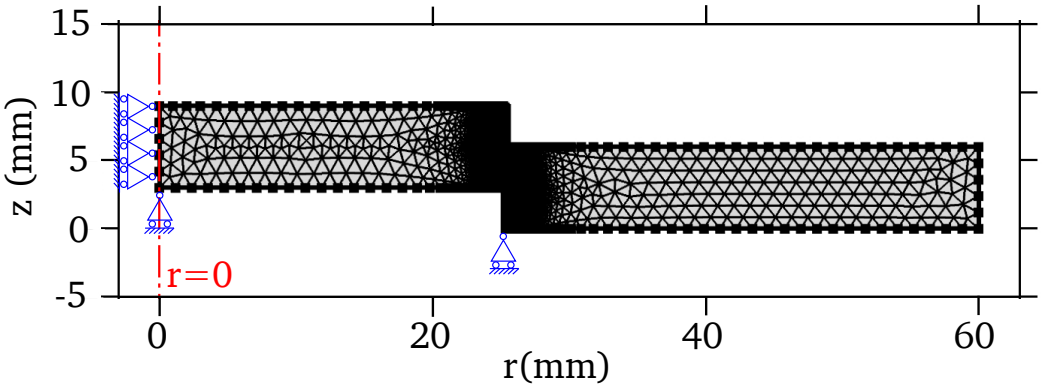

Figure 6-3: FEA model mesh and mechanical boundary conditions of a CFM with a 6-mm-thick 2-inch OD mirror and a 120 mm OD actuating ring. Note that the ring surface of the mirror is at $z = 0$.

While the analytical model provides guidance on whether the interference chosen should be feasible, the stresses distribution within the CFM is more complicated.

Eqn. 6.6-6.8 were developed for a hub-shaft inteference fit in which there is often a long engagement length and most of the shaft is fitted into the hub [159]. In our case, the axial lengths are similar and the mirror is displaced in the z-direction relative to the aluminium ring to produce a bending moment. This will create a tensile stress at the surface of the mirror that is outside the contact region. Furthermore, the interference fits create a stress concentration due to the abrupt transition from uncompressed to compressed material.

We thus used a finite element model to model the stress distribution within the CFM. Fig. 6-3 shows the 2D axi-symmetry model mesh used to study the assembly of a CFM. It consists of two domains: the mirror and the actuating ring. The contact between the two domains was modelled using `Form Assembly` instead of forming a union with a "glued contact" between the two domains. In each do-

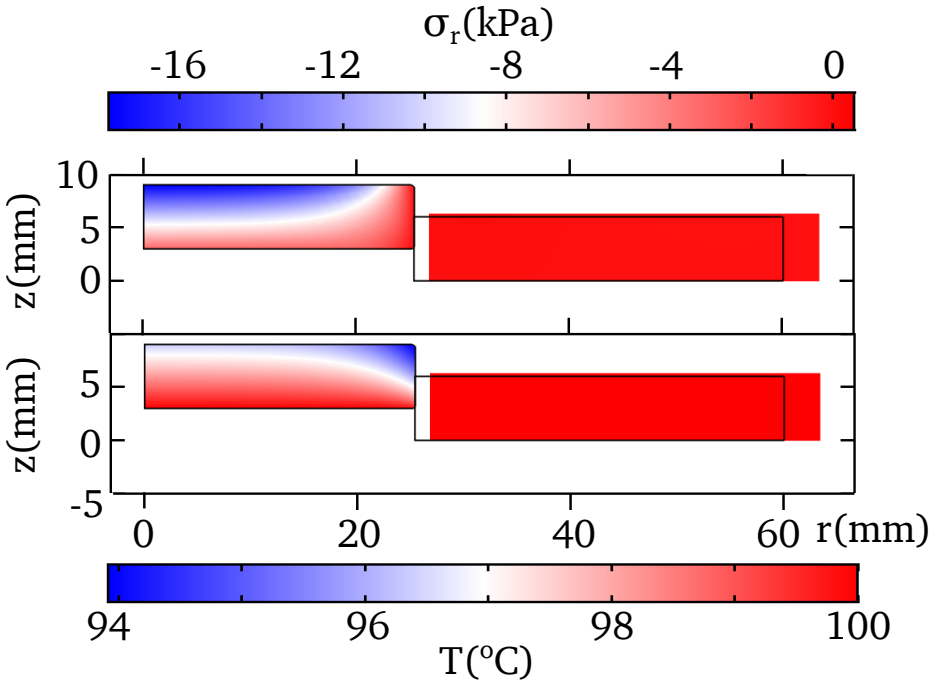

Figure 6-4: FEA simulated radial stress σ_r (upper) and temperature (lower) distributions in the first step of a CFM assembly, in which both components are heated to ca. 100°C During this stage, the fused-silica mirror fits into the aluminium ring but they do no come into contact. The displacements are not to scale.

main, we created a virtual subdomain at the contact edge to control meshing and enable better estimation of stress concentration at and near the contact surface.

The mechanical boundary conditions must allow the composite structure to deform freely but constrain rigid motion degrees of freedom. In a standard 2D model, there are three degrees of freedom to constrain (2 translations and 1 rotation). In 2D axis-symmetry model, translation in r and rotation are constrained. Each component therefore only needs an extra constraint in z at a single point to suppress rigid body motion. These are implemented as shown in Fig. 6-3.

"Diffuse surface" conditions are applied to all surfaces with material emissivities ϵ=0.93 for the fused-silica and ϵ=0.06 for the aluminium. This boundary condition allows radiative heat transfer between the CFM and the surroundings at an ambient temperature of 293 K.

Assembly of the CFM was simulated in a two-step study:

1. Heating of each component: a fixed temperature of 100°C was applied to

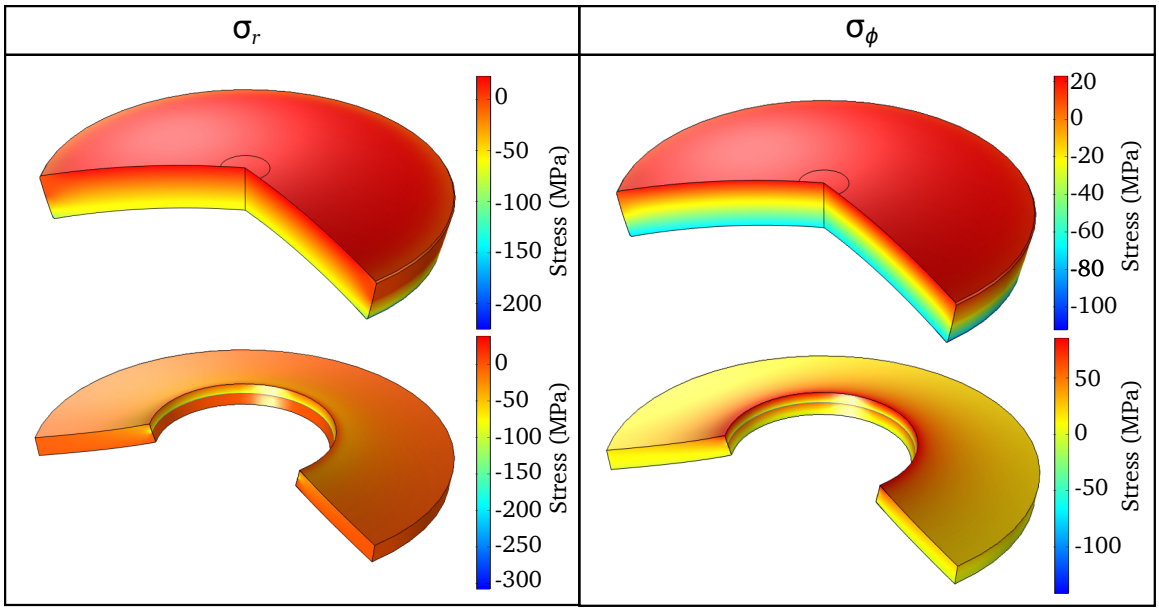

Figure 6-5: Finite element simulation of radial stress σ_r and hoop stress σ_ϕ in fused silica mirror (upper) and aluminium actuating (lower) after cooling to ambient temperature.

the bottom surfaces of each component. The mirror and ring were allowed to expand freely. The radial stress σ_r and temperature fields at equilibrium state are shown in Fig. 6-4. The low thermal conductivity and high emissivity of fused-silica gives rise to an internal temperature gradient, which creates stress within the fused-silica. However, the magnitude of this stress is small due to the low thermal expansion coefficient of fused-silica.

2. Cooling the CFM to ambient temperature: the fixed-temperature boundary condition was disabled and the composite structure allowed to radiatively cool to the ambient temperature of 293 K. The radial stress σ_r and hoop stress σ_ϕ in the fused-silica mirror and actuating ring after cooling is shown in Fig. 6-5. As expected, the mirror is bent so that its upper surface becomes more convex.

The stresses within the fused-silica mirror and the aluminium ring as function of radius at different z positions are shown in Fig. 6-6. The central 80% region of the mirror is predicted to see a linear change in both hoop and radial stresses as a function of z:

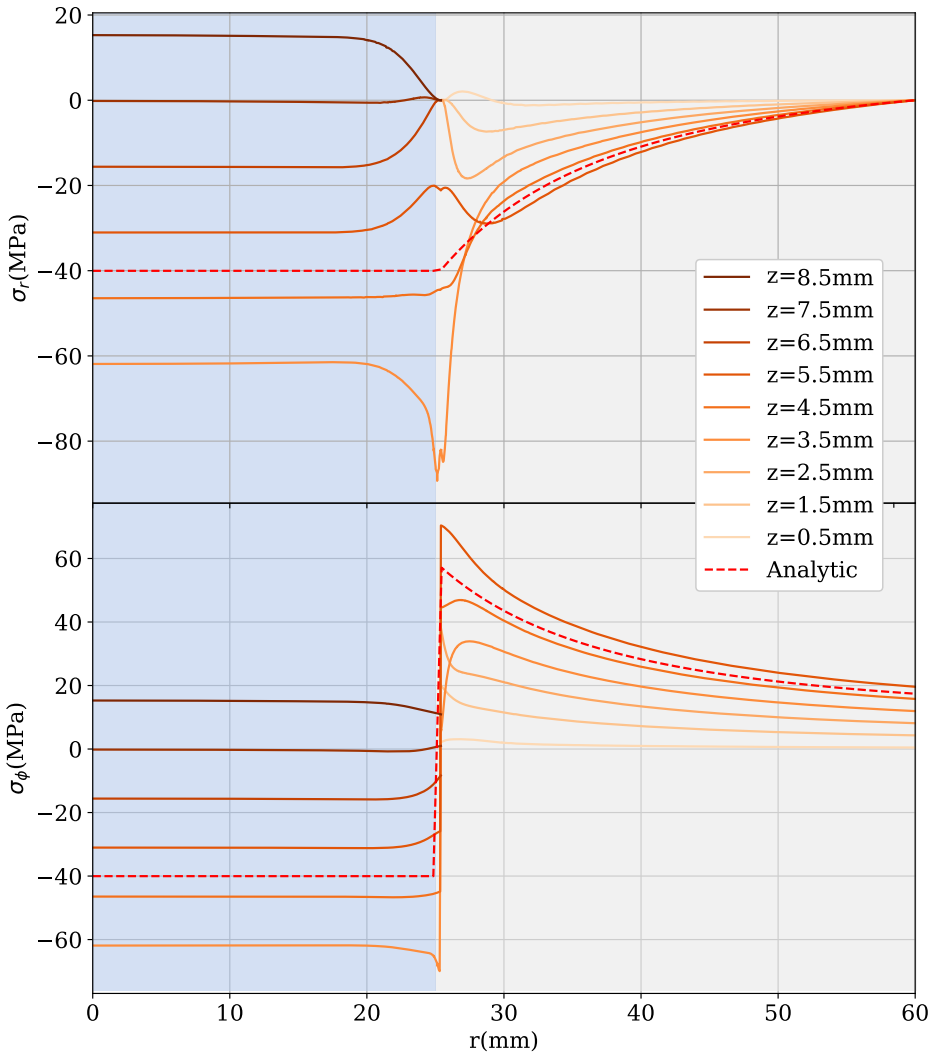

Figure 6-6: FEA simulated radial and hoop stresses as functions of radial distance from CFM's axis of symmetry at various z locations. $z = 0$ mm is defined to be at the rear surface of the actuating ring. The upper surface of the mirror is at $z = 9$ mm. The analytic predictions of stresses are plotted using dashed lines.

$$\sigma_{r/\phi} = 15.4z - 116.8\,\text{MPa}, \quad \text{z} \in [3, 9]\,\text{mm} \tag{6.9}$$

The maximum compressive stress occurs at the centre of the rear surface (z=3 mm) of the mirror and is 70.5 MPa, which is more than 5 times lower than the compressive limit of fused silica according to Griffth's criterion as discussed earlier. The maximum tensile stress occurs at the front surface of the mirror and is 22 MPa, which is 2.3 times smaller than it tensile strength limit.

In the aluminium ring, the radial stress is compressive, whereas the hoop stress is tensile, as expected from our earlier analysis. The magnitudes of these stresses are maximum at the contact surface and decay to zero towards the outer radius.

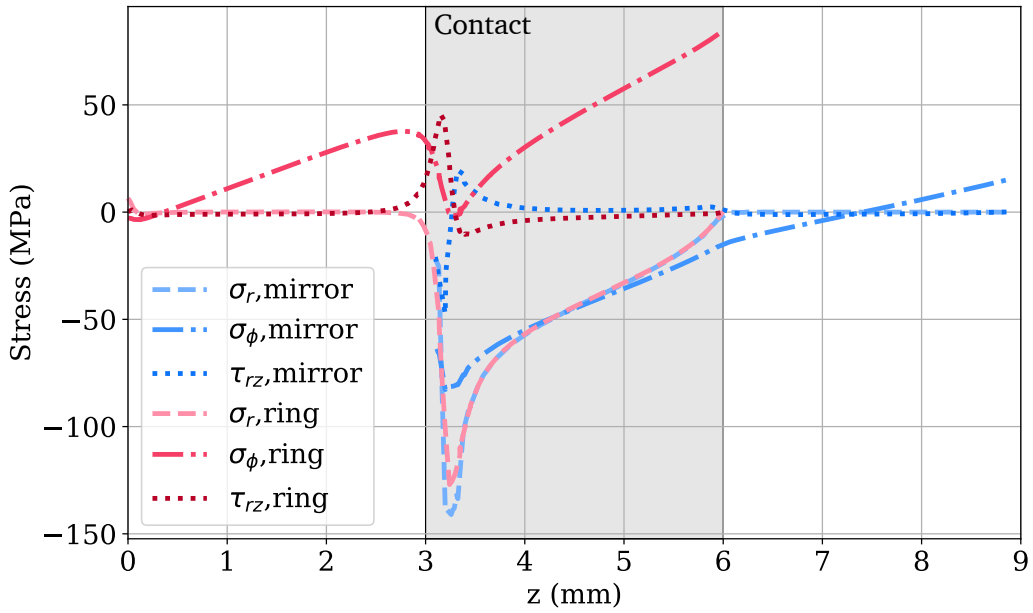

Figure 6-7: Maximum radial (σ_r), hoop (σ_ϕ) and shear stresses τ_{rz} at r=25.4 mm between the fused-silica mirror and the aluminium ring as functions of z.

The maximum values of the stresses at the aluminium-mirror interface (r=25.4 mm) is shown in Fig. 6-7. On the mirror contact surface between z=3 mm and z=6 mm, the compressive hoop stress (dash-dotted) and radial (dashed) stresses are maximum at its rear edge (z=3.2 mm). The small offset from $z = 3$ mm is due to the chamfer on the fused-silica mirror edge. The maximum compressive stress seen by the fused-silica is therefore ≈ 140 MPa, which is 2.8 times smaller that fused silica compressive strength limit. Only the region of the mirror near z=9 mm sees tensile hoop stress. This tensile stress is smaller then fused-silica tensile strength by a factor of at least 2.

The maximum radial stress on the aluminium ring inner surface is also compressive and has a maximum magnitude of ≈ 125 MPa at z=3 mm, as seen in Fig. 6-7. The hoop stress is tensile at the aluminium contact surface, with the maxi-

mum stress reaches 80 MPa at z=6 mm, which is 3.5 times smaller than aluminium tensile yield strength.

There is also a shear stress occuring at the z=3 mm, as shown using dotted-line in Fig. 6-7. The maximum magnitude of this shear stress is ≈50 MPa in both fused silica and aluminium. The shear strength of aluminium 6061-T6 is 207 MPa [196], which is 4 times greater than the shear stress observed here. Griffths criterion for brittle materials stated that the shear limitation for brittle materials could be approximated as three times the tensile strength of the material [76]. This results in a shear limitation of 150 MPa for fuse-silica, which exceeds our maximum shear stress by a factor of 3.

The finite element analysis of stresses in the CFM at its cold state (room temperature) thus shows that none of them should exceed materials limitations. Furthermore, these stresses should reduce during heating of the CFM as the two components return to their state prior to the shrink fit.

6.3 CFM deformation

The deformation of the CFM was also investigated using the FEA. The results are plotted in Fig. 6-8, which shows the static deformation (blue) at ambient temperature for a 2-inch diameter fused silica mirror offset by 3 mm in a 120 mm OD actuating ring with a 75 μm interference. The deviation from the best-fit quadratic is also plotted (red), showing that the deformation is highly quadratic in the central 85% of the mirror. The spherical power is $S \simeq -351$ mD using Eq.5.24 , where the negative sign is due to the convex deformation.

The FEA-predicted deformation of the CFM when heat is applied to the rear surface of the actuating ring is plotted in Fig. 6-9. Heating causes a reduction in the compressive stress and thus mirror returns to its initial state. It also results in less high-order aberration. This simulation also indicates that an actuation range of up 200 mD can be achieved if the CFM is heated up by $\Delta T \approx 43$ °C.

This deformation demonstrates an important advantage of the CFM over the

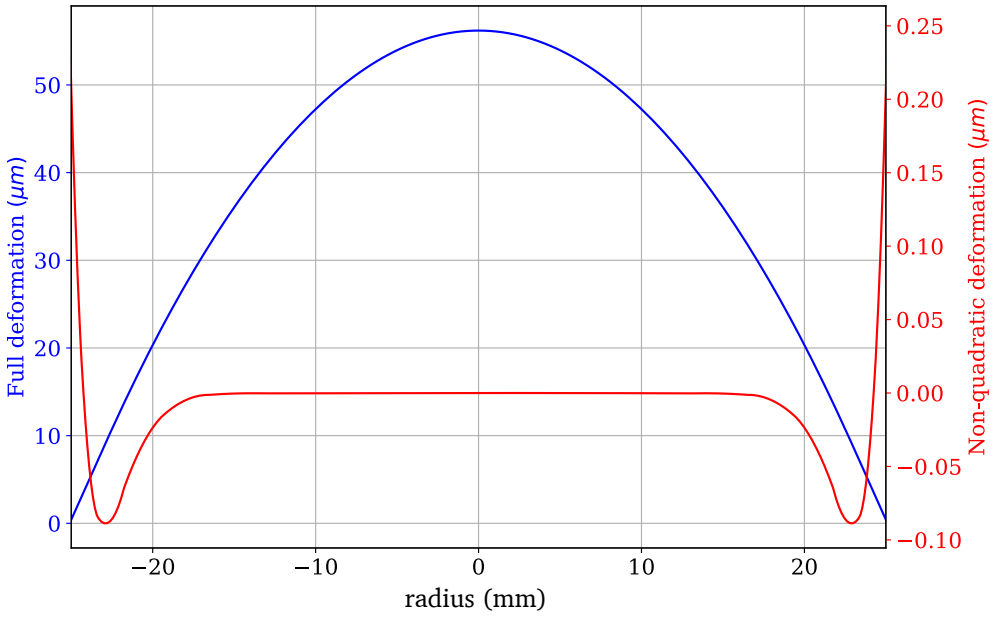

Figure 6-8: FEA simulation of a CFM deformation (blue) at ambient temperature for a 2-inch-diameter mirror enclosed in a 120 mm OD actuating ring. The deviation from the best fit quadratic is shown in red

TBM: more deformation is achieved at the same tensile stress. This is because the CFM provides a compressive stress bias to the structure and therefore takes advantage of the higher compressive strength of fused-silica.

The static deformation is dependent on a number of degrees of freedom: the interference $2\delta r$, the actuating ring thickness t_r, outer diameter OD and axial offset δz. FEA simulation showed that S is directly proportional to the interference. Its dependence on the other parameters is shown in Fig. 6-10. Parametric-sweeps studies in COMSOL shows that the thickness of the aluminium ring that produces the maximum deformation of the CFM is approximately the same as the fused-silica mirror thickness, which is 6 mm in this case (Fig. 6-10). The magnitude of S is also found to increase with increasing ring OD. The rate of increase is however only 0.2 mD/mm for ODs that are greater than 100 mm. The best offset for maximum deformation is $\delta z = 0$ mm, which agrees with our discussion in Section 6.1.

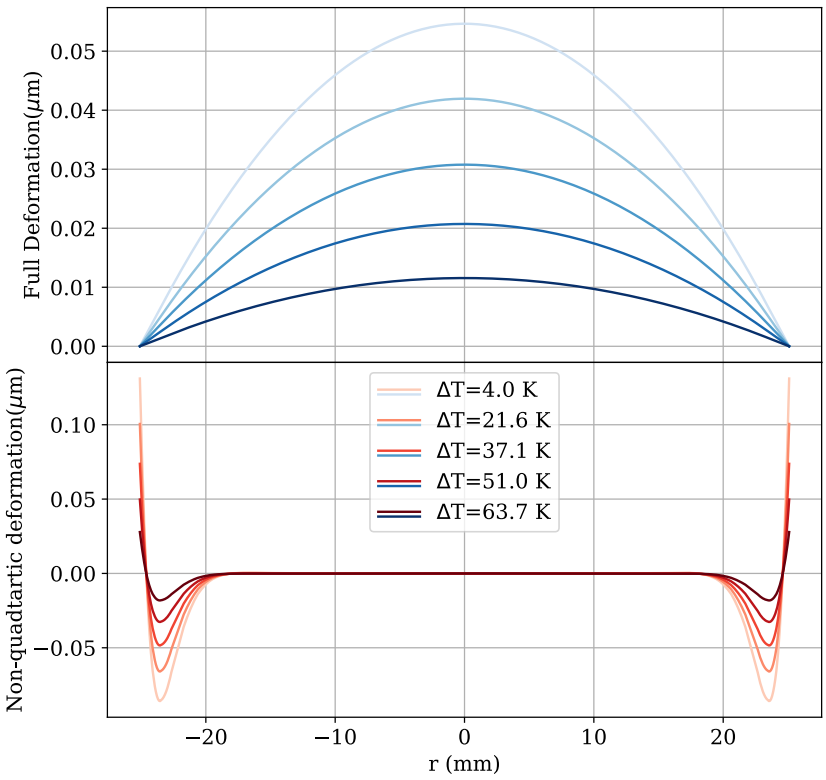

Figure 6-9: FEA simulation of the CFM deformation at different elevated temperatures. The top panel shows the CFM full deformation when there is 0.1, 0.5, 1, 1.5 and 2 W of power dissipated from a heater to heat up the structure. The bottom panel shows the corresponding non-quadratic deformation of those shown in the top panel.

6.4 Assembly of CFM prototypes

Two CFM prototypes were produced:

- The first using a 1-inch diameter 6 mm-thick fused-silica mirror available off-the-shelf from Thorlabs (PF10-03-G01).
- A 2-inch 6m mm-thick diameter CFM with a fused-silica mirror nominally identical to that used for the TBM .

The parameters for these CFM are listed in Table 6.1

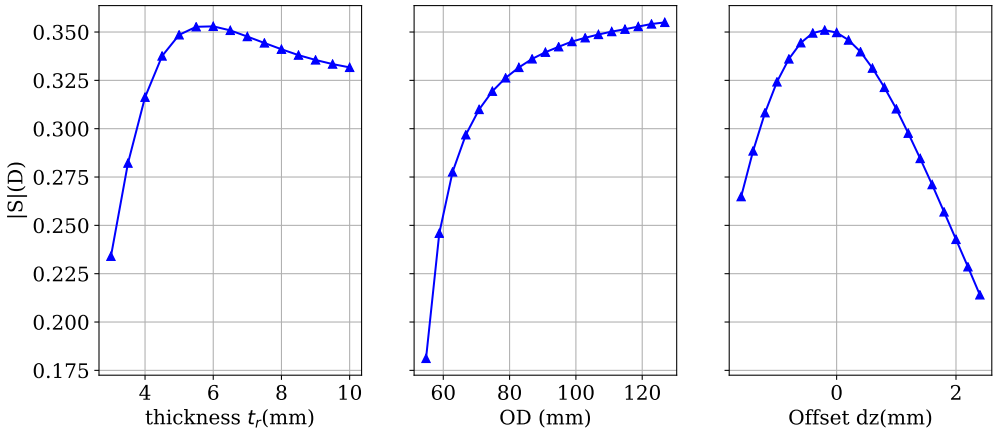

Figure 6-10: *From left to right:* Dependence of the static spherical power S of the CFM on actuating ring parameters: thickness t_r, OD and axial the offset from center of the mirror's barrel δz for $t_r = 6$ mm

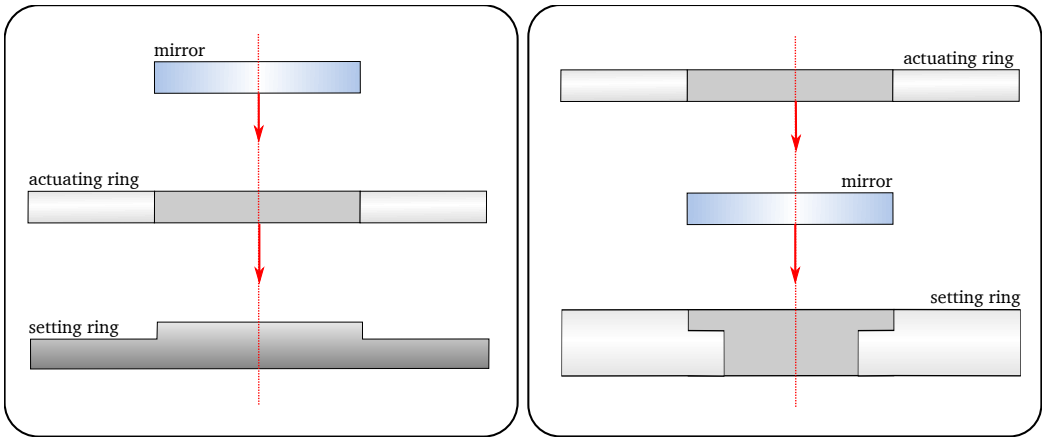

Figure 6-11: Two assembly procedures that have been used to assemble CFM's

Two assembly procedures were investigated, as illustrated in Fig. 6-11. In both, a "setting ring" was used to set the axial location of the mirror in the actuating ring.

Initially, the actuating ring was positioned on top of the setting ring and heated to 100°C, at which point the fused-silica mirror was dropped in as indicated in the left panel of Fig. 6-11. This method required handling of the fused-silica mirror at an elevated temperature, and it was susceptible to misalignment. This method often resulted in cracking of the fused-silica substrate once cooled due to the high shear stress induced at the ring-mirror interface.

Parameter	⌀1"-flat	⌀2"-flat
$\varnothing_{\text{outer}}$)	50 mm	120 mm
thickness	6 mm	5.82 mm
radial interference	18±5μm	37.5±5μm

Table 6.1: Parameters defining aluminium ring dimensions of CFM prototypes with different fused silica geometries. These dimensions are selected for maximising CFM deformation rate.

In the second procedure, the fused-silica mirror was first positioned in the setting ring and then all components were heated to 100°C. The actuating ring was then placed on the setting ring and then cooled slowly to ambient temperature. This procedure is detailed below:

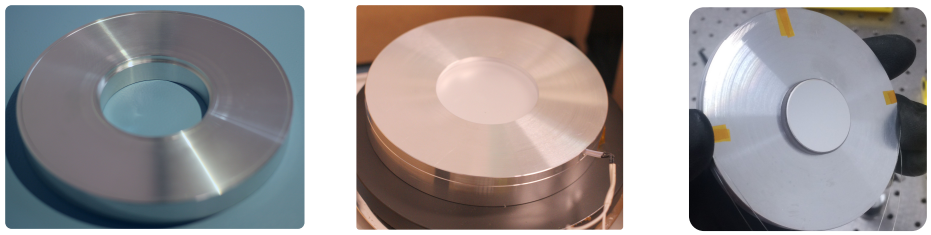

(a) (b) (c)

Figure 6-12: Assembly procedure and the result of the CFM using the second method in Fig. 6-11. (a) is an image of the ring-setter used in this method. Fused silica was allowed to rest in this setting ring before the actuating ring is dropped on top at high temperature, which is shown in (b). The mirror was tightly held within the actuating ring after cooling to ambient temperature, as shown in (c).

1. Measure the diameter of a fused silica mirror using a 50-75 mm micrometer with a resolution of ± 5 μm. Measurements of 5 diameters on a mirrr showed a mean diameter of 50.762±0.006 mm.

2. Use the measured mirror OD and the nominal interference to specify the inner diameter (ID) of the actuating ring. Thus, for the 2-inch mirror, the required ring ID$= 50.762 - 0.075 = 50.687$ mm.

3. Machine the ring and the setting ring. Measure the ring ID using a tri-ball micrometer.

Figure 6-13: Application of heater on CFM prototypes. Left image shows the first layer of kapton tape to electrically insulate actuating ring from NiCr wire. Right image shows a CFM prototype with heater coil wound applied and its resistance reading.

4. Carefully clean all the surfaces of the mirror and the actuating ring, especially the contact surfaces between mirror and the ring, using isopropanol.

5. Place the setting ring, actuating ring on a hot plate or in an oven.

6. Gently place the fused-silica into the setting ring.

7. Enclose hot plate in an insulated box and heat to 100°C.

8. Once temperature reaches reaches 100°C, place actuating ring onto the mirror sitting on the setting ring.

9. If the actuating ring shows difficulty in sliding down, it is most likely caused by an error in the ID of the actuating ring. Increase the temperature by 5°C and repeat. In most cases, the actuating ring should drop down easily at maximum $T \simeq 125$°C .

10. Allow the entire assembly to cool slowly to ambient temperature while resting on the setting ring. Once the CFM has completely cooled, apply heating element to the actuating ring. Initially, the heater consisted of a spiral of $\varnothing 140$ μm 80/20 nichrome wire that was insulated from the back surface of the actuating ring by Kapton tape, as shown in Fig. 6-13. In future versions, we will use custom-made Kapton heater adhered onto either the back surface or the barrel of the actuating ring.

6.5 Characterisation of the CFM static deformation

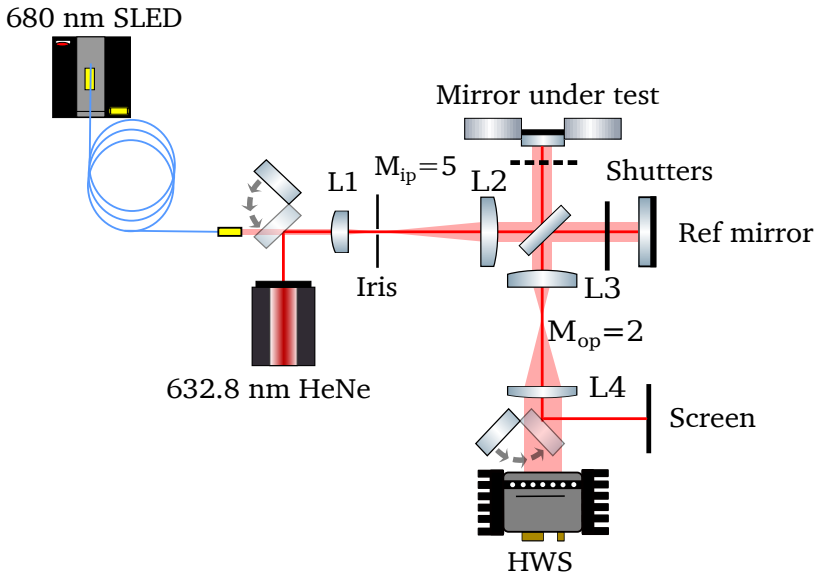

Figure 6-14: Schematic of the system used to test the CFM static deformation. The setup can be used with either a Michelson interferometer or a Hartmann test. The HeNe laser is used in the Michelson interferometer operation. A 680 nm SLED is used for the HWS. Lenses L1 and L2 magnify the sensing beam. Lenses L3 and L4 image both the reference mirror and test mirror surface onto the screen or the HWS.

The static deformation of the CFM at ambient temperature was investigated using the system shown in Fig. 6-14. This system allowed qualitative characterisation using a HeNe interferometry and quantitative characterisation using a HWS, which compared the wavefronts reflected from a flat fused-silica reference mirror and those reflected from the CFM.

The HeNe and collimated SLED beams were magnified by a 5× telescope consisting of lenses L1 and L2. The reflected beams were further magnified to improve spatial resolution and imaged onto the screen and the HWS.

A typical interferogram is shown in Fig. 6-15. It consists of concentric rings, as expected, due to the different curvatures of the wavefronts reflected by the reference mirror and CFM.

The measurement "noise floor" for the HWS was determined by replacing the CFM by a flat mirror of the same specification as the reference mirror. The results

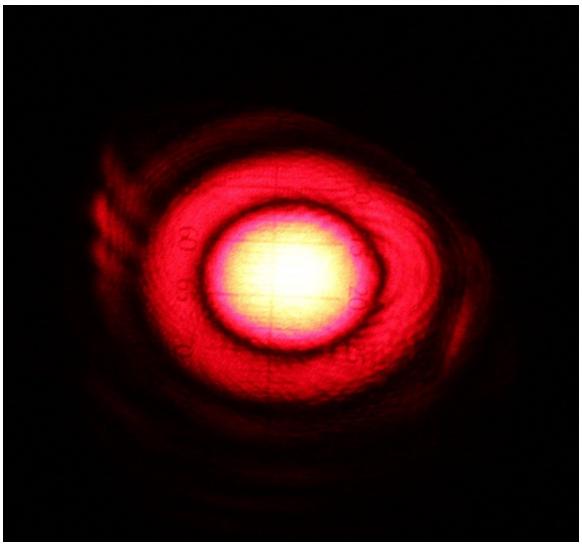

Figure 6-15: Interference pattern observed at the output of Michelson interferometer in the CFM static deformation test

from averaging 100 frames are plotted in Fig. 6-16. The wavefront aberration in Fig. 6-16 arises from the difference in optical paths caused by the beam splitter and air currents, and noise of the CCD array.

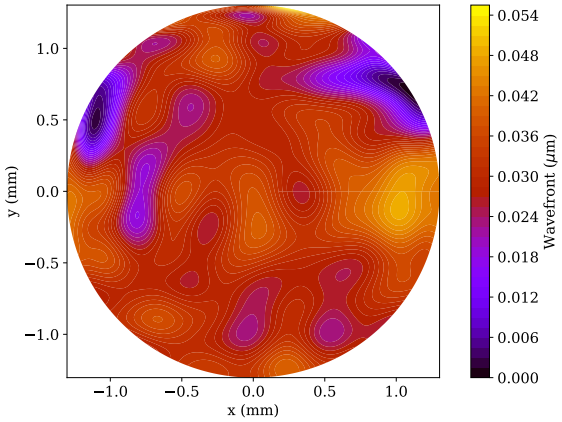

Figure 6-16: The wavefront observed by the HWS when a flat mirror with the same specifications as the reference mirror was placed at the location of the CFM in Fig. 6-14.

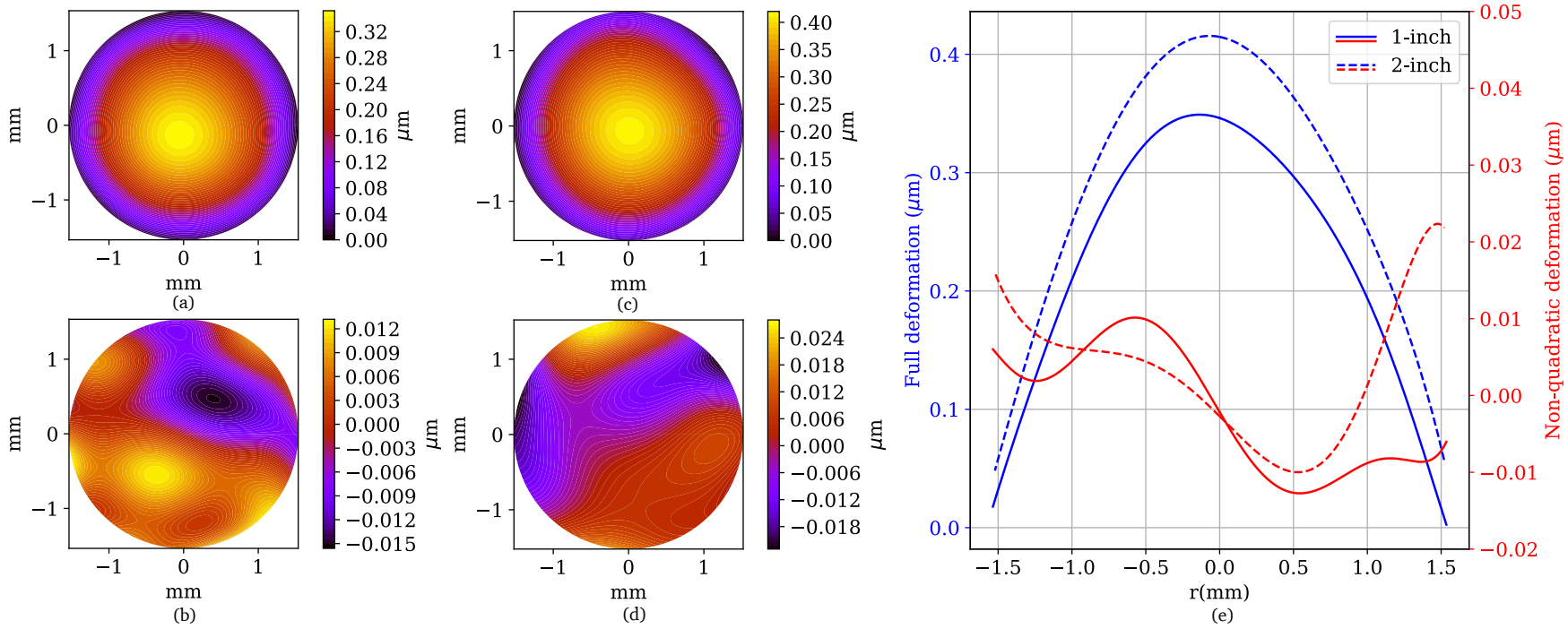

Figure 6-17: Results of static deformation measurement using the HWS: (a) and (c) show the full wavefront change due to the static deformation of the 1-inch and 2-inch CFMs respectively over a 3-mm diameter aperture. (b) and (d) are the residual wavefront map of the same two mirrors after removal of quadratic component. (e) shows a cross-section of the wavefront deformation along the y-axis from (a) and (c) in blue, and the non-quadratic wavefront change from (b) and (d) in red.

The measured static wavefront changes for the 1-inch and 2-inch CFMs are shown in Fig. 6-17(a) and (c) respectively. The spherical powers S measured for these CFMs are -314±6 mD, -346.8±4.8 mD respectively. The deviations from spherical curvature are plotted in Fig. 6-17(b) and (d), showing that wavefront change is highly spherical, which agrees well with the FEA-predicted -316 mD and -350 mD for 1" and 2" CFMs respectively.

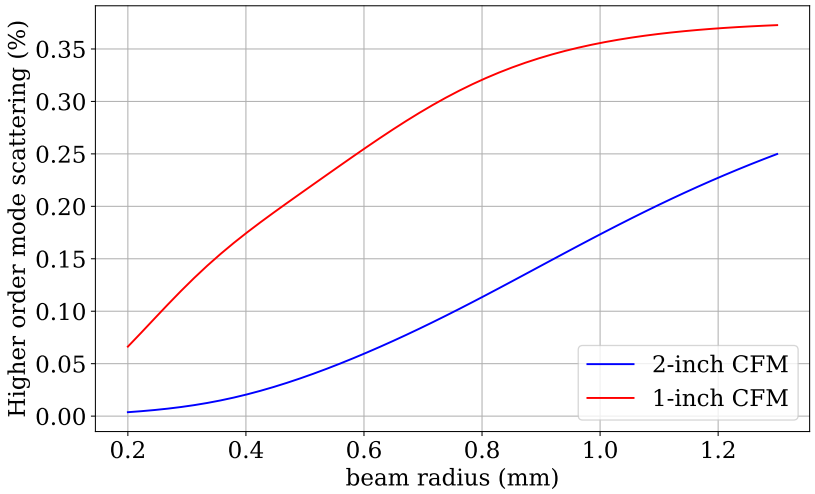

Figure 6-18: Higher order mode scattering estimation due to higher order aberration in the CFM static deformation as a function of science beam radius, computed from the residual maps shown in Fig. 6-17. The blue and red traces represent the 2-inch and 1-inch CFMs respectively.

The estimate higher-oder-mode scattering as due to higher order aberration is presented in Fig. 6-18. This figure shows that the higher order mode scattering in CFM is smaller than that induced by the deformation of the TBM. Over the central 2.6-mm diameter region, the loss due to scattering into higher order modes remains below 0.25% , which meets the aberration requirement for adaptive optics used in A+ upgrade [43].

Creep in mirror deformation

When elastic materials experience stresses, which are not necessarily close to their yield points, the materials can still experience a slow plastic deformation caused

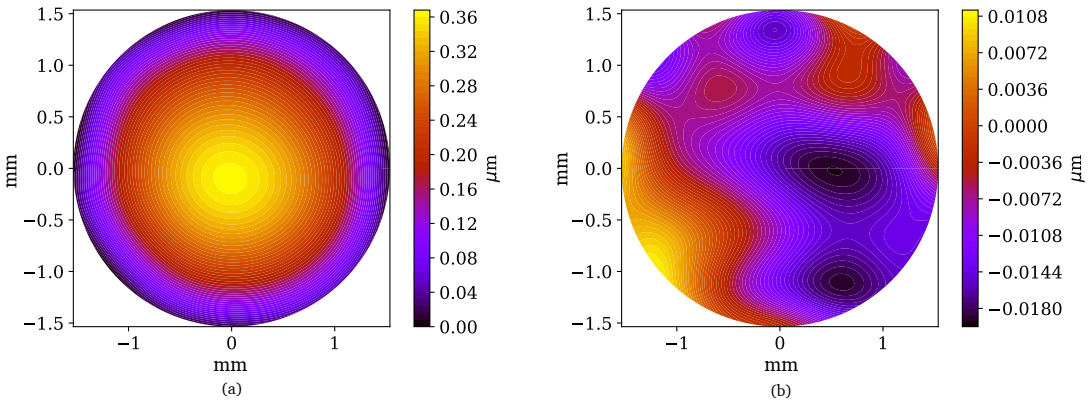

Figure 6-19: (a) Static wavefront change reflected of the 1-inch CFM measured 6 months after its assembly (b) Residual difference after subtraction of (a) from the same measurement at the time of assembly (Fig. 6-17(a))

by a superposition of a large number of discrete events that are mainly localised dislocation movements. These movements are caused by stress release at the microscopic scale. This phenomenon is referred to as *creep* and has been studied in the design of gravitational wave detector suspension system [38, 137, 167, 207, 202, 128]. In the suspension systems, the creep events would couple to the interferometer's readout via lengthening of the suspension fibres that are under tensile stress [57]. Creep can also affect the CFM, and may couple into length noise, as well as spherical power noise in the mode-matching. This source of noise is small and very challenging to measure [34, 97]. However, we can use macroscopic quantities to infer if there are a high number of microscopic creep events in the CFM as the radius of curvature of the CFM would be expected to decrease as the mirror releases stress over a along period of time.

Fig. 6-19 shows the measurement of wavefront deformation by the 1-inch CFM 6 months after its assembly. The measured spherical power was $S = 316 \pm 3$ mD, which remained within the uncertainty range of S in the first measurement.

This result however does not enable a conclusion that there is no creep, but shows encouraging results that the number of creep events is not high. Future measurements aim to monitor the mirror continuously over an extended period of time and take into account of environmental variations to provide a more precise

result.

6.6 Characterisation of the CFM dynamic response

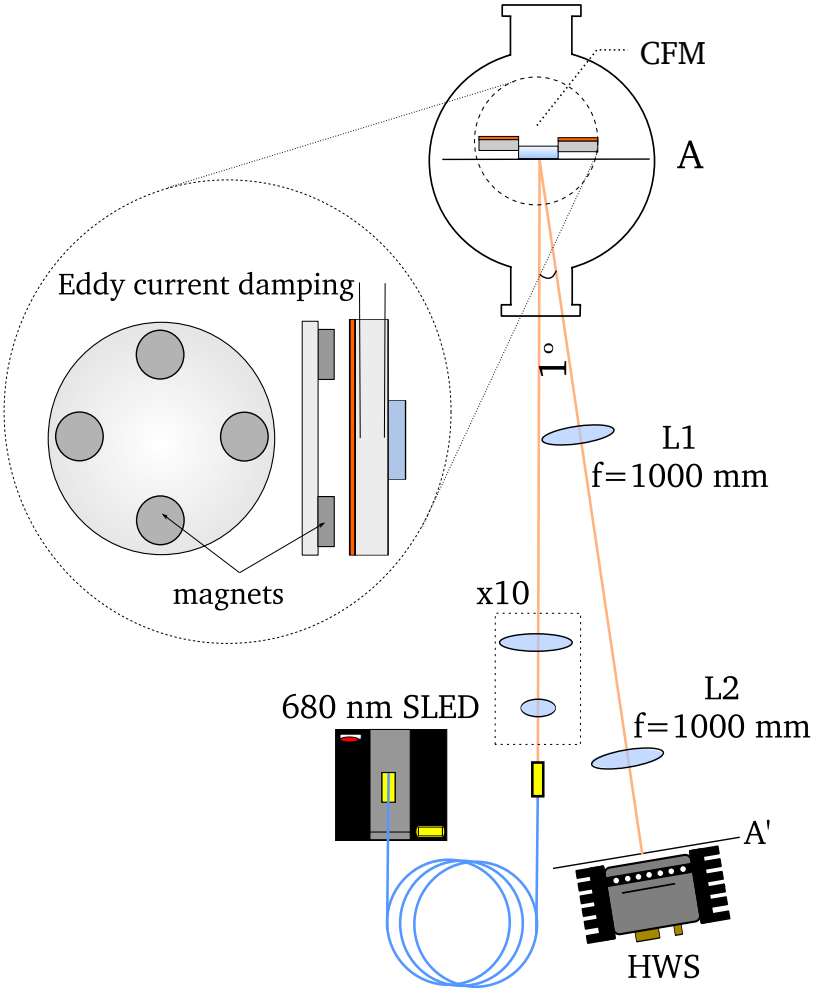

Figure 6-20: A schematic of Hartmann system used to test the CFM actuation. This system is identical to that used for testing the TBM, as shown in Fig. 5-5. The only difference is the replacement of the TBM with the CFM.

The optical layout used to characterise the CFM actuation is shown in Fig. 6-20. It is mostly identical to that used for characterising the TBM.

The wavefront change produced when the CFM is heated to 72.8°C from the ambient temperature (21.1°C) is shown in Fig. 6-21 . For this ΔT=48.7 K, the measured change in the spherical power is ΔS=226.1$\pm$1.1 mD, which translates to an

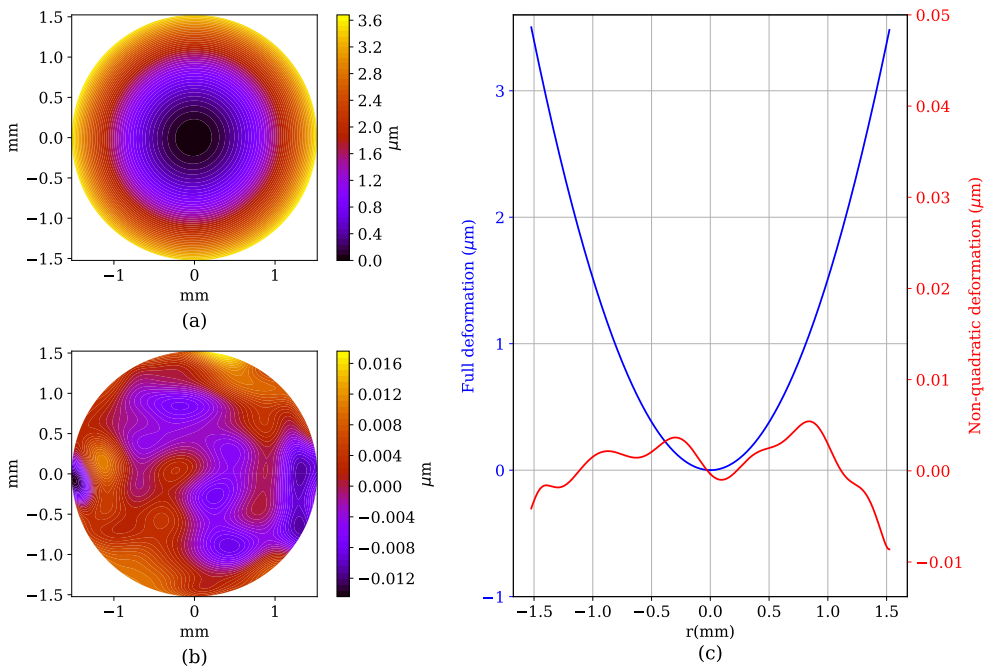

Figure 6-21: (a) The wavefront change at the 2-inch CFM with ΔT = 48.7 K. (b) The residual wavefront after removal of the quadratic component. (c) The y-axis of cross-section of the wavefront change.

actuation coefficient of 4.6 mD/K. The FEA simulation predicts that the actuation coefficient for the 2-inch CFM should be 4.8 mD/K. While the static deformation of the 2-inch CFM falls slightly short of the FEA simulation, its actuation rate agree well with the prediction. The error in static deformation is therefore most likely due to the uncertainty in the inner diameter of the actuating ring and the interference.

Fig. 6-21(b) shows the residual wavefront change after removal of the quadratic component, confirming that there is negligible higher-order aberration in the deformation. The peak-to-valley magnitude of this residual map is only half of that of the residual map of the static deformation residual map. This can be accounted for by two sources: firstly, the actuation range implemented here is only approximately 2/3 of the CFM's maximum deformation. Secondly, the optical layout used here incorporates a common optical path for the reference and signal wavefronts, providing significant "common mode rejection".

The reproducibility of the wavefront change was checked by continually cy-

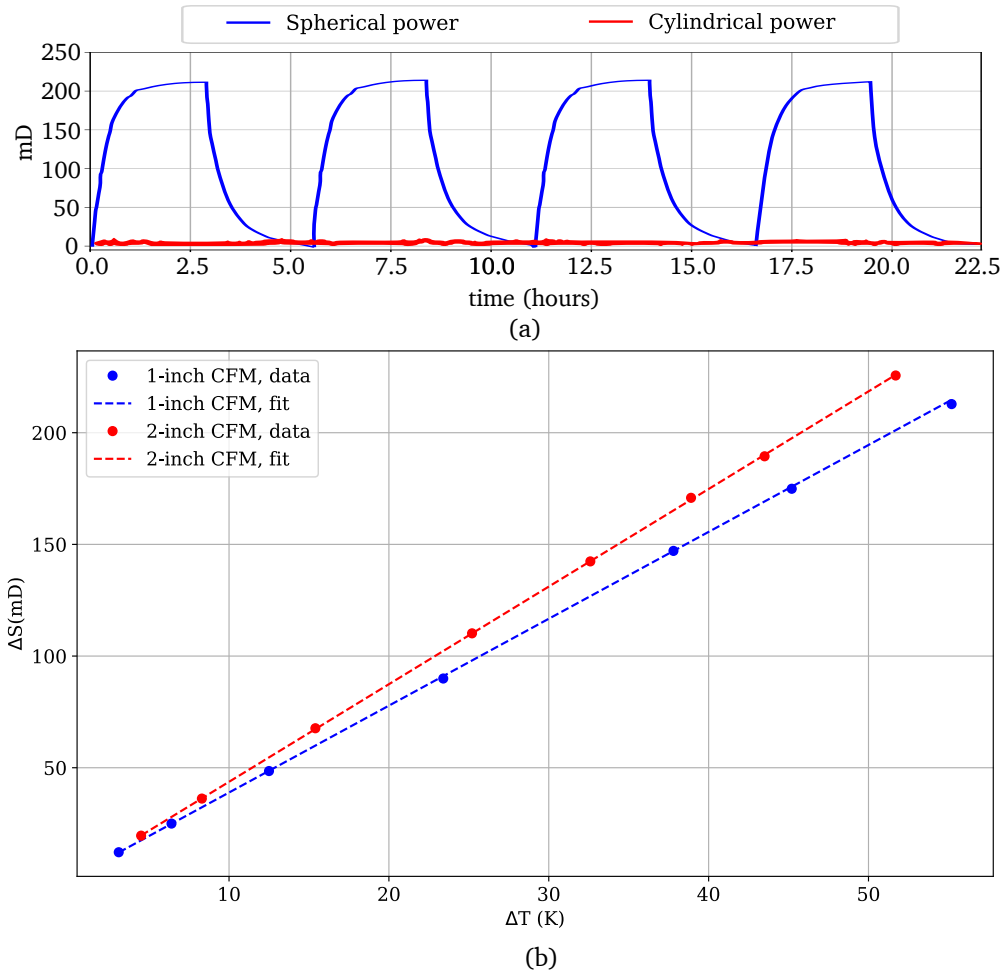

Figure 6-22: (a) Measured change in spherical power of wavefront at the 2-inch CFM shows high reproducibility over multiple power cycles. For a given ΔT, the mirror deformation always gives the same ΔS to within 0.5% uncertainty. (b)The CFM response to ΔT. The linear fits to ΔS result in actuation coefficients of 3.8 and 4.6 mD/K for the 1-inch and 2-inch CFMs respectively.

cling the CFMs . The maximum temperature change was $\sim$55 K, at which ΔS exceeded 200 mD for both 1-inch and 2-inch CFMs. Fig. 6-22(b) shows that the responses of both mirrors were observed to be linear and reproducible. The mirror consistently returned to its initial state when the input was switched off, at which ΔS maintained at ΔS=0.00$\pm$0.01 mD, as shown in Fig. 6-22(a).

The measured and predicted transient response of the CFM spherical power are presented in Fig. 6-23. Fig. 6-23(a) plots the measured spherical power as a function of change in temperature during a heating-cooling cycle, which resembles that

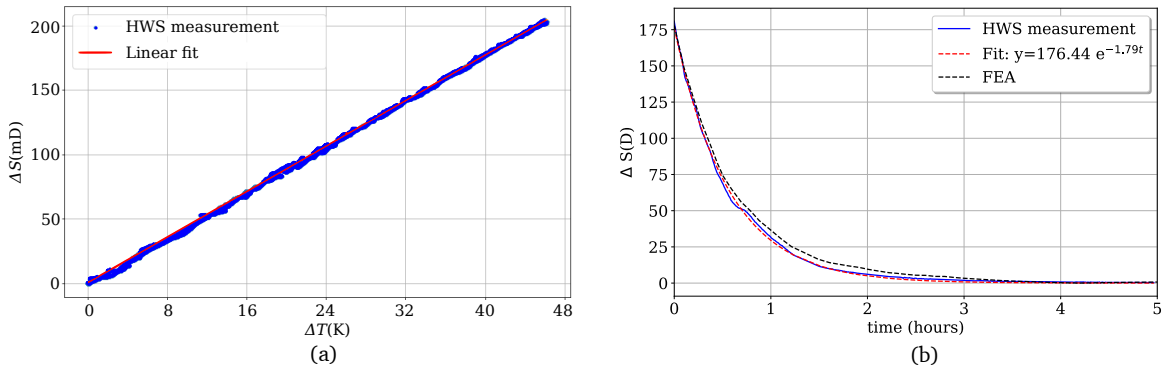

Figure 6-23: (a) A plot of the change in the spherical power ΔS of the 2-inch CFM with change in its temperature as the CFM underwent a power cycle, shown previously in Fig. 6-22(a). (b) The decay of ΔS after the heater power is switched off and plots of the best fit exponential and the FEA prediction.

shown in Fig. 6-22(a). The linear response during the cycle indicates that there is no hysteretic behaviour in the response of the mirror and that the heating and cooling processes are symmetric and can be characterised by a single thermal time constant. An exponential decay function was fitted to the measured ΔS during the cooling process of a 2-inch CFM, as shown in Fig. 6-23. The thermal time constant obtained from the fit is 0.56 hour or 34 minutes, which is comparable to that of the TBM. The thermal time constant predicted by COMSOL is 42 minutes, which is slightly longer and potentially caused by the uncertainties in the materials emissivities and unknowns in the thermal contact at the fused-silica-aluminium interface. The time constant could be decreased by applying a high emissivity coating to the aluminium actuating ring.

6.7 SAMS design considerations

The results discussed in the previous sections demonstrated that the CFM is a potential solution to the problem of SAMS adaptive optics. However, in order to integrate an adaptive optics into a complex and ultra-high-vacuum-compatible suspension system, there are several other design requirements. In particular, since the CFM relies on heating to deform, it is crucial to understand the effect of heating on both the suspension control and it surroundings.

6.7.1 Baseline design for CFM

There are several factors that impact the geometry of the CFM. In this section, I explore the CFM design to come up with a baseline design that satisfy most requirements and provide a baseline model for subsequent modelling.

The main factors under consideration here for the baseline design are:

- Actuation range: minimum 150 mD at maximum T=60$^{\circ}C$.
- Bottom stage mass: minimum 400 g, but aim for 1 kg.
- Stress: maximum 17 MPa in tensile (a safety factor of three has been taken into account)

The degrees of freedom of the CFMs that can be explored to meet these requirements are:

1. *Mirror shape*: the mirrors used in a CFM can be either flat or a plano-concave. Plano-concave mirrors are thinner at the centre and thus allow a greater deformation range but many not have adequate surface quality. Additionally, irregularities at the concave surface might lead to crack growth under high stress.
2. *Mirror thickness (t_m)*:Larger deformations can be achieved using thinner mirrors but the surface quality will not meet LIGO requirement.
3. *Actuating ring thickness (t_r)*: while there is an optimum thickness for a given mirror thickness of the fused-silica, a larger thickness results in a heavier mass, which is desirable for suspension control.
4. *Outer diameter*(OD): The maximum deformation increases with increasing OD.
5. *Offset of actuating ring*: An optimal offset was found for a given CFM geometry. Generally, a reduced offset provides more compression bias, and hence less tensile stress at the front surface, but reduces the actuation range.

Component	Parameters	Value
Fused silica mirror	OD(mm)	50.8
	Density ρ_{SiO_2} (kg/m^3)	2203
	Young's modulus E_{SiO_2}(GPa)	71.2
	Poisson's ratio ν_{SiO_2}	0.15
	Thermal expansion coefficient α_{SiO_2} (K^{-1})	0.55×10^{-6}
Plano-plano	Thickness(mm)	6
Plano-concave	Edge thickness(mm)	12
	Central thickness(mm)	6
	ROC(mm)	52.4
Aluminium ring	OD(mm)	120
	Interference *dr* (μm)	42
	Density ρ_{Al}(kg/m^3)	2700
	Young's modulus E_{Al}(GPa)	69
	Poisson's ratio ν_{Al}	0.33
	Thermal expansion coefficient α_{Al} (K^{-1})	23×10^{-6}
Copper ring	OD(mm)	120
	Interference *dr* (μm)	35
	Density ρ_{Cu}(kg/m^3)	8930
	Young's modulus E_{Cu}(GPa)	110
	Poisson's ratio ν_{Cu}	0.34
	Thermal expansion coefficient α_{Cu} (K^{-1})	17×10^{-6}

Table 6.2: Geometric parameters and material properties used in FEA modelling of CFM's.

6. *Material*: The actuating ring could be made from a material with a greater density, such as copper, to increase the total mass of the bottom stage. However, this reduces the difference in thermal expansion coefficients that the CFM relies on to achieve high actuation range.

Four parameter-sweep studies were performed using the COMSOL FEA model. The four studies corresponded to four permutations of the two choices in the actuating ring materials (aluminium or copper) and the two choices in the fused-silica geometries (flat or plano-concave). The the ring offset and thickness were varied. In all of these studies, we assume that all four permutations of possible CFMs will be assembled at 100°C. The details of parameters in these studies are given in Table 6.2.

From these studies, we compute the CFM spherical power at ambient tempera-

ture, maximum tensile stresses at the front surface and masses. Since the change in the CFM spherical power is directly proportion to change in temperature, an estimation of temperature at which a ΔS= 150 mD can be estimated from the ambient spherical power. This quantity $\Delta T_{\Delta S=100mD}$ is plotted as a contour plot shown in Fig. 6-24. We apply the constraints to this map and determine the feasible region of operation, which is also shown in Fig. 6-24.

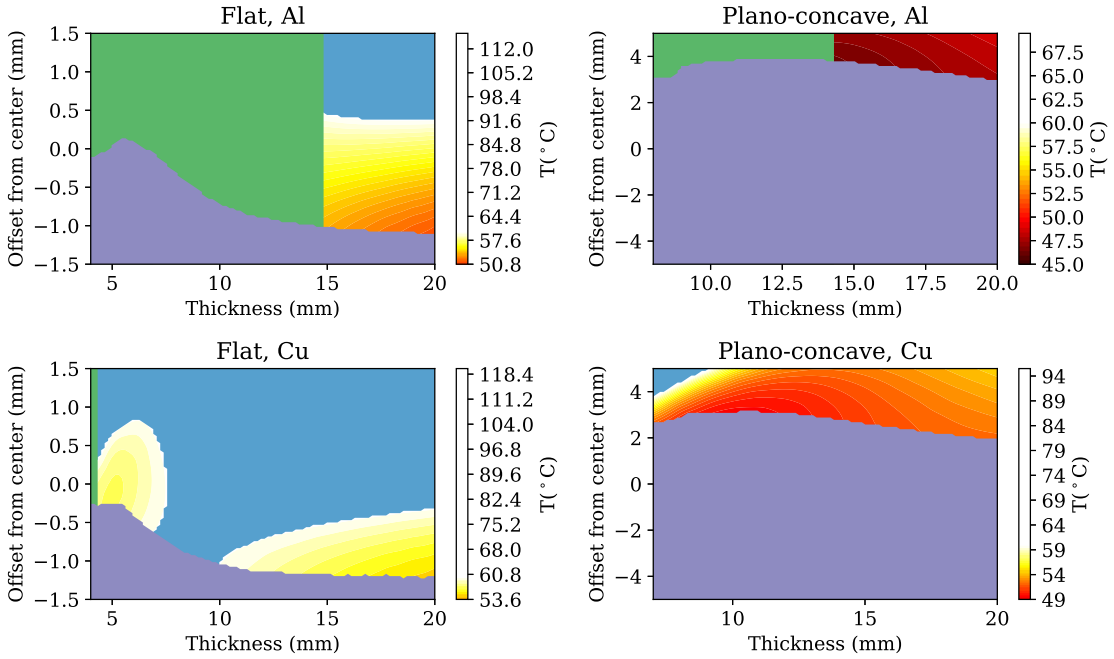

Figure 6-24: The contour map shows the temperature $\Delta T_{\Delta S=150mD}$ at which a change in spherical power of 150 mD is expected. This map is overlaid with three constraints: the minimum mass (green), the maximum allowed stress (purple) and the maximum allowed temperature $\Delta T_{\Delta S=150mD}$ (blue).

The key features observed in Fig. 6-24 are:

- **Mass constraint** ($m \geq 400$ g): High density of copper increases total mass. At 400g, the minimum thickness of aluminium ring required for the flat and plano-concave mirrors are 14.5 mm and 13 mm respectively. At 1kg, flat-mirror aluminium CFM required a 38.8 mm thick ring.

- **Temperature constraint** ($T \leq 60$°C): At 60°C limit, all configurations provide viable option. However, if maximum ΔT was 50°C then only the the plano-

concave mirror with an aluminium actuating ring would be a as the solution

- **Tensile stress constraint** ($\sigma_{\max} < 18$ MPa): The tensile stress increases with actuating ring offset due to the increase in bending moment and a lower compression bias. The plano-concave mirror provides a greater maximum deformation, but also increases the maximum tensile stress.

After a discussion with our LIGO Laboratory collaborators, we selected a flat mirror with a 38.8 mm thick, 120 mm OD aluminium ring as the baseline model for the CFMs, as shown in Fig. 6-25. The plano-concave mirror design offer some advantages but, due to its requirement for a more complex fabrication process, we decide to leave such design for future investigation.

6.7.2 Actuator modeling

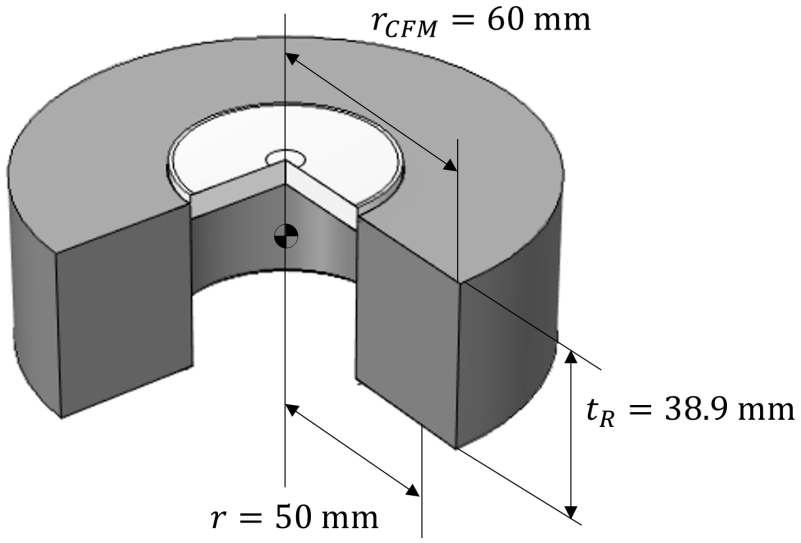

Figure 6-25: Dimensions of the baseline CFM to assist with thermal modeling. The symbol ◓ indicates the position of the CFM center-of-mass.

The CFM relies on the change in temperature. It is therefore important to understand how this heating affects the suspension system and the surroundings. In this section, we summarise the main effects identified. A more detailed discussion and calculation can be found in Appendix G.

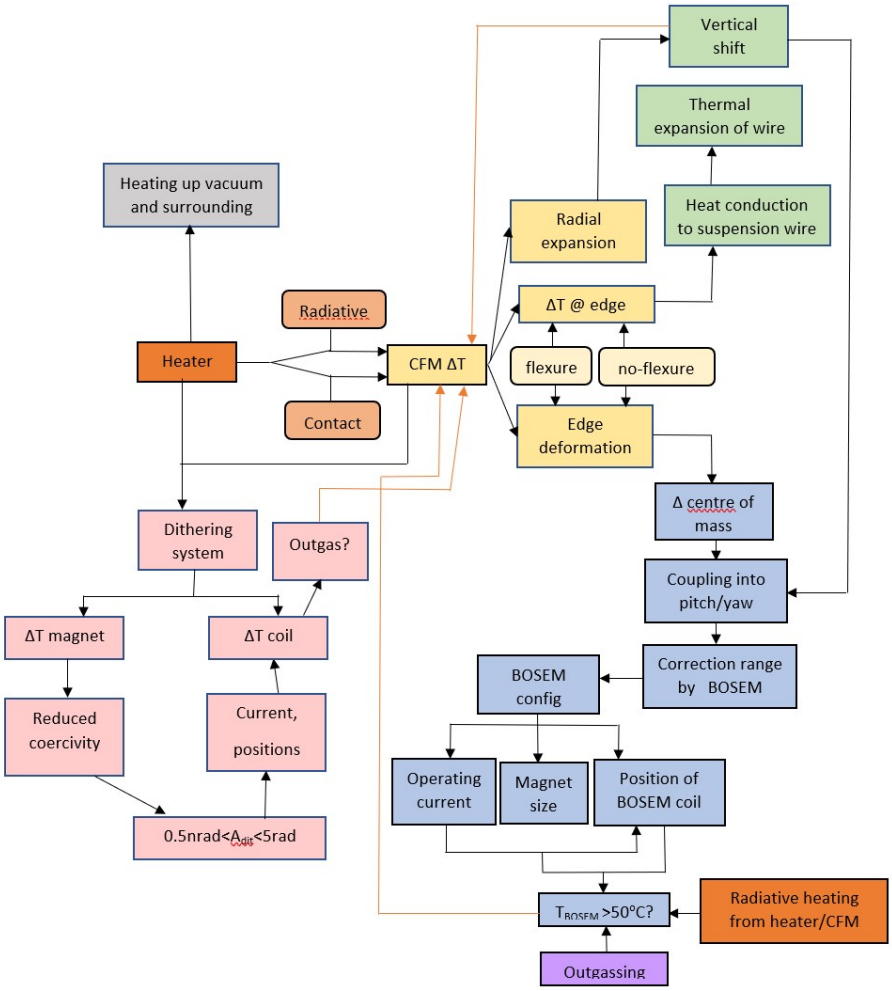

Figure 6-26: A map summarising potential problems caused by the heating of the baseline CFM. The center of the map is the heating of the CFM, which in turn change its deformation and temperature. The coupling into the surroundings are divided into three main groups: the effects on the suspension wires (green), the effects on the tip/tilt angle of the suspended optics which requires correction (blue), the effects on operation of the suspension components at an elevated temperature (pink) and heating of the greater surroundings.

Fig. 6-26 outlines the potential pathways through which the heating of the baseline CFM can affect the surroundings. The effects are summarised below:

1. **Vertical shift of the CFM stage**: Heat will be conducted out to the suspension wires, causing them to expand. The temperature dependence of Young's modulus of steel used for the suspension wires also leads to a lower effective spring constant for the suspension wires. These combined effects cause the CFM to sag by approximately 175μm at a ΔT=40K. The radial thermal expansion of the CFM would shift the CFM upward. This upward shift is however only ≈11 nm. The total vertical shift is therefor 175 μm downwards. Assuming a nominal 1-m ROC mirror in the CFM, this shift would change the pitch of the reflected beam by 350 μrad.

2. **Coupling to tilt due to shift in the CFM centre of mass (COM)**: Deformation of the CFM during heating shifts the COM in the longitudinal direction. This shift in the COM couples strongly to the suspension, resulting in a change in pitch and a change in the location of the front surface of the mirror. The FEA model of the CFM suggests that the COM shift can be described as a linear function of the change in temperature: $\Delta z = 0.71[\mu m/K]\Delta T$. For the baseline suspension system, details of which can be found in Table G.1 in Appendix G, the CFM on the bottom stage will see a pitch change of 1.52 mrad and its front surface will shift longitudinally by 45.6 μm. This effect would therefore be the strongest one caused by the heating of the CFM.

3. **Effect on performance of the dithering coils**: The increase in temperature of the CFM alters the properties of the magnets attached to the CFM-stage for dithering alignment control and reduces the force coupling constant. To maintain the dither amplitude, a greater driving current would be required for the voice-coils, which risks raising the temperature of these voice coil and increasing outgassing. However, calculations show that the this effect is small (see Appendix G for details). Furthermore, the dithering voice coils could be located on another optics, rather than the SAMS mirror.

4. **Heating of the surroundings**: Since an optical layout of SAMS within HAM6 has not been finalised at the time of writing if this thesis, modelling the effect of heating of the surroundings is challenging. However, a simple FEA model indicates that the radiant flux incident on the optical table is small. Only a small temperature increase would be expected ($\approx 1 - 2°C$ change in temperature in the vicinity of SAMS suspension).

The issue of pitch motion coupling due to the shift in the CFM COM is thus probably the most crucial one to address. Furthermore, the 1kg-CFM baseline CFM presented here has a large volume-to-area, which reduces the rate of cooling by radiation and hence will results in a significantly long thermal time constant. It is therefore important to modify the CFM geometry to address these issues. In the next section, a flexure CFM design is proposed to address such issues.

6.8 Flexure compression fit mirror

A 3D-rendered image of the proposed CFM is shown in Fig. 6-27. The full technical drawing of this mirror can be found in Appendix H. The flexure CFM consists of three main parts: the standard CFM configuration at the center with the mirror shrink-fitted into an inner actuating ring, and an outer ring that is connected to the inner ring by thin conical flexures. The thickness of each flexure is 0.5 mm and one edge of each flexure connects directly to front surface of the CFM.

The flexure actuating ring shown in Fig. 6-27 is a potential solution to various problems of the CFM:

- The flexure deformation during heating results in longitudinal shift of the inner ring relative to the outer ring such that it counteracts the effects caused the CFM COM shift described in the previous section.

- Increase the bottom stage mass without adding to much mass onto te actuating ring.

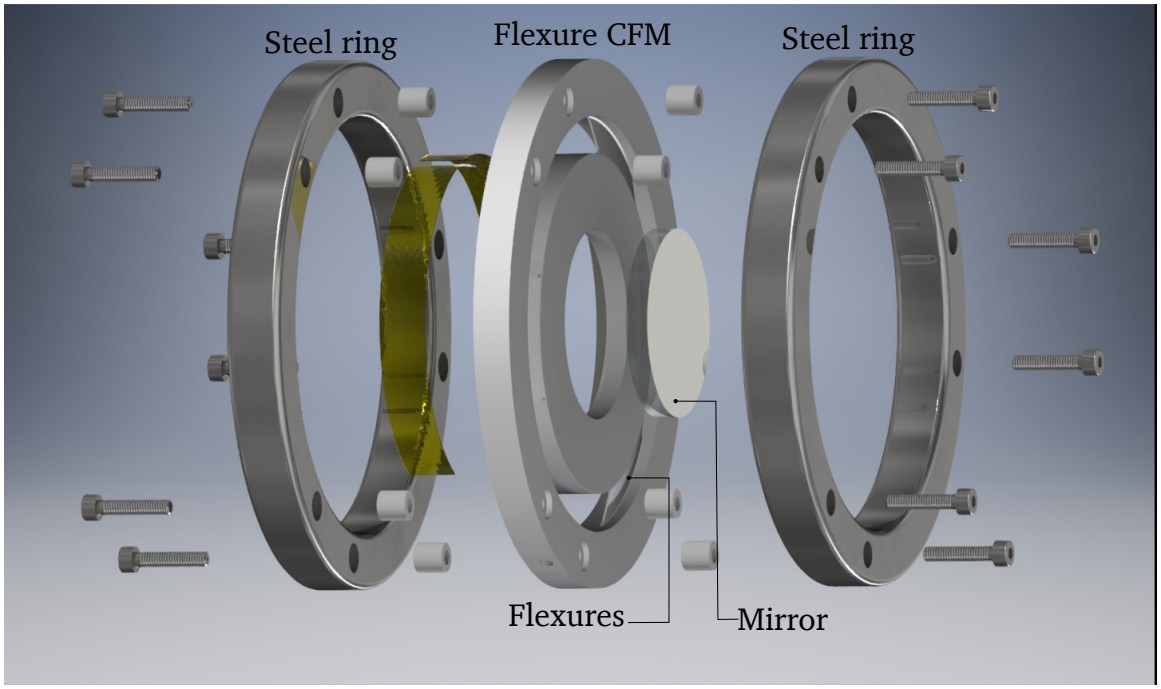

Figure 6-27: 3D rendered image of a proposed flexure compression fit mirror where steel rings can be attached at the edge to increase the overall mass of the bottom stage.

- Increase the thermal resistance for conduction of the heat from the inner ring to the suspension wires, thus reducing the thermal expansion of the wires.

- Allows a quicker and easier integration or removal of a CFM into the SAMS suspension frame as a pair of brackets can now be mounted on the outer ring for interfacing with suspension without risking introduce non-uniform stress that can cause higher-order aberrations.

COMSOL FEA model was used to find the optimum angle for the flexures. The results of the FEA are shown in Fig. 6-28, with the parameters defined on the right image. We defined $z0$ to be the midpoint between the two points of suspension. For the ease of the study, we set z_0 to coincide with the COM z_{CFM} of the CFM when the flexure angle θ is zero, which is the first case in our FEA parametric sweep. Then for each different value of θ , we recompute the CFM COM and find the difference between z_0 and $z_{CFM}(\theta)$ at ambient temperature. This results is in the red curve on the left plot of Fig. 6-28. We then allows the system to heat

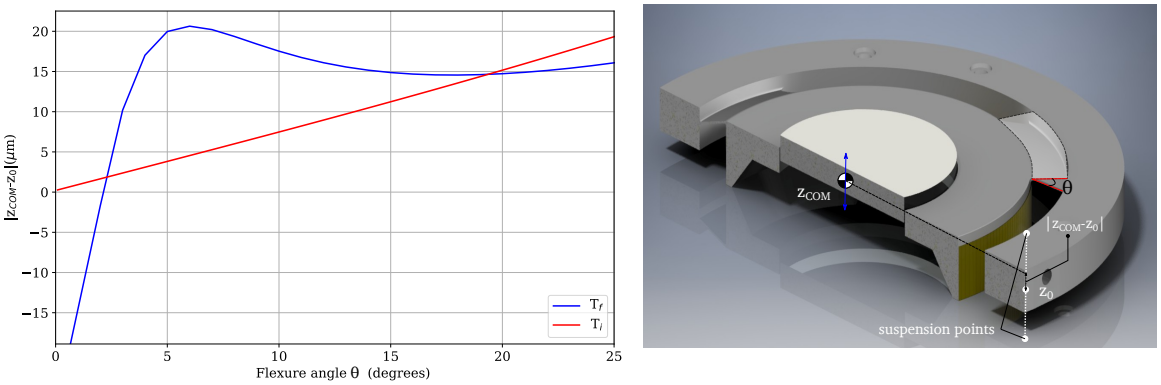

Figure 6-28: Optimisation of the CFM flexure angle θ such that the COM of the structure remains constant relative to suspension points x_0 during heating.

up to 60°C, at which both z_0 and z_{COM} would have changed due to the thermal expansion and bending of structure. These quantities and their difference are re-computed as shown as the blue curve. A design in which the motion of COM does not couple to suspension point will have the same difference between z_{COM} and z_0 at ambient temperature and at elevated temperature, therefore, we select the the θ that corresponds to the intersection of the tow curves on the plot, which is 18.5°. The smaller θ intersection point is not chosen since the shift in COM is more sensitive to error in θ. Due to challenges in fabrication of flexure angle with a precision better than 1°, $\theta = 18°$ was selected instead. The assembly of this flexure CFM is shown in Fig. 6-29.

Initial tests of this design has shown promising results. Fig. 6-30(a) shows the change in the spherical power at the flexure CFFM with the change in its inner ring temperature. The measured actuation coefficient is 4.13 mD/K.

Since a full suspension system had not been available at the point of writing this thesis, we verified the performance of the flexure structure by measuring the mirror deformation under an external stress caused by mounting. The flexure structure is expected to provide isolation of the internal CFM ring such that it can move longitudinally and deform without seeing such external stress. By mounting the standard CFM and the flexure CFM directly onto a half-inch post and compare the two CFMs motion in pitch observed by the HWS, an immediate improvement can be observed in Fig. 6-30(b). Mounting directly on the optical post caused the stan-

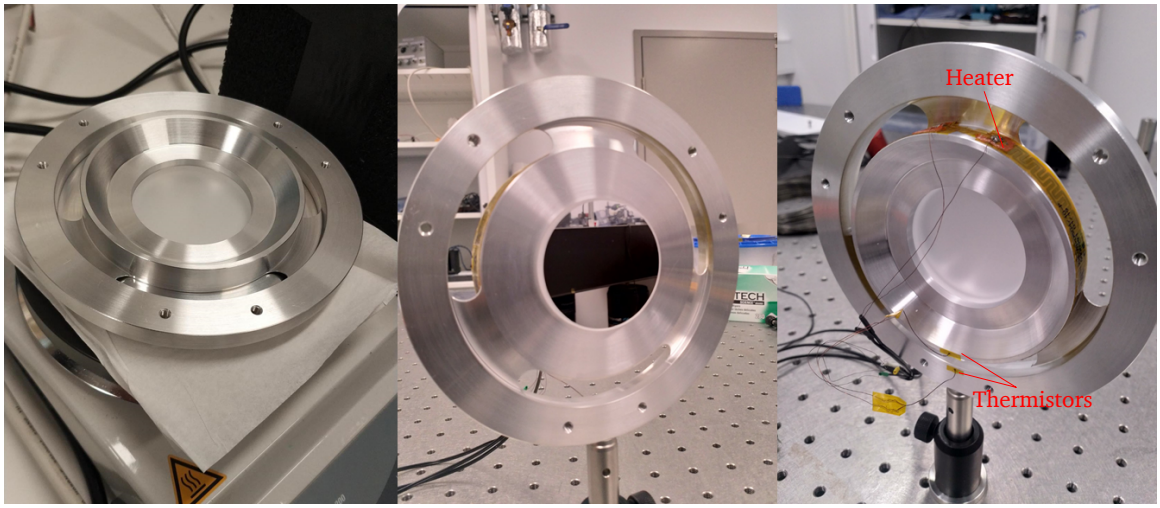

Figure 6-29: *From left to right:* Assembly of the flexure CFM, the front and rear surfaces of the assembled flexure CFM after two Kapton heaters and two thermistors have been integrated into the structure

dard CFM deformation to pivot around the point of contact. This gave rise to a large pitch change of the reflected beam. The flexures instead allows the isolation of the inner ring, which is responsible for the deformation of the mirror while the outer ring deformation pivots about the contact point.

6.9 Thermal noise consideration

The adaptive optics integrated into SAMS must also satisfy thermal noise requirements. Current guideline requires that the thermal noise of SAMS adaptive optics is less than that for motion of the existing tip-tilt stage [186, 74], which is given by the HAM-ISI table motion filtered by a single-stage pedulum suspension [123], and is approximately 2×10^{-12} m/$\sqrt{\text{Hz}}$ at around 10 Hz.

Here we provide an estimate of the CFM Brownian thermal noise using a FEA method. A brief introduction to thermal noise has been presented in Chapter 1.

The method used here is based on a numerical application of the fluctuation-dissipation theorem derived by Callen and Welton [59]. In particular, Levin's [127] direct approach method is used in combination with the numerical dynamic approach by Numata [160] to estimate the internal thermal noise.

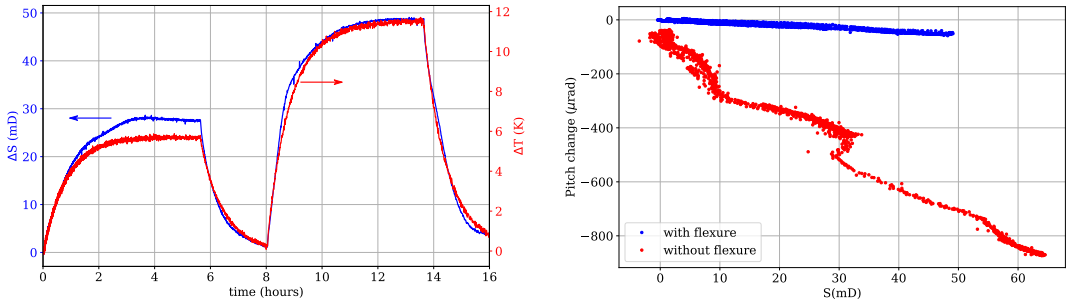

(a) (b)

Figure 6-30: (a): Changes in spherical power and the inner ring temperature of flexure CFM observed by the HWS. (b): Change in pitch of the Hartmann beam reflected off the flexure CFM and the standard CFM as functions of change in spherical power during heating.

The displacement thermal noise power spectral density $S_x(f)$ is given by [59]:

$$S_x(f) = \frac{k_B T}{\pi^2 f^2} |\mathbb{R}[Y(f)]| \tag{6.10}$$

where k_B is the Boltzman's constant and $Y(f) = 1/Z(f)$ is a complex admittance associated with the displacement readout variable $x(t)$, and is the reciprocal of the complex impedance $Z(f)$. Using the fluctuation-dissipation theorem, Levin [127] showed that for a mirror with a Gaussian-distributed, oscillating force of amplitude F_0 which simulates the effect of the incident science beam, this equation can be rewritten it term of F_0 and the average power dissipated W_{diss}:

$$S_x(f) = \frac{2k_B T}{\pi^2 f^2} \frac{W_{\text{diss}}}{F_0^2} \tag{6.11}$$

The homogeneous power dissipation W_{diss} can be calculated with:

$$W_{\text{diss}} = 2\pi f U_{\text{max}} \phi(f) \tag{6.12}$$

where U_{max} is the stored elastic energy of the mirror at its maximum deformation due to the oscillating force and $\phi(f)$ is the loss angle of the material.

The stored elastic energy can be estimated numerically. Consider a force creat-

ing a normal stress σ_x in the normal to the mirror, resulting in a strain of ϵ_x. In the elastic regime, the force and displacement have a linear relationship and the work done by this force is therefore:

$$dU = \frac{1}{2}\sigma_x \epsilon_x dx dy dz \tag{6.13}$$

which can be generalised to include other components of stress:

$$dU = \frac{1}{2}\left(\sigma_x \epsilon_x + \sigma_y \epsilon_y + \sigma_z \epsilon_z + \tau_{xy}\gamma_{xy} + \tau_{xz}\gamma_{xz} + \tau_{yz}\gamma_{yz}\right) \tag{6.14}$$

where σ and τ are normal and shear stresses, ϵ and γ are the normal and shear strains. This quantity is computed at each node in using theFEA and integrated over the entire domain of the CFM to obtain the total stored energy elastic energy, assuming frequency-independent loss angles of 10^{-7} and 10^{-4} radians for the fused-silica and aluminium respectively.

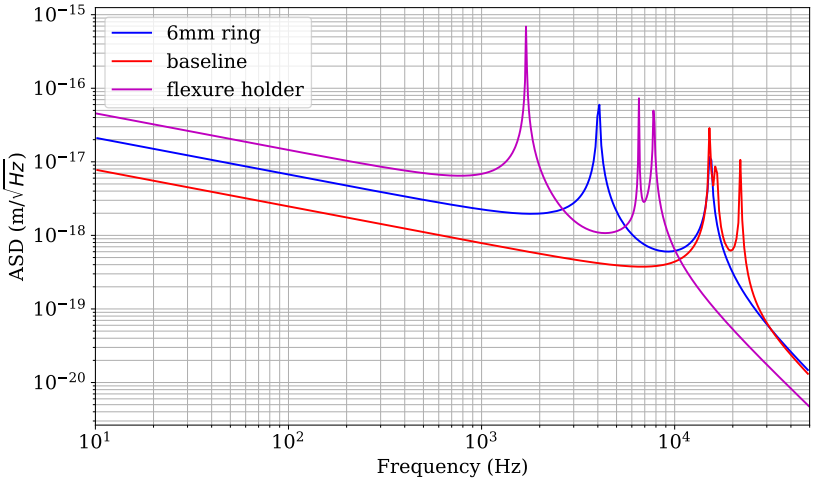

Figure 6-31: Estimated displacement amplitude spectral density due to thermal noise of various compression fit mirror configurations.

Fig. 6-31 shows displacement amplitude spectral density of thermal noise in three different CFM configurations, a baseline 1 kg CFM, the initial 2"-CFM design presented in Section 6.4 and the flexure CFM. As expected, the thermal Brownian

noise of the baseline is the lowest (9×10^{-18} m/$\sqrt{\text{Hz}}$ at 10 Hz) and the first drum-head mode occurs at 15 kHz. The 6mm-thick actuating ring CFM has a slightly higher thermal noise (2×10^{-17} m/$\sqrt{\text{Hz}}$ at 10 Hz). The flexure CFM has the highest thermal Brownian noise (5×10^{-17} m/$\sqrt{\text{Hz}}$ at 10 Hz), and the first drum-head mode in the flexure at 1.8 kHz but its thermal Brownian noise is less than the displacement noise for the current tip-tilt mirror.

6.10 Conclusion

In this chapter, we have described a compression fit mirror, which is another type of thermally-actuated deformable mirrors proposed for SAMS adaptive optics. These mirrors have a linear response to temperature and a large actuation range. The HWS measurements showed that an actuation coefficient up to 5 mD/K could be achieved. The compression-bias design of this mirror allows the CFM to operate at a much greater deformation without risking failure due to stress. It also eliminates the use of epoxy, which was the main cause of failure in the TBM. This also help avoiding the extensive effort and investment to study the use of epoxy in UHV, which could have made the project very costly. Furthermore, there are several geometry parameters of the CFM that can be optimised to cater one's need, whether it is to achieve maximum deformation or to minimise stress.

The flexure design of the CFM leverages from the success of the standard CFM, allowing this adaptive mirror to integrate into the SAMS suspension system better. Further refining of its design, noise characterisation and integration into the suspension system are currently underway to prepare for the first installation by April 2020.

Chapter 7

Conclusion

To improve the sensitivity of the Advanced LIGO detectors, higher circulating laser power and the injection of vacuum-squeezed state of light are necessary. However, high circulating power results in increased absorption-induced optical distortion which degrades the interferometer control and their sensitivity. This effect was evident during commissioning for O3. Furthermore, mode mismatch between various optical interfaces gives rise to loss which limits the benefit of squeezing to 2.2 dB at LHO and 3 dB at LLO . An active wavefront control scheme is thus urgently required. This thesis described new technologies developed and demonstrated in response to these problems: an advanced phase camera and new adaptive optics.

7.1 Phase Camera

The design and demonstration of a new phase camera was detailed in Chapter 3. It allows the capture of high spatial resolution magnitude and phase images of individual optical fields at up to 10 Hz frame rate. This performance is achieved using an all-optical lock-in method in which the RF optical field is demodulated to baseband with a Pockels cell and a polarising beam splitter. It eliminates the use

of any scanning component, which limited the operation of earlier phase cameras during low noise observing due to the risk of backscatter. Using averaging and taking advantage of pixel binning, this phase camera is able to detect a -62dBc sideband signal. The tabletop experiment has thus demonstrated that the phase camera could provide invaluable information about the state of an optical system, which can be used for tuning alignment and mode matching. Ongoing efforts aims to combine these results and the FINESSE simulation to train convolution neural networks to predict misalignment and mismatch in complex optical systems.

7.1.1 Future application of phase cameras

At the time of finalising this thesis, two phase cameras are being assembled at the LIGO Hanford Observatory to investigate the RF-modulation sidebands during the O3 commission break, which will start at the beginning of October 2019. Two different detection schemes will be employed.

The first phase camera will be placed at POP port, where it will look at the individual lower and upper sidebands of the 9 MHz and 45 MHz modulations and at the carrier field. The signals derived from these sidebands are used to control the lengths and alignment of aLIGO. Imaging of the individual sideband will be achieved by a frequency offset of a PSL pickoff to create a reference beam that will be combined with the beam pickoff at POP. The frequency offset is achieved using 2 tunable acousto-optic modulators, which will ensure that the the frequency of the beat note between the reference field and field of interest will always maintain at 25 MHz as required for the operation of the 25 MHz resonant tank in this phase camera. The goal of this test is to observe how the absorption-induced distortion in the test masses, especially that due to point absorbers, affects the RF sideband fields and thus significantly degrades control.

The second phase camera will be placed at the AS port. This phase camera is used in a self-referencing mode to the analyse error signal rather than looking at the individual sideband. There are 4 different resonant tank circuits made for this camera: 9 MHz, 18 MHz, 36 MHz and 45 MHz. The 9 MHz sidebands should not

be coupled to the AS port. However, the differential wavefront distortion due to the point absorbers results in coupling through the AS port and even through the OMC, which causes excess relative intensity noise in the gravitational wave signal readout. Observing this coupling of the 9 MHz field at the AS port will allow us to validate the ongoing simulation efforts, and hence will potentially guide us to the appropriate countermeasures for point absorbers.

A phase camera will be also deployed to Gingin High Optical Power Test Facility to measure and investigate the high-order optical mode excited by the parametric instability in high-circulating-power cavity in a collaboration with the University of Western Australia. Prediction of the parametric instability modes have so far relied entirely on simulations. Observing these modes will help verifying these simulations and advancing our understanding of parametric instability.

Other future plans are in development to broaden the application of phase cameras beyond gravitational wave research. These include depth sensing and photoacoustic and photothermal microscopy.

7.1.2 Camera upgrade

We are also investigating the use of InGaAs phase cameran. The high quantum efficiency of InGaAs will improve the phase camera sensitivity at 1064 nm, therefore enables imaging at very low light condition and increasig the frame rate to hundreds per second.

7.2 SAMS adaptive optics

This thesis also described two new adaptive optics for the suspended adaptive matching stages (SAMS) of gravitational wave detectors: the thermal-bimorph mirror (TBM) and the compression-fit mirror (CFM). Both mirrors have been shown to provide linear response with a large actuation range and small higher order aberration.

The thermal bimorph mirror takes advantage of the differential thermal expansion in a composite structure consisting of a fused-silica mirror and an aluminium plate to generate bending moment that bends the mirror. DA demonstration using a prototype consisting of a 6-mm thick 2" fused-silica mirror and 3-mm thick aluminium plate showed an actuation range as large as 200 mD. The main limitation of this mirror is the peel strength of the bonding epoxy. The use of epoxy would also require extensive testing to determine its vacuum compatibility at an elevated temperature, as well as understanding the effects of various degrees of freedom such as epoxy thickness and curing procedure on the deformation of the mirror.

The compression fit mirror also takes advantage of the difference in thermal expansion coefficients between the fused-silica and the aluminium to generate a change in the mirror curvature. It however relies on the compression stress in a shrink-fit to generate an initial static deformation. This compression stress decreases as the mirror is heated, resulting in a curvature change. The use of the compression stress reduces the tensile stress that occurs in a pure bending structure, thus allows the CFM to operate at a stress level that is well below its tensile yield strength. This design has also freed us from the use of epoxies, thus cutting down the time and cost of the project. The mirror can provide at least 230 mD actuation range and potentially even higher if a higher temperature of operation is allowed. Measurements also shows that the mirror introduces less than 0.4% higher order mode scattering for an incident beam radius as large as 1.3 mm.

7.2.1 Integration into SAMS suspension

At the time of finalising this thesis, the active wavefront control is preparing for a down-selection process to choose the adaptive optics for O4 commissioning and A+ upgrade. This process will decide whether the SAMS mirror will meet LIGO requirements, or if the CO_2 laser actuation needs to be kept as a fall-back option. A CFM prototype will be sent to Caltech for vacuum compatibility testing. Both the fused-silica and aluminium are expected to be compatible. The only component that is currently raising concerns is the Kapton heater. However, LIGO labs

have previously made polyimide-based flexible circuits that are suitable for use in vacuum. The same process could be employed to fabricate heaters for the CFM.

Discussion with MIT is also underway to finalise a design that can be integrated into the SAMS suspension architecture. This design will most likely include the flexural CFM to decouple the CFM center of mass motion from its pitch motion. A steel ring will probably also be added to raise the mass of the bottom stage. Metal parts of the structure will be coated with flame-sprayed ceramic coating to increase the surface emissivity and thus reduce the thermal time constant. Fabrication of a complete suspension stage is expected to finish by April 2020.

7.2.2 Future adaptive mirror upgrade

As the mode matching requirement becomes more stringent with higher level of squeezing, the adaptive optics will need to provide greater control over higher order aberrations. A new design of the CFM that can correct for astigmatism has been modelled and is scheduled for demonstration by early 2020. Furthermore, a new concept of rear reflection CFM has been proposed and is currently under investigation. Such rear reflection will allow the integration of technologies such as infrared heater or Ez:ZBLAN fiber laser to locally correct for very high spatial frequency distortion.

Appendix A

Publications

Publication 1: *A motion-free optical lock-in camera for advanced gravitational wave detectors*, submitted for publication in *Physical Review D*

Publication 2: *A high dynamic-range thermally-actuated bimorph mirror for gravitational wave detectors*, submitted for publication in *Applied Optics*

An optical lock-in camera for advanced gravitational wave interferometers

Huy Tuong Cao, Daniel D. Brown,* Peter Veitch, and David J. Ottaway

Department of Physics and The Institute of Photonics and Advanced Sensing (IPAS), University of Adelaide, SA, 5005, Australia
OzGrav, Australian Research Council Centre of Excellence for Gravitational Wave Discovery
(Dated: August 5, 2019)

Knowledge of the intensity and phase profiles of spectral components in a coherent optical field is critical for a wide range of high-precision optical applications. One of these is interferometric gravitational wave detectors, which rely on such fields for precise control of the experiment. Here we demonstrate a new device, an *optical lock-in camera*, and highlight how they can be used within a gravitational wave interferometer to directly image fields at a higher spatial and temporal resolution than previously possible. This improvement is achieved using a Pockels cell as a fast optical switch which transforms each pixel on a sCMOS array into an optical lock-in amplifier. We demonstrate that the optical lock-in camera can image fields with 2 Mpx resolution at 10 Hz with a sensitivity of -62 dBc when averaged over 2s.

The detection of gravitational waves (GW) [1] has ushered in a new era of gravitational and multi-messenger astronomy. Improving the sensitivity of current and next-generation detectors will ensure that they fulfill their potential to observe this exciting new window on the universe. Reaching these goals however will require a significant reduction in quantum noise which can be achieved by increasing both the circulating optical power stored within the interferometer and the use of squeezed light [2, 3]. To achieve the maximum benefit from these upgrades it is essential that precise control of the optical beams circulating within the interferometer is achieved.

Optical heterodyne techniques, such as Pound-Drever-Hall locking, are used extensively throughout ground-based GW detectors to generate *error signals* with which to control the relative positions and alignments of the suspended optics [4–7]. These systems use radio-frequency (RF) phase-modulation sidebands which are imposed on a carrier field and resonate within the different optical cavities of the interferometer, as shown in Fig. 1. The RF beat-notes which are then demodulated at various photodiode outputs are used to produce the error signals.

Wavefront mismatches from static deformations in the optics or thermal distortions from bulk or small, highly absorbing defects can introduce significant time-dependent offsets in error signal set points. This is due to the sidebands experiencing different resonant conditions within the interferometer and becoming distorted relative to each other resulting in poor spatial overlap. This imbalance leads to a degradation of the error signals and the performance of the control systems. Thus, detailed knowledge of all the carrier and sideband fields is required to fully understand control sensing issues and design adequate solutions for enhancing the detectors further.

Thermal compensation systems (TCS) in LIGO [8] and Virgo [9] aim to reduce the effects of this absorption-induced wavefront distortion in the current generation of detectors. However, these systems use auxiliary probe beams to sense the distortion in core optics. The scanning *phase camera* [10, 11], by contrast, uses the interferometer fields directly to investigate the effect of thermal deformations. They offer a significant potential in helping commission and operate detectors, such as more efficient and optimal tuning of TCS, but have yet to reach their full potential.

The scanning phase camera, developed by Goda et al. [10], measures the transverse intensity and phase distribution of specific RF frequency components within a coherent field. Other common methods for measuring wavefronts—such as Hartmann sensors [12–14], phase retrieval methods [15], spatial wavefront sampling [16], holography [17, 18], and other interferometric techniques [19–21]—measure the superposition of all spectral components in a beam and thus lack any frequency-selectivity. Phase cameras alone enable analysis of each component of the interferometer field.

Phase cameras use the heterodyne beat between the interferometer field and a reference field at a single transverse location, which is recorded using a photodiode and demodulated at the beat frequency of interest. Scanning the field over the photodiode using movable mirrors provides a 2D intensity and phase map. The maximum achievable spatial and temporal resolution is limited by

* daniel.d.brown@adelaide.edu.au

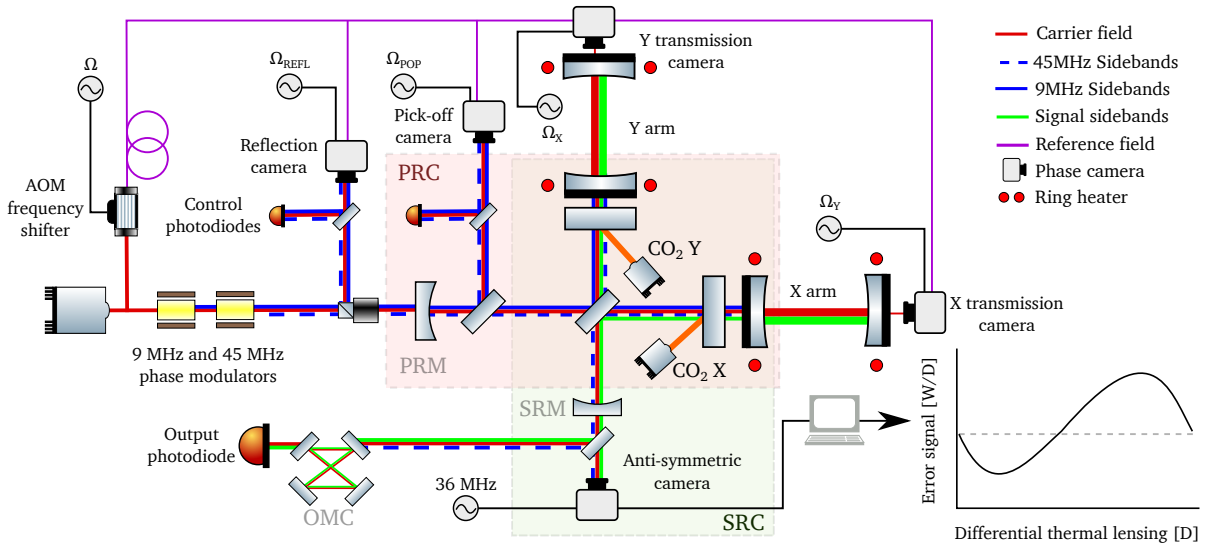

Figure 1. Schematic of a detector similar to LIGO and possible locations for phase cameras. Highlighted are the power recycling (PRC), signal recycling (SRC), output mode cleaner (OMC), the arm cavities (XARM and YARM), the RF modulation sidebands used for control the interferometer, and the cavities in which they resonate. The thermal actuators used to mode-match the interferometer are also shown: ring heaters around each arm-cavity mirror and CO_2 laser beams incident on compensation plates. Five potential locations for phase cameras are shown. Combining the sampled field with a reference field that is offset-locked to the main laser, as shown, and choosing the appropriate switching frequency would allow the amplitude of each field to be mapped.

the mechanical resonances of the scanner and the signal processing. Additionally, the scanning may cause mechanical vibrations and time-varying light scattering, which could be unsuitable for highly sensitive systems such as GW detectors.

In this paper we describe and demonstrate an alternative phase camera approach that has no moving parts. It produces a 2-dimensional map of the intensity and phase of a spectral component within a coherent light field. Its temporal and spatial resolution is determined by the frame rate and pixel size of the camera, thus enabling high resolution and fast capture rates. This is achieved by using a Pockels cell as a fast optical switch which transforms the array of pixels into a parallel array of optical lock-in amplifiers.

We begin with an overview of the operating principle of the optical lock-in phase camera. In Section II we discuss potential applications of the camera in a GW detector. The experimental realization of the phase camera is outlined in Section III. Measured intensity and phase maps are compared with the predictions of a numerical model of the test system. Finally, we demonstrate that the sensitivity is shot-noise limited and can thus be improved simply by averaging.

I. Principle of Operation

To illustrate the operation of the new camera we consider a beam consisting of two components: a reference field $E_r(x,y)\exp[i(\omega_r t + \varphi_r(x,y))]$ and a signal field $E_s(x,y)\exp[i(\omega_s t + \varphi_s(x,y))]$. We wish to determine the spatial distribution of the amplitude and phase of the signal field relative to a reference field, which is phase-locked to and perhaps frequency offset from the input carrier field, as shown in magenta in Fig. 1.

Measuring this composite field using a photodetector would yield a voltage

$$V(x,y) \propto E_r(x,y)^2 + E_s(x,y)^2 + 2E_r(x,y)E_s(x,y)\sin\left(\Omega t + \varphi(x,y)\right) \quad (1)$$

where $\Omega = \omega_r - \omega_s$ and $\varphi(x,y) = \varphi_r(x,y) - \varphi_s(x,y)$. However, the frequency of the heterodyne beat is much larger than the bandwidth of a typical pixelated camera and would not be measurable. Thus, we synchronously amplitude modulate the field incident on each pixel as shown in Fig. 2. In this example, a square-wave amplitude modulation is applied to the beam at a frequency Ω, with a phase $\phi = \varphi$ that yields the largest signal. For in-phase modulation the pixel detector observes intensities that are greater than the unmodulated intensity,

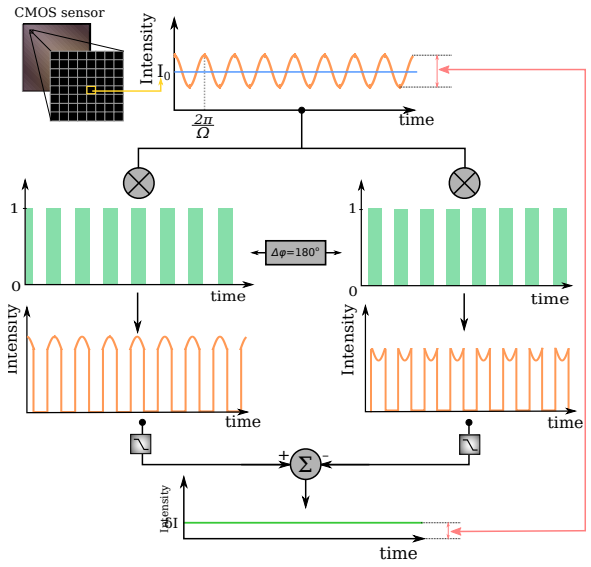

Figure 2. The operation of the new camera can be visualized by considering the beat signal measured by a single pixel. Synchronous intensity modulation of the incident light field at frequency Ω allows the pixel to extract a DC signal that is a function of the magnitude and phase of the beat.

resulting in a DC output $(V_r + V_s)/2 + \delta V$, where the $V_{r/s}$ are due to the $E_{r/s}(x,y)^2$ terms in Eq.1 and δV is due to the RMS average of the $E_r(x,y)E_s(x,y)$ term. Similarly, for the modulation phase $\phi = \varphi + \pi$, the pixel observes intensities that are less than the unmodulated intensity, $(V_r+V_s)/2-\delta V$. Subtraction of these provides $2\delta V \propto E_r(x,y)E_s(x,y)$ [22].

The optimum demodulation phase ϕ is not known a priori. Thus we record four camera images, V_ϕ at $\phi = \{0, \pi/2, \pi, 3\pi/2\}$ for example. Combining these images yields the magnitude and phase of the heterodyne beat:

$$\mathbf{I} \equiv V_0 - V_\pi \tag{2}$$

$$\mathbf{Q} \equiv V_{3\pi/2} - V_{\pi/2} \tag{3}$$

$$|E_r(x,y)E_s(x,y)| \propto \sqrt{(\mathbf{I})^2 + (\mathbf{Q})^2}, \tag{4}$$

$$\varphi = \arctan\left(-\frac{\mathbf{Q}}{\mathbf{I}}\right). \tag{5}$$

where we refer to **I** and **Q** as the "in-phase" and "quadrature" signals. The heterodyne beat has thus been demodulated to baseband by the optical switching, and hence the analogy to a lock-in amplifier.

A schematic of a practical realization is shown in Fig.3. The composite beam is first filtered using a polarizer and then circularly polarized using a quarter-wave plate. It then passes through a Pockels cell (PC) driven with a half-wave voltage that switches the polarization of the beam between s and p linear polarization. The polarizer converts this polarization modulation into an amplitude modulation. Typical camera images and the result of processing using Eq. 4 and 5 are shown in Fig. 3.

The maximum image rate could in principle be doubled by recording both the transmitted and reflected beams simultaneously. In practice it is difficult to overlap the images from both cameras to enable an accurate subtraction. Additional differential effects, such as variation in the responsivity of the sCMOS arrays and aberrations in the polarizing beamsplitter, also reduce the performance in dual camera operation.

II. Optical Lock-in cameras for gravitational wave detectors

The interferometer shown in Fig.1 uses two sets of phase-modulation sidebands at 9 MHz and 45 MHz to control the length and alignment of the interferometer cavities [23]. The reflected RF fields are used to control the positions of the mirrors so that (a) the carrier is resonant in the the power recycling cavity (PRC) and arm cavities, (b) the 9 MHz sidebands are resonant in the PRC, and (c) the 45 MHz sidebands transmit through the PRC and are resonant in the SRC. Ideally, the upper and lower sidebands within each pair have the same spatial distribution and amplitude. However, as discussed earlier, differential wavefront distortion upsets this balance and degrades this ideal resonant condition.

Locations for phase cameras that could be used to investigate the sideband fields are also shown in Fig.1. In the simplest operating mode, a phase camera would analyze the heterodyne beat of the sampled carrier and a sideband field. An independent frequency-offset reference field could be used to diagnose the carrier and sideband fields individually. Imaging these simultaneously would require additional optical lock-in cameras. Alternatively the fields could be imaged sequentially with one camera which has a fixed demodulation frequency and its own frequency shifter. The frequency of the reference can then be changed to pick which RF field is demodulated and imaged.

The balance of the 9 MHz sideband pair and the mode-matching into the PRC can be analyzed using the *Pick-off camera* and *Reflection camera*, respectively. The balance of the 45 MHz sideband pair could be analyzed using the *Anti-symmetric camera*. Additionally, the differential wavefront distortion leads to 9 MHz sideband

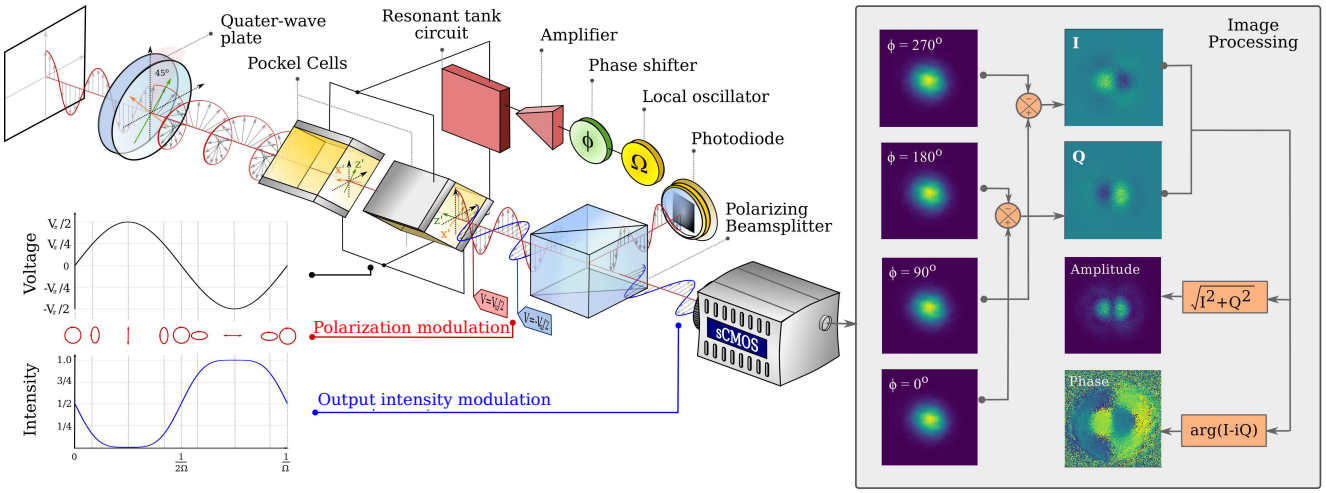

Figure 3. A schematic layout of the new camera. The quarter-wave plate, Pockels cell and polarizing beamsplitter form an optical switch that intensity modulates the beam incident on the sCMOS camera. Spatially-resolved magnitude and phase maps of the heterodyne beat between a reference field and a signal field that is frequency shifted from a reference field is calculated using four camera images acquired with modulation phases separated by $\pi/2$.

fields in the SRC, resulting in a 36 MHz heterodyne beat.

The high spatial resolution and sampling speed of the optical lock-in camera could thus be used to measure the spatial distribution and amplitudes of individual sideband fields. These images can then be used to investigate the effect of differential wavefront distortion on the interferometer control, optimize thermal compensation systems, and investigate the effect of any high-spatial-frequency wavefront distortions.

Lastly, the field circulating within each arm cavity could be analyzed using the *X and Y transmission cameras*. This will enable imaging of unexpected higher-order mode content in the arm cavities. For example, parametric instabilities which produce sidebands at ≈10–100 kHz around the carrier. The optical lock-in camera can image these fields and form part of future active control schemes to identify and suppress such instabilities [24, 25].

III. Test setup

We follow the approach used by Goda et al. [10] to demonstrate the operation and sensitivity of the optical lock-in camera. A schematic of the test system is shown in Fig.4. It consists of two parts: a test field generator that produces a reference and signal field and the lock-in camera itself to image them.

The test field consists of a large amplitude, TEM_{00} mode and a higher-order mode of a high-finesse, ≈ 4000, ring cavity that has a free spectral range of 540 MHz. The TEM_{00} mode is produced by phase-locking a Nd:YAG NPRO to a TEM_{00} mode of the ring cavity using the Pound-Drever-Hall technique [4] and the electro-optic phase modulator EOM1.

Higher-order modes are excited in the cavity by misaligning the incident beam using M1 and M2 and phase-modulating the beam at the cavity offset frequency using EOM2. The odd number of mirrors in the ring cavity breaks the resonance degeneracy between odd- and even-parity optical modes due to the odd-parity modes accumulating an additional π phase shift during each round trip [26, 27]. In our cavity, the TEM_{30} and TEM_{12} Hermite-Gauss modes resonate closest to the TEM_{00} mode, at offset frequencies of 15.7 MHz and 15.3 MHz respectively.

For the test described here, we chose to drive EOM2 at 15.4 MHz as it enabled the excitation of both modes. The beam emitted by the ring cavity therefore consists of a large-amplitude TEM_{00} reference field with frequency ω_r, and a smaller-amplitude TEM_{30} and TEM_{12} signal field oscillating mostly at the 15.4 MHz-shifted frequency, ω_s.

The performance of the camera is affected by the sCMOS properties. A high dynamic range, bit-depth, and linearity are crucial as we must subtract images to remove the offset due to the high power carrier. A high frame rate is also required as four frames are required to produce the intensity and phase images, and to allow averaging of of shot noise, provided it does not result in

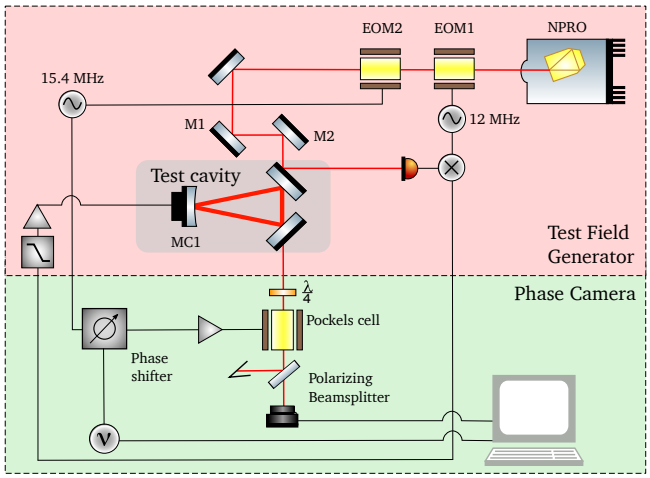

Figure 4. Schematic of the optical system used to demonstrate the camera. The test field generator shown in the red box is used to produce a beam consisting of a reference and signal field.

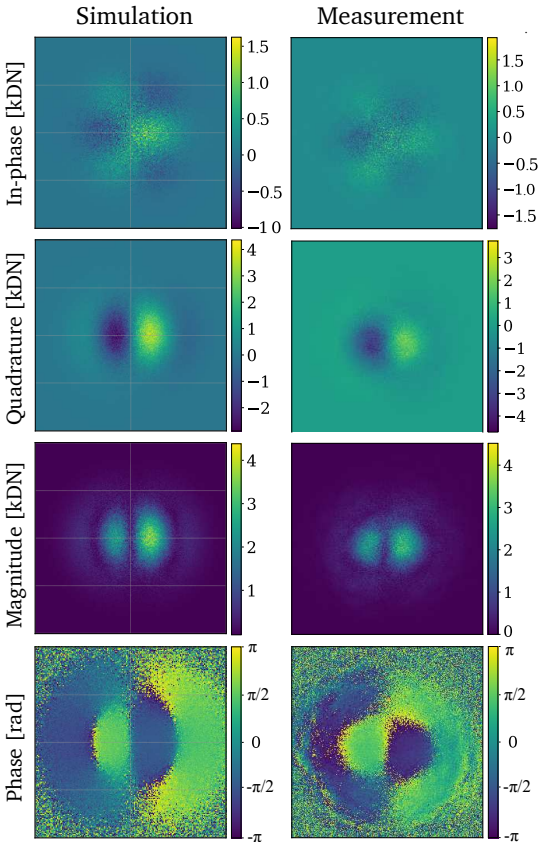

Figure 5. Comparison between camera measurements and the predictions from a FINESSE simulation. The digitized pixel values are given in units of thousands of digital-numbers (kDN) and plotted using the false-color scale bars.

an unacceptable reduction in dynamic range or spatial resolution.

In this work we use a Zyla 4.2 sCMOS camera, which has a sensor size of 2048x2048 pixels, a dynamic range of 89 dB, a 16-bit readout, a maximum frame rate of 100 fps and a quantum efficiency of 5% at 1064 nm. The camera window was anti-reflection coated for the 1064 nm. The rolling-frame shutter for this camera does not affect the measurement process as the demodulation phases for each pixel are still separated by $\pi/2$.

IV. RESULTS

Typical **I** and **Q** images and the result of a numerical simulation of the test-field generator using FINESSE[28] are shown in Fig. 5. In this case, the TEM_{30} mode is apparent in the Q demodulation while the TEM_{12} mode occurs mostly in the I demodulation. Only the two central maxima of the TEM_{30} mode are observed in this demonstration as the amplitude of the TEM_{00} reference field is much smaller at the location of the outer maxima.

The FINESSE simulation used plausible misalignments and included shot noise to reproduce outputs of the optical system. For the simulation shown in Fig.5, the ratio of the power in higher-order mode to that in the TEM_{00} was 14% for the TEM_{30} and 8% for the TEM_{12} modes, and thus the magnitude is dominated by the TEM_{30} mode but the phase shows some influence of the weaker TEM_{12} mode, which degrades the spatial resolution we are able to demonstrate below.

The sensitivity of the optical lock-in camera was investigated by removing the 15.4 MHz modulation from EOM2 and recording frames with the demodulation phase alternating between 0 and π. An image typical of individual V_0 and V_π frames is shown in Fig. 6(a). The magnitude of a typical $V_0 - V_\pi$ image is show in Fig.6(b). The RMS average of the residual values can be decreased by averaging multiple $V_0 - V_\pi$ pairs as shown in Fig.6(c). It is also apparent from Fig.6(c) that the decrease in the RMS is $\propto 1/\sqrt{N_{\mathrm{ave}}}$ where N_{ave} is the number of pairs in the average, thereby showing that the residuals in Fig.6(b) are due to pixel shot noise.

The improvement in sensitivity due to averaging was demonstrated by reinstating the 15.4 MHz modulation of EOM2 and recording twenty frames at each of the four demodulation phases. The magnitude and phase of the beat with $N_{\mathrm{ave}} = 1$ and $N_{\mathrm{ave}} = 20$ are shown in

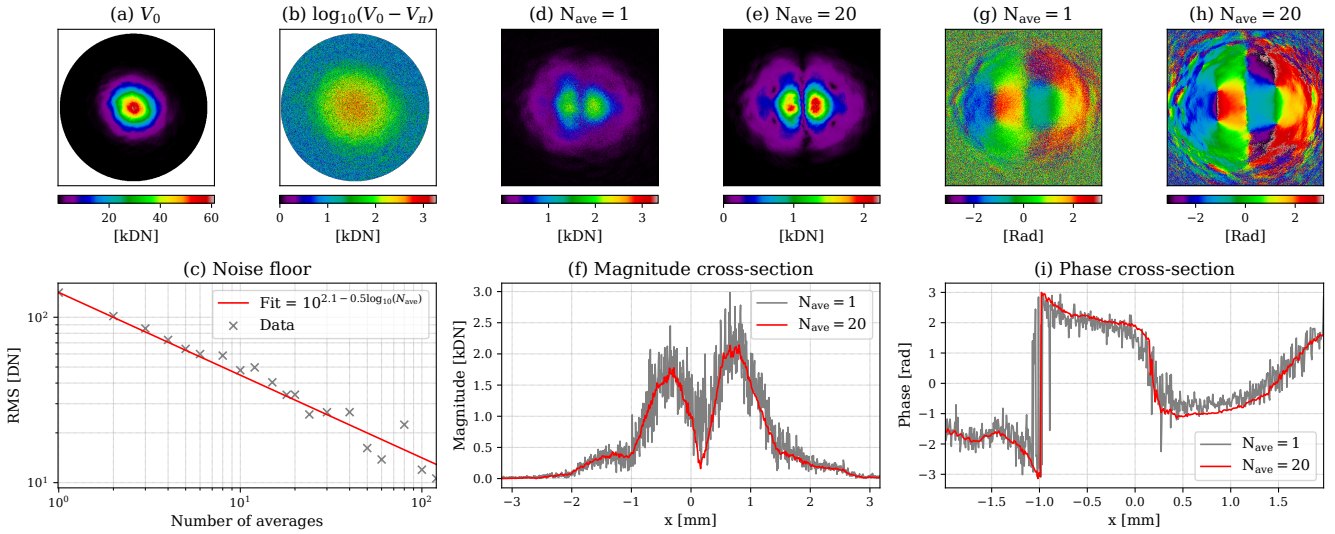

Figure 6. Typical images of (a) V_0 or V_π image, and (b) $\log_{10}(|V_0 - V_\pi|)$ for a single pair of images. (c) Shows how the RMS of $|V_0 - V_\pi|$ decreases with averaging. (d, e) Maps of the magnitude of the heterodyne beat for $N_{ave} = 1$ and $N_{ave} = 20$. (g,h) Maps of the phase of the heterodyne beat for $N_{ave} = 1$ and $N_{ave} = 20$. Images (e) and (h) were taken with 2×2 pixel binning. (f) Plot of the magnitude variation along the center of (d) and (e). (i) Plot of the Phase variation along the center of (f) and (g).

Fig. 6(d) and (e), and (f) and (g) respectively. Averaging over 20 frames improves the signal-to-noise ratio in the maps as seen in Fig. 6(f) and (i). In addition to the averaging, pixel-binning can also be employed for further SNR improvements without sacrificing speed—as was used for the $N_{ave} = 20$ cases above, where 2×2 binning was employed.

The minimum signal power detectable can be estimated from the ratio of the digital number (DN) noise on the central peaks in Fig. 6(g), approximately 0.1 kDN, to the DN of the reference field in Fig. 6(a), approximately 60 kDN: as $2E_sE_r/(E_r)^2 \approx 0.1/60$ and thus $(E_s/E_r)^2 \approx -62$ dB below the power in the reference field, a 12 dB improvement on that reported by Goda et al. [10].

The relatively poor signal-to-noise associated with the outer maxima of the TEM_{30} signal field is due to the small diameter of the TEM_{00} reference field in the test system. It could be improved by using a larger diameter reference field that is frequency-offset locked to the signal field, or by using a liquid crystal attenuator or spatial light modulator [29–31].

To analyze the output of phase cameras it will be important to extract the relative phase of the higher order modes in a beam. Fig.7 shows how the modal content extracted from the in-phase and quadrature images varies with demodulation phase. We can see that the TEM_{12} mode is out-of-phase with the carrier at 85° and the TEM_{30} at 135°—this phase relationship agrees well with that predicted by the FINESSE model.

V. CONCLUSION

In this work we have introduced a new type of phase camera, the optical lock-in camera, and demonstrated its ability to produce high spatial resolution maps of the phase and intensity of a coherent light field. This is achieved with a higher acquisition rate and resolution than previous phase camera implementations. The camera is both more compact and does not rely on any mechanically moving parts, thus reducing scattered light and enabling operation during scientific observations in gravitational wave interferometers.

The phase and intensity of a specific frequency component of a beam is imaged by creating a heterodyne beat with a reference field and synchronously amplitude modulating it. The key element is the Pockels cell which acts as a fast optical switch to provide the amplitude modulation. By switching over the entire field optically, rather than electronically, and imaging with a sCMOS array, each pixel can behave as an optical lock-in amplifier.

The results of our proof-of-principle measurements are in excellent agreement with the predictions of a

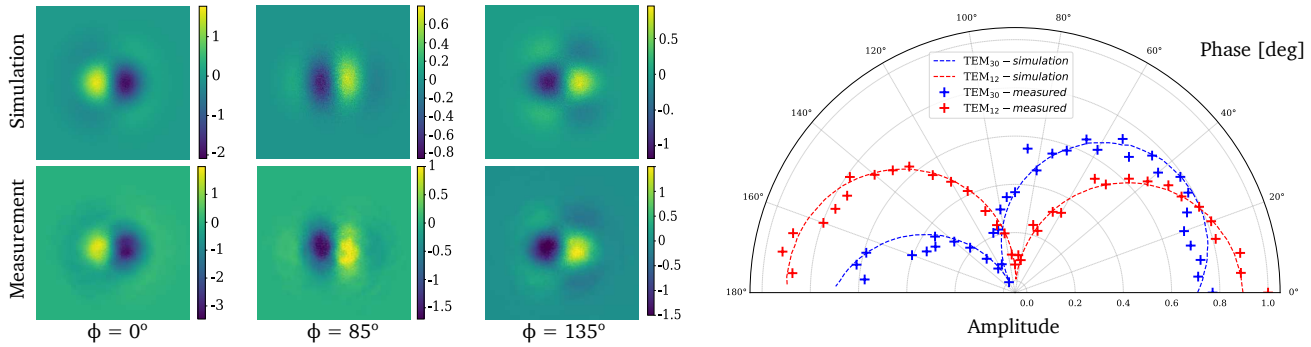

Figure 7. The measured and simulated demodulated signal mode content. $\phi = 0^o, 85^o, 135^o$ are shown on the left with the corresponding simulation showing the individual modes. The data and model have been scale normalized.

theoretical FINESSE model in our test system. We also demonstrate that the sensitivity is limited purely by shot-noise and can be improved by simple averaging, resulting in a noise floor of -62 dBc from data recorded in 2s. The performance can be easily improved by using faster or more sensitive cameras, such as InGaAs arrays which can achieve > 100 Hz frame rates, or by sacrificing spatial resolution for faster acquisition rates on dense sCMOS arrays, by region-of-interest extraction or pixel-binning.

Various applications of this camera in advanced gravitational wave detectors have been highlighted. The additional information provided by them should enable better diagnostics of high spatial frequency effects within an interferometer. This will provide a new tool for improving both their duty-cycle and sensitivity. This will be particularly important for the thermal compensation systems as ever increasing stored optical power is used in current and future generations of detectors. These cameras can also offer the ability to image physical processes such as parametric instabilities, offering a new method to monitor them or to act as a sensor in an active suppression scheme.

This project was funded by the Australian Research Council grants DP150103359 and CE170100004.

[1] B. P. Abbott et al. Gw150914: The advanced ligo detectors in the era of first discoveries. *Phys. Rev. Lett.*, 116:131103, Mar 2016. doi: 10.1103/PhysRevLett.116.131103. URL `https://link.aps.org/doi/10.1103/PhysRevLett.116.131103`.

[2] Patrick Kwee, John Miller, Tomoki Isogai, Lorenzo Barsotti, and Matthew J. Evans. Decoherence and degradation of squeezed states in quantum filter cavities. *Physical Review D*, 90, 09 2014. doi: 10.1103/PhysRevD.90.062006.

[3] Daniel Töyrä, Daniel D. Brown, McKenna Davis, Shicong Song, Alex Wormald, Jan Harms, Haixing Miao, and Andreas Freise. Multi-spatial-mode effects in squeezed-light-enhanced interferometric gravitational wave detectors. *Phys. Rev. D*, 96:022006, Jul 2017. doi: 10.1103/PhysRevD.96.022006. URL `https://link.aps.org/doi/10.1103/PhysRevD.96.022006`.

[4] Eric D. Black. An introduction to pound-drever-hall laser frequency stabilization. *American Journal of Physics*, 69(1):79–87, 2001. doi:10.1119/1.1286663. URL `https://doi.org/10.1119/1.1286663`.

[5] Peter Fritschel, Nergis Mavalvala, David Shoemaker, Daniel Sigg, Michael Zucker, and Gabriela González. Alignment of an interferometric gravitational wave detector. *Appl. Opt.*, 37(28):6734–6747, Oct 1998. doi:10.1364/AO.37.006734. URL `http://ao.osa.org/abstract.cfm?URI=ao-37-28-6734`.

[6] Guido Mueller, Qi ze Shu, Rana Adhikari, D. B. Tanner, David Reitze, Daniel Sigg, Nergis Mavalvala, and Jordan Camp. Determination and optimization of mode matching into optical cavities by heterodyne detection. *Opt. Lett.*, 25(4):266–268, Feb 2000. doi:10.1364/OL.25.000266. URL `http://ol.osa.org/abstract.cfm?URI=ol-25-4-266`.

[7] Kazuhiro Agatsuma, Martin van Beuzekom, Laura van der Schaaf, and Jo van den Brand. Phase camera experiment for advanced virgo. *Nuclear Instruments and Methods in Physics Research Section A: Accelerators, Spectrometers, Detectors and Associated Equipment*, 824:598 – 599, 2016. ISSN 0168-9002. doi:https://doi.org/10.1016/j.nima.2015.09.106. URL `http://www.sciencedirect.com/science/article/pii/S016890021501195X`. Frontier Detectors for Frontier Physics: Proceedings of the 13th Pisa Meeting on Advanced Detectors.

[8] Aidan F. Brooks, Benjamin Abbott, Muzammil A.

Arain, Giacomo Ciani, Ayodele Cole, Greg Grabeel, Eric Gustafson, Chris Guido, Matthew Heintze, Alastair Heptonstall, Mindy Jacobson, Won Kim, Eleanor King, Alexander Lynch, Stephen O'Connor, David Ottaway, Ken Mailand, Guido Mueller, Jesper Munch, Virginio Sannibale, Zhenhua Shao, Michael Smith, Peter Veitch, Thomas Vo, Cheryl Vorvick, and Phil Willems. Overview of advanced ligo adaptive optics. *Appl. Opt.*, 55(29):8256–8265, Oct 2016. doi:10.1364/AO.55.008256. URL http://ao.osa.org/abstract.cfm?URI=ao-55-29-8256.

[9] A Rocchi, E Coccia, V Fafone, V Malvezzi, Y Minenkov, and L Sperandio. Thermal effects and their compensation in advanced virgo. *Journal of Physics: Conference Series*, 363:012016, jun 2012. doi:10.1088/1742-6596/363/1/012016. URL https://doi.org/10.1088%2F1742-6596%2F363%2F1%2F012016.

[10] Keisuke Goda, David Ottaway, Blair Connelly, Rana Adhikari, Nergis Mavalvala, and Andri Gretarsson. Frequency-resolving spatiotemporal wave-front sensor. *Opt. Lett.*, 29(13):1452–1454, Jul 2004. doi:10.1364/OL.29.001452. URL http://ol.osa.org/abstract.cfm?URI=ol-29-13-1452.

[11] Kazuhiro Agatsuma, Laura van der Schaaf, Martin van Beuzekom, David Rabeling, and Jo van den Brand. High-performance phase camera as a frequency selective laser wavefront sensor for gravitational wave detectors. *Opt. Express*, 27(13):18533–18548, Jun 2019. doi:10.1364/OE.27.018533. URL http://www.opticsexpress.org/abstract.cfm?URI=oe-27-13-18533.

[12] Aidan F. Brooks, Thu-Lan Kelly, Peter J. Veitch, and Jesper Munch. Ultra-sensitive wavefront measurement using a hartmann sensor. *Opt. Express*, 15(16):10370–10375, Aug 2007. doi:10.1364/OE.15.010370. URL http://www.opticsexpress.org/abstract.cfm?URI=oe-15-16-10370.

[13] B.C. Platt R.V.Shack. Production and use of a lenticular hartmann screen. *Journal of the Optical Society of America*, 61:656âĂŞ660, 1971.

[14] B. Stocklasa, L. Motka, J. Rehacek, Z. Hradil, and L.L. Sánchez-Soto. Wavefront sensing reveals optical coherence. *Nature Communication*, 5(3275), February 2014. URL https://www.nature.com/articles/ncomms4275.

[15] Peiguang Zhang, Chengliang Yang, Zihao Xu, Zhaoliang Cao, Quanquan Mu, and Li Xuan. High-accuracy wavefront sensing by phase diversity technique with bisymmetric defocuses diversity phase. *Scientific Report*, 7 (15361), November 2017. URL https://www.nature.com/articles/s41598-017-15597-x.

[16] F. Soldevila, V. Durán, P. Clemente, J. Lancis, and E. Tajahuerce. Phase imaging by spatial wavefront sampling. *Optica*, 5(2):164–174, Feb 2018. doi:10.1364/OPTICA.5.000164. URL http://www.osapublishing.org/optica/abstract.cfm?URI=optica-5-2-164.

[17] Christian Schulze, Darryl Naidoo, Daniel Flamm, Oliver A. Schmidt, Andrew Forbes, and Michael Duparré. Wavefront reconstruction by modal decomposition. *Opt. Express*, 20(18):19714–19725, Aug 2012. doi:10.1364/OE.20.019714. URL http://www.opticsexpress.org/abstract.cfm?URI=oe-20-18-19714.

[18] Angela Dudley, Giovanni Milione, Robert R. Alfano, and Andrew Forbes. All-digital wavefront sensing for structured light beams. *Opt. Express*, 22(11):14031–14040, Jun 2014. doi:10.1364/OE.22.014031. URL http://www.opticsexpress.org/abstract.cfm?URI=oe-22-11-14031.

[19] Shay Wolfling, Emmanuel Lanzmann, Moshe Israeli, Nissim Ben-Yosef, and Yoel Arieli. Spatial phase-shift interferometry—a wavefront analysis technique for three-dimensional topometry. *J. Opt. Soc. Am. A*, 22(11):2498–2509, Nov 2005. doi:10.1364/JOSAA.22.002498. URL http://josaa.osa.org/abstract.cfm?URI=josaa-22-11-2498.

[20] Tarquin D. Ralph, Paul A. Altin, David S. Rabeling, David E. McClelland, and Daniel A. Shaddock. Interferometric wavefront sensing with a single diode using spatial light modulation. *Appl. Opt.*, 56(8):2353–2358, Mar 2017. doi:10.1364/AO.56.002353. URL http://ao.osa.org/abstract.cfm?URI=ao-56-8-2353.

[21] Gordon D. Love, Thomas J. D. Oag, and Andrew K. Kirby. Common path interferometric wavefront sensor for extreme adaptive optics. *Opt. Express*, 13(9):3491–3499, May 2005. doi:10.1364/OPEX.13.003491. URL http://www.opticsexpress.org/abstract.cfm?URI=oe-13-9-3491.

[22] See Supplemental Material at [URL will be inserted by publisher] for more detailed derivation of the optical lock-in camera mathematics.

[23] Kiwamu Izumi and Daniel Sigg. Advanced LIGO: length sensing and control in a dual recycled interferometric gravitational wave antenna. *Classical and Quantum Gravity*, 34(1):015001, dec 2016. doi:10.1088/0264-9381/34/1/015001. URL https://doi.org/10.1088%2F0264-9381%2F34%2F1%2F015001.

[24] Chunnong Zhao, Li Ju, Qi Fang, Carl Blair, Jiayi Qin, David Blair, Jerome Degallaix, and Hiroaki Yamamoto. Parametric instability in long optical cavities and suppression by dynamic transverse mode frequency modulation. *Phys. Rev. D*, 91:092001, May 2015. doi:10.1103/PhysRevD.91.092001. URL https://link.aps.org/doi/10.1103/PhysRevD.91.092001.

[25] Y B Ma, J Liu, Y Q Ma, C Zhao, L Ju, D G Blair, and Z H Zhu. Thermal modulation for suppression of parametric instability in advanced gravitational wave detectors. *Classical and Quantum Gravity*, 34(13):135001, jun 2017. doi:10.1088/1361-6382/aa7340. URL https://doi.org/10.1088%2F1361-6382%2Faa7340.

[26] S. J. Waldman. The enhanced LIGO output mode cleaner. Technical report T080144, LIGO Scientific Collaboration, Feb 2009.

[27] K. Arai. On the accumulated round-trip gouy phase for general optical cavity. Technical report T1300189, LIGO Scientific Collaboration, Mar 2013.

[28] Daniel David Brown and Andreas Freise. Finesse, May 2014. URL `http://www.gwoptics.org/finesse`. You can download the binaries and source code at `http://www.gwoptics.org/finesse`.

[29] S.Nayar and V.Branzoi. Adaptive dynamic range imaging: optical control of pixel exposures over space and time. In *Proceedings Ninth IEEE International Conference on Computer Vision*, pages 1168–1175 vol.2, Oct 2003. doi:10.1109/ICCV.2003.1238624.

[30] Yang Zhongdong, Wang Peng, Li Xiaohui, and Sun Changku. 3d laser scanner system using high dynamic range imaging. *Optics and Lasers in Engineering*, 54:31 – 41, 2014. ISSN 0143-8166. doi: https://doi.org/10.1016/j.optlaseng.2013.09.003. URL `http://www.sciencedirect.com/science/article/pii/S0143816613002790`.

[31] Hidetoshi Mannami, Ryusuke Sagawa, Yasuhiro Mukaigawa, Tomio Echigo, and Yasushi Yagi. Adaptive dynamic range camera with reflective liquid crystal. *Journal of Visual Communication and Image Representation*, 18(5):359 – 365, 2007. ISSN 1047-3203. doi:https://doi.org/10.1016/j.jvcir.2007.06.002. URL `http://www.sciencedirect.com/science/article/pii/S1047320307000508`. Special issue on High Dynamic Range Imaging.

A high dynamic-range thermally-actuated bimorph mirror for gravitational wave detectors

HUY TUONG CAO [1,2,*], AIDAN BROOKS[3], SEBASTIAN W.S. NG [1,2], DAVID OTTAWAY [1,2], ANTONIO PERRECA [4,5], JONATHAN W. RICHARDSON [3], ARIA CHADERJIAN [3] AND PETER J. VEITCH [1,2]

[1] *Department of Physics, University of Adelaide, Adelaide, SA 5005, Australia*
[2] *OzGrav, Australian Research Council Centre of Excellence for Gravitational Wave Discovery*
[3] *LIGO Laboratory, California Institute of Technology, Pasadena, CA 91125, USA*
[4] *University of Trento, Department of Physics, I-38123 Povo, Trento, Italy*
[5] *INFN, Trento Institute for Fundamental Physics and Applications, I-38123 Povo, Trento, Italy*
[*] *huy.cao@adelaide.edu.au*

Abstract: Adaptive optics are crucial for overcoming the fabrication limits on mirror curvature in high-precision interferometry. We describe a low-cost thermally-actuated bimorph mirror with 200 mD linear response, which meets dynamic range and low aberration requirements for the A+ upgrade of the Laser Interferometer Gravitational-wave Observatory (LIGO). Its deformation and operation limits were measured and verified against finite element simulation.

1. Introduction

The continuously increasing sensitivity of the Advanced LIGO (aLIGO) gravitational wave (GW) interferometers has allowsed detection of ten binary black hole mergers [1–3] and a binary neutron star coalescence [4] within the span of two years. The detection rate should increase dramatically as the sensitivity of the interferometers improves. One of the key upgrades to aLIGO is the injection of frequency-dependent vacuum-squeezed light into the interferometer output port to reduce the impact of quantum fluctuations [5, 6]. Frequency-dependent squeezing is generated by reflecting the vacuum-squeezed light off a low-loss optical cavity [7]. The sensitivity will be further improved by implementing a balanced homodyne readout to reduce the coupling of length noise and scattering into in the signal recycling cavity [8]. In combination with improvements in the thermal noise of the test mass coatings, these upgrades are predicted to provide a five-fold increase in the detection rate [9] during the upcoming A+ upgrade.

To facilitate the sensitivity enhancement from the squeezed light injection, optical losses must be minimized [6]. Optical fabrication limits result in static mode-mismatch between the optical cavities. Adaptive optics provide a dynamic solution to minimise these losses. However, these optics require a wavefront correction range of 200 mD [10] and low defocus noise in audio band. Their surface quality must also have a surface figure better than $\lambda/10$ with a 10-5 scratch-dig over central 80%, which rules out many existing deformable mirror technologies that achieve large actuation range by minimising mirror thickness, which sacrifices surface figures [11–13]. Additionally, the mirror must be isolated from ambient vibrations via a multi-stage suspension system, thereby preventing the use of electrically complex systems that might compromise the isolation [14, 15]. The outgassing requirements for ultra-high-vacuum prohibit the use of commonly available deformable mirrors [16].

To circumvent these restrictions the adaptive optics used in GW detectors commonly use thermal actuation of the refractive index of optics substrates through which the science beam is transmitted [17–20]. However, the addition of transmissive adaptive optics are often subjected to loss due to absorption or scattering. Therefore, development of new reflective adaptive optics is crucial to miminise optical losses. We present here a low cost, high dynamic range, front surface

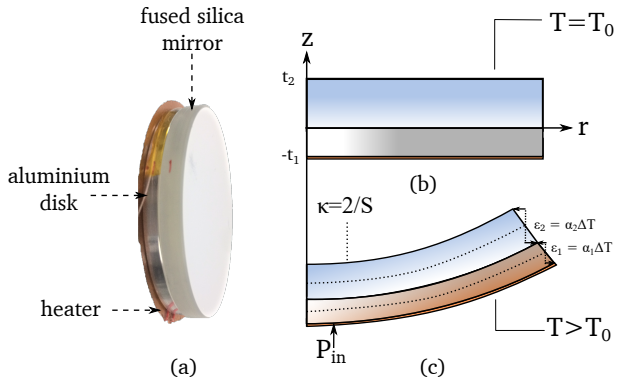

Fig. 1. A schematic of the thermally actuated bimorph mirror. *(a)*: The mirror is a bonded assembly of a fused silica mirror, aluminium disk and resistive film heater. *(b)*: At room temperature T_0, the assembly is unstressed and has a natural radius of r_0. *(c)*: when current is applied to the heater, the assembly temperature rises resulting in differential expansion of the aluminium and fused silica. This results in an increase in curvature of the mirror surface.

deformable mirror that uses only LIGO-vacuum-compatible materials and can be easily adapted to replace existing beam-steering mirrors in GW detectors.

2. Modelling and analysis

The thermally-actuated bimorph mirror consists of a fused-silica front surface mirror, thickness t_1, that is bonded at temperature T_0 to an aluminium-6061 plate, thickness t_2, as shown in Fig.(1). These materials where chosen due to the large difference in thermal expansion coefficients, α_1 and α_2 respectively.

At bonding temperature, the bimorph is in a relaxed state, if we assume that curing of the epoxy bond does not create stress, and the curvature of the mirror is unchanged. Increasing the temperature produces differential expansion, creating a radial shear force and thus concave deformation of the mirror.

Mirror deformation

The extensive work on bi-metallic strips and semiconductor bimorph actuators [21–23] was used to guide the design of the mirror. Assuming that the thickness of epoxy used for the bonding is negligible, the change in radius of curvature R and spherical power S of the mirror due to a change in temperature ΔT is given by [21]:

$$\frac{S}{2} = \frac{1}{R} = \frac{6\Delta\alpha\Delta T(1+m)^2}{(t_1+t_2)\left(3(1+m)^2+(1+mn)\left(m^2+(1/mn)\right)\right)} \tag{1}$$

where $\Delta\alpha = \alpha_1 - \alpha_2$ is the difference between thermal expansion coefficients, $m = t_2/t_1$ is the ratio of the thicknesses, $n = E_2'/E_1'$ is the ratio of the modified Young's modulii $E_i' = E_i/(1-\nu_i)$ and ν_i are the Poisson ratios.

Eq.(1) shows that larger deformations can be achieved with smaller total thicknesses for a given thickness ratio. Given a fused silica mirror thickness, the thickness ratio for the maximum deformation depends solely on the ratio of the modified Young's modulii:

$$\frac{t_2}{t_1} = \left(\sqrt{\frac{1}{n^2}-\frac{1}{n^3}}+\frac{1}{n}\right)^{1/3} + \left(n\sqrt{\frac{1}{n^2}-\frac{1}{n^3}}+\frac{1}{n}\right)^{-1/3} \tag{2}$$

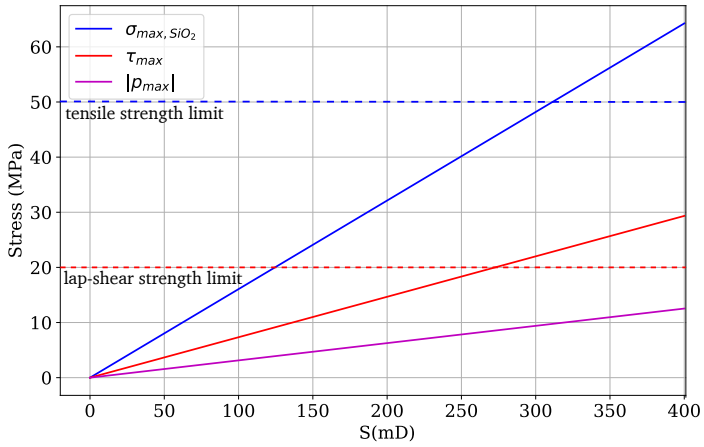

Fig. 2. Maximum tensile stress in fused silica, interfacial shear and peel stress as functions of spherical power as predicted by Eq.(3), (4) and (5) for a standard thermal-bimorph mirror design with 6-mm-thick fused silica and 3-mm-thick aluminium. The dashed lines represent tensile yield strength of fused-silica (blue) and lap-shear strength of the bonding epoxy (red). MasterBond epoxy tensile strength, which limits the maximum allowed peel stress, exceeds 70 MPa and is therefore not included in this plot.

For a fused silica - aluminium bimorph, the maximum distortion is achieved when $m = 1.94$. To achieve high optical quality, a mirror thickness of 6 mm was selected. Maximum deformation is therefore achieved with a 3 mm aluminium plate. Assuming a minimum mirror thickness of 6 mm to ensure adequate optical properties, an aluminium plate thickness of 3 mm is required for maximum deformation. The thermal-bimorph mirror design can also be easily adapted to mirrors that are readily available off-the-shelf.

Stress analysis

The maximum stresses during heating occur at the interface between the two materials: the fused silica surface is in tension, the aluminium surface is in compression and the epoxy will experience lap-shear and peel stresses [21, 22] .

The maximum tensile stress in the fused silica is given by [24]:

$$\sigma_{\max} = \frac{S}{2}\left[\frac{1}{6tt_2}\left(\frac{E_1 t_1^3}{1-\nu_1} + \frac{E_2 t_2^3}{1-\nu_2}\right) + \frac{t_2 E_2}{2(1-\nu_2)}\right] \tag{3}$$

The dependence of $\sigma_{\max}$ on S is plotted in Fig.(2).

The tensile strength of fused silica varies between 50-55 MPa, depending on surface flaws [25–27], whereas its compressive strength exceeds 1100 MPa [26, 27]. Tensile failure of the fused silica would most likely result in structural rupture due to its brittle nature.

Aluminium 6061-T6 has a tensile strength of 310 MPa and a yield strength of 276 MPa. Its minimum compressive yield strength is similar to its tensile yield strength [28]. Compressive failure of the aluminium is therefore not expected to be the limiting factor.

The maximum lap-shear stress $\tau_{\max}$ and peel stress $p_{\max}$ applied to the epoxy are given by [29]:

$$\tau_{\max} = \frac{\Delta\alpha\Delta T}{k\kappa} \tag{4}$$

$$p_{\max} = \frac{\mu}{\kappa}\Delta\alpha\Delta T \tag{5}$$

where the sum of the interfacial compliances κ of the two layer, is given by:

$$\kappa = \frac{2(1+\nu_1)t_1}{3E_1} + \frac{2(1+\nu_2)t_2}{3E_2} \tag{6}$$

Compliance is defined as the inverse of stiffnessSN:and . k and μ are given by:

$$k = \lambda_1 + \lambda_2 + \frac{t^2}{4(D_1+D_2)}, \quad \mu = \frac{t_1 D_1 - t_2 D_2}{2(D_1+D_2)}, \tag{7}$$

where λ_i and D_i are in-plane compliances and flexural rigidities of each layer:

$$\lambda_i = \frac{1-\nu_i^2}{E_i t_i}, \quad D_i = \frac{E_i t_i^3}{12(1-\nu_i^2)}, \tag{8}$$

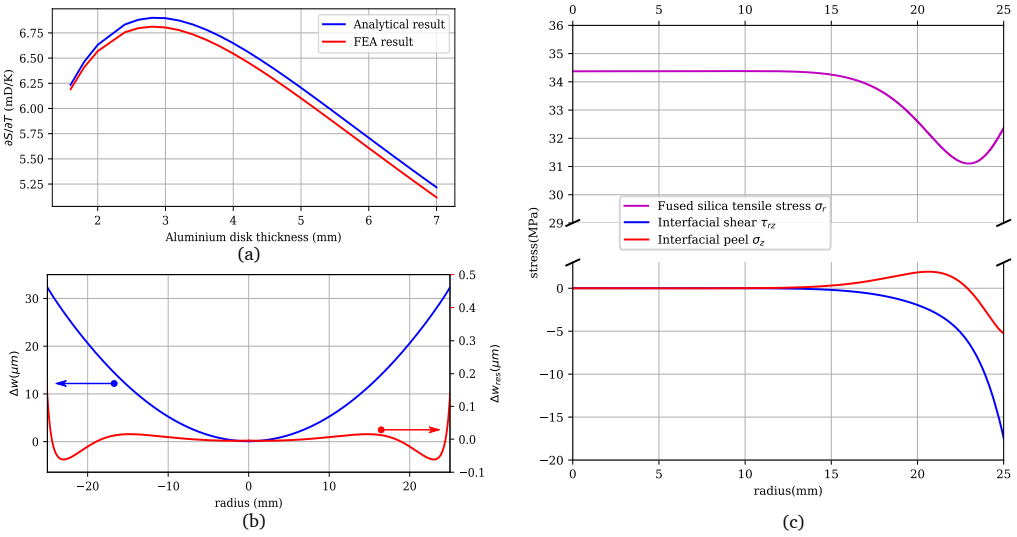

Fig. 3. (a) Actuation coefficient $\partial S/\partial T$ predicted by the FEA model and Eq.(1). (b) Mirror deformation for $P_{\text{in}} = 600$ mW (blue), and deviation from best-fit quadratic (red). (c) Tensile stress in the fused silica, and shear stress and peel stress applied to the epoxy.

Rearrangement of Eq.(1) and substitution into Eq.(4) and (5) yields the maximum interface shear and peel stresses as a function of S, which are plotted in Fig.(2).

The epoxy used in the thermal-bimorph mirror is MasterBond EP30-2, as it is approved for use in the LIGO vacuum at room temperature [30]. It has a lap-shear strength of 20-25 MPa when bonding two aluminium surfaces [31], and the lap-shear strength of the aluminium-aluminium bond sets an upper limit for the lap-shear strength of aluminium-glass bond. The tensile and compressive strengths are 70-75 MPa and 95-100 MPa, respectively. Failure of the epoxy bond would therefore most likely be caused by the interface shear stress exceeding the lap-shear strength, triggering slow delamination of the bond.

Finite element analysis

The analytic expressions for the deformation and stresses were developed for bimetallic strips, for which the length-to-thickness ratio is very large and the thermal conductivity and emissivity of the two materials are similar. To verify the deformation and stress of the thermal-bimorph mirror a finite element analysis (FEA) was conducted.

An axi-symmetric FEA simulation of the bimorph mirror was performed in COMSOL with the structure simply-supported constraint around the circumference of the actuator. The mirror was uniformly heated on its rear surface with an input power P_{in}, and was cooled via radiation to the surroundings at an ambient temperature of 293 K from aluminium and fused silica surfaces with emissivities of 0.06 and 0.93 respectively.

The predicted actuation coefficient, $\partial S/\partial T$, for a 6 mm thick fused silica mirror is plotted as a function of the thickness of the aluminium disc in Fig.(3)(a). While the model confirms that the maximum actuation rate occurs for a aluminium thickness of about 3 mm, the actuation coefficient is 2% smaller than that calculated using Eq.(1). Eq.(1) is derived for a bimetallic structure, whose width-to-thickness ratio is much greater andSN:the thermal conductivity of both materials are comparable. Fused-silica has a low thermal conductivity, which results in a thermal gradient within the substrates that cause causes deviation from the deformation predicted by the analytic expression.

The predicted of the deformation in the optical axis (z component) of the mirror for a heating power of 600 mW is plotted in Fig.(3)(b). The deformation is highly quadratic with $S \simeq 180$ mD. The deviation from the best-fit quadratic is also plotted, showing that most of the deviation occurs outside the mirror's central 80%.

The predicted tensile stress in the fused silica, and the interfacial lap-shear and peel stresses are plotted as a function of radius in Fig.(3)(c), for S=180 mD. The stress in the fused silica is $\simeq$ 75% of the lower limit for its tensile strength. The lap-shear stress is 25% higher than that calculated using Eq.(4) and approaches the epoxy's lap-shear strength. The peel stress is comparable to that calculated using Eq.(5).

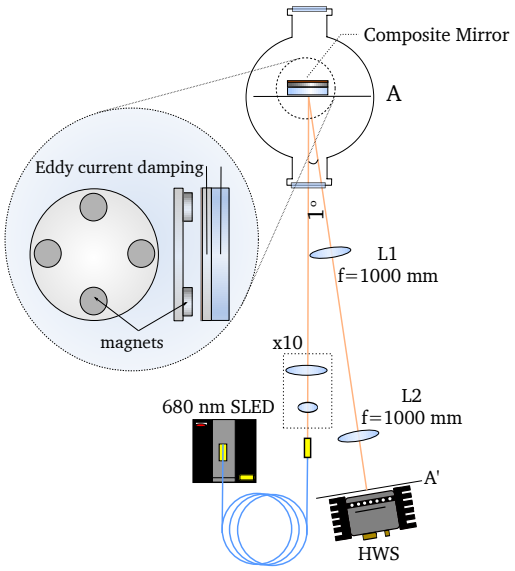

Fig. 4. A schematic of the system used to test the thermal-bimorph mirror. The mirror is isolated from the surroundings by suspending it as a pendulum within a vacuum, and suppressing the motion using eddy-current damping. The 10X telescope projects a large diameter, 680 nm probe beam onto the mirror with an angle-of-incidence of 0.5°. The lenses L1 and L2 image the mirror surface onto the Hartmann wavefront sensor (HWS).

3. Characterisation of the thermal-bimorph mirror

Thermal-bimorph mirrors were produced using 6 mm thick fused-silica mirrors and 2" diameter, 3 mm thick aluminium discs. They were bonded using a thin layer of Master Bond EP30-2 and cured at room temperature for 48 hours as per manufacturer recommendation [31]. A 2" diameter circular, Kapton-encapsulated heater was attached to the rear surface of the aluminium, the temperature of which was measured using a thermistor.

The mirror was suspended by thin wires bonded to its barrel, to allow free expansion and thermal isolation, and placed within a vacuum tank, as shown in Fig.(4). The pendulum oscillations of the suspension were suppressed by eddy-current damping of the aluminium disc from rare-earth magnets located 5 mm from the rear surface.

The response of the thermal-bimorph mirror was measured by projecting the output of a single-mode-fiber-coupled 680 nm super-luminescent diode onto the mirror surface and imaging the wavefront of the reflected beam onto a Hartmann wavefront sensor [32, 33]. This provides a single-shot sensitivity to wavefront change of 1 nm_{RMS} and an accuracy of 0.25 nm [33].

4. Results

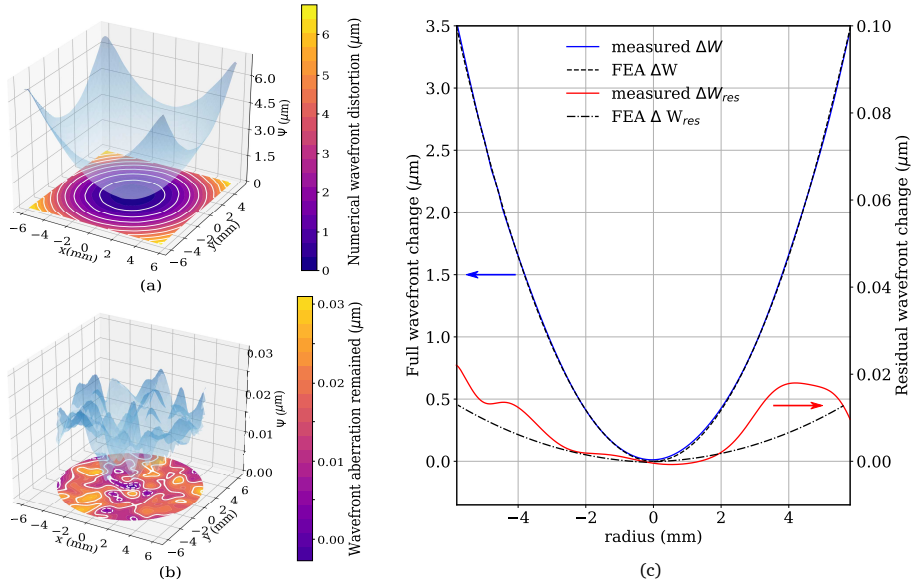

Fig. 5. (a) Measured wavefront change for ΔT = 26 K. (b) Residual wavefront change after removal of spherical power. (c) Cross-section of measured and FEA-predicted total and residual wavefront change.SN:There is no "c"

4.1. Steady-state response

The observed wavefront change is in good agreement with predictions. Fig.(5) shows that the wavefront change is largely quadratic with S = 195.8 mD for 0.69 W of electrical heating, for which ΔT = 26 K. The reproducibility of the wavefront change was checked by continually cycling the mirror over a three week period: yielding a maximum variation of 0.1 mD when S = 200 mD. The actuation coefficient of the thermal-bimorph mirror is 6.77 mD/K, as shown in Fig.(6)(a).

Removing the quadratic component of the wavefront change yields the residual error shown in Fig.(5)(b), which would scatter light from an incident Gaussian beam. This map is obtained

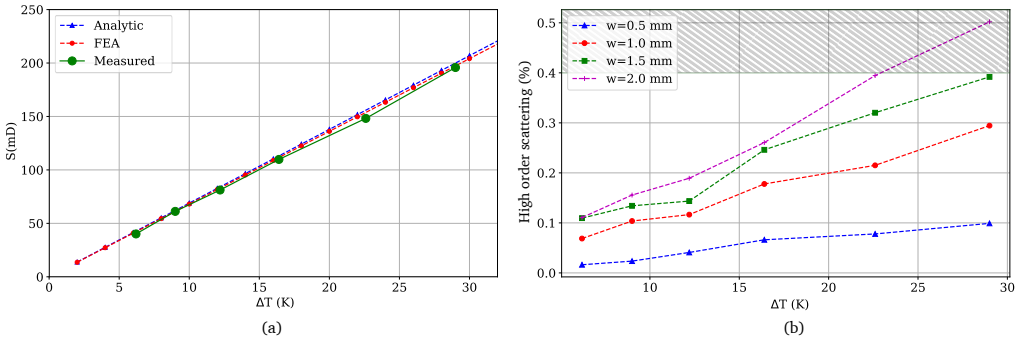

Fig. 6. (a) Measured spherical power from Hartmann sensor (green) shows good agreement with analytic and FEA predictions, (b) Estimated higher order scattering from residual wavefront as a function of change in temperature for various Gaussian beam radii. The shaded region indicates the maximum scattering allowed.

from averaging 100 Hartmann frames during thermal equilibrium. The observed peak-to-valley amplitude of the error was observed to reduce from 100 μm at a single frame capture to 25 μm, suggesting that the error is largely random and thus probably associated with the measurement process. Nevertheless, the fractional energy scattered out of a Gaussian beam by the observed error was calculated using overlap integrals and is plotted for various beam radii in Fig.(6)(b). Due to spatial-dependence of the residual aberration, science beam of different radii incident on the mirror will see different degree of high-order mode scattering. The result indicates that an actuation range up to 200 mD can be accommodated for a beam radius up to 2 mm with scatter less than 0.4% as required [34].

4.2. Transient response

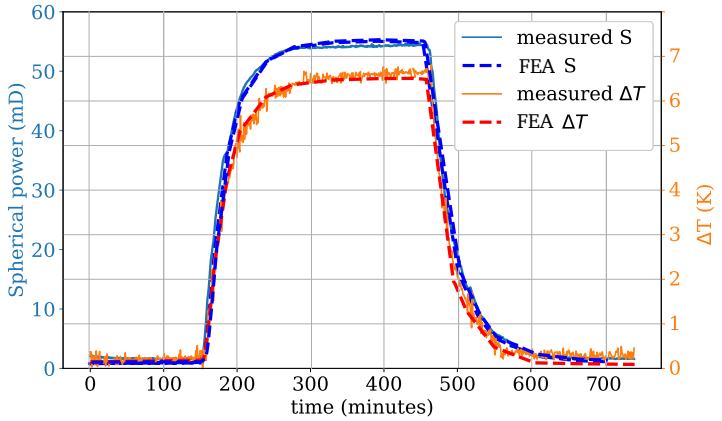

Fig. 7. Step response of thermal-bimorph mirror's temperature and spherical power with a step input of 0.17 W, compared to time-dependent FEA simulations

The observed transient response of the thermal-bimorph mirror and the FEA prediction are plotted in Fig.(7). Spherical power changes linearly with measured temperature. There is no apparent hysteresis occuring in a heating-cooling cycle. The thermal time constant of the mirror is 35 minutes, which could be reduced by coating the aluminium with a high-emissivity oxide. Furthermore, mirrors used in current thermal bimorph mirrors are aluminium-coated.

Highly-reflective dielectric coatings at 1064 nm are often used for LIGO's auxiliary optics. Their difference in emissivity will also changeSN:effect the thermal time constant of the mirror.

4.3. Actuation limit

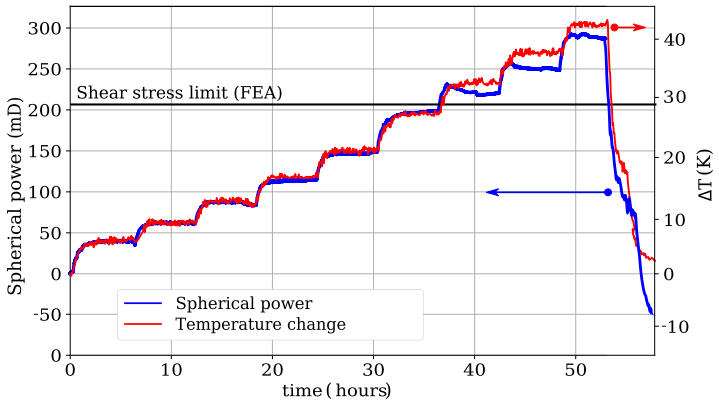

Fig. 8. Response of the thermal-bimorph mirror to step-change increases in the heating power. The horizontal line shows the FEA prediction of the temperature increase and resulting S for which the interfacial shear stress is equal to 25 MPa, the upper limit of the EP30-2 lap-shear strength

The actuation limit was investigated by increasing the equilibrium temperature of the mirror via a series of step changes in heating power over about 2 days. The resulting temperature and spherical power are compared to the lap-shear strength of the epoxy in Fig.(8). After exceeding the lap-shear strength limit of the epoxy, a drop in spherical power was observed. The curvature of the mirror also did not return to its original value when the heating power was removed. We believe this failure is due to incremental delamination of the epoxy bond as the fused silica was not ruptured.

5. Conclusion

We have described a thermally-actuated bimorph deformable mirror suitable for active wavefront control in gravitational wave detectors. These mirrors are low-cost and have simple assembly from readily available components. Our approach enables the use of mirror substrates with a thickness sufficient to enable a good surface figure. Using a 2" diameter, 6mm thick, fused silica mirror, We demonstrated 200 mD of spherical power actuation with a linear actuation coefficient and very low higher-order aberrations that meet the requirements for A+ upgrade of the advanced gravitational wave detectors.

The thermal-bimorph mirror is thus a candidate for reducing optical losses due to mode mismatch and improving the coupling of vacuum-squeezed light into the interferometer, both of which will increase its sensitivity and increase the detection rate. Such performance means that these mirrors will also be useful for applications that require active mode control and low scatter, such as wavefront compensation in high power lasers.

Funding

Australian Research Council CE170100004. National Science Foundation PHY-0757058.

Acknowledgement

This research was conducted jointly with the support of the Australian Research Council Centre of Excellence for Gravitational Wave Discovery and the National Science Foundation under the LIGO cooperative agreement.

References

1. B. P. Abbott and others., "Observation of gravitational waves from a binary black hole merger," Phys. Rev. Lett. **116**, 061102 (2016).
2. B. P. Abbott *et al.*, "Gw151226: Observation of gravitational waves from a 22-solar-mass binary black hole coalescence," Phys. Rev. Lett. **116**, 241103 (2016).
3. B. P. Abbott *et al.*, "Gw170104: Observation of a 50-solar-mass binary black hole coalescence at redshift 0.2," Phys. Rev. Lett. **118**, 221101 (2017).
4. B. P. Abbott *et al.*, "Multi-messenger observations of a binary neutron star merger," The Astrophys. J. **848**, L12 (2017).
5. L. Barsotti, J. Harms, and R. Schnabel, "Squeezed vacuum states of light for gravitational wave detectors," Reports on Prog. Phys. **82**, 016905 (2018).
6. E. Oelker, L. Barsotti, S. Dwyer, D. Sigg, and N. Mavalvala, "Squeezed light for advanced gravitational wave detectors and beyond," Opt. Express **22**, 21106–21121 (2014).
7. P. Kwee, J. Miller, T. Isogai, L. Barsotti, and M. Evans, "Decoherence and degradation of squeezed states in quantum filter cavities," Phys. Rev. D **90**, 062006 (2014).
8. P. Fritschel, M. Evans, and V. Frolov, "Balanced homodyne readout for quantum limited gravitational wave detectors," Opt. Express **22**, 4224–4234 (2014).
9. E. Oelker, T. Isogai, J. Miller, M. Tse, L. Barsotti, N. Mavalvala, and M. Evans, "Audio-Band Frequency-Dependent Squeezing for Gravitational-Wave Detectors," Phys. Rev. Lett. **116**, 041102 (2016).
10. L. McCuller, "Beam Layout Requirements Imposed by Wavefront Actuators," Tech. Rep. T1900144, LIGO Scientific Collaboration (2019).
11. D. Alaluf, R. Bastaits, K. Wang, M. Horodinca, G. Martic, B. Mokrani, and A. Preumont, "Unimorph mirror for adaptive optics in space telescopes," Appl. Opt. **57**, 3629–3638 (2018).
12. R. Cousty, T. Antonini, M. Aubry, H. T. Krol, and A. Moreau, "Monomorph deformable mirrors: from ground-based facilities to space telescopes," in *Proc. SPIE 10562,* vol. 10562 (2017).
13. S. G. Alcock, J. P. Sutter, K. J. Sawhney, D. R. Hall, K. McAuley, and T. Sorensen, "Bimorph mirrors: The good, the bad, and the ugly," Nucl. Instruments Methods Phys. Res. Sect. A: Accel. Spectrometers, Detect. Assoc. Equip. **710**, 87 – 92 (2013). The 4th international workshop on Metrology for X-ray Optics, Mirror Design, and Fabrication.
14. K. L. Wlodarczyk, E. Bryce, N. Schwartz, M. Strachan, D. Hutson, R. R. J. Maier, D. Atkinson, S. Beard, T. Baillie, P. Parr-Burman, K. Kirk, and D. P. Hand, "Scalable stacked array piezoelectric deformable mirror for astronomy and laser processing applications," Rev. Sci. Instruments **85**, 024502 (2014).
15. J.-C. Sinquin, J.-M. LurÃğon, and C. Guillemard, "Deformable mirror technologies for astronomy at cilas," in *Proc. SPIE 7015,* vol. 7015 (2008).
16. T. G. Bifano, J. A. Perreault, P. A. Bierden, and C. E. Dimas, "Micromachined deformable mirrors for adaptive optics," in *Proc. SPIE 2002,* vol. 4825 (2002).
17. P. W. and, "Thermal compensation in the ligo gravitational-wave interferometers," in *Frontiers in Optics 2009/Laser Science XXV/Fall 2009 OSA Optics & Photonics Technical Digest,* (Optical Society of America, 2009), p. AOThA5.
18. A. F. Brooks, B. Abbott, M. A. Arain, G. Ciani, A. Cole, G. Grabeel, E. Gustafson, C. Guido, M. Heintze, A. Heptonstall, M. Jacobson, W. Kim, E. King, A. Lynch, S. O'Connor, D. Ottaway, K. Mailand, G. Mueller, J. Munch, V. Sannibale, Z. Shao, M. Smith, P. Veitch, T. Vo, C. Vorvick, and P. Willems, "Overview of advanced ligo adaptive optics," Appl. Opt. **55**, 8256–8265 (2016).
19. R. Lawrence, M. Zucker, P. Fritschel, P. Marfuta, and D. Shoemaker, "Adaptive thermal compensation of test masses in advanced LIGO," Class. Quantum Gravity **19**, 1803–1812 (2002).
20. M. Kasprzack, B. Canuel, F. Cavalier, R. Day, E. Genin, J. Marque, D. Sentenac, and G. Vajente, "Performance of a thermally deformable mirror for correction of low-order aberrations in laser beams," Appl. Opt. **52**, 2909–2916 (2013).
21. S. Timoshenko, "Analysis of bi-metal thermostats," J. Opt. Soc. Am. **11**, 233–255 (1925).
22. E. Suhir, "Interfacial stresses in bimetal thermostats," J. Appl. Mech. **56**, 595 (1989).
23. W. Benecke and W. Riethmuller, "Applications of silicon microactuators based on bimorph structures," in *IEEE Micro Electro Mechanical Systems, , Proceedings, 'An Investigation of Micro Structures, Sensors, Actuators, Machines and Robots',* (1989), pp. 116–120.
24. S. Timoshenko and S. Woinowsky-Krieger, *Theory of Plates and Shells* (McGraw-Hill, New York, USA, 1959).
25. "Momentive mechanical properties of fused quartz glass," https://www.momentive.com/en-US/categories/quartz/mechanical-properties/#. Accessed: 2019-01-30.
26. Corning Specialty Materials Division, *Corning HPFSÂő 7979, 7980, 8655 Fused Silica* (2014).
27. Tosoh USA Inc., *Fused silica glass* (2013).

28. A. I. H. Committee, *ASM Handbook Volume 2: Properties and Selection: Nonferrous Alloys and Special Purpose Materials* (ASM International, 1990), chap. Properties of Wrought Aluminum and Aluminum Alloys, pp. 62–122.
29. E. Suhir, "Stresses in Bi-Metal Thermostats," Transactions ASME **53** (1986).
30. D. Coyne, "LIGO Vacuum Compatible Materials List," (2014).
31. Master Bond, *Master Bond EP30-2 Technical Data Sheet*.
32. T.-L. Kelly, P. J. Veitch, A. F. Brooks, and J. Munch, "Accurate and precise optical testing with a differential hartmann wavefront sensor," Appl. Opt. **46**, 861–866 (2007).
33. A. F. Brooks, T.-L. Kelly, P. J. Veitch, and J. Munch, "Ultra-sensitive wavefront measurement using a hartmann sensor," Opt. Express **15**, 10370–10375 (2007).
34. A. F. Brooks, "Design Requirement Document of the A+ Active Wavefront Control Sensors and Actuators," Tech. Rep. E1800480-v1, LIGO Scientific Collaboration (2018).

Appendix B

Principle of phase camera

Consider a linearly polarised light field of interest that consists of a strong carrier field with real amplitude of A_0 at frequency ω_0 and a weak radio-frequency sideband A_{m1} at separated in frequency domain by Ω_{m1} from the carrier.Assuming that this field is s-linearly polarised. This overall field of interest can be expressed as the following:

$$\begin{aligned}\overrightarrow{E}(x,y,t) &= A_0(x,y)e^{i(\omega_0 t+\phi_0(x,y))}\hat{\mathbf{y}} + A_{\mathrm{m1}}(x,y)e^{i(\omega_0+\Omega_{\mathrm{m1}})t+\phi_{\mathrm{m1}}(x,y)}\hat{\mathbf{y}} \\ &= e^{i\omega_0 t}\left[\tilde{A}_0(x,y) + \tilde{A}_{\mathrm{m1}}(x,y)e^{i\Omega_{\mathrm{m1}}t}\right]\hat{\mathbf{y}} \end{aligned} \tag{B.1}$$

where $\tilde{A}$ represents the complex amplitude that contains both information about amplitude $A(x,y)$ and phase $\phi(x,y)$. The intensity of this light field is therefore given by:

$$I(x,y,t) = \left|\tilde{A}_0(x,y)\right|^2 + \left|\tilde{A}_{\mathrm{m1}}(x,y)\right|^2 + 2A_0(x,y)A_{\mathrm{m1}}(x,y)\cos\left(\Omega_{\mathrm{m1}}t - \Delta\phi(x,y)\right) \tag{B.2}$$

where $\Delta\phi(x,y) = \phi_{\mathrm{c}}(x,y) - \phi_{\mathrm{m1}}(x,y)$ is the phase difference between carrier and sideband field. This RF beat signal often encodes information regarding the state of an optical system. As discussed previously, common camera is unable to observe this beat signal due to its high frequency in the range between tens and hundreds

of MHz.

Optical switching

Optical switching in the advanced phase camera is realised as intensity modulation using a chain of quarter wave plate (QWP), Pockels cell (PC) and polarising beam splitter (PBS). Here we will use standard Jones calculus to investigate the effect of these polarising component. First we rewrite equation B.1 as Jones vector:

$$E_{\text{in}} = \begin{bmatrix} 0 \\ 1 \end{bmatrix} e^{i\omega_0 t} \left[\tilde{A}_0(x,y) + \tilde{A}_{\text{m1}}(x,y) e^{i\Omega_{\text{m1}} t} \right] = \begin{bmatrix} 0 \\ 1 \end{bmatrix} \tilde{E}_{\text{in}} e^{i\omega_0 t} \tag{B.3}$$

The Jones matrix for QWP whose fast axis aligned with with y-axis is given by:

$$\mathbf{J}_{\text{QWP}} = e^{i\pi/4} \begin{bmatrix} 1 & 0 \\ 0 & -i \end{bmatrix} \tag{B.4}$$

The purpose of a QWP is to transform the linearly polarised field to circularly polarised field, which allows synchronous demodulation by the PC and simplify electronics required. Therefore the fast axis of the QWP needs to be at 45° relative to incoming field coordinates:

$$\begin{aligned} \mathbf{J}_{\text{QWP},45^\circ} &= \mathbf{R}(-45^\circ)\mathbf{J}_{\text{QWP}}\mathbf{R}(45^\circ) \\ &= \frac{e^{i\pi/4}}{2} \begin{bmatrix} 1+i & 1-i \\ 1-i & 1+i \end{bmatrix} \end{aligned} \tag{B.5}$$

The output field after the QWP and before PC is therefore:

$$\begin{aligned} E_{\text{QWP:PC}} &= \mathbf{J}_{\text{QWP},45^\circ} E_{\text{in}} \\ &= \frac{e^{i\pi/4}}{2} \begin{bmatrix} 1-i \\ 1+i \end{bmatrix} \tilde{E}_{\text{in}} e^{i\omega_0 t} \\ &= \frac{1-i}{2} \begin{bmatrix} 1 \\ i \end{bmatrix} \tilde{E}_{\text{in}} e^{i(\omega_0 t+\pi/4)} \end{aligned} \tag{B.6}$$

The Pockels cell is a variable linear retarder whose Jones matrix can be written as [28]:

$$\mathbf{J}_{\text{PC}}(\delta) = \begin{bmatrix} 1 & 0 \\ 0 & e^{-i\delta} \end{bmatrix} \tag{B.7}$$

The purpose of the Pockels cell is to switch polarisation of the incoming field synchronously between s and p polarisations, as defined by the field coordinate system. The Pockels cell is therefore rotated by 45° relative to the transverse optical coordinates:

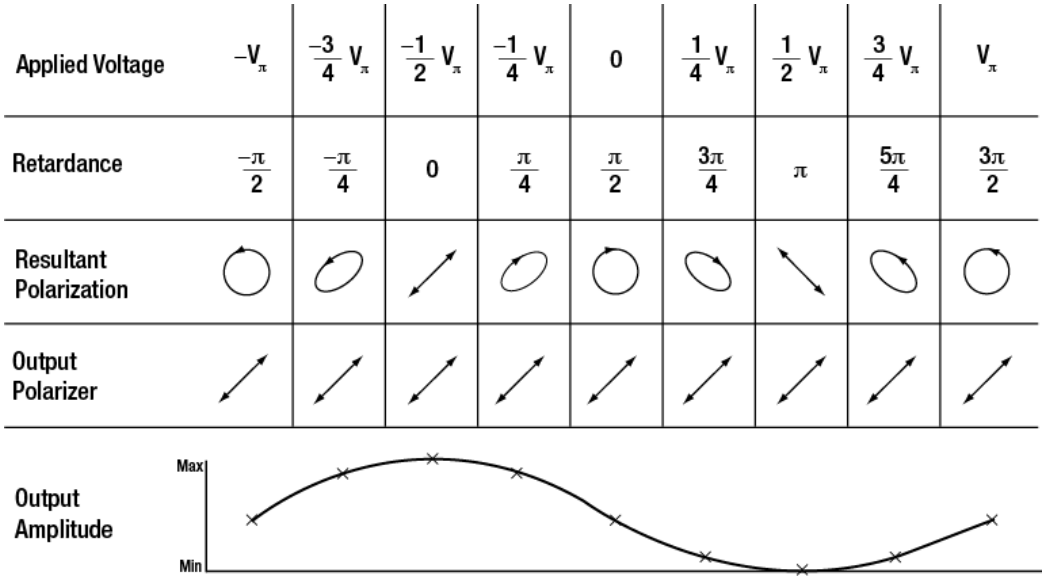

Figure B-1: Effects of Pockels cell at variable voltage on output polarisation given circularly polarised input field [111]. At zero applied voltage, the output polarization remains circular, half of incident light will be transmitted. At $V_{\text{applied}} = -V_{\pi/2}$ (quarter wave voltage) and $_{\text{applied}} = V_{\pi/2}$,the polarisation states are orthogonal, thus allowing either no transmission or full transmission of the incident field.

$$\begin{aligned}\mathbf{J}_{\text{PC},45^\circ}(\delta) &= \mathbf{R}(-45^\circ)\mathbf{J}_{\text{PC}}(\delta)\mathbf{R}(45^\circ) \\ &= \frac{1}{2}\begin{bmatrix} 1+e^{-i\delta} & 1-e^{-i\delta} \\ 1-e^{-i\delta} & 1+e^{-i\delta} \end{bmatrix}\end{aligned} \tag{B.8}$$

The output field from the Pockels cell is therefore:

$$\begin{aligned}E_{\text{PC:PBS}} &= \mathbf{J}_{\text{PC},45^\circ} E_{\text{QWP:PC}} \\ &= \frac{1}{2}\begin{bmatrix} 1-ie^{-i\delta} \\ 1+ie^{-i\delta} \end{bmatrix} \tilde{E}_{\text{in}} e^{i(\omega_0 t+\pi/4)}\end{aligned} \tag{B.9}$$

Consider the case in which the camera is placed at the transmission of PBS, therefore, only p-polarised light is incident on the camera:

$$\begin{aligned}E_{\text{PBS:Cam}} &= \mathbf{J}_{\text{PBS,t}} E_{\text{PC:PBS}} \\ &= \frac{1}{2}\begin{bmatrix} 1 & 0 \\ 0 & 0 \end{bmatrix}\begin{bmatrix} 1-ie^{-i\delta} \\ 1+ie^{-i\delta} \end{bmatrix} \tilde{E}_{\text{in}} e^{i(\omega_0 t+\pi/4)} \\ &= \frac{1}{2}\begin{bmatrix} 1-ie^{-i\delta} \\ 0 \end{bmatrix} \tilde{E}_{\text{in}} e^{i(\omega_0 t+\pi/4)}\end{aligned} \tag{B.10}$$

An electric field of the same frequency as that of the sideband field of interest is applied across the Pockels cell. Supposing that the modulation depth is given by $\Gamma_1 = \pi(V_1/V_\pi)$ where V_π is half-wave voltage that is characteristic to the Pockels cell crystal in use. The optical field at the camera is given by:

$$E_{\text{PBS:Cam}}(x,y,t) = \frac{1}{2}\left[1-ie^{-i\Gamma_1 \sin(\Omega_{\text{m1}} t+\varphi)}\right] \tilde{E}_{\text{in}} e^{i(\omega_0 t+\pi/4)} \tag{B.11}$$

Intensity detection

The signal seen by a pixel at position x_i, y_j on the camera is time averaged optical power incident over exposure time Δt, which can be expressed as following:

$$\overline{P}(x_i, y_j) = \frac{\epsilon_0 c}{2} \int_{t_0}^{t_0+\Delta t} dt \int_{x_i-\delta x/2}^{x_i+\delta x/2} \int_{y_j-\delta y/2}^{y_j+\delta y/2} dxdy \tilde{E}^{\dagger}_{\text{PBS:Cam}}(x, y, t) \tilde{E}_{\text{PBS:Cam}}(x, y, t) \tag{B.12}$$

We first evaluate the form of the integrand, which describes intensity of the incident light field.

$$\begin{aligned} I_{\text{PBS:Cam}}(x, y, t) &= \tilde{E}^{\dagger}_{\text{PBS:Cam}}(x, y, t) \tilde{E}_{\text{PBS:Cam}}(x, y, t) \\ &= \frac{1}{2} \left\{1 - \sin\left[\Gamma_1 \sin\left(\Omega_{\text{m1}} + \varphi\right)\right]\right\} \\ &\times \left[\left|\tilde{A}_0(x, y)\right|^2 + \left|\tilde{A}_{\text{m1}}(x, y)\right|^2 + A_0(x, y) A_{\text{m1}}(x, y) \cos(\Omega_{\text{m1}} t - \Delta\phi(x, y))\right] \end{aligned} \tag{B.13}$$

The first term of the product is the switching effect, whereas the second term is the intensity of the initial field, as seen previously (equation B.1). The first term can rewritten in term of Jacobi-Anger expansion for real-value:

$$\sin\left[\Gamma_1 \sin\left(\Omega_{\text{m1}} + \varphi\right)\right] = -2 \sum_{n=1}^{\infty} (-1)^n J_{2n-1}(\Gamma_1) \cos\left[(2n-1)\left(\Omega_{\text{m1}} t + \varphi\right)\right] \tag{B.14}$$

where J_{2n-1} is Bessel function of the first kind of order $2n-1$. Now let:

$$I_{\text{DC}}(x, y) = \left|\tilde{A}_0(x, y)\right|^2 + \left|\tilde{A}_{\text{m1}}(x, y)\right|^2$$

Equation B.13 can be rewritten as the sum of three terms:

$$\begin{aligned} I_{\text{PBS:Cam}}(x,y,t) = \frac{1}{2}\left[I_{\text{DC}}(x,y) + A_0(x,y)A_{\text{m1}}\cos(\Omega_{\text{m1}}t - \Delta\phi(x,y))\right] \\ + \sum_{n=1}^{\infty} I_{\text{DC}}(x,y)(-1)^n J_{2n-1}(\Gamma_1)\cos\left[(2n-1)\left(\Omega_{\text{m1}}t + \varphi\right)\right] \\ + \sum_{n=1}^{\infty}(-1)^n J_{2n-1}(\Gamma_1)A_0(x,y)A_{\text{m1}}(x,y)\cos(\Omega_{\text{m1}}t - \Delta\phi(x,y)) \\ \times \cos\left[(2n-1)\left(\Omega_{\text{m1}}t + \varphi\right)\right] \end{aligned} \tag{B.15}$$

Using trigonometric identity $2\cos\alpha\cos\beta = \cos(\alpha-\beta) + \cos(\alpha+\beta)$, the third term can be further expanded as:

$$\begin{aligned} &\frac{A_0(x,y)A_{\text{m1}}(x,y)}{2}\sum_{nu=1}^{\infty}(-1)^n J_{2n-1}(\Gamma_1)\cos\left[(2n-2)\Omega_{\text{m1}}t + (2n-1)\varphi + \Delta\phi(x,y)\right] \\ &+ \frac{A_0(x,y)A_{\text{m1}}(x,y)}{2}\sum_{n=1}^{\infty}(-1)^n J_{2n-1}(\Gamma_1)\cos\left[(2n)\Omega_{\text{m1}}t + (2n-1)\varphi - \Delta\phi(x,y)\right] \end{aligned} \tag{B.16}$$

There are thus 4 terms in the integrand of equation B.12. Using sum rule, we evaluate each term separately. Assuming that the size of pixel is sufficiently small such that spatial dependence term ($A_0(x,y),\ A_{\text{m1}}(x,y),\ \Delta\phi(x,y)$) are slowly varying function relative the scale of the pixel, it is then reasonable to approximate the spatial dependence integral by trapezoidal rule:

$$\int_{x_i-\delta x/2}^{x_i+\delta x/2}\int_{y_i-\delta y/2}^{y_i+\delta y/2} dx\,dy\,F(x,y) \simeq f(x_i,y_i)\delta x\delta y = F_{i,j}\delta\Sigma \tag{B.17}$$

Term 1:

The integral of the first term is thus can be simplified to:

$$\overline{P}_1(x_i,y_i) = \frac{\epsilon_0 c}{4}\delta\Sigma\int_{t_0}^{t_0+\Delta t} dt\ I_{\text{DC};i,j} + A_{0;i,j}A_{\text{m1};i,j}\left[\cos\Delta\phi_{i,j}\sin(\Omega_{\text{m1}}t) + \sin\Delta\phi_{i,j}\cos(\Omega_{\text{m1}}t)\right] \tag{B.18}$$

where we have used trigonometry identity $\cos(\alpha - \beta) = \cos\alpha\cos\beta + \sin\alpha\sin\beta$ to separate $\cos(\Omega_{\mathrm{m1}}t - \Delta\phi_{i,j})$ into spatial and temporal dependent parts. Performing integration with respect to time, we arrive at the following expression:

$$\frac{\epsilon_0 c}{4}\delta\Sigma\left\{I_{\mathrm{DC};i,j}\Delta t + \frac{A_{0;i,j}A_{\mathrm{m1};i,j}}{\Omega_{\mathrm{m1}}}\left[\sin(\Omega_{\mathrm{m1}}t_0 - \Delta\phi_{i,j}) - \sin(\Omega_{\mathrm{m1}}t_0 - \Delta\phi_{i,j} - \Omega_{\mathrm{m1}}\Delta t)\right]\right\} \tag{B.19}$$

The second term of the sum in equation B.19 is maximum when $\Delta t = n\pi/\Omega\ \forall n \in \mathbb{N} n > 0$ and minimum when $\Delta t = 2n\pi/\Omega\ \forall n \in \mathbb{N}, n > 0$ (i.e. when exposure term is multiples of sideband's period). For the maximum case, the expression is:

$$\frac{\epsilon_0 c}{4}\delta\Sigma\left\{I_{\mathrm{DC};i,j}\Delta t + \frac{2A_{0;i,j}A_{\mathrm{m1};i,j}}{\Omega_{\mathrm{m1}}}\right\} \tag{B.20}$$

We can now compare the signal strength between the two terms in the equation.Recall that $I_{\mathrm{DC};i,j} = |A_{0;i,j}|^2 + |A_{\mathrm{m1};i,j}|^2$. Sidebands often arises from phase modulation within gravitational wave detector with small modulation index on the order of 0.1-0.2 radians. The amplitude of the carrier field and sideband fields are dictated by the modulation index as well the optical cavity within which each fields interact with. However, for the currently planned method of detection, it is reasonable to assume the carrier field in used is significantly higher than that of sideband, so that observation of sideband structure is not possible with standard camera. Here, we simplify it by only consider modulation index effect. For some modulation Γ_0 and input field magnitude E_0, the magnitude of carrier field and sideband field after phase modulation are $J_0(\Gamma_0)E_0$ and $J_1(\Gamma_0)E_0$ respectively. The ratio of power between the carrier and a sideband is then:

$$\frac{|A_0|^2}{|A_{\mathrm{m1}}|^2} = \frac{J_1(\Gamma_0)^2}{J_0(\Gamma_0)^2} \tag{B.21}$$

For small argument $0 < \Gamma_0 \ll \sqrt{\nu + 1}$ of Bessel function of order ν, which is applicable in our cases :

$$J_\nu(\Gamma_0) \sim \frac{1}{\nu!}\left(\frac{\Gamma_0}{2}\right)^\nu \tag{B.22}$$

$J_0(\Gamma_0)$ and $J_1(\Gamma_0)$ are thus 1 and $\Gamma_0/2$ respectively, therefore:

$$\frac{|A_0|^2}{|A_{\mathrm{m1}}|^2} \sim \frac{\Gamma_0^2}{4} \tag{B.23}$$

and $I_{\mathrm{DC},i,j} \sim \left(1+\frac{\Gamma_0^2}{4}\right)|A_{0;i,j}|^2$ and $A_{0;i,j}A_{\mathrm{m1};i,j} \sim \frac{\Gamma_0}{2}|A_{0;i,j}|^2$. Using minimum exposure time on camera used in this experiment $\Delta t = 1\times10^{-3}$s, modulation frequency is often between 10^7 and 10^8Hz range. An estimated ratio between the signal strength between the two terms in B.20 is given by:

$$\begin{aligned}\frac{I_{\mathrm{DC};i,j}\Delta t}{2A_{0;i,j}A_{\mathrm{m1};i,j}/\Omega_{\mathrm{m1}}} &\sim \frac{\Delta t\Omega_{\mathrm{m1}}}{\Gamma_0} \\ &\approx \frac{10^{-3}\times10^7}{0.1} = 10^5\end{aligned} \tag{B.24}$$

This means the camera must have a dynamic range of ∼100 dB to observe effect of the beat signal. The first term of the integral is therefore dominated by the first term of the integral $\epsilon_0 c\delta\Sigma I_{\mathrm{DC};i,j}\Delta t/4$, which is a half of that observed when the input beam is incident directly on the camera as discussed in last section.

Term 2:

The second term consists of pure oscillations, it is thus expected to be averaged out to zero. This term has already separated into spatial and temporal dependence. Integration of the second term with respect to space and time results in:

$$\begin{aligned}\delta\Sigma\frac{\epsilon_0 c}{2}\frac{I_{\mathrm{DC};i,j}}{\Omega_{\mathrm{m1}}}\sum_{n=1}^{\infty}\frac{(-1)^n J_{2n-1}(\Gamma_1)}{2n-1}\{&\sin\left[(2n-1)(\Omega_{\mathrm{m1}}t_0+\Omega_{\mathrm{m1}}\Delta t+\varphi)\right] \\ &-\sin\left[(2n-1)(\Omega_{\mathrm{m1}}t_0+\varphi)\right]\}\end{aligned} \tag{B.25}$$

We first test for convergence of the series. Now for each n^{th} term of the series, we have:

$$|a_n| \leq \frac{2J_{2n-1}(\Gamma_1)}{2n-1} \tag{B.26}$$

notice that for $\Gamma_1 < \pi/2$, $2J_{2n-1} > 0 \forall n \in \mathbb{N}, n > 0$. One can numerically evaluate

the following series and show that:

$$\begin{aligned} \sum_{n=1}^{\infty} |a_n| &< \sum_{n=1}^{\infty} \frac{2J_{2n-1}(\Gamma_1)}{2n-1} \lesssim 1.18 \\ \therefore \sum_{n=1}^{\infty} a_n &< \sum_{n=1}^{\infty} |a_n| < 1.18 \end{aligned} \tag{B.27}$$

This set an upper limit for the series in equation B.25. We thus can compare the magnitude of this signal with the DC signal in term 1:

$$\frac{I_{\mathrm{DC};i,j}\Delta t/2}{I_{\mathrm{DC};i,j}\sum_{n=1}^{\infty} a_n/\Omega_{\mathrm{m1}}} > 10^{-3}10^{7} = 10^{4} \tag{B.28}$$

This lower bound is most likely to be an overestimation. It is thus expected the signal from this oscillating term is between 90 to 100 dB smaller than that of the DC signal in term 1.

Term 3 and 4

Expanding the third term results in a DC term from $n = 1$ and a sum of oscillatory terms that is similar to that of second term. The fourth term contains purely oscillatory term. These oscillatory terms can all be shown to be negligible and not detectable as in the case of second term. We are thus left with the results from integration of the DC term existing in term 3:

$$\overline{P}_{3;i,j} = -\frac{\epsilon_0 c}{4} J_1(\Gamma_1) A_{0;i,j} A_{\mathrm{m1};i,j} \cos\left(\Delta\phi_{i,j} + \varphi\right) \Delta t \tag{B.29}$$

Construct amplitude and phase

Collecting all of non-negligible term, we have an expression for the intensity observed by a pixel at (x_i, y_j):

$$\overline{P}_{i,j} \simeq \frac{\epsilon_0 c}{4} \delta\Sigma \left\{ |A_{0;i,j}|^2 + |A_{\mathrm{m1};i,j}|^2 - J_1(\Gamma_1) A_{0;i,j} A_{\mathrm{m1};i,j} \cos(\Delta\phi_{i,j} + \varphi) \right\} \Delta t \tag{B.30}$$

The expression δI presented in the previous section is described by:

$$J_1(\Gamma_1)A_{0;i,j}A_{\mathrm{m1};i,j}\cos(\Delta\phi_{i,j}+\varphi)$$

If $\Gamma_1 = \pi/2$ and the sideband is generate with a modulation index $\Gamma_0 = 0.1$, the magnitude analysis shows that the interference beat is on the order of 30dB smaller than that I_{DC} term in equation B.30, which is detectable by most standard scientific camera. However, the image is still dominated with I_{DC} term. This can be removed by two sets of images: one at $\varphi = \varphi'$, and one at $\varphi = \varphi' + \pi$ (out-of-phase demodulation). This results in two sets of images:

$$\overline{P}^{0}_{i,j} \simeq \frac{\epsilon_0 c}{4}\delta\Sigma\left\{|A_{0;i,j}|^2 + |A_{\mathrm{m1};i,j}|^2 - J_1(\Gamma_1)A_{0;i,j}A_{\mathrm{m1};i,j}\cos(\Delta\phi_{i,j}+\varphi')\right\}\Delta t \quad \text{(B.31)}$$

$$\overline{P}^{\pi}_{i,j} \simeq \frac{\epsilon_0 c}{4}\delta\Sigma\left\{|A_{0;i,j}|^2 + |A_{\mathrm{m1};i,j}|^2 + J_1(\Gamma_1)A_{0;i,j}A_{\mathrm{m1};i,j}\cos(\Delta\phi_{i,j}+\varphi')\right\}\Delta t \quad \text{(B.32)}$$

By computing $\overline{P}^{\pi}_{i,j} - \overline{P}^{0}_{i,j}$, we eliminate the common part that is the strong I_{DC} signal and obtain the *in-phase* demodulation signal:

$$\mathbb{I}_{i,j} = \frac{\epsilon_0 c}{2}\delta\Sigma J_1(\Gamma_1)A_{0;i,j}A_{\mathrm{m1};i,j}\cos(\Delta\phi_{i,j}+\varphi')\Delta t \quad \text{(B.33)}$$

To reconstruct both amplitude and phase, the *quadrature-phase* signal is also required. This can be obtained from taking an extra two sets of images at demodulation phases $\varphi = \varphi' + \pi/2$ and $\varphi = \varphi' + 3\pi/2$:

$$\overline{P}^{\pi/2}_{i,j} \simeq \frac{\epsilon_0 c}{4}\delta\Sigma\left\{|A_{0;i,j}|^2 + |A_{\mathrm{m1};i,j}|^2 + J_1(\Gamma_1)A_{0;i,j}A_{\mathrm{m1};i,j}\sin(\Delta\phi_{i,j}+\varphi')\right\}\Delta t \quad \text{(B.34)}$$

$$\overline{P}^{3\pi/2}_{i,j} \simeq \frac{\epsilon_0 c}{4}\delta\Sigma\left\{|A_{0;i,j}|^2 - |A_{\mathrm{m1};i,j}|^2 + J_1(\Gamma_1)A_{0;i,j}A_{\mathrm{m1};i,j}\sin(\Delta\phi_{i,j}+\varphi')\right\}\Delta t \quad \text{(B.35)}$$

Subtracting $\overline{P}^{3\pi/2}_{i,j}$ from $\overline{P}^{\pi/2}_{i,j}$ thus results in:

$$\mathbb{Q}_{i,j} = \frac{\epsilon_0 c}{2}\delta\Sigma J_1(\Gamma_1)A_{0;i,j}A_{\mathrm{m1};i,j}\sin(\Delta\phi_{i,j}+\varphi')\Delta t \quad \text{(B.36)}$$

From here, we see that the amplitude of the beat note between the two fields

A_0 and A_{m1} can be computed from:

$$\mathbb{I}_{ij}^2 + \mathbb{Q}_{i,j}^2 = \left[\frac{\epsilon_0 c}{2}\delta\Sigma\Delta t J_1(\Gamma_1)\right]^2 A_{0;i,j}^2 A_{\mathrm{m1};i,j}^2 \tag{B.37}$$

$$\therefore |A_{0;i,j}A_{\mathrm{m1};i,j}| \propto \sqrt{\mathbb{I}_{ij}^2 + \mathbb{Q}_{i,j}^2} \tag{B.38}$$

The phase map can be obtained from the ratio between $\mathbb{I}_{ij}$ and $\mathbb{Q}_{ij}$:

$$\begin{aligned}\frac{\mathbb{I}_{ij}}{\mathbb{Q}_{ij}} &= \frac{\sin(\Delta\phi_{i,j} + \varphi')}{\cos(\Delta\phi_{i,j} + \varphi')} \\ &= \tan(\Delta\phi_{i,j} + \varphi') \\ &= \frac{\tan\Delta\phi_{i,j} + \tan\varphi'}{1 - \tan\Delta\phi_{i,j}\tan\varphi'}\end{aligned} \tag{B.39}$$

Now we use the following trigonometry identity:

$$\arctan(\alpha) + \arctan(\beta) = \arctan\left(\frac{\alpha+\beta}{1-\alpha\beta}\right)$$

The phase map is then simply inverse tangent of ratio between *in-phase* and *quadrature-phase* signals and some offset due to demodulation phase:

$$\Delta\phi_{i,j} = \arctan\left(\frac{\mathbb{I}_{ij}}{\mathbb{Q}_{i,j}}\right) - \varphi' \tag{B.40}$$

Therefore, we have shown how this new technique allow us to construct the amplitude and phase of an RF beatnote in an optical field.

Appendix C

Zernike decomposition of wavefront

The following contents describe mathematic framework of constructing wavefront using Zernike decomposition implemented in module `HSM_Zernike`. The work implemented is based closely on the work by Lane and Tallon [122], ming Dai [146] and Noll [158] on using Zernike polynomials to construct wavefront with Shack-Hartmann sensors.

C.1 Compute Zernike coefficients from gradients data

Consider a random wavefront ϕ that has some distortion. In the pupil plane of interest with radius R, this wavefront can be expanded into a set of orthogonal basis functions $\{F_i(\mathbf{r})\}$:

$$\phi(R\mathbf{r}) = \sum_{i=1}^{\infty} a_i F_i(\mathbf{r}) \tag{C.1}$$

where $\mathbf{r}$ denotes a positional vector. The summation index in C.1 is ignored as the piston is of no interest for wavefront correction system and can't be retrieved from gradient data acquired with a Hartmann sensor. Here we discuss the implementation of Zernike polynomials for describing wavefronts that are used in the

work covered in this thesis. Equation C.1 can be rewritten as:

$$\phi(R\mathbf{r}) = \sum_{i=1}^{\infty} a_i Z_i(\mathbf{r}) \tag{C.2}$$

where Z_i are Zernike polynomial bases evaluated on a unit circle $\rho \leq 1$:

$$Z_i(\mathbf{r}) = Z_n^m(\mathbf{r}) = N_n^m R_n^m(r\rho)\Theta^m(\theta) \tag{C.3}$$

the azimuthal term $\Theta(\theta)$is given by:

$$\Theta(\theta) = \begin{cases} \cos(m\theta) & \text{if } m \geq 0, \\ -\sin(m\theta) & \text{if } m \leq 0 \end{cases} \tag{C.4}$$

the radial polynomials $R(\rho)$ is given by:

$$R_m^n(\rho) = \sum_{s=0}^{\frac{n-|m|}{2}} \frac{(-1)^s (n-s)!}{\left(\frac{n-|m|}{s} - s\right)! \left(\frac{n+|m|}{s} - s\right)!} \rho^{n-2s} \tag{C.5}$$

These polynomials satisfy orthogonality condition:

$$\int_0^1 R_n^m(\rho) R_{n'}^{m'}(\rho) \rho d\rho = \frac{1}{2(n+1)} \delta_{nn'} \tag{C.6}$$

The normalising coefficient of Zernike polynomials is defined to be:

$$N_{nm} = \sqrt{(2 - \delta_{m0})(n+1)} \tag{C.7}$$

such that the Zernike polynomials are normalised to π over a unit circle.

The integers n and m indices are subjected to the following constraints:

$$\begin{gathered} n \geq 0, \\ (n - |m|) \text{ is even,} \\ |m| \leq n \end{gathered} \tag{C.8}$$

Here we have chosen OSA convention for single index i:

$$i = \frac{n(n+2)+m}{2} \tag{C.9}$$

Function `Zernike_nm_indices(i)` will generate two arrays of n and m indices when user specify i orders of Zernike polynomials to use. Once these indices have been generated,N_n^m, $R_n^m(\rho)$ and $\Theta^m(\theta)$ (equations C.5, C.4 and C.7) are generated by functions `Rnm(rho,n,m)`,`Theta_nm(theta,m)` and `Nnm(n,m)`. `rho` is an array of radial position normalised to a unit circle and `theta` is the corresponding azimuthal positions.

In Hartmann wavefront sensors,the gradient of an unknown wavefront is sampled within small areas called subapertures. Suppose there are k aperatures. The x and y derivatives at each aperture can be written as:

$$\left.\frac{\partial\phi}{\partial x}\right|_j = \sum_{i=1}^{\infty} a_i \left.\frac{\partial Z_i(\mathbf{r})}{\partial x}\right|_j \tag{C.10}$$

$$\left.\frac{\partial\phi}{\partial y}\right|_j = \sum_{i=1}^{\infty} a_i \left.\frac{\partial Z_i(\mathbf{r})}{\partial y}\right|_j \tag{C.11}$$

where $j = 1, 2, ..., k$. A matrix representation of this system of equations is:

$$\mathbf{S} = \mathbf{G}\mathbf{A} = \mathbf{G}\begin{bmatrix}\mathbf{A}_f \\ \mathbf{A}_r\end{bmatrix} \tag{C.12}$$

where $\mathbf{S}$ is a $k \times 1$ array of wavefront slopes obtained from Hartmann sensor measurements. $\mathbf{A}$ is array of exact Zernike coefficients representing the wavefront, which is divided into $\mathbf{A}_f$, which is an array of the first $\mathrm{N}N$ coefficients, and $\mathbf{A}_r$ which containing remaining coefficients. Matrix $\mathbf{G}$ contain the average gradients

of basis functions at each subaperture, as determined by Hartmann sensor:

$$\begin{bmatrix} \frac{\partial Z_1(r,\theta)_1}{\partial x} & \frac{\partial Z_2(r,\theta)_1}{\partial x} & \cdots & \frac{\partial Z_M(r,\theta)_1}{\partial x} \\ \frac{\partial Z_1(r,\theta)_1}{\partial y} & \frac{\partial Z_2(r,\theta)_1}{\partial y} & \cdots & \frac{\partial Z_M(r,\theta)_1}{\partial y} \\ \vdots & \vdots & & \vdots \\ \frac{\partial Z_1(r,\theta)_k}{\partial x} & \frac{\partial Z_2(r,\theta)_k}{\partial x} & \cdots & \frac{\partial Z_M(r,\theta)_k}{\partial x} \\ \frac{\partial Z_1(r,\theta)_k}{\partial y} & \frac{\partial Z_2(r,\theta)_k}{\partial y} & \cdots & \frac{\partial Z_M(r,\theta)_1}{\partial y} \end{bmatrix} \tag{C.13}$$

M is used here instead of infinity, but can be replaced with infinity when necessary. However,since there is always a finite number of subapertures k, the exact solution to equation C.12 cannot be obtained. In general, one would seek to obtain only the first N coefficients of $\mathbf{A}_f$ based on $2k$ slope measurements and N is often less than $2k$. In this case, the unknown wavefront is approximated by:

$$\hat{\phi}(R\mathbf{r}) = \sum_{i=1}^{N} b_i Z_i(r,\theta) \tag{C.14}$$

where $\{b_i\}$ is an $N \times 1$ array of estimated coefficients and a similar matrix equation can be rewritten with the following form:

$$\tilde{\mathbf{S}} = \mathbf{HB} \tag{C.15}$$

where $\mathbf{B} = \{b_i\}$ and $\mathbf{H}$ is a $2k \times N$ matrix, whose form is similar to that of matrix $\mathbf{G}$ given in C.13. The least-squared solution toC.15 is:

$$\mathbf{B} = \mathbf{H}^{+}\mathbf{S} \tag{C.16}$$

where $\mathbf{H}^{+}$ is the generalised inverse matrix of $\mathbf{H}$: $\mathbf{H}^{+} = (\mathbf{H}^T\mathbf{H})^{-1}\mathbf{H}^T$.In the work covered within the scope of this thesis,inversion of matrix $\mathbf{H}$ is performed using singular-value decomposition algorithm since $\mathbf{H}$ is often rank-deficient.

In module `HSM_Zernike`, user can call function `compute_Zernike_from_hsg( hsgradients, i,R0)` to compute estimated Zernike coefficients directly from

an `HS_Gradients()` instance `hsgradients`, which contains slope measurements and centroid coordinates. `i` is again the index of Zernike functions up to which the coefficients will be evaluated. `R0` is the radius of the circular pupil in metric unit, that will be normalised to a unit circle. This value is optional. If not defined, the function will define `R0` to be radius of the largest circle that can be fitted within the range of positional coordinates provided. The function `compute_Zernike_from_hsg` then constructs the slope array from `hsgradients` and call for function `H_nm_construct(x,y,i)` to construct **H** matrix, given normalised coordinates `x` and `y`. Function `Hnm_construct(x,y,i` in turn calls function `Zderivs(x,y,n,m)` to evaluate derivatives of Zernike functions at given coordinates. Here the derivatives were evaluated by the following recursive relation [190]:

$$\begin{aligned}\frac{\partial}{\partial x}Z_m^m &= n\left[b_{n-1,m-1}^{nm}Z_{n-1}^{\alpha_m|m-1|} + \alpha_m \operatorname{sgn}(m+1)b_{n-1,m+1}^{nm}Z_{n-1}^{\alpha_m|m+1|}\right] \\ &\quad + b_{n-2,m}^{nm}\frac{\partial}{\partial x}Z_{n-2}^m \qquad \text{(C.17)}\\ \frac{\partial}{\partial y}Z_m^m &= n\left[-\alpha_m \operatorname{sgn}(m-1)b_{n-1,m-1}^{nm}Z_{n-1}^{-\alpha_m|m-1|} + b_{n-1,m+1}^{nm}Z_{n-1}^{-\alpha_m|m+1|}\right] \\ &\quad + b_{n-2,m}^{nm}\frac{\partial}{\partial y}Z_{n-2}^m \qquad \text{(C.18)}\end{aligned}$$

where:

$$b_{n'm'}^{nm} = \frac{N_{nm}}{N_{n'm'}} \qquad \text{(C.19)}$$

$$\alpha_m = \begin{cases} +1 & \text{if } m \geq 0, \\ -1 & \text{if } m < 0 \end{cases} \qquad \text{(C.20)}$$

The initial conditions for the recursion is:

$$\frac{\partial}{\partial x}Z_n^{\pm n} = N_{nn}n\rho^{n-1}\Theta_{\pm(n-1)}(\theta)\delta_{\mp m,1} \qquad \text{(C.21)}$$

$$\frac{\partial}{\partial y}Z_n^{\pm n} = \mp N_{nn}n\rho^{n-1}\Theta_{\mp(n-1)}(\theta)\delta_{\pm n,1} \qquad \text{(C.22)}$$

For a Zernike mode Z_n^m, function `Zderivs(x,y,n,m)` calls for `dZ_IC(rho,theta,m)` to generate initial conditions (finding $\frac{\partial Z_m^m}{\partial}$)

```
import sys
import os

hspath = os.path.abspath('')
if hspath not in sys.path:
    sys.path.append(hspath)

from HS_Centroids import *
from HS_Gradients import *
import numpy as np
import matplotlib.pyplot as plt
from scipy import special as sc
from scipy import interpolate
import matplotlib



def cart2pol(x, y):
    rho = np.sqrt(x**2 + y**2)
    phi = np.arctan2(y, x)
    return(rho, phi)
def Zernike_nm_indices(i):
    iarr = np.arange(1,i+1,1)
    nroot= np.roots([1,1,-2*(i+1)])
    nroot = nroot[nroot>0]
    nmax = int(np.floor(nroot))
    # order of mode in max n:
    nmodem = int(np.floor((nroot-nmax)*(nmax+2)))
    # Generate n coeff array up to nmax:
    n = np.zeros([0,1])
    for iN in range(1,nmax+1):
        n = np.vstack([n,iN*np.ones([iN+1,1])])
    if nmodem != 0:
        n = np.vstack([n,(nmax+1)*np.ones([nmodem,1])])
    # Generate corresponding m indices vector:
```

```
    m = np.zeros(np.shape(iarr))
    for iI in iarr:
        m[iI-1] =  (iI*2) -n[iI-1]*(n[iI-1]+2)
    return n,m
def Nnm(n,m):
    # Return normalization coefficient a given Znm:
    Nnm = np.sqrt((2-np.equal(0,m).astype(int8))*(n+1))
    return Nnm


def Rnm_coeff(n,m):
    # Find coeeficient to evvaluate sum of radial term in zernike m,n order
    m = np.abs(m)
    smax = int((n-m)/2 )
    Rc = np.zeros([smax+1,1])
    for iS in range(smax+1):
        Rc[iS] = ((-1)**iS * sc.factorial(n-iS))/(sc.factorial(iS)*
        sc.factorial((n+m)/2-iS)*sc.factorial((n-m)/2-iS) )
    return Rc
def Rnm(rho,n,m):
    # Compute radial term of Zenike order m,n
    Rc = Rnm_coeff(n,m)
    Rmn = np.zeros(np.shape(rho))
    for ic,iS in enumerate(Rc):
        Rmn += iS*rho**(n-2*ic)
    return Rmn
def Theta_nm(theta,m):
    # Compute azimuthal part of Zernike:
    if m >= 0:
        Theta_mn = np.cos(m*theta)
    else:
        Theta_mn = -np.sin(m*theta)
    return Theta_mn
def Znm(rho,theta,n,m):
    # Compute Zernike polynmial of order n,m
    Znm = Nnm(n,m)*Rnm(rho,n,m)*Theta_nm(theta,m)
    return Znm
```

```
def Zderivs_Znm(rho,theta,n,m):
    # Return first terms in recursive relationship
    a = np.sign(m) + 1*(m==0)
    if n == 0:
        Znmx1 = np.zeros(np.shape(rho))
        Znmy1=Znmx1
        bnm = np.zeros((1,3))
    else:
        narr =  np.array([(n-1),(n-1),(n-2)*(n>=2)])
        marr = np.array([m-1,m+1,m])
        Nn = Nnm(n,m)*np.ones([1,3])
        Nd = Nnm(narr,marr)
        #print(narr,marr)
        bnm = Nn/Nd
        #print(bnm)
        nZarr = narr[:2]
        mZarr = np.array([a*np.abs(m-1),a*np.abs(m+1)])
        Znmx1 = n*(bnm[:,0]*Znm(rho,theta,nZarr[0],mZarr[0]) +
        a*np.sign(m+1)*bnm[:,1]*Znm(rho,theta,nZarr[1],mZarr[1]))
        Znmy1 = n*(-a*np.sign(m-1)*bnm[:,0]*Znm(rho,theta,nZarr[0],
        -mZarr[0]) + bnm[:,1]*Znm(rho,theta,nZarr[1],-mZarr[1]))
    return  Znmx1, Znmy1, bnm[:,2]

def dZ_IC(rho,theta,m):
    # Return initial condition for recursively findin drivatives of Zernike:
    n=m
    if n >= 0:
        dxZn = Nnm(n,n)*n*rho**(n-1)*Theta_nm(theta,n-1)*(-n==1)
        dyZn = -Nnm(n,n)*n*rho**(n-1)*Theta_nm(theta,-n+1)*(n==1)
    else:
        n=np.abs(n)
        dxZn = Nnm(n,n)*n*rho**(n-1)*Theta_nm(theta,-n+1)*(n==1)
        dyZn = Nnm(n,n)*n*rho**(n-1)*Theta_nm(theta,n-1)*(-n==1)
        #print(dxZn,dyZn)
    return dxZn, dyZn
```

```
def Zderivs(x,y,n,m):
    rho, phi = cart2pol(x,y)
    # Acquire initial condition, check for value of m and acquire
    #the first state to initialise iteration
    dZxIC, dZyIC = dZ_IC(rho,phi,m)
    # Implement recursive process for evaulation:
    nstep = int((n-abs(m))/2)
    n_recurse = np.arange(abs(m),n+1,2)
    dZnmdx = dZxIC
    dZnmdy = dZyIC
    #print(n_recurse)
    for iN in n_recurse:
        #print(iN)
        idZnmdx,idZnmdy, bnm2 = Zderivs_Znm(rho,phi,iN,m)
        dZnmdx = bnm2*dZnmdx
        dZnmdy = bnm2*dZnmdy
        dZnmdx += idZnmdx
        dZnmdy += idZnmdy
    return dZnmdx,dZnmdy

def Hnm_construct(x,y,j):
    # Construct a  2k x  j matrix of zernike derivatives in x and y:
    Hnm = np.zeros([2*len(x),j])
    # Generat all of n,m indices up order j:
    n,m = Zernike_nm_indices(j)
    # Looping through all indices to generate matrix of derivative:
    for ij in range(j):
        iZdx, iZdy = Zderivs(x,y,n[ij],m[ij])
        Hnm[::2,ij] = iZdx
        Hnm[1::2,ij]= iZdy
    return Hnm

def Zernike_solve(S,Hnm):
    # Pseudo-inverse Hnm matrix:
    Hinv = np.linalg.pinv(Hnm)
```

```
    Bcoeff = np.matmul(Hinv,S)
    return Bcoeff

def compute_Zernike_from_hsg(hsgradients,i,R0=None):
    ''' Compute Zernike coefficients from HS gradients,
    assuming that centre of the pupil is at center of gradient map
    Input:
        hsgradient: HS_Gradients instance
        R0: Radius of region to be normalised for Zernike coeff
        i: maximum order of Zernike polynomial coeff to reconstruct
    Output
        b coefficient
    '''
    grads = hsgradients.gradients[:,:2]
    cents = hsgradients.gradients[:,2:]

    if R0 is None:
        Rpupil = np.min([abs(cents[:,0].min()),cents[:,0].max()
        ,abs(cents[:,1].min()),cents[:,1].max()])
    else:
        Rpupil = R0
    cents = cents/Rpupil
    grads = grads*Rpupil
    # Construct slope vector:
    S = np.empty([2*len(cents[:,0])])
    S[::2] = grads[:,0]
    S[1::2] = grads[:,1]
    # Construct H matrix
    Hmat = Hnm_construct(cents[:,0],cents[:,1],i)
    # Solve for Zernike coefficients:
    bcoeff = Zernike_solve(S,Hmat)
    return bcoeff

def construct_slope_vector(hsgradients, R0=None):
    grads = hsgradients.gradients[:,:2].copy()
    cents = hsgradients.gradients[:,2:].copy()
```

```
    if R0 is None:
        Rpupil = np.min([abs(cents[:,0].min()),cents[:,0].max()
        ,abs(cents[:,1].min()),cents[:,1].max()])
    else:
        Rpupil = R0
    cents = cents/Rpupil
    grads = grads*Rpupil
    # Construct slope vector:
    S = np.empty([2*len(cents[:,0])])
    S[::2] = grads[:,0]
    S[1::2] = grads[:,1]
    return S, cents

def bar_plot_zernike(bnm, i=None, logplot = False):
    ''' Plotting bar graph from zernike coefficient:'''
    if i is None:
        iplot = 14
    else:
        if i>len(bnm):
            raise Exception('number␣of␣orders␣to␣plot␣must␣be
␣␣␣␣␣␣␣␣␣␣␣␣␣␣␣␣less␣than␣number␣of␣coefficients␣defined')
        else:
            iplot = i
    n,m = Zernike_nm_indices(iplot)
    n = n[:,0]
    xticklabel = []
    for iN,iM in zip(n,m):
        xticklabel.append(str(int(iN))+','+str(int(iM)))
    bcoeffnm = 1e9*bnm[:iplot]

    if logplot is True:
        bp_max10 = np.max(np.sign(bcoeffnm)*np.ceil(np.log10(abs(bcoeffnm))))
        bp_min10 = np.min(np.sign(bcoeffnm)*np.ceil(np.log10(abs(bcoeffnm))))
        # generate interval
        iNval = []
```

```
        for iNeg in np.arange(bp_min10,0):
            iNval.append(np.linspace(-10**abs(iNeg),-2*10**(abs(iNeg)-1),9))
        iNval = np.ravel(np.asarray(iNval))
        zeroNval = np.linspace(-1,1,3)
        iPval = []
        for iPos in np.arange(0,bp_max10):
            iPval.append(np.linspace(2*10**(abs(iPos)),10**(abs(iPos)+1),9))
        iPval = np.ravel(np.asarray(iPval))
        yticks = np.hstack([iNval,zeroNval,iPval])

        fig=plt.figure(figsize=(10,6))
        ax = fig.add_subplot(111)
        ax.bar(np.arange(len(bcoeffnm))+1,bcoeffnm, width=0.5)
        ax.set_yscale('symlog')
        ax.set_ylabel('Zernike coefficient amplitude (nm)')
        xticks = np.arange(1,iplot+1)
        plt.yticks(yticks)
        plt.xticks(xticks, xticklabel)
        plt.xlabel('Zernike mode (n,m)')
        ax.grid(True,which='minor',linestyle='-')
        ax.grid(True,which='major',linestyle='--')
        plt.show()
    else:
        fig=plt.figure(figsize=(10,6))
        ax = fig.add_subplot(111)
        ax.bar(np.arange(len(bcoeffnm))+1, bcoeffnm, width =.5)
        xticks = np.arange(1,iplot+1)
        plt.xticks(xticks, xticklabel)
        plt.xlabel('Zernike mode (n,m)')
        ax.set_ylabel('Zernike coefficient amplitude (nm)')
        ax.grid(True,which='minor',linestyle='-')
        ax.grid(True,which='major',linestyle='--')
        plt.show()

def construct_spherical_gradient(R,cents):
    S = 2/R
```

```
    gradx = (S)*cents[:,0]
    grady = (S)*cents[:,1]
    gradients = np.vstack([gradx,grady]).transpose()
    return gradients

def construct_residual_gradient(hsg,R):
    cents = hsg.gradients[:,2:]
    grads = hsg.gradients[:,:2]
    S_grads = construct_spherical_gradient(R,cents)
    grad_res = grads- S_grads
    hsc_ref = HS_Centroids()
    hsc_res = HS_Centroids()
    hsc_ref.centroids = hsg.gradients[:,2:]/
        (hsg.pixel_size*hsg.magnification)+hsg.origin
    mod_factor = hsg.pixel_size /(hsg.lever_arm * hsg.magnification)
    displacement = grad_res/mod_factor
    hsc_res.centroids=hsc_ref.centroids+displacement

    hsg_res = HS_Gradients(hsc_ref,hsc_res)
    hsg_res.pixel_size = hsg.pixel_size
    hsg_res.magnification = hsg.magnification
    hsg_res.lever_arm = hsg.lever_arm
    hsg_res.construct_gradients()
    return hsg_res

def construct_wf(r,phi,bcoeff):
    i = len(bcoeff)
    n,m = Zernike_nm_indices(i)
    WFrms = np.zeros(np.shape(r))
    for ij in range(i):
        WFrms+= bcoeff[ij]*Znm(r,phi,n[ij],m[ij])
    return WFrms

def compute_rms_error_from_zernike(bcoeff):
    WF_rms = sqrt((bcoeff**2).sum())
    return WF_rms
```

```
def compute_rms_error_from_hsg(hsg,R,i):
    '''Compute wavefront rms error (flat pupil) using gradient data
    and compute deviation from best fit'''
    # First compute residual gradient:
    hsg_res = construct_residual_gradient(hsg,R)
    # Solve for Zernike coefficients from hsg_res:
    bcoeff_res = compute_Zernike_from_hsg(hsg_res,i)
    # Compute wf rms error from zernike coefficient:
    wf_rms = compute_rms_error_from_hsg(bcoeff)
    return wf_rms

def compute_Gauss_rms_error_from_hsg(hsg,R,i,w0, R0 = None):
    ''' Compute Gaussian weighted rms error from using gradient data
    ande rms error from best fit:
    Input:
        hsg: HS_gradient instance containing gradient with center of
         deformation assume to be at origin (0,0)
        R:  radius of curvature of the best fit spherical wavefront
        w0: beam radius of target Gaussian beam for weighting
        i: Number of order to be used for wavefront reconstruction,
        R0: radius of pupil to be normalised
    Output:
        WFrms_error_Gauss: Gaussian weighted wavefront rms error
    '''
    grads = hsg.gradients[:,:2].copy()
    cents = hsg.gradients[:,2:].copy()
    if R0 is None:
        Rpupil = np.min([abs(cents[:,0].min()),cents[:,0].max(),
        abs(cents[:,1].min()),cents[:,1].max()])
    else:
        Rpupil = R0
    # First compute residual gradient :
    hsg_res = construct_residual_gradient(hsg,R)
    # Solve for Zernike coefficients from hsg_res:
    bcoeff_res = compute_Zernike_from_hsg(hsg_res,i,Rpupil)
```

```
    # Reconstruct wavefront from bcoeff_res:
    nsample = 500
    dr = 1/nsample
    dphi = 2*np.pi/nsample
    r = np.arange(0,1,dr)
    phi = np.arange(0,2*np.pi,dphi)
    R, PHI = np.meshgrid(r,phi)
    WF_res =  construct_wf(R,PHI,bcoeff_res)
    # Compute gaussian weighted residual wavefront rms error:
    w0_norm = w0/Rpupil
    Gauss = sqrt(2/(np.pi*w0_norm**2))*exp(-(R**2)/(w0_norm**2))
    WFrms_remnsqred_Gauss_int = ((WF_res**2)*R*dr*dphi*Gauss**2).sum()
    Norm_factor = (Gauss**2*R*dr*dphi).sum()
    WFrms_error_Gauss = sqrt(WFrms_remnsqred_Gauss_int/np.pi)/Norm_factor
    return  WFrms_error_Gauss
```

Appendix D

Gaussian Beam Optics

D.1 Fundamentals of Gaussian beam

Gaussian beam is an important solution of Helmholtz (Maxwell) paraxial wave equations. Consider the famous Maxwell's equation:

$$\begin{aligned} \nabla \times \mathbf{E} &= -\frac{\partial \mathbf{B}}{\partial t} \\ \nabla \cdot \mathbf{B} &= 0 \\ \nabla \times \mathbf{B} &= \mu \mathbf{J} + \frac{1}{c^2}\frac{\partial \mathbf{E}}{\partial t} \\ \nabla \cdot \mathbf{E} &= \frac{\rho}{\epsilon} \end{aligned} \tag{D.1}$$

Under the assumption of monochromatic fields varying in time as$\exp^{-i\omega t}$, the Maxwell equations can be reduced to Helmholtz equation:

$$(\nabla^2 + k^2)\mathbf{U}(\mathbf{r}, t) = 0 \tag{D.2}$$

where $k = 2\pi/\lambda$ is the wave number and $\mathbf{U}(\mathbf{r}, t)$ is a complex amplitude field, which can describe either electric or magnetic field. One possible solution Eq. **??** is

is a plane wave:

$$\mathbf{U}(\mathbf{r}) = \mathbf{A}(\mathbf{r})e^{-ikz} \tag{D.3}$$

where $\mathbf{A}(\mathbf{r})$ represents a complex amplitude envelope. Under the assumption that the envelope $\mathbf{A}$ varies slowly with z - the axis of propagation so that $\partial_z \mathbf{A} \ll \mathbf{A}/\lambda$, then the Helmholtz can be approximated by the paraxial Helmholtz equation:

$$\nabla_\perp^2 A(\mathbf{r}) - 2ik\partial_z A(\mathbf{r}) = 0 \tag{D.4}$$

This assumption is appropriate for laser source since light field from laser varies slowly with the propagation direction. Here, $\nabla_\perp^2 = \partial_x^2 + \partial_y^2$ is the transverse Laplacian. A simple solution to equation D.4 is the complex paraboloid wave:

$$A(\mathbf{r}) = \frac{A_0}{2q(z)}, \quad q(z) = z + iz_R \tag{D.5}$$

z_R is the Rayleigh range:

$$z_R = \frac{\pi\omega_0^2}{\lambda} \tag{D.6}$$

with ω_0 being the beam waist. In order to separate the phase and amplitude portions of the wave, it is useful to rewrite parameter $q(z)$ as:

$$\frac{1}{q(z)} = \frac{1}{R(z)} - i\frac{\lambda}{\pi w^2(z)} \tag{D.7}$$

where R is the radius of curvature.

Substitution of Eq. D.7 into Eq. D.5 results in the expression for a Gaussian beam:

$$U(r,z) = A_0 \frac{w_0}{w(z)} e^{-\frac{r^2}{w^2}} e^{-ikz - ik\frac{r^2}{2R(z)} + i\zeta(z)} \tag{D.8}$$

where:

$$w(z) = w_0\sqrt{1+\left(\frac{z}{z_R}\right)^2} \tag{D.9}$$

$$R(z) = z\left[1+\left(\frac{z}{z_R}\right)^2\right] \tag{D.10}$$

$$\zeta(z) = \tan^{-1}\left(\frac{z}{z_R}\right) \tag{D.11}$$

where $\zeta(z)$ is referred to as the Gouy phase.

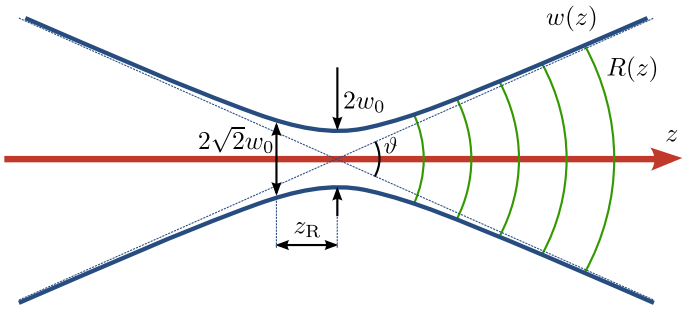

Figure D-1: Diagram demonstrating the characteristics of Gaussian beam propagation.The thick dark lines represent the beam size $\omega(z)$, which is minimum at the waist ω_0. z_R is the Rayleight range, at which the cross-section area of the beam is doubled. Angle of divergence ϑ can be approximated as $2\omega_0/z_R$

Hermite-Gaussian modes

The fundamental Gaussian beam is not the only solution to the paraxial Helmholtz equation. Hermite-Gaussian modes are a complete set of solutions to the paraxial Helmholtz Equation in rectangular coordinate. They are given in the form of:

$$\begin{aligned} U_{mn}(x,y,z) =& A_{mn}\frac{w_0}{w(z)}H_m\left(\frac{\sqrt{2}x}{w(z)}\right)H_n\left(\frac{\sqrt{2}y}{w(z)}\right)\exp\left(-\frac{x^2+y^2}{w^2(z)}\right) \\ &\times\exp\left[-ikz-\frac{ik(x^+y^2)}{2R(z)}+i(m+n+1)\zeta(z)\right] \end{aligned} \tag{D.12}$$

where $H(\eta)$ are Hermite polynomials.

D.2 Accumulation of Gouy phase

Gouy phase, as given by Eq. D.11 describes the phase lag between a Gaussian beam relatively to the beam waist in excess of the perfect plane wave that occurs as a function of propagation along optical axis.

In an optical system consisting of multiple lenses, there are however a number of waists. We thus would be more interested in the phase accumulated relatively to a single reference point. This is particularly useful for analysis of an optical cavity.

Erden and M.Ozaktas [88] showed description of beam parameters in term of ABCD matrix and parameter of input beam. These start with the expression [174, 15]

$$q_{\text{out}} = \frac{Aq_{\text{in}} + B}{Cq_{\text{in}} + D} \tag{D.13}$$

Beam size, radius of Gouy phase can rewritten as [88]:

$$w_{\text{out}}^2 = w_{\text{in}}^2 \left(A + \frac{B}{R_{\text{in}}} \right)^2 + \frac{B^2\lambda^2}{\pi^2 w_{\text{in}}^2} \tag{D.14}$$

$$\frac{1}{R_{\text{out}}} = \frac{\left(C + \frac{D}{R_{\text{in}}} \right)\left(A + \frac{B}{R_{\text{in}}} \right) + \frac{BD\lambda^2}{\pi^2 w_{\text{in}}^4}}{\left(A + \frac{B}{R_{\text{in}}} + \frac{B^2\lambda^2}{\pi^2 w_{\text{in}}^4} \right)} \tag{D.15}$$

$$\tan\zeta = \frac{B}{\left(A + \frac{B}{R_{\text{in}}} \right)\frac{\pi w_{\text{in}}^2}{\lambda}} \tag{D.16}$$

Erden and M.Ozaktas [88] also derives expressions for ABCD elements in term

of beam parameters:

$$A = \frac{w_{\text{out}}}{w_{\text{in}}} \cos\zeta - \frac{B}{R_{\text{in}}} \tag{D.17}$$

$$B = \frac{\pi w_{\text{in}} w_{\text{out}}}{\lambda} \sin\zeta \tag{D.18}$$

$$C = \frac{A}{R_{\text{out}}} - \frac{\frac{1}{R_{\text{in}}}\left(A + \frac{B}{R_{\text{in}}}\right) + \frac{B\lambda^2}{\pi^2 w_{\text{in}}^4}}{\left(A + \frac{B}{R_{\text{in}}}\right)^2 + \frac{B^2\lambda^2}{\pi^2 w_{\text{in}}^4}} \tag{D.19}$$

$$D = \frac{1 + BC}{A} \tag{D.20}$$

in which the last expression is the result of unitary property of ABCD matrix: $AD - BC = 1$

Now we compute the quantity $\frac{A+D}{2}$ and simplify the expression with SYMPY package:

$$\begin{aligned} \frac{A+D}{2} &= \frac{1}{2}\frac{A^2 + BC + 1}{A} \\ &= \frac{1}{2}\left(\frac{w_{\text{in}}}{w_{\text{out}}} + \frac{w_{\text{out}}}{w_{\text{in}}}\right)\cos\zeta + \frac{1}{2}\left(\frac{1}{R_{\text{out}}} - \frac{1}{R_{\text{in}}}\right)\frac{\pi w_{\text{in}} w_{\text{out}}}{\lambda}\sin\zeta \end{aligned} \tag{D.21}$$

The self-consistent requirement of an eigensolution toan optical resonator means that after each round trip, the beam reproduces itself. Therefore: $w_{\text{out}} = w_{\text{in}}$ and $R_{\text{out}} = R_{\text{in}}$. Eq. D.21 therefore simplifies to:

$$\frac{A+D}{2} = \cos\zeta \tag{D.22}$$

or using trigonometry identity $\cos^2\alpha = \frac{\cos 2\alpha + 1}{2}$, we have:

$$\frac{A+D+2}{4} = \frac{\cos\zeta + 1}{2} = \cos^2\frac{\zeta}{2} \tag{D.23}$$

There is an ambiguity in the sign of ζ due to the multi-value nature of inverse cosine:

$$\cos(|\zeta|) = \cos(-|\zeta|) \tag{D.24}$$

This same ambiguity lies in square-root term when we try to find ζ from D.23

This problem is addressed by using the sign of element B since the sign of ζ dictates the sign of B:

$$\zeta = 2\cos^{-1}\left(\operatorname{sgn} B\sqrt{\frac{BA+D+2}{4}}\right) \tag{D.25}$$

This is the expression used in Chapter 3 to characterise the ring cavity.

D.3 Triangular cavity modes

The self-consistency requirement of the cavity modes means that the total phase shift after each round must be a multiples of 2π. Using parameters from Chapter 3, we have:

$$q2\pi = kL_p - (m+\frac{1}{2})\zeta_h(L_p) - (n+\frac{1}{2})\zeta_v(L_p) \tag{D.26}$$

which can be rearranged to give frequencies of cavity modes:

$$\nu_{q,mn} = FSR\left[1 + \left(m+\frac{1}{2}\right)\zeta_h(L_p) + \left(n+\frac{1}{2}\right)zeta_v(L_p)\right] \tag{D.27}$$

where $FSR = c/L_p$ is the free spectral range. The round-trip Gouy phase accumulation derived from ABCD matrix $\mathcal{C}_{h/v}$ in term of cavity parameters is:

$$\begin{aligned}
\zeta_h &= 2\cos^{-1}\left\{\operatorname{sgn}\left[-\frac{L_p}{2}\left(2-\frac{L_p\cos\theta}{R}\right)\right]\sqrt{-\frac{2-\frac{L_p\cos\theta}{R}}{2}}\right\} \\
\zeta_v &= 2\cos^{-1}\left\{\operatorname{sgn}\left[\frac{L_p}{2}\left(2-\frac{L_p}{R\cos\theta}\right)\right]\sqrt{\frac{2-\frac{L_p}{R\cos\theta}}{2}}\right\}
\end{aligned} \tag{D.28}$$

Appendix E

Image matching for phase camera dual operation

The below functions are used to assist with image matching of optical field seen by s- and p- cameras in the dual camera operation of a phase camera as discussed in section

```
import sys
import os
import numpy as np
import matplotlib.pyplot as plt
import scipy.ndimage as snd
from scipy.optimize import fmin_powell
from PIL import Image

subject_img = []
target_img = []



def correl_mismatch(im1, im2):
    """ Return negative correlation coefficient between two images
    flattened to 1D"""
    correl = np.corrcoef(im1.ravel(), im2.ravel())[0,1]
```

```
    return -correl

def xy_trans_img_fine(img, x_y_trans):
    """ Return copy of 'img' translated by 'x_y_trans'
    'x_y_trans' is a sequence or array length 2,representing
    the (x, y) translations in pixels
    ------------
    img: array shape(M,N)
       2D image to transform with translation 'x_pix_trans'
    x_y_trans: float, of the form [y_trans, x_trans]
       Number of pixels to translate 'img_slice';
       can be positive, negative, and does not need to be an integer
    """
    x_y_trans = np.array(x_y_trans)
    # Resample image using bilinearr iterpolation (order=1)
    trans_img = snd.affine_transform(img, [1, 1], -x_y_trans, order=1)
    return trans_img

def xytrans_rot_img(img, xy_trans_theta_rot):
    """ Return copy of 'img' translated by 'xy_trans' and
    rotated by 'theta_rot' about image centroid """
    # Translation by [y_trans, x_trans]
    x_y_trans = np.array([xy_trans_theta_rot[0], xy_trans_theta_rot[1]])
    # Resample image using bilinearr iterpolation (order=1)
    trans_img = snd.affine_transform(img, [1, 1], -x_y_trans, order=1)
    # Rotation about centre of mass
    theta = xy_trans_theta_rot[2]
    trans_rot_img = snd.rotate(trans_img,theta, reshape=False)

    return trans_rot_img

def cost_func_transrot(xy_trans_theta_rot):
    """ Give cost function at translation  and rotation values
    'xy_trans_theta_rot'
    """
    transformed = xytrans_rot_img(subject_img, xy_trans_theta_rot)
```

```
    return correl_mismatch(transformed, target_img)

def powell_parameters(guess_parr):
    best_params = fmin_powell(cost_func_transrot,guess_parr)
    return best_params

def recenter_img(img):
    """ Return copy of image 'img' with center of mass
    recentered to image's center
    """
    height  = np.shape(img)[0]
    width = np.shape(img)[1]
    xcenter = height/2
    ycenter = width/2
    center = np.array([ycenter, xcenter])
    COM = snd.center_of_mass(img)
    translation = center - COM
    recentered = xy_trans_img_fine(img, translation)

    return recentered

font = {'family' : 'Times New Roman',
        'size'   : 22}
##================================================
# Define directory in images are stored:
cam1 = {}
cam1['location'] = 'E:/17-06-27-NullTest/Signal_1/Pos0/'
cam1['prefix'] = 'img_'
cam1['suffix'] = '_Zyla4.2_1_000.tif'
cam1['first_frame'] = 0
cam1['no_of_frames'] = 500

cam2 = {}
cam2['location'] = 'E:/17-06-27-NullTest/Signal_1/Pos0/'
cam2['prefix'] = 'img_'
cam2['suffix'] = '_Zyla4.2_2_000.tif'
```

```
cam2['first_frame'] = 0
cam2['no_of_frames'] = 500

##=================================================
## Read image files:

iframe = 1
iframe_str = str(iframe).zfill(9)

# Cam1
filename1 = cam1['location']+cam1['prefix']+iframe_str+cam1['suffix']
im1 = Image.open(filename1)
imarray1 = np.array(im1,dtype=np.int64)

# Cam2
filename2 = cam2['location']+cam2['prefix']+iframe_str+cam2['suffix']
im2 = Image.open(filename2)
imarray2 = np.array(im2,dtype=np.int64)
imarray2 = np.fliplr(imarray2)

# Recenter both images:
imarray1 = recenter_img(imarray1)
imarray2 = recenter_img(imarray2)
corrcoeff1= correl_mismatch(imarray1,imarray2)
##=============================================================
## Matching image from cam2 to cam1:

subject_img = imarray2
target_img = imarray1
par0 = [0,0,-6]
best_params = powell_parameters(par0)
transformed_im2 = xytrans_rot_img(imarray2,best_params)
corrcoeff2= correl_mismatch(imarray1,transformed_im2)

## Residual image:
res_im = imarray1 - transformed_im2
```

```
fig1 = plt.figure()
plt.imshow(imarray1, origin= 'lower', aspect = 'equal', cmap = 'jet')
cbar = plt.colorbar()
cbar.set_label('Intensity (DN)')

fig2 = plt.figure()
plt.imshow(transformed_im2, origin= 'lower', aspect = 'equal', cmap = 'jet')
cbar = plt.colorbar()
cbar.set_label('Intensity (DN)')

fig3 = plt.figure()
plt.plot(imarray1.ravel(),transformed_im2.ravel(),'.')
plt.xlabel('Pixels in image 1')
plt.ylabel('Pixels in image 2')
plt.title('Correlation Coefficient: %s'%-corrcoeff2)

fig4 = plt.figure()
plt.imshow(res_im, origin= 'lower', aspect = 'equal', cmap = 'jet')
cbar = plt.colorbar()
cbar.set_label('Residual (DN)')
# fig4, ax1 = plt.subplots()
# ax1.plot(fine_rot, fine_mismatches,'b-')
# ax1.set_xlabel('Angle of rotation (degrees)')
# ax1.set_ylabel('Mean absolute difference (DN)',color='b')
# ax1.tick_params('y',colors='b')

# ax2 = ax1.twinx()
# ax2.plot(fine_rot,corrcoeffs,'r-')
# ax2.set_ylabel('Correlation Coefficient',color = 'r')
# ax2.tick_params('y',colors='r')
# fig4.tight_layout()
plt.show()
```

Appendix F

FINESSE simulation of phase camera

In this appendix, I attach the code for simulation of our phase camera set up, as shown in chapter 3. FINESSE [51] is one of the leading package for optical simulation in frequency domain and has been used extensively in LIGO community to better understand gravitational wave interferometer performance [36].

Notice that in current version of finesse, treatment of polarisations has not been implemented. The quarter wave plate, Pockels cell and polarising beam splitter are simulated by the built in amplitude modulator `mod AM1` (see below). The phase shifting at Pockels cell in phase camera is implemented according by shifting the phase parameter of `mod AM1`.

PhaseCam_finesse

September 3, 2019

In [1]:
```
import pykat
import matplotlib.pyplot as plt
import numpy as np

pykat.init_pykat_plotting(fmts=['svg'])
```

```
C:\Users\Cao\Anaconda3\lib\site-packages\h5py\__init__.py:36: FutureWarning: Conversion of the
  from ._conv import register_converters as _register_converters
```

```
                                                ..-
    PyKat 1.1.331                              _                  '(
                                              \`.|\.__...-"""-_." )
        ..+-----.._                           /  ' `             .-'
    . '            `:                        7/* _/._\     \    (
   (        '::;;+;;:                        `-"' =" /,`"" `) /
   L.        \`:::a:f                              c_/     n_'
   ..`--...___`.  .    ,
    `^-...____:   +.      www.gwoptics.org/pykat
```

In [3]:
```
base = pykat.finesse.kat()
base.parse("""
# Simulation of current experimental setup
# Three mirror ring cavity:
        # M1, M2: flat, R = 0.99,  loss = 0.0001
        # M3: RoC = 1 m, R = 0.997, loss = 0.0001 #Example loss, there is no recorded c

        # side: 24 mm, 2x264.2 mm

## Pre-Cavity Component
##=============================================================================

l NPRO 10m 0 nl                                 # NPRO laser, 1064 nm, 10 mW

#s sltoEOM1 0.570 nl nEOM1in
#mod EOM1 12M 0.3  1 pm nEOM1in nEOM1out               # modulator 1 for locking
```

```
s sNPROtoSM1 1.038 nl nSM1in                # distance from EOM1 to steering mirror 1

bs2 SM1 1 0 0 45 nSM1in nSM1out dump dump        # steering mirror 1

s sSM1toSM2 0.326 nSM1out nEOM2in                # space between 1st and 2nd steering r

mod EOM2 15.4M 0.35 1 pm nEOM2in nEOM2out        # modulator 2 to create RF field

s sEOm2toSM2 0.245 nEOM2out nSM2in

bs2 SM2 1 0 0 45 nSM2in nSM2out dump dump        # steering mirror 2

s sSM2toSM3 0.232 nSM2out nSM3in               # space between 2nd and 3rd steering m

bs2 SM3 1 0 0 -45 nSM3in nSM3out dump dump         # steering mirror 3

attr SM3 xbeta 100u
attr SM3 ybeta 100u

s sSM2toMC 0.15065 nSM3out nMC1UNC1in               # Space between 3rd steering mirr
#s sSM2toMC 1 nl nMC1UNC1in

## Mode Cleaner Cavity
##=============================================================================

## First flat mirror, modelled as bs-s-bs
bs MC1UNC1 0.04 0.95 0 43.7 nMC1UNC1in dump nMC1UNC1trans dump
s sMC1substrate1 7.22m 1.4496 nMC1UNC1trans nMC1HRin                              # S
bs2 MC1HR 0.995 0.0001 0 28.4637 nMC1HRin nMC1HRrefl nMC1HRtrans nMC1HRfromMC3       #
s sMC1substrate2 7.22m 1.4496 nMC1HRrefl nMC1UNC2in
bs MC1UNC2 0.04 0.95 0 28.4637 nMC1UNC2in dump nMC1UNC2trans dump
s sMC1HRtosMC2HR 24m nMC1HRtrans nMC2HRin                                      # Spac

## Second flat mirror,
bs2 MC2HR 0.995 0.0001 0 43.7 nMC2HRin nMC2HRrefl nMC2HRtrans dump
s sMC2substrate 7.22m nMC2HRtrans nMC2UNCin                                      # MC
bs MC2UNC 0.04 0.95 0 28.4637 nMC2UNCin dump nMC2UNCtrans dump
s sMC2HRtoMC3 264m nMC2HRrefl nMC3in                                              # U

## MC3, curved mirror, RoC 1 meter
bs2 MC3 0.9997 0.0001 0 2.6 nMC3in nMC3refl dump dump                              #
attr MC3 Rc 1
s sMC3toMC1HR 264m nMC3refl nMC1HRfromMC3                                      # dist

s s1 0 nMC2UNCtrans no
```

```
        cav MC MC2HR nMC2HRin MC2HR nMC2HRrefl

        trace 2
        """)
```

In [4]:
```
kat = base.deepcopy()
kat.parse("""
s s1 1 nMC2UNCtrans n1
lens lens1 1 n1 n2
s s2 0.2 n2 nAM1in
mod AM1 15.4M 1.5 1 am 0 nAM1in nAM1out
s sAM1tolens2 0.2 nAM1out n3
lens lens2 1 n3 n4
s s3 0.2 n4 nCCD

beam outputCCD nCCD
xaxis outputCCD x lin -5 5 200
x2axis outputCCD y lin -5 5 200

phase 3
maxtem 4
"""
)
phases = []
for n in np.arange(0,90,2):
    phases.append(n)
    phases.append(n+180)
    phases.append(n+90)
    phases.append(n+270)

kat.MC3.xbeta = 24e-6
kat.MC3.ybeta = 10e-6
kat.EOM2.f = 15.4e6
#demod_phase = np.array([0,90,180,270])
kat.SM3.xbeta = 200e-6
kat.SM3.ybeta = 250e-6
images = np.empty((len(phases),201,201))
for (idx,iphase) in enumerate(phases):
    kat.AM1.phase = iphase
    out = kat.run(cmd_args=['-cr=on'])
    images[idx,:,:]= np.reshape(out.z,(201,201))
    print(out)
```

```
Removed existing object 's1' of type <class'pykat.components.pykat.components.space_70'> to ad
----------------------------------------------------------------
Running kat - Started at 2019-06-26 00:55:47.137033


100% | ETA:  0:00:00 | Calculating
```

Appendix G

Thermal modelling of SAMS suspension

G.1 A baseline model of suspension

In order to testing various derived couplings in this document, we use a simple baseline model with a simple CFM at the bottom stage without no flexure holder and a mass of 1 kg. CFM's dimension has been selected to satisfy actuation and tensile stress requirement (see E1900126). The lower stage use 4 wire suspension, and upper stage use 2 wire suspension. The parameters and definition of these parameters are given in table G.1 and figure G-3.

Symbol	Parameter	Value
	Lower stage	
m_2	Bottom stage mass	1 kg
$\varnothing_M$	CFM's outer diameter	120 mm
t_R	Thickness of actuating ring	38.8 mm
dz	Actuating ring offset from mirror's barrel	-1.1 mm
t_M	Mirror's thickness	6 mm
d_2	Distance between initial COM x_n to the line joining suspension points	0 mm
s_3	x-displacement of suspension points from COM	30 mm
Ω_2	Angle between suspension wire and vertical	0 rad
	Upper stage	
m_2	Top stage mass	0.5 kg
d_0	Distance between COM x_m to the upper suspension point	15 mm
d_1	Distance between COM x_m to the line joining lower suspension points	15 mm
s_2	x-displacement of lower suspension points from COM	30 mm
Ω_1	Angle between upper suspension wire and vertical	0 rad
	Suspension	
l_2	Length of bottom stage suspension wire	150 mm
$\varnothing_{\textbf{wire}}$	Suspension wire cross sectional diameter	127 μm
	Temperatures	
T_h	Maximum CFM temperature	60°C
T_a	Ambient temperature	20°C
	Material properties	
	Steel wire	
E_0	Young's modulus at room temperature	210 GPa
∂E_T	Thermal coefficient for Young's modulus	-3.02e-4 1/K
α	Thermal expansion coefficient of steel wire	12e-6 1/K

Table G.1: Table of parameters used in a baseline SAMS design

Vertical shift of bottom mass

Vertical shift due to thermal dependent properties of suspension wires

The two main thermal properties that affect the length of suspension wires are thermal expansion of steel wire and temperature-dependent Young's modulus. For steel musics wires used in SAMS suspension, we assume a linear thermal expansion coefficient of 12 μm/m/K. Young's modulus dependence on temperature of steel is presented by a phenomenological exponential function from [179]:

$$E(\Delta T) = E_0 \exp\left[-\frac{1}{2}\left(\frac{\Delta T}{e_3}\right)^{e_1} - \frac{1}{2}\left(\frac{\Delta T}{e_4}\right)^{e_2}\right] \tag{G.1}$$

where $e_1 = 3.768,\ e_2 = 1,\ e_3 = 639°\text{C},\ e_4 = 1650°\text{C}$ and ΔT is the change in temperature from 20°C. The region between $\Delta T = 0$ to 40 K can be well approximated by a linear function of the form:

$$E(\Delta T) = E_0\left(1 + \partial E_T \Delta T\right) \tag{G.2}$$

where E_0 is Young's modulus measured at 20^oC, which is 210 GPa and ∂E_T is linear coefficient given by -3.02e-4 GPa/GPa/K. In order to evaluate the stretch in the wire by these thermal effects. We first needs to obtain the temperature profile for a suspension wire heated from one end. Assuming the upper stage is large with large surface area and is far away from the bottom stage where the heat source is installed, its temperature with be approximately constant at ambient temperature T_a. In equilibrium, due to high thermal conductivity of both aluminium and steel wires, the heated end of fibre will be at the same temperature as the actuating ring. Here, we assume an upper limit of $T_h = 60°\text{C}$. Thus we define $\delta T = T_h - T_a$ as the difference in temerature between the two ends of the wire. Furthermore, with high thermal conductivity of steel, heat conduction is assumed to be the dominating process when compared to radiation. The temperature profile along the wire is

therefore simply described by a linear equation:

$$T(x) = \frac{\delta T}{l}x + T_a \tag{G.3}$$

where x is distance from the wire's cold end at the upper stage. Now to solve for the stretch of the wires, we consider Hooke's law which relate stress and strain, in which we include thermal strain caused by thermal expansion:

$$\begin{aligned} \sigma &= E(\epsilon - \alpha\Delta T) \\ \therefore \frac{mg}{4A} &= E_0(1 + \partial E_T \Delta T(x)) \left(\frac{du}{dx} - \alpha\frac{\delta T}{l}x\right) \end{aligned} \tag{G.4}$$

where u is displacement along x-axis, A is the cross-sectional area a steel wire and $1/4$ in stress accounts for the load's being shared between four suspension wires

Equation G.4 can be re-arranged and integrated to obtain the displacement of the wire:

$$\Delta l = \frac{mg}{4AE_0}\int_0^l dx \frac{1}{1 + \partial E_T \frac{\delta T}{l}x} + \alpha\int_0^l dx \frac{\delta T}{l}x \tag{G.5}$$

An expression for the stretching of the wire can then be simply derived to be:

$$\Delta l = \frac{mg}{4AE_0}\frac{l}{\partial E_T \delta T}\ln\left(1 + \partial E_T \delta T\right) + \frac{\alpha \delta T l}{2} \tag{G.6}$$

For a bottom mass m of 1 kg, and suspension wires of 127 μm in diameter, at T=60°C results in a stretch of 175 μm, in which 139 μm change is caused by temperature-dependent Young's modulus.

Vertical shift due to thermal expansion of aluminium disc

FEA model shows that as the CFM heats up, the radius of a 120 mm OD CFM can change up to 56 μm at ΔT = 40 K. This would create a small angle Ω_T between a suspension wire and the vertical (see figure G-1). Consider a baseline design in which the mirror is suspended vertically in its cold state. As the radius changes by Δr, the distance l' can be found from $l + \Delta l$ and initial wire's length l:

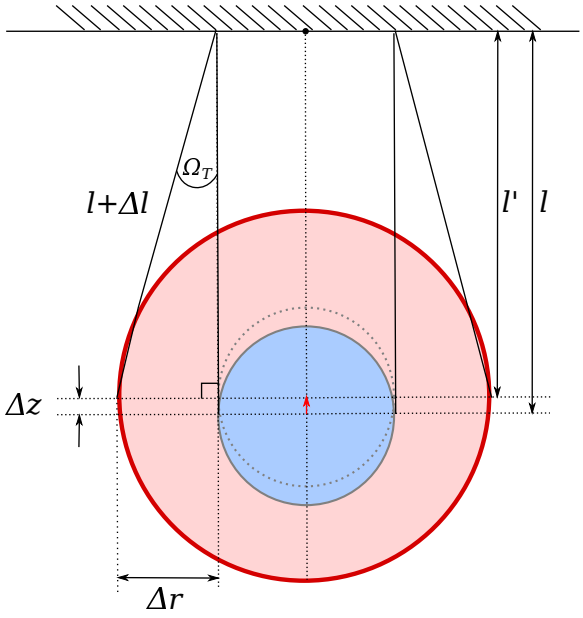

Figure G-1: Front view of a suspended CFM as it is heated up (not to scale). Radial expansion creates and angle between suspension wire and the vertical, effectively shortens the wire and shift the suspended optics upward

$$l' = \sqrt{(l + \Delta l)^2 - \Delta r^2} \tag{G.7}$$

and the shift Δz, which is the overall shift due to both wire extension and CFM radial expansion, is the difference between l' and l. Using $\Delta z = 56\mu$m and $l = 150$mm, we found $\Delta z = -174.986\mu$m, which means the dominating effect is still due to wire extension discussed in previous section. Radial expansion only shifts the mass upward by 10.5 nm.

Notice that the radial change at different positions along the barrel of the optics will vary. There is a 2.1 nm difference in upward shift between the front and back of a 1kg 120-mm-OD CFM, whose barrel length is approximate 40 mm. This difference will thus couple through as a change in pitch of a reflected beam , which is estimated to be 107 nrad at $\Delta T = 40$K. This change in pitch is much smaller than that caused by shift in optics' centre of mass, which will be discussed subsequently.

In conclusion, for our baseline design, we expect a sag in suspended CFM's position of approximately 175 μm at $\Delta T = 40$K. For a nominal 1 m ROC mirror, this implies a change in pitch of 350 μrad for beam reflected off the CFM.

Change in pitch due to shift in centre of mass

Single pendulum

The change in convexity of CFM with increasing temperature results in shift of its COM along the optical axis (*x*-axis in figure G-2) from x_n to $x'_n = x_n + \Delta x$. Assuming that the CFM is suspended symmetrically from it COM at cold state at distance r. The mass can be divided into two equal halved with masses $m_1 = m_2 = m/2$ of effective thicknesses of $t/2$. Therefore, the position of a CFM in its cold state can be given by:

$$\begin{aligned} x_n &= \frac{m_1 x_{m1} + m_2 x_{m2}}{m} \\ &= \frac{1}{2m}\left[m x_{m_1} + m\left(x_{m1} + \frac{t}{2}\right)\right] \\ &= x_{m1} + \frac{t}{2} \end{aligned} \tag{G.8}$$

Now consider that CFM's COM shifts to more positive x by Δx at some temperature $T > T_{\text{ambient}}$. This would be equivalent to adding some extra mass Δm onto one half of the initial mass and removed the same amount of Δm from the other half. We can then find an expression for this Δm in term of Δx:

$$\begin{aligned} x'_n &= \frac{(m/2 - \Delta m)x_{m1} + (m/2 + \Delta m)(x_{m1} + t/2)}{m} \\ &= x_n + \frac{\Delta m t}{2m} = x_n + \Delta x \\ \therefore \Delta m &= \frac{2m\Delta x}{t} \end{aligned} \tag{G.9}$$

We can thus treat the effect of shift in CFM's COM as applying two equal but opposing forces at the COM's of the mass' two halve at $t/4$ from x_n:

$$F_1 = \frac{2mg\Delta x}{t}\hat{z} \tag{G.10}$$

$$F_2 = -\frac{2mg\Delta x}{t}\hat{z} \tag{G.11}$$

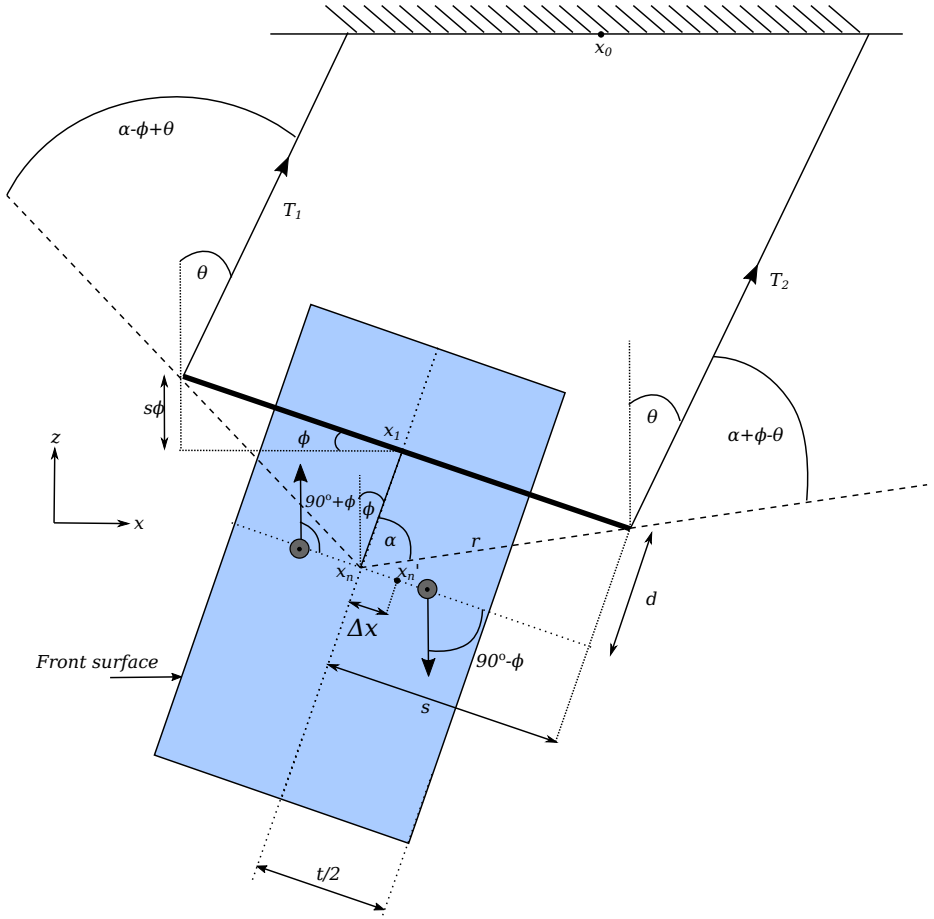

Figure G-2: Side view of a cylindrical mass in with tilt and longitudinal motion in an single pendulum suspension

The two forces cancel one another out but provide a torque that tilts the mass around y-axis:

$$\begin{aligned}\Sigma\tau_y &= -mg\frac{\Delta x}{2}\left[\sin\left(\frac{\pi}{2}+\phi\right)+\sin\left(\frac{\pi}{2}-\phi\right)\right] \\ &= -mg\Delta x\cos\phi \simeq mg\Delta x\left(1-\frac{\phi^2}{2}\right)\end{aligned} \tag{G.12}$$

We can write down the equations of motion (e.o.m) for tilt and longitudinal motions of the a mass in single pendulum suspension, following Calum Torrie's

formulation in [200]:

$$m\ddot{x}_n = -\frac{mg}{l\cos\Omega}(x_n - x_0) + \frac{mgd}{l\cos\Omega}\phi \tag{G.13}$$

$$I_y\ddot{\phi} = \frac{mgd}{l\cos\Omega}(x_n - x_0) - \left(mgd + \frac{mgd^2}{l\cos\Omega} + \frac{mgs^2\sin^2\Omega}{l\cos\Omega} + 2ks^2\cos^2\Omega\right)\phi \tag{G.14}$$

where the parameters in used are:

$l =$ the length of a wire

$\Omega =$ angle formed between suspension wire with the vertical in zy-plane, assumed to be zero for baseline design

$k =$ spring constant of suspension wire

$s = r\sin\alpha =$ the half separation of 2 wires in x-direction

$d = r\cos\alpha =$ the distance the wires break-off above the line through COM

$x_0 =$ the midpoint of the line joining two suspension wires in x-direction

with $\Omega = 0$, equations G.13 and G.14 are simplified to:

$$m\ddot{x}_n = -\frac{mg}{l}(x_n - x_0) + \frac{mgd}{l}\phi \tag{G.15}$$

$$I_y\ddot{\phi} = \frac{mgd}{l}(x_n - x_0) - \left(mgd + \frac{mgd^2}{l} + 2ks^2\right)\phi \tag{G.16}$$

Since there is no forces acting on the mass longitudinally:

$$\Sigma F = 0 = -\frac{mg}{l}(x_n - x_0) + \frac{mgd}{l}\phi$$

$$x_n = x_0 + d\phi \tag{G.17}$$

If $d = 0$, then tilt and longitudinal motion become uncoupled.

The shift in COM results in a torque acting on the suspended mass as discussed

above. The e.o.m for tilt then becomes:

$$\Sigma\tau = -mg\Delta x\left(1-\frac{\phi^2}{2}\right) = \frac{mgd^2}{l}\phi - \left(mgd + \frac{mgd^2}{l} + 2ks^2\right)\phi$$
$$\therefore \phi = \frac{1}{\Delta x}\left[-\left(d+\frac{2ks^2}{mg}\right) + \sqrt{\left(d+\frac{2ks^2}{mg}\right)^2 + 2\Delta x^2}\right] \tag{G.18}$$

Had we used the first order approximation of $\cos\phi = 1$ for small angle, ϕ could have been found as:

$$\phi = \frac{\Delta x}{d+\frac{2ks^2}{mg}} + \mathcal{O}\left(\Delta x^3\right) \tag{G.19}$$

By performing Taylor series expansion of the square-root term in expression G.18, equation G.19 can be obtained:

$$\sqrt{\left(d+\frac{2ks^2}{mg}\right)^2 + 2\Delta x^2} \simeq d + \frac{2ks^2}{mg} + \frac{\Delta x^2}{d+\frac{2ks^2}{mg}} + \mathcal{O}\left(\Delta x^4\right) \tag{G.20}$$

Sanity check of expression G.19 reveals expected physical behaviours:

- As $k \to \infty$ (suspension wire becomes highly stiff), there is no tilt of the optics

- As $s \to \infty$ (suspension points are far away COM), tilt also reduces

- As $m \to 0$ (mass of suspended optics becomes smaller), tilt also reduces

Double pendulum suspension

SAMS suspension would be a two-stage suspension. The e.o.m's for longitudinal and tilt motion of a double pendulum are:

$$m_1\ddot{x}_n = -(m_1+m_2)g\theta_1 + m_2 g\theta_2 \tag{G.21}$$

$$m_2\ddot{x}_m = -m_2 g\theta_2 \tag{G.22}$$

$$\begin{aligned} I_{1y}\ddot{\phi_1} = &-(m_1+m_2)gd_0(\phi_1-\theta_1) - 2k_1 s_0^2\cos^2\Omega_1\phi_1 - m_2 g d_1(\phi_1-\theta_2) \\ &- 2k_2 s_2^2\cos^2\Omega_2(\phi_1-\phi_2) - \frac{(m_1+m_2)gs_0\sin^2\Omega_1}{l_1\cos\Omega_1}\phi_1 \\ &- \frac{m_2 g s_2^2\sin^2\Omega_2}{l_2\cos\Omega_2}(\phi_1-\phi_2) \end{aligned} \tag{G.23}$$

$$I_2\ddot{\phi_2} = -m_2 g d_2(\phi_2-\theta_2) - 2k_2 s_2^2\cos^2\Omega_2(\phi_2-\phi_1) - \frac{m_2 g s_2\sin^2\Omega_2}{l_2\cos\Omega_2}(\phi_2-\phi_1) \tag{G.24}$$

where:

$$\theta_1 = \frac{x_n - x_0 - \phi_1 d_0}{l_1\cos\Omega_1} \tag{G.25}$$

$$\theta_2 = \frac{x_m - x_n - \phi_2 d_2 - \phi_1 d_1}{l_2\cos\Omega_2} \tag{G.26}$$

The parameters used are defined in figure G-3

For SAMS suspension, the top stage will be a single loop suspension and the e.o.m's for tilt and longitudinal motion (equations G.21 to G.23) can be rewritten in the form of matrix of coupled equations:

$$\begin{bmatrix} 0 \\ -m_2 g\Delta x\frac{s_2}{s_3} \\ 0 \\ -m_2 g\Delta x \end{bmatrix} = \begin{bmatrix} k_{11} & k_{12} & k_{13} & k_{14} \\ k_{21} & k_{22} & k_{23} & k_{24} \\ k_{31} & k_{32} & k_{33} & k_{34} \\ k_{41} & k_{42} & k_{43} & k_{44} \end{bmatrix} \begin{bmatrix} x_n \\ \phi_1 \\ x_m \\ \phi_2 \end{bmatrix} \tag{G.27}$$

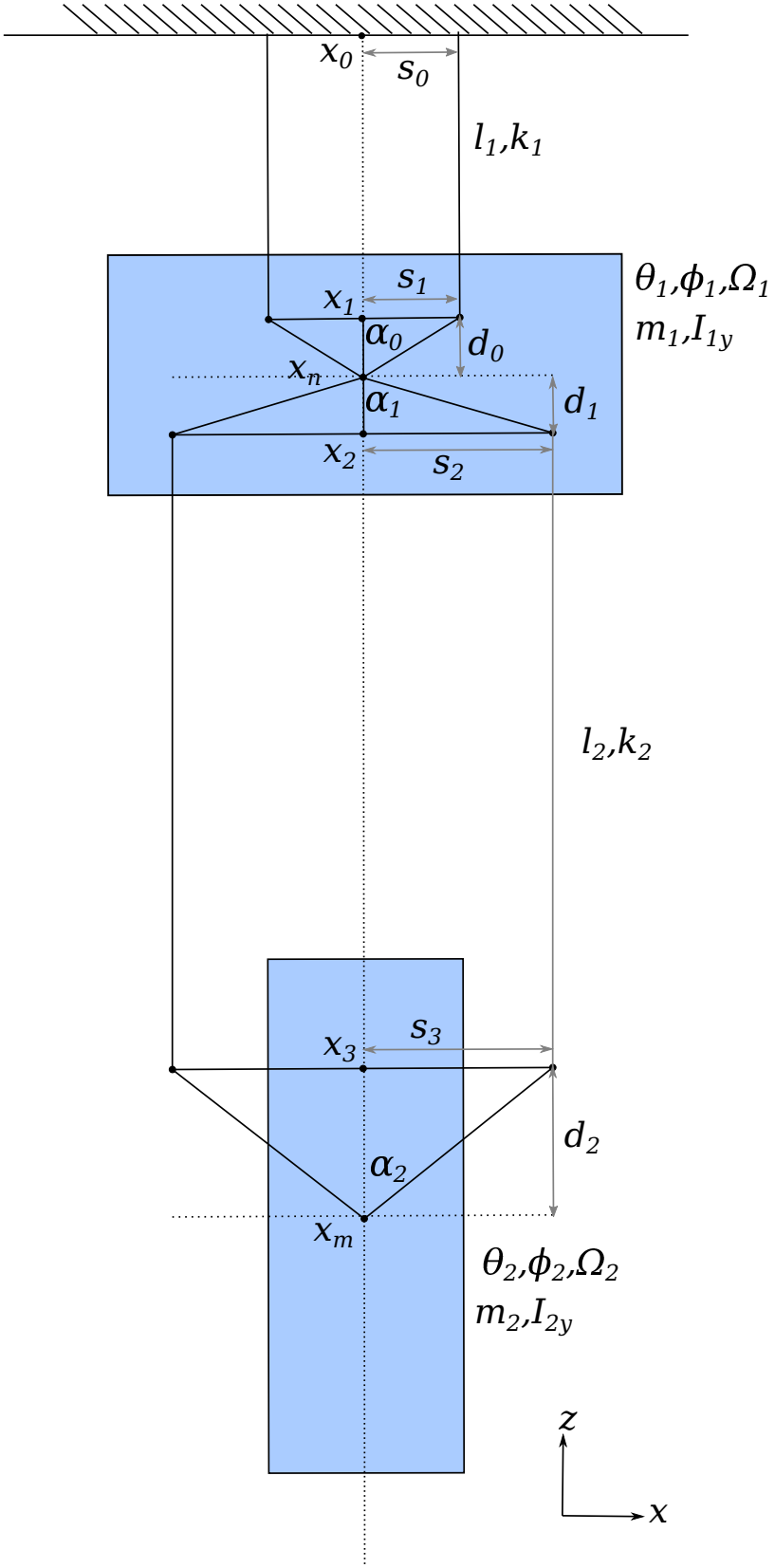

Figure G-3: Schematics of double pendulum suspension from the side

and k_{ij} coefficients are given as following:

$$
\begin{aligned}
k_{11} &= -\frac{(m_1+m_2)g}{l_1\cos\Omega_1} - \frac{m_2 g}{l_2\cos\Omega_2}, k_{12} = \frac{(m_1+m_2)gd_0}{l_1\cos\Omega_1} - \frac{m_2 g d_1}{l_2\cos\Omega_2} \\
k_{13} &= \frac{m_2 g}{l_2\cos\Omega_2}, k_{14} = -\frac{m_2 g d_1}{l_2\cos\Omega_2}, k_{21} = \frac{(m_1+m_2)gd_0}{l_1\cos\Omega_1} - \frac{m_2 g d_1}{l_2\cos\Omega_2} \\
k_{22} &= -(m_1+m_2)gd_0\left(1+\frac{d_0}{l_1\cos\Omega_1}\right) - m_2 g d_1\left(1+\frac{d_1}{l_2\cos\Omega_2}\right) \\
&\quad - 2k_2 s_2^2\cos^2\Omega_2 - \frac{m_2 g s_2^2\sin^2\Omega_2}{l_2\cos\Omega_2} \\
k_{23} &= \frac{m_2 g d_1}{l_2\cos\Omega_2}, k_{24} = \frac{m_2 g(d_1 d_2 + s_2^2\sin^2\Omega_2)}{l_2\cos\Omega_2} + 2k_2 s_2^2\cos^2\Omega_2 \\
k_{31} &= \frac{m_2 g}{l_2\cos\Omega_2}, k_{32} = \frac{m_2 g d_1}{l_2\cos\Omega_2}, k_{33} = -\frac{m_2 g}{l_2\cos\Omega_2}, k_{34} = \frac{m_2 g d_2}{l_2\cos\Omega_2} \\
k_{41} &= \frac{m_2 g d_2}{l_2\cos\Omega_2}, k_{42} = -\frac{m_2 g d_2 d_1}{l_2\cos\Omega_2} + 2k_2 s_2^2\cos^2\Omega_2 + \frac{m_2 g s_2\sin^2\Omega_2}{l_2\cos\Omega_2} \\
k_{43} &= \frac{m_2 g d_2}{l_2\cos\Omega_2}, k_{44} = -\frac{m_2 g d_2^2}{l_2\cos\Omega_2} - 2k_2 s_2^2\cos^2\Omega_2 - \frac{m_2 g s_2\sin^2\Omega_2}{l_2\cos\Omega_2}
\end{aligned}
\tag{G.28}
$$

This system of equations can be solved for change in longitudinal translation and tilt of each mass, albeit being rather complicated. The baseline model assumes that $\Omega_1 = \Omega_2 = 0$, $d_2 = 0$. The four degress of freedom that describe tilt and longitudinal motion of the system is then solved to be:

$$x_n = \Delta x \frac{d_0 m_2(s_2+s_3)}{s_3(d_0 m_1 + d_0 m_2 + d_1 m_2)} \tag{G.29}$$

$$\phi_1 = \Delta x \frac{m_2(s_2+s_3)}{s_3(d_0 m_1 + d_0 m_2 + d_1 m_2)} \tag{G.30}$$

$$x_m = \Delta x \frac{m_2(d_0 s_2 + d_0 s_3 + d_1 s_2 + d_1 s_3)}{s_3(d_0 m_1 + d_0 m_2 + d_1 m_2)} \tag{G.31}$$

$$\phi_2 = \frac{\Delta x m_2(d_0 g m_1 s_3 + d_0 g m_2 s_3 + d_1 g m_2 s_3 + 2k_2 s_2^3 + 2k_2 s_2^2 s_3)}{2k_2 s_2^2(d_0 m_1 + d_0 m_2 + d_1 m_2)} \tag{G.32}$$

For $s_2 = s_3$, these equations reduce to:

$$x_n = 2\Delta x \frac{d_0 m_2}{d_0 m_1 + d_0 m_2 + d_1 m_2} \tag{G.33}$$

$$\phi_1 = 2\Delta x \frac{m_2}{d_0 m_1 + d_0 m_2 + d_1 m_2} \tag{G.34}$$

$$x_m = 2\Delta x \frac{m_2(d_0+d_1)}{d_0m_1+d_0m_2+d_1m_2}$$
$$= x_n + \frac{2\Delta x m_2 d_1}{d_0m_1+d_0m_2+d_1m_2} \quad \text{(G.35)}$$
$$\phi_2 = \frac{\Delta x m_2(d_0gm_1+d_0gm_2+d_1gm_2+4k_2s_2^2)}{2k_2s_2^2(d_0m_1+d_0m_2+d_1m_2)}$$
$$= \frac{\Delta x m_2 g}{2k_2s_2^2} + \phi_1 \quad \text{(G.36)}$$

A few key points observe here are:

- Tilt angle of bottom stage optics are sum of upper stage tilt as well as tilt caused by the shift in CFM COM in the single pendulum suspension
- Greater vertical separation between suspension points of upper and lower sets of wires reduce the coupling of COM shift from lower stage to upper stage
- As the upper stage increases in mass, it effectively becomes stiffer and less susceptible to tilt and longitudinal motion caused by shift in COM of bottom stage
- If $d_0 = 0$ (i.e. the suspension point of the upper stage is at its centre of mass) then there is no longitudinal change of upper mass as it is pivoted at its COM.

The shift in COM of a CFM is linear with its change in temperature. For a baseline 1kg configuration optics with 6 mm 2-inch diameter mirror and 120 mm OD, 38-mm-thick actuating ring, FEA model shows that this shift can be described as a linear function $\Delta x = 0.71[\mu m/K]\Delta T$. At $T = 60°$C, $\Delta x = 28.4\mu m$ from its cold state. Assuming the following parameters:

$E = 210$ GPa : Suspension wire Young's modulus

$\varnothing_{\text{wire}} = 127\mu m$: Diameter of suspension wire

$l_2 = 150$ mm

$s_2 = 30$ mm

$m_1 = 0.5$ kg

$d_0 = d_1 = 15$ mm

Since the bottom stage has 4 wire suspension architecture, k_2 would become $2k_2$. The change in tilt of the bottom stage is dominated by the induced change in top stage:

$$\phi_1 = 1.52\text{mrad}$$
$$\phi_2 = 4.4\mu\text{rad} + \phi_1$$

The longitudinal change of each stage is:

$$x_n = 22.8\mu m$$
$$x_m = 45.6\mu m$$

The new COM x'_m is therefore 74μm relative to x_0. At $T = 60°$, the mirror's front surface is 23.0095 mm from its COM, compared to 23.046 mm at $T = 20°$. The mirror's front surface thus has shifted longitudinally by 74μm-(46μm - 9.5μm) = 37.5 μm.

Effects on electromagnetic linear actuators

This section focuses on thermal effects on electromagnetic linear actuators, which include dithering voicecoils for alignment error signal and BOSEMs at upper stage for active damping and DC steering. For the baseline model, actuators are assued to have the same parameter as those in HTTS. These parameters are given in Table G.2:

Heat conduct from CFM to the magnets attached directly onto the optics would result in magnet's magnetisation. A magnet's remanance magnetic field B_r is defined as the value B at the point on the hysteresis curve where H is reduced zero. B_r drifts with changes in temperature. Reversible temperature coefficient (RTC) is

BOSEM Specifications [120]		
Symbol	**Parameter**	**Value**
R_c	Coil resistance	42.7 Ω
L_c	Coil inductance	11.9 mH
N	Number of windings	800
$\varnothing_w$	wire diameter	0.202 mm (AWG 32)
K_c	Force coupling constant	0.021 N/A (with $\varnothing$2mm$\times$3mm magnet)
$I_{c,max}$	Maximum coil current	100 mA
Driver Specifications [12]		
V_s	Supply voltage	$\pm$14 V
$I_{o,max}$	Maximum output current	500 mA
R_s	Series resistance	1200Ω, 3W
$I_{R_s,max}$	Maximum resistor current	50 mA (not a strong constraint)
Target operating conditios		
θ_d	Angle amplitude	$\geq$ 0.5 nrad, optimal: 5 nrad
f_d	Frequency	2-3 kHz

Table G.2: Assumed BOSEM's parameters for computation of thermal effect on SAMS linear actuator. The two main limiting factors are the maximum coil current and supply voltage.

a quantity used to describe this drift:

$$\text{RTC} = \frac{\Delta B_r}{B_r}\frac{1}{\Delta T} \times 100\% \tag{G.37}$$

Current magnets used is HAM Tip-Tilt Suspension (HTTS) are Samarium-Cobalt (SmCo) 2:17 magnets (the 2:17 ratio implies that a composition of 2 rare earth samarium atoms per 17 atoms of transition metals, which consist of mainly colbalt and traces of copper, iron, zirconium and hafnium). SmCo 2:17 has one of the best performing RTC, at typically -0.035%/°C [67, 129]. The typical B_r of SmCo 2:17 at room temperature is between 1.08 - 1.10 T [136] at room temperature T=20°C. For $\Delta T = 40K$, the change in B_r is thus:

$$\begin{aligned}\Delta B_r(T) &= B_r(T = 20°\text{C})\frac{\text{RTC}\Delta T}{100} \\ &= -0.0154 \text{ T}\end{aligned} \tag{G.38}$$

The change in magnetisation M can thus be approximated by:

$$\Delta M \approx \frac{\Delta B_r}{\mu_0} \tag{G.39}$$

where μ_0 is vacuum permeability $4\pi \times 10^{-7}$ H/m. The change in dipole moment p_m of a volume V with uniform magnetisation $M + \Delta M$ is:

$$\Delta p_m = \Delta M V = \pi r^2 l \frac{\Delta B_r}{\mu_0} \tag{G.40}$$

Assuming the same magnet's dimension as in current HTTS, which is ⌀-2-mm $\times$ 3-mm-long, the change is -4.62$\times 10^{-4}$ J/T for ΔT =40 K (p_m(T=20K) $= 0.033$J/T). This change in dipole moment would consequently reduce force coupling constant between coils and magnets. We follow formulation from [29] to estimate this change in coupling constant K_c.

Consider a current element with current density $\boldsymbol{dJ} = (j_x, j_y, j_z)$ at position $\boldsymbol{r'} = (x', y', z')$. Then the distance between this current element and an arbitrary test point in space $\boldsymbol{r} = (x, y, z)$ is:

$$\imath = ||\boldsymbol{r} - \boldsymbol{r'}|| \tag{G.41}$$

Then the magnetic vector potential at the test point due to this current element is given by:

$$\mathbf{A}(\boldsymbol{r}) = \frac{\mu_0}{4\pi} \frac{\boldsymbol{dJ}}{\imath} \tag{G.42}$$

and the magnetic field is given by $\mathbf{B} = \nabla \times \mathbf{A}$.

$$\boldsymbol{B} = \frac{\mu_0}{4\pi} \frac{1}{\imath^3} \left[j_z(y - y') + j_y(z - z'), j_z(x - x') + j_x(z - z'), j_x(y - y') + j_y(x - x') \right] \tag{G.43}$$

The potential energy U of a dipole moment $\Delta \boldsymbol{M} = (\Delta M_x, \Delta M_y, \Delta M_z)$ is given by the dot product between $\boldsymbol{B}$ and m, the force on this dipole moment placed in the field is given as $d\boldsymbol{F} = \nabla U = \nabla(\Delta \boldsymbol{M} \cdot \boldsymbol{B})$. Ignoring the edge effect, then $\Delta \boldsymbol{M} = (0, 0, M_z)$ and $d\boldsymbol{F} = \Delta M_z \nabla dB_z$. The change in force coupling constant is

Magnets	Material	RTC (%/K)	$\frac{\Delta M}{M}$	$K_{c(20°C)}$(N/A)	$K_{c(60°C)}$(N/A)
⌀2×3 mm	SmCo 2:17	-0.035	-0.014	0.021	0.027
⌀5×10 mm	NdFeB	-0.1	-0.04	0.393	0.388

Table G.3: Effect of increasing magnet's temperature by $\Delta T = 40K$ to force coupling of SmCo and NdFeB magnets

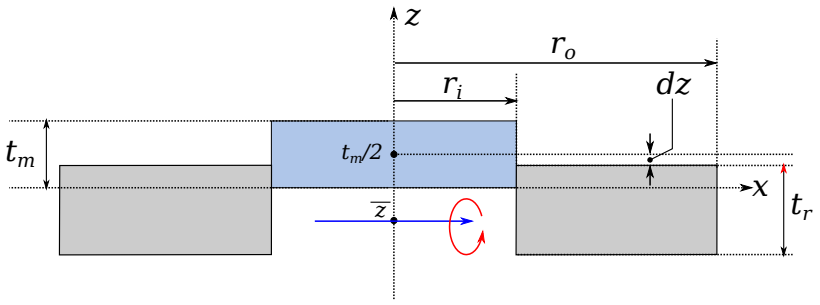

Figure G-4: Diagram showing cross-section of CFM in x-y plane

therefore proportional to change in magnetisation. Table G.3 summaries the effect of increasing temperature from 20°C to 60°C on the force coupling constant for both ⌀2×mm SmCo 2:17 magnet (used in existing tip-tilt suspension) and ⌀5×10mm NdFeB magnet (used in small triple suspension). The change in force coupling constant assist with estimating operating temperature of voice coil in the next section. However, one can see from table G.3 that the effect caused by reduced magnetisation at an elevated temperature is small.

Dithering voice coil requirement

To compute operation requirements on dithering voice coil, we first find the moment of inertia about its COM. Consider diagram G-4, $\overline{x}$ and $\overline{y}$ components of COM is 0 due to symmetry. $\overline{z}$ component of COM is given by:

$$\overline{z} = \frac{M_z}{m_{\text{CFM}}} = \frac{1}{m_{\text{CFM}}} \iiint z\rho(r,\theta,z) r dr d\theta dz \tag{G.44}$$

where M_z is the z moment, which is given by the integral term in equation G.44. This integral can be computed by evaluating the moment of mirror and actuating

ring separately:

$$\begin{aligned} M_z &= \rho_{SiO_2} \int_0^{t_M} z dz \int_0^{2\pi} d\theta \int_0^{r_i} r dr + \rho_{Al} \int_{-t_r+\frac{t_M}{2}+dz}^{\frac{t_M}{2}+dz} z dz \int_0^{2\pi} d\theta \int_{r_i}^{r_o} r dr \\ &= m_M \frac{t_M}{2} + m_R \left(\frac{t_M}{2} - \frac{t_R}{2} + dz \right) \end{aligned} \tag{G.45}$$

where m_M and m_M are the masses of mirror and actuating ring respectively and $m_{\text{CFM}} = m_M + m_R$. The coordinate of CFM's COM is therefore given by:

$$\left(0, 0, \frac{1}{m_M + m_R} \left[m_M \frac{t_M}{2} + m_R \left(\frac{t_M}{2} - \frac{t_R}{2} + dz \right) \right] \right) \tag{G.46}$$

The pitch and yaw moment of inertia I_x and I_y of the CFM about its COM can now be evaluated:

$$I_{\text{CFM,x(y)}} = \sum I_{i,x(y)} = I_{M,x(y)} + I_{R,x(y)} \tag{G.47}$$

Using parallel axis theorem, the moment of inertia of the mirror about x- or y-axis through CFM COM is the sum of a cylinder's moment of inertia about x-y axis through its own COM and $m_m d^2_{COM_m \to COM_{CFM}}$, where $d_{COM_m \to COM_{CFM}}$ is the distance between mirror's COM to CFM COM:

$$I_{M,x(y)} = m_M \left[\frac{1}{4} r_i^2 + \frac{1}{12} t_m^2 + \left(\frac{t_M}{2} - \overline{z} \right)^2 \right] \tag{G.48}$$

Similarly, $I_{r,x(y)}$ is given by:

$$I_{R,x(y)} = m_R \left[\frac{t_o^2 + r_i^2}{4} + \frac{t_R^2}{12} + \left(\overline{z} + \frac{t_R - t_R}{2} - dz \right)^2 \right] \tag{G.49}$$

For the parameters of the baseline CFM, the pitch and yaw moment of inertia is 1170 kg·mm^2. Supposed that the actuator moment arm r is 50 mm from the centre

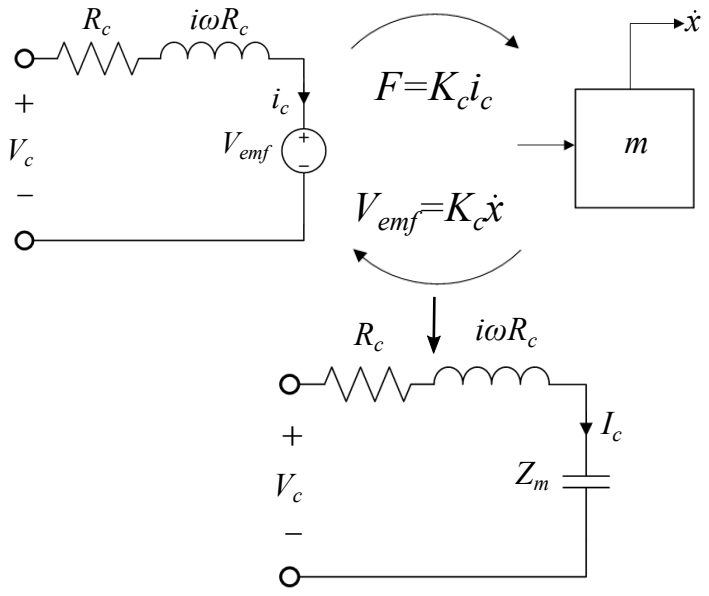

Figure G-5: A lumped-mass diagram allows combining electrical domain and mechanical domain to solve electrical requirements for driving a suspended optics. In electrical domain, we have a dithering voice coil with some resistance R_c and inductance L_c, which is driven by some voltage V_c. This generates a current i_c, which induces a force on the magnet attached to the suspended optics of mass m and causes to move with some velocity $\dot{x}$ mechanical domain. This magnitude of this force is dependent on force coupling constant K_c. The moving mass results in change in magnetic field, which in turn induces a back emf in the circuit. The electrical and mechanical domains are therefore coupled. Lumped mass model allows rewriting the interaction with the moving mass a capacitor with impedance Z_m.

of optics. The apparent mass seen by a dithering actuator is:

$$m = \frac{I_{R,(x,y)}}{4r^2} = 0.117 \text{ kg} \tag{G.50}$$

Following [157], we can present CFM and dithering voice coil as a lumped mass equivalent model and write down an expression for mechanical impedance Z_m.

$$Z_m = \frac{K_c^2}{i\omega m} \tag{G.51}$$

where K_c is the force coupling constant given in Table G.2. The lumped mass model diagram is presented in figure G-5. The total impedance of the equivalent

circuit can then be derived:

$$Z_c = R + i\omega L + \frac{K_c^2}{i\omega m}$$
$$= 42.7\Omega + i149.5\Omega - i0.3\mu\Omega = 42.7\Omega + i149.5\Omega \text{ at f = 2 kHz} \quad \text{(G.52)}$$

Considering the requirement on dithering amplitude θ_d, as given in table G.2, the required current to induce this dithering amplitude is given by:

$$I_c = \frac{m\omega^2 r\theta_d}{K_c} \quad \text{(G.53)}$$

and the required supply voltage is therefore:

$$V_0 = (2R_s + Z_c)I_c \quad \text{(G.54)}$$

As indicated in table G.2, existing BOSEM driver uses 1200 Ω, which replaces the original 100Ω design as 100 Ω resistor provided 10-time-greater actuation range than expected for existing tip-tilt suspension [90]. This change can thus be reversed to provide a sufficient actuation to a larger moment. Here in table G.4, we summarise three scenarios in which different resistors and magnets are used and show the required supply voltage to drive the dithering coil. Both choices of SmCo 2:17 and NdFeB are suitable for generating minimum required dithering amplitude of 0.5 nrad if we switch back to 100 Ω series resistor in coil driver. The maximum dithering amplitude achieved with SmCo 2:17 magnet is 1.76 nrad. Using ⌀5×10 mm NdFeB magnet allows increasing this maximum dithering amplitude up 33 nrad. The driving current in both condition is approximately 78.5 mA at maximum voltage supply of 28 V. Previous temperature measurements of BOSEM coil operatin in vacuum have shown that the relation between current and temperature can be fitted with the following relation [75]:

$$T = 0.0059I^2 - 0.4579I + 32.425 \text{ for I} \geq 50 \text{ mA} \quad \text{(G.55)}$$

Therefore the estimate temperature of dithering coil at maximum dithering capacity is 32.9, which is below out-gassing limit.

$\boldsymbol{\theta_d}$(nrad)	$\boldsymbol{I_c}$(mA)	$\boldsymbol{V_o}$(V)	$\boldsymbol{T_c}$(°C)
Case 1: R_s=1200Ω, K_c=0.0207N/A			
0.24	10.9	27.9	-
Case 2: R_s=100Ω, K_c=0.0207N/A			
0.5	22.3	7.93	-
1.76	78.5	27.9	32.9
Case 3: R_s=100Ω, K_c=0.0388			
0.5	1.2	0.42	-
5	11.9	4.23	-
33	78.6	27.9	32.9

Table G.4: Required current and supply voltage at different dithering mangnitude of the baseline CFM for three scenarios: in case 1, a 1200 Ω series resistor is used, with SmCo magnet. The maximum dithering amplitude is 0.24 nrad given power supply voltage, which is below requirement. By switching back to 100Ω resistor, the minimum dithering amplitude can be met with SmCo 2:17 magnets in case 2. The maximum dithering amplitude achieved in this case is 1.76 mrad, at which the coil current is 78.5 mA and the estimated operating temperature of a BOSEM is 32.9°C. This maximum dithering amplitude can be improved further by using a ⌀5×10 mm NdFeB (in case 3) to meet the maximum dithering amplitude required (5 nrad).

Appendix H

Technical drawings of the flexure CFM

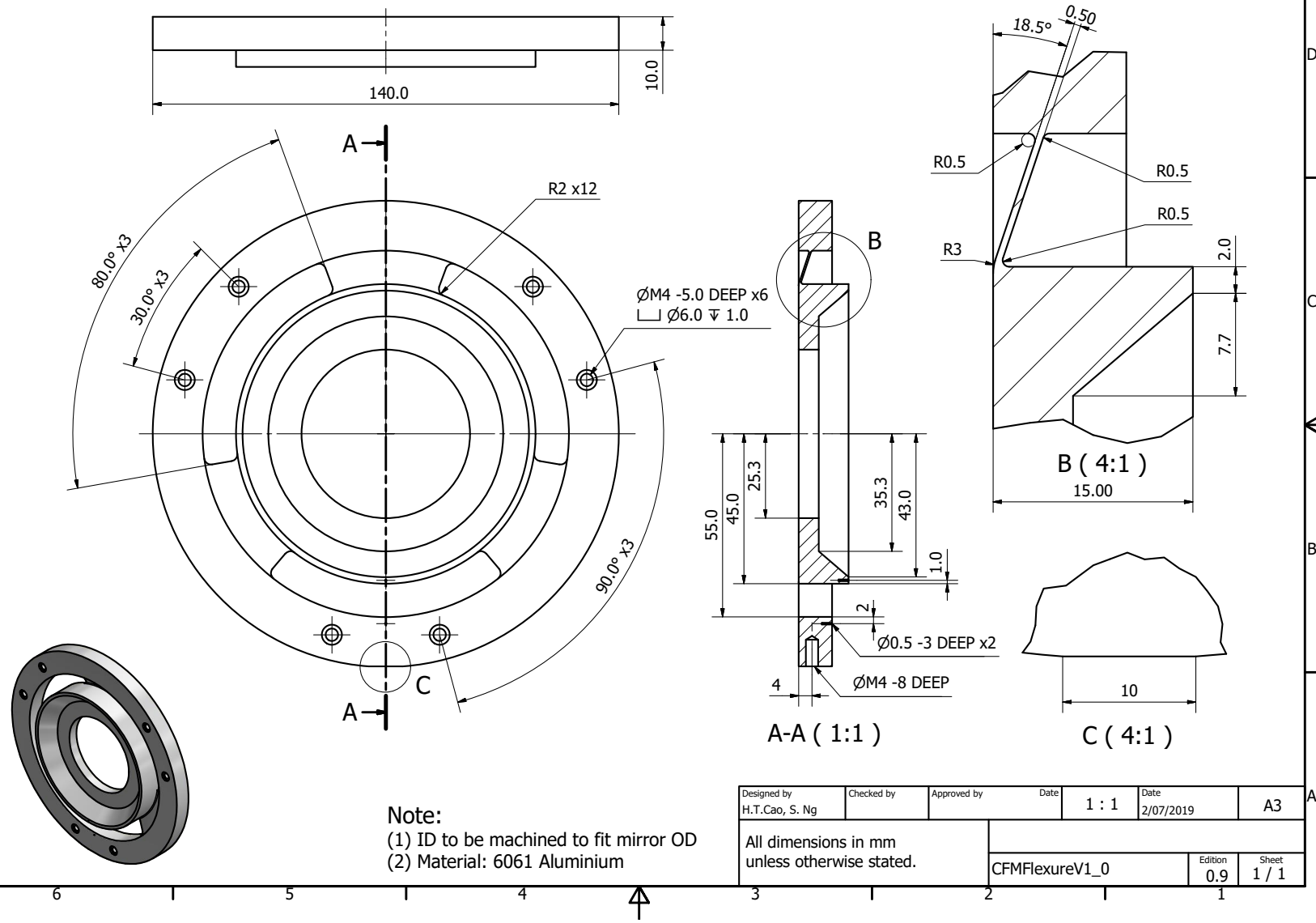

Note:
(1) ID to be machined to fit mirror OD
(2) Material: 6061 Aluminium

Designed by	Checked by	Approved by	Date		Date	
H.T.Cao, S. Ng				1 : 1	2/07/2019	A3
All dimensions in mm unless otherwise stated.				CFMFlexureV1_0	Edition 0.9	Sheet 1 / 1

Bibliography

[1] J Aasi et al. Advanced LIGO. *Classical and Quantum Gravity*, 32(7):074001, March 2015. doi: 10.1088/0264-9381/32/7/074001. URL https://doi.org/10.1088%2F0264-9381%2F32%2F7%2F074001.

[2] B. P. Abbott and others. Observation of gravitational waves from a binary black hole merger. *Phys. Rev. Lett.*, 116:061102, Feb 2016. doi: 10.1103/PhysRevLett.116.061102. URL https://link.aps.org/doi/10.1103/PhysRevLett.116.061102.

[3] B. P. Abbott et al. Gw150914: First results from the search for binary black hole coalescence with advanced ligo. *Phys. Rev. D*, 93:122003, Jun 2016. doi: 10.1103/PhysRevD.93.122003. URL https://link.aps.org/doi/10.1103/PhysRevD.93.122003.

[4] B. P. Abbott et al. Gw151226: Observation of gravitational waves from a 22-solar-mass binary black hole coalescence. *Phys. Rev. Lett.*, 116:241103, Jun 2016. doi: 10.1103/PhysRevLett.116.241103. URL https://link.aps.org/doi/10.1103/PhysRevLett.116.241103.

[5] B. P. Abbott et al. GW170608: Observation of a 19 solar-mass binary black hole coalescence. *The Astrophysical Journal*, 851(2):L35, dec 2017. doi: 10.3847/2041-8213/aa9f0c. URL https://doi.org/10.3847%2F2041-8213%2Faa9f0c.

[6] B. P. Abbott et al. Gw170104: Observation of a 50-solar-mass binary black hole coalescence at redshift 0.2. *Phys. Rev. Lett.*, 118:221101, Jun 2017. doi: 10.1103/PhysRevLett.118.221101. URL https://link.aps.org/doi/10.1103/PhysRevLett.118.221101.

[7] B. P. Abbott et al. Gw170814: A three-detector observation of gravitational waves from a binary black hole coalescence. *Phys. Rev. Lett.*, 119:141101, Oct 2017. doi: 10.1103/PhysRevLett.119.141101. URL https://link.aps.org/doi/10.1103/PhysRevLett.119.141101.

[8] B. P. Abbott et al. Gw170817: Observation of gravitational waves from a binary neutron star inspiral. *Phys. Rev. Lett.*, 119:161101, Oct 2017. doi: 10.

1103/PhysRevLett.119.161101. URL https://link.aps.org/doi/10.1103/PhysRevLett.119.161101.

[9] B. P. Abbott et al. Prospects for observing and localizing gravitational-wave transients with advanced ligo, advanced virgo and kagra. *Living Reviews in Relativity*, 21(1):3, Apr 2018. ISSN 1433-8351. doi: 10.1007/s41114-018-0012-9. URL https://doi.org/10.1007/s41114-018-0012-9.

[10] B. P. Abbott et al. Gw170817: Implications for the stochastic gravitational-wave background from compact binary coalescences. *Phys. Rev. Lett.*, 120: 091101, Feb 2018. doi: 10.1103/PhysRevLett.120.091101. URL https://link.aps.org/doi/10.1103/PhysRevLett.120.091101.

[11] R. Abbott and S. Waldman. Thermal coatings for in-vacuum radiation cooling. Technical Report T070054, LIGO Scientific Collaboration, March 2007. URL https://labcit.ligo.caltech.edu/~abbott/files/T070054-00.pdf.

[12] Rich Abbott and Jeffrey Kissel. SUS HAM-A Coil Driver Design Study. Technical Report T1200264-v4, LIGO Scientific Collaboration, May 2012. URL https://dcc.ligo.org/LIGO-T1200264.

[13] Ossama M.Ramy Y. Abdelslam. *Analysis and Optimization of Autofrettaged and Shink-fitted Compound Cylinders Under Thermomechanical Load*. PhD thesis, Concordia University, November 2012.

[14] Alex Abramovich et al. LIGO: The Laser Interferometer Gravitational-Wave Observatory. *Science*, 256(5055):325–333, April 1992. doi: 10.1126/science.256.5055.325.

[15] A.E.Siegman. *Lasers*, chapter 13, page 663. University Science, Mill Valley,California, 1986.

[16] Kazuhiro Agatsuma, Martin van Beuzekom, Laura van der Schaaf, and Jo van den Brand. Phase camera experiment for advanced virgo. *Nuclear Instruments and Methods in Physics Research Section A: Accelerators, Spectrometers, Detectors and Associated Equipment*, 824:598 – 599, 2016. ISSN 0168-9002. doi: https://doi.org/10.1016/j.nima.2015.09.106. URL http://www.sciencedirect.com/science/article/pii/S016890021501195X. Frontier Detectors for Frontier Physics: Proceedings of the 13th Pisa Meeting on Advanced Detectors.

[17] Kazuhiro Agatsuma, Laura van der Schaaf, Martin van Beuzekom, David Rabeling, and Jo van den Brand. High-performance phase camera as a frequency selective laser wavefront sensor for gravitational wave detectors. *Opt. Express*, 27(13):18533–18548, Jun 2019. doi: 10.1364/OE.27.

018533. URL http://www.opticsexpress.org/abstract.cfm?URI=oe-27-13-18533.

[18] Kiwamu Izumi an Daniel Sigg. Frequency response of aLIGO interferometer:part 2. Technical Report T1500461, LIGO Scientific Collaboration, December 2015. URL https://dcc.ligo.org/LIGO-T1500461.

[19] Kiwamu Izumi an Daniel Sigg. Frequency response of aLIGO interferometer:part 2. Technical Report T1500559, LIGO Scientific Collaboration, December 2015. URL https://dcc.ligo.org/LIGO-T1500559.

[20] Kiwamu Izumi an Daniel Sigg. Frequency response of aLIGO interferometer:part 1. Technical Report T1500325, LIGO Scientific Collaboration, January 2016. URL https://dcc.ligo.org/LIGO-T1500325.

[21] Paola Leaci and. Searching for continuous gravitational wave signals using LIGO and virgo detectors. *Journal of Physics: Conference Series*, 354: 012010, mar 2012. doi: 10.1088/1742-6596/354/1/012010. URL https://doi.org/10.1088%2F1742-6596%2F354%2F1%2F012010.

[22] Dana Z. Anderson. Alignment of resonant optical cavities. *Appl. Opt.*, 23(17): 2944–2949, Sep 1984. doi: 10.1364/AO.23.002944. URL http://ao.osa.org/abstract.cfm?URI=ao-23-17-2944.

[23] Koji Arai. OMC thermal noise calculation. Presentation, January 2018. URL https://dcc.ligo.org/LIGO-G1800149. version 1.

[24] Koji Arai. OMC HOM sideband resonant structure (and possible mitigation of 9th-order 9MHz sideband resonance. Electronic logbook, 2019. URL https://alog.ligo-wa.caltech.edu/aLOG/index.php?callRep=46667.

[25] Muzamil Arain, Antonio Lucianetti, Rodica Martin, Guido Mueller, Volker Quetschke, David Reitz, David Tanner, and Wan Wu. AdvLIGO Phase Modulator Assembly Document. Technical Report T0900475-v2, LIGO Scientific Collaboration, January 2009. URL https://dcc.ligo.org/DocDB/0006/T0900475/002/EOM-assembly_v2.pdf.

[26] Muzamil A. Arain and Guido Mueller. Design of the Advanced LIGO recycling cavities. *Optics Express*, 16(14):10018–10032, June 2008.

[27] S M Aston, M A Barton, A S Bell, N Beveridge, B Bland, A J Brummitt, G Cagnoli, C A Cantley, L Carbone, A V Cumming, L Cunningham, R M Cutler, R J S Greenhalgh, G D Hammond, K Haughian, T M Hayler, A Heptonstall, J Heefner, D Hoyland, J Hough, R Jones, J S Kissel, R Kumar, N A Lockerbie, D Lodhia, I W Martin, P G Murray, J O'Dell, M V Plissi, S Reid, J Romie, N A Robertson, S Rowan, B Shapiro, C C Speake, K A Strain,

K V Tokmakov, C Torrie, A A van Veggel, A Vecchio, and I Wilmut. Update on quadruple suspension design for advanced LIGO. *Classical and Quantum Gravity*, 29(23):235004, oct 2012. doi: 10.1088/0264-9381/29/23/235004. URL https://doi.org/10.1088%2F0264-9381%2F29%2F23%2F235004.

[28] R.M.A Azzam and N.M.Bashara. *Ellipsometry and polarized light*, chapter Propagation of polarized light through polarizing optical system. North-Holland Pub. Co., 1977.

[29] Mark Barton. Calculation and measurement of OSEM actuator sweet spot position. Technical Report T1000164, LIGO Scientific Collaboration, May 2010.

[30] F. Bayer-Helms. Coupling coefficients of an incident wave and the modes of a spherical optical resonator in the case of mismatching and misalignment. *Appl. Opt.*, 23(9):1369–1380, May 1984. doi: 10.1364/AO.23.001369. URL http://ao.osa.org/abstract.cfm?URI=ao-23-9-1369.

[31] W. Benecke and W. Riethmuller. Applications of silicon microactuators based on bimorph structures. In *IEEE Micro Electro Mechanical Systems, , Proceedings, 'An Investigation of Micro Structures, Sensors, Actuators, Machines and Robots'*, pages 116–120, Feb 1989.

[32] T. Bifano, S. Cornelissen, and P.Bierden. Mems deformable mirrors in astronomical adaptive optics. In *Proceedings of SPIE - The International Society for Optical Engineering*, volume 7736, 2010.

[33] Thomas Bifano. Mems deformable mirrors. *Nature Photonics*, 5, 2011.

[34] I.A Bilenko and S.L Lourie. Measurements of effective noise temperature in fused silica fiber violin modes. *Physics Letters A*, 305(1):31 – 36, 2002. ISSN 0375-9601. doi: https://doi.org/10.1016/S0375-9601(02)01417-2. URL http://www.sciencedirect.com/science/article/pii/S0375960102014172.

[35] Eric D. Black. An introduction to poundâĂŞdreverâĂŞhall laser frequency stabilization. *American Journal of Physics*, 69(1):79–87, 2001. doi: 10.1119/1.1286663. URL https://doi.org/10.1119/1.1286663.

[36] Charlotte Bond, Daniel Brown, Andreas Freise, and Kenneth A. Strain. Interferometer techniques for gravitational-wave detection. *Living Reviews in Relativity*, 19(1):3, Feb 2017. ISSN 1433-8351. doi: 10.1007/s41114-016-0002-8. URL https://doi.org/10.1007/s41114-016-0002-8.

[37] Max Born and Emil Wolf. *Principles of Optics*. Cambridge University Press, 2006.

[38] S. Braccini, L. Barsotti, C. Bradaschia, G. Cella, A. Di Virgilio, I. Ferrante, F. Fidecaro, I. Fiori, F. Frasconi, A. Gennai, A. Giazotto, F. Paoletti, R. Passaquieti, D. Passuello, R. Poggiani, E. Campagna, G. Guidi, G. Losurdo, F. Martelli, M. Mazzoni, B. Perniola, F. Piergiovanni, R. Stanga, F. Vetrano, A. VicerÃl', L. Brocco, S. Frasca, E. Majorana, A. Pai, C. Palomba, P. Puppo, P. Rapagnani, F. Ricci, G. Ballardin, R. BarillÃl', R. Cavalieri, E. Cuoco, V. Dattilo, D. Enard, R. Flaminio, A. Freise, S. Hebri, L. Holloway, P. La Penna, M. Loupias, J. Marque, C. Moins, A. Pasqualetti, P. Ruggi, R. Taddei, Z. Zhang, F. Acernese, S. Avino, F. Barone, E. Calloni, R. De Rosa, L. Di Fiore, A. Eleuteri, L. Giordano, L. Milano, S. Pardi, K. Qipiani, I. Ricciardi, G. Russo, S. Solimeno, D. Babusci, G. Giordano, P. Amico, L. Bosi, L. Gammaitoni, F. Marchesoni, M. Punturo, F. Travasso, H. Vocca, C. Boccara, J. Moreau, V. Loriette, V. Reita, J.M. Mackowski, N. Morgado, L. Pinard, A. Remillieux, M. Barsuglia, M.A. Bizouard, V. Brisson, F. Cavalier, A.C. Clapson, M. Davier, P. Hello, S. Krecklbergh, F. Beauville, D. Buskulic, R. Gouaty, D. Grosjean, F. Marion, A. Masserot, B. Mours, E. Tournefier, D. Tombolato, D. Verkindt, M. Yvert, S. Aoudia, F. Bondu, A. Brillet, E. Chassande-Mottin, F. Cleva, J.P. Coulon, B. Dujardin, J.D. Fournier, H. Heitmann, C.N. Man, A. Spallicci, and J.Y. Vinet. Measurement of the seismic attenuation performance of the virgo superattenuator. *Astroparticle Physics*, 23(6):557 – 565, 2005. ISSN 0927-6505. doi: https://doi.org/10.1016/j.astropartphys.2005.04.002. URL `http://www.sciencedirect.com/science/article/pii/S092765050500068X`.

[39] Matthew Brett. Calculating transformations between images. online, 2016. URL `https://matthew-brett.github.io/teaching/optimizing_space.html`.

[40] A.F. Brooks, R.X. Adhikari, S. Ballmer, L. Barsotti, P.Fulda, A.Perecca, and D.Ottaway. Active wavefront control in and beyond Advanced LIGO. Technical Report T1500188, LIGO Scientific Collaboration, June 2015.

[41] Aidan Brooks. Sr3 heater actuator update. Presentation, November 2015. URL `https://dcc.ligo.org/LIGO-G1501373`. version 1.

[42] Aidan Brooks. HWSX measurements for lock around 1180229526. Electronic logbook, May 2017. URL `https://alog.ligo-wa.caltech.edu/aLOG/index.php?callRep=36545`.

[43] Aidan Brooks. Design requirement document of a+ active wavefront control sensors and actuators. Technical Report T1800480, LIGO Scientific Collaboration, November 2018. URL `https://dcc.ligo.org/LIGO-T1800480`. version 1.

[44] Aidan Brooks. Sams in o4. Presentation, April 2019. URL `https://dcc.ligo.org/LIGO-G1900769`.

[45] Aidan Brooks, Peter Fritschel, Fabrice Matichardad, Minkyun Noh, and Callum Torrie. Sams design requirements document. Technical Report T1400341, LIGO Scientific Collaboration, February 2019.

[46] Aidan Brooks, Hiro Yamamoto, Daniel Brown, Evan Hall, Garilynn Billingsey, Gabriele Vajente, and Maie Kasprzack. The point absorbers and aligo. Presentation, April 2019. URL https://dcc.ligo.org/LIGO-G1900203. version 5.

[47] Aidan F. Brooks. *Hartmann Wavefront Sensors for Advanced Gravitational Wave Interferometers*. PhD thesis, University of Adelaide, July 2007.

[48] Aidan F. Brooks, Thu-Lan Kelly, Peter J. Veitch, and Jesper Munch. Ultra-sensitive wavefront measurement using a hartmann sensor. *Opt. Express*, 15(16):10370–10375, Aug 2007. doi: 10.1364/OE.15.010370. URL http://www.opticsexpress.org/abstract.cfm?URI=oe-15-16-10370.

[49] Aidan F. Brooks, David Hosken, Jesper Munch, Peter J. Veitch, Zewu Yan, Chunnong Zhao, Yaohui Fan, Li Ju, David Blair, Phil Willems, Bram Slagmolen, and Jerome Degallaix. Direct measurement of absorption-induced wavefront distortion in high optical power systems. *Appl. Opt.*, 48(2):355–364, Jan 2009. doi: 10.1364/AO.48.000355. URL http://ao.osa.org/abstract.cfm?URI=ao-48-2-355.

[50] Aidan F. Brooks, Benjamin Abbott, Muzammil A. Arain, Giacomo Ciani, Ayodele Cole, Greg Grabeel, Eric Gustafson, Chris Guido, Matthew Heintze, Alastair Heptonstall, Mindy Jacobson, Won Kim, Eleanor King, Alexander Lynch, Stephen O'Connor, David Ottaway, Ken Mailand, Guido Mueller, Jesper Munch, Virginio Sannibale, Zhenhua Shao, Michael Smith, Peter Veitch, Thomas Vo, Cheryl Vorvick, and Phil Willems. Overview of Advanced LIGO adaptive optics. *Appl. Opt.*, 55(29):8256–8265, Oct 2016. doi: 10.1364/AO.55.008256. URL http://ao.osa.org/abstract.cfm?URI=ao-55-29-8256.

[51] Daniel David Brown and Andreas Freise. Finesse, May 2014. URL http://www.gwoptics.org/finesse. You can download the binaries and source code at http://www.gwoptics.org/finesse.

[52] Benjamin Buchler. *Electro-Optic Control of Quantum Measurements*. PhD thesis, Australian National University, September 2001.

[53] Alessandra Buonanno and Yanbei Chen. Quantum noise in second generation, signal-recycled laser interferometric gravitational-wave detectors. *Phys. Rev. D*, 64:042006, Jul 2001. doi: 10.1103/PhysRevD.64.042006. URL https://link.aps.org/doi/10.1103/PhysRevD.64.042006.

[54] Alessandra Buonanno and Yanbei Chen. Optical noise correlations and beating the standard quantum limit in advanced gravitational-wave

detectors. *Classical and Quantum Gravity*, 18(15):L95–L101, jul 2001. doi: 10.1088/0264-9381/18/15/102. URL https://doi.org/10.1088%2F0264-9381%2F18%2F15%2F102.

[55] Alessandra Buonanno and Yanbei Chen. Signal recycled laser-interferometer gravitational-wave detectors as optical springs. *Phys. Rev. D*, 65:042001, Jan 2002. doi: 10.1103/PhysRevD.65.042001. URL https://link.aps.org/doi/10.1103/PhysRevD.65.042001.

[56] Alessandra Buonanno, Yanbei Chen, and Nergis Mavalvala. Quantum noise in laser-interferometer gravitational-wave detectors with a heterodyne readout scheme. *Phys. Rev. D*, 67:122005, Jun 2003. doi: 10.1103/PhysRevD.67.122005. URL https://link.aps.org/doi/10.1103/PhysRevD.67.122005.

[57] G. Cagnoli, L. Gammaitoni, J. Kovalik, F. Marchesoni, M. Punturo, S. Braccini, R. De Salvo, F. Fidecaro, and G. Losurdo. Mechanical shot noise induced by creep in suspension devices. *Physics Letters A*, 237(1):21 – 27, 1997. ISSN 0375-9601. doi: https://doi.org/10.1016/S0375-9601(97)00710-X. URL http://www.sciencedirect.com/science/article/pii/S037596019700710X.

[58] G. Cagnoli, L. Gammaitoni, J. Hough, J. Kovalik, S. McIntosh, M. Punturo, and S. Rowan. Very high Q measurements on a fused silica monolithic pendulum for use in enhanced gravity wave detectors. *Phys. Rev. Lett.*, 85:2442–2445, Sep 2000. doi: 10.1103/PhysRevLett.85.2442. URL https://link.aps.org/doi/10.1103/PhysRevLett.85.2442.

[59] Herbert B. Callen and Theodore A. Welton. Irreversibility and generalized noise. *Phys. Rev.*, 83:34–40, Jul 1951. doi: 10.1103/PhysRev.83.34. URL https://link.aps.org/doi/10.1103/PhysRev.83.34.

[60] B Canuel, R Day, E Genin, P La Penna, and J Marque. Wavefront aberration compensation with a thermally deformable mirror. *Classical and Quantum Gravity*, 29(8):085012, apr 2012. doi: 10.1088/0264-9381/29/8/085012. URL https://doi.org/10.1088%2F0264-9381%2F29%2F8%2F085012.

[61] Sean M. Carroll. Lecture notes on General Relativity: Weak Fields and Gravitational Radiation. Online lecture note, December 1997. URL https://ned.ipac.caltech.edu/level5/March01/Carroll3/Carroll6.html.

[62] Carlton M. Caves. Quantum-mechanical noise in an interferometer. *Phys. Rev. D*, 23:1693–1708, Apr 1981. doi: 10.1103/PhysRevD.23.1693. URL https://link.aps.org/doi/10.1103/PhysRevD.23.1693.

[63] Carlton M. Caves and Bonny L. Schumaker. New formalism for two-photon quantum optics. i. quadrature phases and squeezed states. *Phys. Rev. A*,

31:3068–3092, May 1985. doi: 10.1103/PhysRevA.31.3068. URL https://link.aps.org/doi/10.1103/PhysRevA.31.3068.

[64] Carlton M. Caves, Kip S. Thorne, Ronald W. P. Drever, Vernon D. Sandberg, and Mark Zimmermann. On the measurement of a weak classical force coupled to a quantum-mechanical oscillator. i. issues of principle. *Rev. Mod. Phys.*, 52:341–392, Apr 1980. doi: 10.1103/RevModPhys.52.341. URL https://link.aps.org/doi/10.1103/RevModPhys.52.341.

[65] LIGO Scientific Collaboration. Instrument science white paper 2019. Technical Report T1900409, LIGO Scientific Collaboration, September 2014.

[66] ASM International Handbook Committee. *ASM Handbook Volume 2: Properties and Selection: Nonferrous Alloys and Special Purpose Materials*, chapter Properties of Wrought Aluminum and Aluminum Alloys, pages 62–122. ASM International, October 1990.

[67] Steve Constatinides. Understanding and Using Reversible Temperature Coefficient. Technical report, ARNOLD Magnetic Technologies, 2009. URL https://www.arnoldmagnetics.com/wp-content/uploads/2017/10/Understanding-and-Using-Reversible-Temperature-Coefficients-Constant.pdf.

[68] Thomas Corbitt and Nergis Mavalvala. Review: Quantum noise in gravitational-wave interferometers. *Journal of Optics B: Quantum and Semiclassical Optics*, 6(8):S675–S683, jul 2004. doi: 10.1088/1464-4266/6/8/008. URL https://doi.org/10.1088%2F1464-4266%2F6%2F8%2F008.

[69] Boston Michromachines Corporation. Control of BMC SLM architecture in vacuum enviroenment, May 2017. private communication.

[70] Tosoh Corporation. Fused silica glass. brochure, 2019.

[71] RaphaÃńl Coustra, Tania Antonini, Marie Aubry, HÃľlÃĺne T. Krol, and AurÃľlien Moreau. Monomorph deformable mirrors: from ground-based facilities to space telescopes. In *International Conference on Space Optics ICSO 2016*, volume 10562, 2017. doi: 10.1117/12.2296247. URL https://doi.org/10.1117/12.2296247.

[72] Dennis Coyne and Aidan Brooks. Sr3 roc actuator concept sketches. Presentation, August 2015. URL https://dcc.ligo.org/LIGO-G1501030. version 1.

[73] Dennis Coyne and Bob Taylor. Material qualification rga test result: Masterbond ep30-2 epoxy. Technical Report E1000386, LIGO Scientific Collaboration, 2010. URL https://dcc.ligo.org/LIGO-E1000386/public.

[74] Dennis Coyne and Bob Taylor. aLIGO ISC Beam Steering: Tip-Tilt Suspension Design. Technical Report T000042, LIGO Scientific Collaboration, November 2010.

[75] Dennis Coyne and Bob Taylor. Maximum b-osem current. Technical Report T1400341, LIGO Scientific Collaboration, July 2014.

[76] Stephen H. Crandall, Norman C. Dahl, and Thomas J. Lardner. *An Introduction to the Mechanics of Solid*. McGraw-Hill Science/ Engineering/ Math, 2 edition, 1999.

[77] A V Cumming, A S Bell, L Barsotti, M A Barton, G Cagnoli, D Cook, L Cunningham, M Evans, G D Hammond, G M Harry, A Heptonstall, J Hough, R Jones, R Kumar, R Mittleman, N A Robertson, S Rowan, B Shapiro, K A Strain, K Tokmakov, C Torrie, and A A van Veggel. Design and development of the advanced LIGO monolithic fused silica suspension. *Classical and Quantum Gravity*, 29(3):035003, jan 2012. doi: 10.1088/0264-9381/29/3/035003. URL https://doi.org/10.1088%2F0264-9381%2F29%2F3%2F035003.

[78] Curt Cutler and Daniel E. Holz. Ultrahigh precision cosmology from gravitational waves. *Phys. Rev. D*, 80:104009, Nov 2009. doi: 10.1103/PhysRevD.80.104009. URL https://link.aps.org/doi/10.1103/PhysRevD.80.104009.

[79] Curt Cutler and Kip S. Thorne. An overview of gravitational-wave sources. In *General Relativity and Gravitation*, pages 71–111. World Scientific, 2002. doi: 10.1142/9789812776556_0004. URL https://doi.org/10.1142/9789812776556_0004.

[80] H Dimmelmeier, J A Font, and E MÃijller. Gravitational waves from relativistic rotational core collapse in axisymmetry. *Classical and Quantum Gravity*, 19(7):1291–1296, mar 2002. doi: 10.1088/0264-9381/19/7/308. URL https://doi.org/10.1088%2F0264-9381%2F19%2F7%2F308.

[81] J. C.and others Driggers. Improving astrophysical parameter estimation via offline noise subtraction for advanced ligo. *Phys. Rev. D*, 99:042001, Feb 2019. doi: 10.1103/PhysRevD.99.042001. URL https://link.aps.org/doi/10.1103/PhysRevD.99.042001.

[82] Jennifer C. Driggers, Jan Harms, and Rana X. Adhikari. Subtraction of newtonian noise using optimized sensor arrays. *Phys. Rev. D*, 86:102001, Nov 2012. doi: 10.1103/PhysRevD.86.102001. URL https://link.aps.org/doi/10.1103/PhysRevD.86.102001.

[83] M. R. Drout, A. L. Piro, B. J. Shappee, C. D. Kilpatrick, J. D. Simon, C. Contreras, D. A. Coulter, R. J. Foley, M. R. Siebert, N. Morrell, K. Boutsia, F. Di Mille, T. W.-S. Holoien, D. Kasen, J. A. Kollmeier, B. F. Madore, A. J.

Monson, A. Murguia-Berthier, Y.-C. Pan, J. X. Prochaska, E. Ramirez-Ruiz, A. Rest, C. Adams, K. Alatalo, E. Bañados, J. Baughman, T. C. Beers, R. A. Bernstein, T. Bitsakis, A. Campillay, T. T. Hansen, C. R. Higgs, A. P. Ji, G. Maravelias, J. L. Marshall, C. Moni Bidin, J. L. Prieto, K. C. Rasmussen, C. Rojas-Bravo, A. L. Strom, N. Ulloa, J. Vargas-González, Z. Wan, and D. D. Whitten. Light curves of the neutron star merger gw170817/sss17a: Implications for r-process nucleosynthesis. *Science*, 358(6370):1570–1574, 2017. ISSN 0036-8075. doi: 10.1126/science.aaq0049. URL https://science.sciencemag.org/content/358/6370/1570.

[84] Sheila Dwyer. *Quantum noise reduction using squeezed states in LIGO*. PhD thesis, Masschussetts Institute of Technology, 2005.

[85] A. Einstein. Zur elektrodynamik bewegter kÃűrper. *Annalen der Physik*, 322(10):891–921, 1905. doi: 10.1002/andp.19053221004. URL https://onlinelibrary.wiley.com/doi/abs/10.1002/andp.19053221004.

[86] Omega Engineering. Kapton flexible heaters user's guide. Manual, 2005. URL https://assets.omega.com/manuals/M1249.pdf.

[87] Inc. Epoxy Technology. Epo-tek 353nd technical data sheet. Data sheet, March 2012.

[88] M.Fatih Erden and Haldun M.Ozaktas. Accumulated gouy phase shift in gaussian beam propagation through first order optical systems. *Journal of Optical Society of America A*, 14(9):2190–2194, September 1997.

[89] Matthew Evans, Slawek Gras, Peter Fritschel, John Miller, Lisa Barsotti, Denis Martynov, Aidan Brooks, Dennis Coyne, Rich Abbott, Rana X. Adhikari, Koji Arai, Rolf Bork, Bill Kells, Jameson Rollins, Nicolas Smith-Lefebvre, Gabriele Vajente, Hiroaki Yamamoto, Carl Adams, Stuart Aston, Joseph Betzweiser, Valera Frolov, Adam Mullavey, Arnaud Pele, Janeen Romie, Michael Thomas, Keith Thorne, Sheila Dwyer, Kiwamu Izumi, Keita Kawabe, Daniel Sigg, Ryan Derosa, Anamaria Effler, Keiko Kokeyama, Stefan Ballmer, Thomas J. Massinger, Alexa Staley, Matthew Heinze, Chris Mueller, Hartmut Grote, Robert Ward, Eleanor King, David Blair, Li Ju, and Chunnong Zhao. Observation of parametric instability in advanced ligo. *Phys. Rev. Lett.*, 114:161102, Apr 2015. doi: 10.1103/PhysRevLett.114.161102. URL https://link.aps.org/doi/10.1103/PhysRevLett.114.161102.

[90] David Feldbaum. Engineer Change Request: Replacement of the coil-series resistors in the HAM-Aux and Tip/Tilt Coil drivers. Technical Report E1201027, LIGO Scientific Collaboration, November 2012.

[91] M. Fishbach et al. A Standard Siren Measurement of the Hubble Constant from GW170817 without the Electromagnetic Counterpart. *The Astrophysical*

Journal, 871(1):L13, jan 2019. doi: 10.3847/2041-8213/aaf96e. URL https://doi.org/10.3847%2F2041-8213%2Faaf96e.

[92] Tobin T Fricke, Nicolás D Smith-Lefebvre, Richard Abbott, Rana Adhikari, Katherine L Dooley, Matthew Evans, Peter Fritschel, Valery V Frolov, Keita Kawabe, Jeffrey S Kissel, Bram J J Slagmolen, and Sam J Waldman. DC readout experiment in enhanced LIGO. *Classical and Quantum Gravity*, 29 (6):065005, feb 2012. doi: 10.1088/0264-9381/29/6/065005. URL https://doi.org/10.1088%2F0264-9381%2F29%2F6%2F065005.

[93] Peter Fritschel, David Shoemaker, and Rainer Weiss. Demonstration of light recycling in a michelson interferometer with fabry–perot cavities. *Appl. Opt.*, 31(10):1412–1418, Apr 1992. doi: 10.1364/AO.31.001412. URL http://ao.osa.org/abstract.cfm?URI=ao-31-10-1412.

[94] Peter Fritschel, Rolf Bork, Gabriela González, Nergis Mavalvala, Dale Ouimette, Haisheng Rong, Daniel Sigg, and Michael Zucker. Readout and control of a power-recycled interferometric gravitational-wave antenna. *Appl. Opt.*, 40(28):4988–4998, Oct 2001. doi: 10.1364/AO.40.004988. URL http://ao.osa.org/abstract.cfm?URI=ao-40-28-4988.

[95] Peter Fritschel, Matthew Evans, and Valery Frolov. Balanced homodyne readout for quantum limited gravitational wave detectors. *Opt. Express*, 22 (4):4224–4234, Feb 2014. doi: 10.1364/OE.22.004224. URL http://www.opticsexpress.org/abstract.cfm?URI=oe-22-4-4224.

[96] Keisuke Goda, David Ottaway, Blair Connelly, Rana Adhikari, Nergis Mavalvala, and Andri Gretarsson. Frequency-resolving spatiotemporal wave-front sensor. *Opt. Lett.*, 29(13):1452–1454, Jul 2004. doi: 10.1364/OL.29.001452. URL http://ol.osa.org/abstract.cfm?URI=ol-29-13-1452.

[97] Andri M. Gretarsson and Peter R. Saulson. Monitoring the thermal and non-thermal excitation of fibers. *Review of Scientific Instruments*, 76(5):054502, 2005. doi: 10.1063/1.1898218. URL https://doi.org/10.1063/1.1898218.

[98] Jan Harms. Terrestrial gravity fluctuations. *Living Reviews in Relativity*, 18(1): 3, Dec 2015. ISSN 1433-8351. doi: 10.1007/lrr-2015-3. URL https://doi.org/10.1007/lrr-2015-3.

[99] Jan Harms, Yanbei Chen, Simon Chelkowski, Alexander Franzen, Henning Vahlbruch, Karsten Danzmann, and Roman Schnabel. Squeezed-input, optical-spring, signal-recycled gravitational-wave detectors. *Phys. Rev. D*, 68:042001, Aug 2003. doi: 10.1103/PhysRevD.68.042001. URL https://link.aps.org/doi/10.1103/PhysRevD.68.042001.

[100] Gregg Harry. Mechanical loss of epoxies. Presentation, May 2014. URL https://dcc.ligo.org/public/0114/G1400597/001/G1400597.pdf.

[101] J. Hartmann. Bemerkungen uber den bau und die justirung von spektrographen. *Zt. Instrumentenkd*, 20(47), 1990.

[102] Yaron Hefetz, Nergis Mavalvala, and Daniel Sigg. Principles of calculating alignment signals in complex resonant optical interferometers. *J. Opt. Soc. Am. B*, 14(7):1597–1606, Jul 1997. doi: 10.1364/JOSAB.14.001597. URL http://josab.osa.org/abstract.cfm?URI=josab-14-7-1597.

[103] Patrice Hello and Jean-Yves Vinet. Analytical models of thermal aberrations in massive mirrors heated by high power laser beams. *Journal de Physique*, 51(12):1267–1282, 1990. doi: 10.1051/jphys:0199000510120126700. URL https://hal.archives-ouvertes.fr/jpa-00212444.

[104] Patrice Hello and Jean-Yves Vinet. Analytical models of transient thermoelastic deformations of mirrors heated by high power cw laser beams. *Journal de Physique*, 51(20):2243–2261, 1990. doi: 10.1051/jphys:0199000510200224300. URL https://hal.archives-ouvertes.fr/jpa-00212526.

[105] Richard W. Henry and Sharon C. Glotzer. A squeezed-state primer. *American Journal of Physics*, 56(4):318–828, 1988.

[106] M Hewitson, K Danzmann, H Grote, S Hild, J Hough, H LÃijck, S Rowan, J R Smith, K A Strain, and B Willke. Charge measurement and mitigation for the main test masses of the GEO 600 gravitational wave observatory. *Classical and Quantum Gravity*, 24(24):6379–6391, nov 2007. doi: 10.1088/0264-9381/24/24/013. URL https://doi.org/10.1088%2F0264-9381%2F24%2F24%2F013.

[107] S Hild, H Grote, J Degallaix, S Chelkowski, K Danzmann, A Freise, M Hewitson, J Hough, H LÃijck, M Prijatelj, K A Strain, J R Smith, and B Willke. DC-readout of a signal-recycled gravitational wave detector. *Classical and Quantum Gravity*, 26(5):055012, feb 2009. doi: 10.1088/0264-9381/26/5/055012. URL https://doi.org/10.1088%2F0264-9381%2F26%2F5%2F055012.

[108] Scott A. Hughes and Kip S. Thorne. Seismic gravity-gradient noise in interferometric gravitational-wave detectors. *Phys. Rev. D*, 58:122002, Nov 1998. doi: 10.1103/PhysRevD.58.122002. URL https://link.aps.org/doi/10.1103/PhysRevD.58.122002.

[109] Momentive Inc. Momentive mechanical properties of fused quartz glass. https://www.momentive.com/en-US/categories/quartz/mechanical-properties/#, 2019. Accessed: 2019-01-30.

[110] Corning Incorporated. Corning HPFS®7979, 7980, 8655 fused silica. brochure, 2014.

[111] Thorlabs Incorporated. Free-space electro-optic modulators lab facts. online, 2019. URL https://www.thorlabs.com/newgrouppage9.cfm?objectgroup_id=9703.

[112] Kiwamu Izumi. *Muti-Color Interferometry for Lock Acquisition of Laser Interferometric Gravitational-wave Detectors*. PhD thesis, The University of Tokyo, 2012.

[113] Kiwamu Izumi and Daniel Sigg. Advanced LIGO: length sensing and control in a dual recycled interferometric gravitational wave antenna. *Classical and Quantum Gravity*, 34(1):015001, Dec 2016. doi: 10.1088/0264-9381/34/1/015001. URL https://doi.org/10.1088%2F0264-9381%2F34%2F1%2F015001.

[114] Marie Kasprzack. *Thermally Deformable Mirrors: a new Adaptive Optics scheme for Advanced Gravitational Wave Interferometers*. PhD thesis, Université Paris Sud - Paris XI, 2014.

[115] Marie Kasprzack, Benjamin Canuel, Fabien Cavalier, Richard Day, Eric Genin, Julien Marque, Daniel Sentenac, and Gabriele Vajente. Performance of a thermally deformable mirror for correction of low-order aberrations in laser beams. *Appl. Opt.*, 52(12):2909–2916, Apr 2013. doi: 10.1364/AO.52.002909. URL http://ao.osa.org/abstract.cfm?URI=ao-52-12-2909.

[116] Thu-Lan Kelly, Peter J. Veitch, Aidan F. Brooks, and Jesper Munch. Accurate and precise optical testing with a differential hartmann wavefront sensor. *Appl. Opt.*, 46(6):861–866, Feb 2007. doi: 10.1364/AO.46.000861. URL http://ao.osa.org/abstract.cfm?URI=ao-46-6-861.

[117] F. Ya. Khalili. Quantum variational measurement in the next generation gravitational-wave detectors. *Phys. Rev. D*, 76:102002, Nov 2007. doi: 10.1103/PhysRevD.76.102002. URL https://link.aps.org/doi/10.1103/PhysRevD.76.102002.

[118] Nutsinee Kijbunchoo. Lho squeezer update. Presentation, August 2019. URL https://dcc.ligo.org/LIGO-G1901583. version 1.

[119] H. J. Kimble, Yuri Levin, Andrey B. Matsko, Kip S. Thorne, and Sergey P. Vyatchanin. Conversion of conventional gravitational-wave interferometers into quantum nondemolition interferometers by modifying their input and/or output optics. *Phys. Rev. D*, 65:022002, Dec 2001. doi: 10.1103/PhysRevD.65.022002. URL https://link.aps.org/doi/10.1103/PhysRevD.65.022002.

[120] Jeffrey Kissel. Suspension Controls Design Summary Table. Technical Report G100968, LIGO Scientific Collaboration, September 2011. URL https://dcc.ligo.org/LIGO-100968.

[121] P. Kwee, J. Miller, T. Isogai, L. Barsotti, and M. Evans. Decoherence and degradation of squeezed states in quantum filter cavities. *Phys. Rev. D*, 90: 062006, Sep 2014. doi: 10.1103/PhysRevD.90.062006. URL https://link.aps.org/doi/10.1103/PhysRevD.90.062006.

[122] R. G. Lane and M. Tallon. Wave-front reconstruction using a shack–hartmann sensor. *Appl. Opt.*, 31(32):6902–6908, Nov 1992. doi: 10.1364/AO.31.006902. URL http://ao.osa.org/abstract.cfm?URI=ao-31-32-6902.

[123] Brian Lantz. Lho ham2 and ham3 relative motion - thoughts. Presentation, June 2016. URL https://dcc.ligo.org/LIGO-G160139. version 1.

[124] Brian Lantz, Stefan Danilishin, Stefan Hild, Eric Gustafson, Dennis Coyne, Volker Quetschke, Giles Hammond Rana Adhikari, Matthew Evans, and Riccardo Bassiri. Instrument Science White Paper 2018. Technical Report T1800133, LIGO Scientific Collaboration, June 2018.

[125] Ryan Lawrence. *Active Wavefront Correction in Laser Interferometric Gravitational Wave Detectors*. PhD thesis, Massachusettes Institute of Technology, February 2003. URL https://labcit.ligo.caltech.edu/~rana/docs/Theses/Thesis-Ryan.pdf.

[126] Ryan Lawrence, Michael Zucker, Peter Fritschel, Phil Marfuta, and David Shoemaker. Adaptive thermal compensation of test masses in advanced LIGO. *Classical and Quantum Gravity*, 19(7):1803–1812, mar 2002. doi: 10.1088/0264-9381/19/7/377. URL https://doi.org/10.1088%2F0264-9381%2F19%2F7%2F377.

[127] Yu. Levin. Internal thermal noise in the ligo test masses: A direct approach. *Phys. Rev. D*, 57:659–663, Jan 1998. doi: 10.1103/PhysRevD.57.659. URL https://link.aps.org/doi/10.1103/PhysRevD.57.659.

[128] Yuri Levin. Creep events and creep noise in gravitational-wave interferometers: Basic formalism and stationary limit. *Phys. Rev. D*, 86:122004, Dec 2012. doi: 10.1103/PhysRevD.86.122004. URL https://link.aps.org/doi/10.1103/PhysRevD.86.122004.

[129] J. F. Liu and M. H. Walmer. Thermal stability and performance data for smco 2:17 high-temperature magnets on ppm focusing structures. *IEEE Transactions on Electron Devices*, 52(5):899–902, May 2005. ISSN 0018-9383. doi: 10.1109/TED.2005.845868.

[130] Zhanwei Liu, Paul Fulda, Muzammil A. Arain, Luke Williams, Guido Mueller, D. B. Tanner, and D. H. Reitze. Feedback control of optical beam spatial profiles using thermal lensing. *Appl. Opt.*, 52(26):6452–6457, Sep 2013. doi: 10.1364/AO.52.006452. URL http://ao.osa.org/abstract.cfm?URI=ao-52-26-6452.

[131] Gabrian International LTD. 6061 aluminum alloy: Properties. Datasheet, 2016. URL https://www.gabrian.com/wp-content/uploads/2018/09/6061-Aluminum-Alloy-Properties-1.pdf.

[132] Y B Ma, J Liu, Y Q Ma, C Zhao, L Ju, D G Blair, and Z H Zhu. Thermal modulation for suppression of parametric instability in advanced gravitational wave detectors. *Classical and Quantum Gravity*, 34(13):135001, jun 2017. doi: 10.1088/1361-6382/aa7340. URL https://doi.org/10.1088%2F1361-6382%2Faa7340.

[133] P.-Y. Madec. Overview of deformable mirror technologies for adaptive optics and astronomy. In *Adaptive Optics Systems III*, volume 8447, 2012. doi: 10.1117/12.924892. URL https://doi.org/10.1117/12.924892.

[134] Michele Maggiore. *Gravitational Waves: Volume 1: Theory and Experiments*. Oxford University Press, Oxford, 2008.

[135] Michele Maggiore. *Gravitational Waves: Volume 2: Astrophysics and Cosmology*. Oxford University Press, Oxford, 2008.

[136] Eclipse Magnetics. Samarium Cobalt Magnets, SmCo Magnets Datasheet. Atlas Way, Sheffield, S4 7QQ, England, 2019. URL https://www.eclipsemagnetics.com/media/wysiwyg/datasheets/magnet_materials_and_assemblies/samarium_cobalt_magnets_datasheet.pdf.

[137] Szabolcs Márka, Akiteru Takamori, Masaki Ando, Alessandro Bertolini, Giancarlo Cella, Riccardo DeSalvo, Mitsuhiro Fukushima, Yukiyoshi Iida, Florian Jacquier, Seiji Kawamura, Yuhiko Nishi, Kenji Numata, Virginio Sannibale, Kentaro Somiya, Ryutaro Takahashi, Hareem Tariq, Kimio Tsubono, Jose Ugas, Nicolas Viboud, Chenyang Wang, Hiroaki Yamamoto, and Tatsuo Yoda. Anatomy of the TAMA SAS seismic attenuation system. *Classical and Quantum Gravity*, 19(7):1605–1614, mar 2002. doi: 10.1088/0264-9381/19/7/351. URL https://doi.org/10.1088%2F0264-9381%2F19%2F7%2F351.

[138] D. V. Martynov et al. Sensitivity of the advanced ligo detectors at the beginning of gravitational wave astronomy. *Phys. Rev. D*, 93:112004, Jun 2016. doi: 10.1103/PhysRevD.93.112004. URL https://link.aps.org/doi/10.1103/PhysRevD.93.112004.

[139] *Master Bond EP30-2 Technical Data Sheet*. Master Bond, 2017.

[140] F. Matichard, B. Lantz, K. Mason, R. Mittleman, B. Abbott, S. Abbott, E. Allwine, S. Barnum, J. Birch, S. Biscans, D. Clark, D. Coyne, D. DeBra, R. DeRosa, S. Foley, P. Fritschel, J.A. Giaime, C. Gray, G. Grabeel, J. Hanson, M. Hillard, J. Kissel, C. Kucharczyk, A. Le Roux, V. Lhuillier, M. Macinnis, B. OâĂŹReilly, D. Ottaway, H. Paris, M. Puma, H. Radkins, C. Ramet, M. Robinson, L. Ruet, P. Sareen, D. Shoemaker, A. Stein, J. Thomas, M. Vargas, and J. Warner. Advanced ligo two-stage twelve-axis vibration isolation and positioning platform. part 1: Design and production overview. *Precision Engineering*, 40:273 – 286, 2015. ISSN 0141-6359. doi: https://doi.org/10.1016/j.precisioneng.2014.09.010. URL http://www.sciencedirect.com/science/article/pii/S0141635914001561.

[141] D.E. McClelland, N. Mavalvala, Y. Chen, and R. Schnabel. Advanced interferometry, quantum optics and optomechanics in gravitational wave detectors. *Laser & Photonics Reviews*, 5(5):677–696, 2011. doi: 10.1002/lpor.201000034. URL https://onlinelibrary.wiley.com/doi/abs/10.1002/lpor.201000034.

[142] Lee McCuller. Beam layout requirements imposed by wavefront actuators. Technical Report T1900144, LIGO Scientific Collaboration, April 2019. URL https://dcc.ligo.org/LIGO-T1900144. version 3.

[143] Lee McCuller and Lisa Barsotti. Design requirement document of the a+ filter cavity and relay optics for frequency dependent squeezing. Technical Report T1800447, LIGO Scientific Collaboration, June 2019. URL https://dcc.ligo.org/LIGO-T1800447. version 4.

[144] Brian J. Meers. Recycling in laser-interferometric gravitational-wave detectors. *Phys. Rev. D*, 38:2317–2326, Oct 1988. doi: 10.1103/PhysRevD.38.2317. URL https://link.aps.org/doi/10.1103/PhysRevD.38.2317.

[145] John Miller, Lisa Barsotti, Salvatore Vitale, Peter Fritschel, Matthew Evans, and Daniel Sigg. Prospects for doubling the range of advanced ligo. *Phys. Rev. D*, 91:062005, Mar 2015. doi: 10.1103/PhysRevD.91.062005. URL https://link.aps.org/doi/10.1103/PhysRevD.91.062005.

[146] Guang ming Dai. Modal wave-front reconstruction with zernike polynomials and karhunen–loève functions. *J. Opt. Soc. Am. A*, 13(6):1218–1225, Jun 1996. doi: 10.1364/JOSAA.13.001218. URL http://josaa.osa.org/abstract.cfm?URI=josaa-13-6-1218.

[147] Charles W. Misner, Kip S. Thorne, and John A. Wheeler. *Gravitation*. W.H.Freeman and Company, San Francisco, 1973.

[148] J. Mizuno, K.A. Strain, P.G. Nelson, J.M. Chen, R. Schilling, A. Rüdgier, . Winkler, and K. Danzmann. Resonant sideband extraction: a new configurationfor interferometric gravitational wave detectors. *Physics Letters A*, 75(5):273–276, 1993.

[149] Jun Mizuno. *Comparison of optical configurations for laser-interferometric gravitational-wave detector*. PhD thesis, Max-Planck-Institut für Quantenoptik, 1995.

[150] Euan Morrison, Brian J. Meers, David I. Robertson, and Henry Ward. Automatic alignment of optical interferometers. *Appl. Opt.*, 33(22):5041–5049, Aug 1994. doi: 10.1364/AO.33.005041. URL http://ao.osa.org/abstract.cfm?URI=ao-33-22-5041.

[151] Minkyun Noh. Sams - suspension interface. Presentation, February 2019. URL https://dcc.ligo.org/LIGO-E1900056. version 3.

[152] Minkyun Noh. Sams -piezo deformable mirror update. Presentation, March 2019. URL https://dcc.ligo.org/LIGO-E1900093. version 5.

[153] Minkyun Noh. Sams -piezo deformable mirror update ii. Presentation, June 2019. URL https://dcc.ligo.org/LIGO-E1900111. version 1.

[154] Minkyun Noh. Sams - mirror-flexure assembly dimension and tolerance. Presentation, April 2019. URL https://dcc.ligo.org/LIGO-E1900127. version 2.

[155] Minkyun Noh. Sams - drawing updates and mirror metrology. Presentation, May 2019. URL https://dcc.ligo.org/LIGO-E1900128. version 1.

[156] Minkyun Noh. Sams - concept and initial design document. Technical Report E1900206, LIGO Scientific Collaboration, July 2019. URL https://dcc.ligo.org/LIGO-E1900206. version 1.

[157] Minkyun Noh and Fabrice Matichard. Dithering and tip-tilt inertia. Technical Report E1900051, LIGO Scientific Collaboration, February 2019. URL https://dcc.ligo.org/LIGO-E1900051.

[158] Robert J. Noll. Zernike polynomials and atmospheric turbulence. *J. Opt. Soc. Am.*, 66(3):207–211, Mar 1976. doi: 10.1364/JOSA.66.000207. URL http://www.osapublishing.org/abstract.cfm?URI=josa-66-3-207.

[159] Robert L. Norton. *Interference Fits*, chapter Chapter 9: Shafts, Keys and Couplings, pages 597–600. Prentice Hall, 1997.

[160] Kenji Numata. *Direct measurement of mirror thermal noise*. PhD thesis, University of Tokyo, December 2002.

[161] E. Oelker, L. Barsotti, S. Dwyer, D. Sigg, and N. Mavalvala. Squeezed light for advanced gravitational wave detectors and beyond. *Opt. Express*, 22(17): 21106–21121, Aug 2014. doi: 10.1364/OE.22.021106. URL http://www.opticsexpress.org/abstract.cfm?URI=oe-22-17-21106.

[162] Eric Oelker, Tomoki Isogai, John Miller, Maggie Tse, Lisa Barsotti, Nergis Mavalvala, and Matthew Evans. Audio-band frequency-dependent squeezing for gravitational-wave detectors. *Phys. Rev. Lett.*, 116:041102, Jan 2016. doi: 10.1103/PhysRevLett.116.041102. URL https://link.aps.org/doi/10.1103/PhysRevLett.116.041102.

[163] Eric Oelker, Tomoki Isogai, John Miller, Maggie Tse, Lisa Barsotti, Nergis Mavalvala, and Matthew Evans. Audio-band frequency-dependent squeezing for gravitational-wave detectors. *Phys. Rev. Lett.*, 116:041102, Jan 2016. doi: 10.1103/PhysRevLett.116.041102. URL https://link.aps.org/doi/10.1103/PhysRevLett.116.041102.

[164] David J Ottaway, Peter Fritschel, and Samuel J. Waldman. Impact of upconverted scattered light on advanced interferometric gravitational wave detectors. *Opt. Express*, 20(8):8329–8336, Apr 2012. doi: 10.1364/OE.20.008329. URL http://www.opticsexpress.org/abstract.cfm?URI=oe-20-8-8329.

[165] Shin Oya, Aurelien Bouvier, Olivier Guyon, Makoto Watanabe, Yutaka Hayano, Hideki Takami, Masanori Iye, Masayuki Hattori, Yoshihiko Saito, Meguru Itoh, Stephen Colley, Mathew Dinkins, Michael Eldred, and Taras Golota. Performance of the deformable mirror for subaru LGSAO. In *Proceedings of SPIE - The International Society for Optical Engineering*, volume 6272 III, 2006.

[166] Teledyne Photometrics. Linearity. online, 2016. URL https://www.photometrics.com/resources/learningzone/linearity.

[167] M. V. Plissi, K. A. Strain, C. I. Torrie, N. A. Robertson, S. Killbourn, S. Rowan, S. M. Twyford, H. Ward, K. D. Skeldon, and J. Hough. Aspects of the suspension system for geo 600. *Review of Scientific Instruments*, 69(8):3055–3061, 1998. doi: 10.1063/1.1149054. URL https://doi.org/10.1063/1.1149054.

[168] Jade Powell, Sarah E. Gossan, Joshua Logue, and Ik Siong Heng. Inferring the core-collapse supernova explosion mechanism with gravitational waves. *Phys. Rev. D*, 94(12):1–13, 2016.

[169] M. J. D. Powell. An efficient method for finding the minimum of a function of several variables without calculating derivatives. *The Computer Journal*, 7(2):155–162, 01 1964. ISSN 0010-4620. doi: 10.1093/comjnl/7.2.155. URL https://doi.org/10.1093/comjnl/7.2.155.

[170] S. Reid and I.W. Martin. Development of Mirror Coatings for Gravitational Wave Detectors. *Coating*, 6(61), 2016. URL https://doi.org/10.3390/coatings6040061.

[171] R.Malueg. Detector array fixed-pattern noise compensation. US Patent 3,949,162, April 1976.

[172] Gonçalo Rodrigues. *Adaptive Optics with Segmented Deformable Bimorph Mirrors*. PhD thesis, Université Libre de Bruxelles, February 2010.

[173] R.W.P.Drever, J.L.Hall, F.V.Kowalski, J.Hough, G.M.Ford, A.J.Monley, and H.Ward. Laser phase and frequency stabilization using an optical resonator. *Applied Physics B*, 31(2):97–105, 1983.

[174] Bahaa E.A. Saleh and Malvin Carl Teich. *Fundamentals of Photonics*. John Wiley and Sons, Inc, New York, 1991.

[175] Peter R. Saulson. Terrestrial gravitational noise on a gravitational wave antenna. *Phys. Rev. D*, 30:732–736, Aug 1984. doi: 10.1103/PhysRevD.30.732. URL https://link.aps.org/doi/10.1103/PhysRevD.30.732.

[176] Peter R. Saulson. *Fundamentals of Interferometric Gravitational Wave Detectors*. World Scientific, Singapore, 1994.

[177] J.-F. Sauvage, T. Fusco, C. Petit, E. Fedrigo S. Meimon, M. Suarez Valles, M. Kasper, N. Hubin, J.-L. Beuzit, J. Charton, A. Costille, . Rabou P, D. Mouillet, P. Baudoz, T. Buey, A. Sevin, F. Wildi, and K. Dohlen. SAXO, the eXtreme Adaptive Optics System of SPHERE: overview and calibration procedure . In *Proceedings of SPIE - The International Society for Optical Engineering*, volume 7736, 2010.

[178] Bernard Schutz. *The First Course in General Relativity*, chapter 9, pages 203–226. Cambridge University Press, 2009.

[179] Mina Seif, Joseph Main, Jonathan Weigand, Fahim Sadek, Lisa Choe, Chaso Zhang, John Gross, William Luecke, and David McColskey. Nist Technical Note 1907: Temperature-dependent material modeling for strutural steels: formulation and application. Technical Report 1907, National Institute of Standards and Technology, April 2016. URL http://dx.doi.org/10.6028/NIST.TN.1907.

[180] Stuart L. Shapiro and Saul A. Teukosly. *Black Holes, White Dwarfs and Neutron Stars: The Physics of Compact Objects*. Wiley-VCH, Ithaca, New York, 1983.

[181] Julia Sheldakova, Ilya Galaktionov, Alexander Nikitin, Alexey Rukosuev, and Vadim Samarkin Vladimir Toporovsky, Alexis Kudryashov. Stacked-actuators deformable mirror vs bimorph mirror for laser beam shaping. In *International Conference on Space Optics âĂŤ ICSO 2016*, volume 10904, 2019. doi: 10.1117/12.2509521. URL https://doi.org/10.1117/12.2509521.

[182] Daniel Sigg and Nergis Mavalvala. Principles of calculating the dynamical response of misaligned complex resonant optical interferometers. *J. Opt. Soc. Am. A*, 17(9):1642–1649, Sep 2000. doi: 10.1364/JOSAA.17.001642. URL http://josaa.osa.org/abstract.cfm?URI=josaa-17-9-1642.

[183] Daniel Sigg, Nergis Mavalvala, Joseph Giaime, Peter Fritschel, and David Shoemaker. Signal extraction in a power-recycled michelson interferometer with fabry–perot arm cavities by use of a multiple-carrier frontal modulation scheme. *Appl. Opt.*, 37(24):5687–5693, Aug 1998. doi: 10.1364/AO.37.005687. URL http://ao.osa.org/abstract.cfm?URI=ao-37-24-5687.

[184] Jean-Christophe Sinquin, Jean-Marie LurÃğon, and Claude Guillemard. Deformable mirror technologies for astronomy at cilas. *Proceedings of SPIE - The International Society for Optical Engineering*, 7015, 07 2008. doi: 10.1117/12.787400.

[185] Bram Slagmolen. *Direct Measurement of Spectral Distribution of Thermal Noise*. PhD thesis, The Australian National University, December 2004.

[186] Bram J. J. Slagmolen, Adam J. Mullavey, John Miller, David E. McClelland, and Peter Fritschel. Tip-tilt mirror suspension: Beam steering for advanced laser interferometer gravitational wave observatory sensing and control signals. *Review of Scientific Instruments*, 82(12):125108, 2011. doi: 10.1063/1.3669532. URL https://doi.org/10.1063/1.3669532.

[187] M S Stefszky, C M Mow-Lowry, S S Y Chua, D A Shaddock, B C Buchler, H Vahlbruch, A Khalaidovski, R Schnabel, P K Lam, and D E McClelland. Balanced homodyne detection of optical quantum states at audio-band frequencies and below. *Classical and Quantum Gravity*, 29(14):145015, jun 2012. doi: 10.1088/0264-9381/29/14/145015. URL https://doi.org/10.1088%2F0264-9381%2F29%2F14%2F145015.

[188] J. Steinlechner. Development of mirror coatings for gravitational-wave detectors. *Philosophical Transactions of the Royal Society A: Mathematical, Physical and Engineering Sciences*, 376(2120), April 2018. URL https://doi.org/10.1098/rsta.2017.0282.

[189] Sebastian Steinlechner, Bryan W. Barr, Angus S. Bell, Stefan L. Danilishin, Andreas Gläfke, Christian Gräf, Jan-Simon Hennig, E. Alasdair Houston, Sabina H. Huttner, Sean S. Leavey, Daniela Pascucci, Borja Sorazu, Andrew Spencer, Kenneth A. Strain, Jennifer Wright, and Stefan Hild. Local-oscillator noise coupling in balanced homodyne readout for advanced gravitational wave detectors. *Phys. Rev. D*, 92:072009, Oct 2015. doi: 10.1103/PhysRevD.92.072009. URL https://link.aps.org/doi/10.1103/PhysRevD.92.072009.

[190] Philip C. L. Stephenson. Recurrence relations for the cartesian derivatives of the zernike polynomials. *J. Opt. Soc. Am. A*, 31(4):708–715, Apr 2014. doi: 10.

1364/JOSAA.31.000708. URL http://josaa.osa.org/abstract.cfm?URI=josaa-31-4-708.

[191] Kenneth A. Strain, Guido Müller, Tom Delker, David H. Reitze, David B. Tanner, James E. Mason, Phil A. Willems, Daniel A. Shaddock, Malcolm B. Gray, Conor Mow-Lowry, and David E. McClelland. Sensing and control in dual-recycling laser interferometer gravitational-wave detectors. *Appl. Opt.*, 42(7):1244–1256, Mar 2003. doi: 10.1364/AO.42.001244. URL http://ao.osa.org/abstract.cfm?URI=ao-42-7-1244.

[192] E. Suhir. Stresses in Bi-Metal Thermostats. *Transactions of the ASME*, 53, September 1986.

[193] E. Suhir. Interfacial stresses in bimetal thermostats. *Journal of Applied Mechanics*, 56:595, 1989. doi: 10.1115/1.3176133.

[194] ANDOR Technology. ANDOR zyla 4.2 specification, 2015.

[195] ANDOR Technology. *Zyla sCMOS Hardwire Guide*, 2015.

[196] MATWEB. Aluminum 6061-T6; 6061-T651, 2019. URL http://www.matweb.com/search/datasheet.aspx?matguid=b8d536e0b9b54bd7b69e4124d8f1d20a. Accessed on: 12 February 2019.

[197] A Thuring and Lastzka. Just another mode matching tool (jammt), 2011. URL http://www.sr.bham.ac.uk/dokuwiki/doku.php?id=geosim:jammt.

[198] S. Timoshenko. Analysis of bi-metal thermostats. *J. Opt. Soc. Am.*, 11 (3):233–255, Sep 1925. doi: 10.1364/JOSA.11.000233. URL http://www.osapublishing.org/abstract.cfm?URI=josa-11-3-233.

[199] S. Timoshenko and S. Woinowsky-Krieger. *Theory of Plates and Shells*. McGraw-Hill, New York, USA, 1959.

[200] Calum Torrie. *Development of Suspension for the GEO 600 Gravitaional Wave Detector*. PhD thesis, Department of Physics and Astronomy, University of Glasgow, 2000.

[201] Calum Torrie, Eduardo Sanchez, and Don Griffith. Top Level Conceptual Layout of A+. Drawing, June 2019. URL https://dcc.ligo.org/LIGO-D1800027. version 18.

[202] G. Vajente. Crackling noise in advanced gravitational wave detectors: A model of the steel cantilevers used in the test mass suspensions. *Phys. Rev. D*, 96:022003, Jul 2017. doi: 10.1103/PhysRevD.96.022003. URL https://link.aps.org/doi/10.1103/PhysRevD.96.022003.

[203] Gabriele Vajente. Thoughts on the phase camera. Presentation, June 2019. URL https://dcc.ligo.org/LIGO-G1901154. version 1.

[204] L van der Schaaf, K Agatsuma, M van Beuzekom, M Gebyehu, and J van den Brand. Advanced virgo phase cameras. *Journal of Physics: Conference Series*, 718, July 2008. doi: 10.1088/1742-6596/718/7/072008. URL http://iopscience.iop.org/article/10.1088/1742-6596/718/7/072008/pdf.

[205] Daniel Vander-Hyde. TCS commissioning for o3. Presentation, March 2019. URL https://dcc.ligo.org/LIGO-G1900287. version 1.

[206] Peter Veitch and Aidan Brooks. Tcs hartmann sensor software architecture. Technical Report T1000155, LIGO Scientific Collaboration, May 2015. URL https://dcc.ligo.org/LIGO-T1000155. version 5.

[207] Nicole Virdone, Juri Agresti, Alessandro Bertolini, Riccardo DeSalvo, Rosalia Stellacci, Justin Kamp, Maddalena Mantovani, Virginio Sannibale, Marco Tarallo, and Lisa Kaltenegger. Extended-time-scale creep measurement on maraging cantilever blade springs. *Nuclear Instruments and Methods in Physics Research Section A: Accelerators, Spectrometers, Detectors and Associated Equipment*, 593(3):597 – 607, 2008. ISSN 0168-9002. doi: https://doi.org/10.1016/j.nima.2008.05.032. URL http://www.sciencedirect.com/science/article/pii/S016890020800778X.

[208] Thomas Vo, Daniel Brown, Daniel Vander-Hyde, and Georgia Mansell. 2018-11-30 TCS settings. Presentation, November 2018. URL https://dcc.ligo.org/LIGO-G1802250. version 2.

[209] Andrew Wade. *Quantum Limited Measurements in Gravitational Wave Detectors*. PhD thesis, Australian National University, 2016.

[210] Steven Weinberg. *Gravitation and Cosmology: Principles and Applications of General Theory of Relativity*. John Wiley and Sons, Inc., Massachusettes, 1972.

[211] Hiro Yamamoto. Effect of ITM thermal lens in beam reflection. Technical Report T0810007, LIGO Scientific Collaboration, November 2008.

[212] Amnon Yariv. *Optical Electronics*. Oxford University Press, 4th edition, 1991.

[213] Hang Yu. SRC detuning induced by differential ITM thermal lens. Technical Report T1700246, LIGO Scientific Collaboration, May 2017.

[214] Hang Yu, Peter Fritschel, and Vivishek Sudhir. Exploring the BHD readut sensitivity and requirements. Presentation, August 2017. URL https://dcc.ligo.org/LIGO-G1702485. version 1.

[215] Teng Zhang, Hang Yu, Vivishek Sudhir, Calum Torrie, Ken Strain, Hartmut Grote, Koji Arai, Michael Zucker, Rana Adhikari, Sebastian Steinlechner, Joseph Briggs, Peter Fritschel, and Stefan Hild. Plans for the A+ balanced homodyne readout. Presentation, July 2018. URL `https://dcc.ligo.org/LIGO-G1800459`. version 3.

[216] Chunnong Zhao, Li Ju, Qi Fang, Carl Blair, Jiayi Qin, David Blair, Jerome Degallaix, and Hiroaki Yamamoto. Parametric instability in long optical cavities and suppression by dynamic transverse mode frequency modulation. *Phys. Rev. D*, 91:092001, May 2015. doi: 10.1103/PhysRevD.91.092001. URL `https://link.aps.org/doi/10.1103/PhysRevD.91.092001`.